THÈSE

Pour obtenir le grade de

Docteur

Délivré par **UNIVERSITÉ de MONTPELLIER**

Préparée au sein de l'école doctorale
Information, Structures et Systèmes (I2S)

Et de l'unité de recherche
Institut d'Électronique et des Systèmes (IES)

Spécialité: **Électronique**

Présentée par
Raffaello SECONDO

Upgrades of the RadMon V6 and its Integration on a Nanosatellite for the Analysis and the Comparative Study of the CHARM and Low Earth Orbit Environments

Améliorations du RadMon V6 et son intégration dans un nanosatellite pour l'analyse et l'étude comparative des environnements CHARM et LEO.

Soutenue le 24/04/2017 devant le jury composé de

Dr. Laurent DUSSEAU, Professeur, Université de Montpellier-IES/CSU	Directeur de Thèse
Dr. Paul PERONNARD, Ingénieur CERN	Co-encadrant de Thèse
Dr. Robert VAN ZYL, Professeur, Cape Peninsula University of Technology	Rapporteur
Dr. Jean-Luc AUTRAN, Professeur, Université de Provence Aix-Marseille, IM2NP	Rapporteur
Dr. Lionel TORRES, Professeur, Université de Montpellier – LIRMM	Président du Jury
Dr. Jean-Roch VAILLÉ, Maitre des Conférences, Université de Montpellier-IES, Univ. Nîmes	Co-encadrant de Thèse
Dr. Gilles Despaux, Professeur Université de Montpellier-IES	Examinateur
Dr. Eric LORFÉVRE, Ingénieur CNES	Examinateur

Ai miei genitori, Luigi e Fulvia Secondo, per il grande e costante sostegno che continuano a darmi ogni giorno.

. . .

To my parents Luigi and Fulvia Secondo, for their great and continuous support, which they keep giving me every day.

SUMMARY

Radiation fields in the CERN accelerator complex are characterized by mixed particles with broad energy ranges. A Radiation Monitoring System, called "RadMon", was developed for the distributed, on-line measurement of the complex radiation fields and their effect on the electronics installed in areas with a harsh radiation environment. The most recent version of the RadMon revealed a critical issue soon after deployment in the tunnel and the experimental areas. Multiple Cell Upsets (MCUs) arising from micro-latchup events started showing up on the SRAM-based particle flux sensors equipped by the system, ultimately affecting the measurement and resulting in corrupted data and accuracy losses. A study of the generation of this effect was performed, and a solution using an on-line detection and correction algorithm embedded on an FPGA, was evaluated and implemented on the RadMon device.

Furthermore, in the framework of the project CELESTA, a feasibility study was carried out to validate the adaptation of the RadMon to a 1U CubeSat payload. The research was supported by the CERN Knowledge Transfer as a collaboration between the University of Montpellier, the Centre Spatial Universitaire and CERN. Experimental tests were performed at the new CHARM facility, which allows the characterization of small components, as well as large systems, in a mixed-field representative of the Low Earth Orbit.

A stand-alone payload module for 1U CubeSats was developed and equipped with sensors of ionizing dose and high energy hadron fluence. In addition a Latchup Experiment was added on the module as part of the scientific goals of the mission. Results of experimental tests led to the definition of a new procedure for the radiation qualification of small satellites at system level. Details of the characterization and the choice of components are presented together with the approach followed.

The payload is the first small satellite module ever designed at CERN. It represents the first step of an increasing interest towards radiation qualification at CHARM of electronics for low orbit space missions.

Keywords: Radiation Monitoring, Radiation Qualification, Dosimetry, CubeSat, Radiation Environment.

RÉSUMÉ

Les travaux de recherche présentés dans cette thèse ont été réalisée au CERN, l'Organisation Européen pour la Recherche Nucléaire, en collaboration avec le Centre Spatial Universitaire et l'Institut d'Electronique et des systèmes de l'Université de Montpellier. Les objectifs scientifiques s'articulent autour des effets des radiation sur l'électronique, et en particulier sur les systèmes de surveillance de radiations au CERN et les possibles applications de cette technologie pour des petites satellites.

L'activité de recherche a été organisé en suivant deux taches parallèles: premièrement le suivi d'opération, l'amélioration et la mise en place des nouveaux moniteurs de radiations, Radiation Monitors ou "RadMons", récemment installés dans le complexe d'accélérateur du CERN. En deuxième temps une étude de faisabilité a été conduite pour vérifier l'adaptation du système RadMon dans sa dernière version, la version 6 (V6) pour fonctionner comme charge utile scientifique embarquée dans un satellite "CubeSat" ayant 1 unité pour dimension. Le travail de recherche a compris une étude approfondie des capteurs de radiation embarqués sur le module RadMon, ainsi que la qualification sous radiation de plusieurs composants électroniques. Cette étude a permis de converger vers une version optimisée du RadMon, ainsi que la conception d'un module autonome pour la mesure de dose et des effets singuliers en orbite terrestre basse (LEO). Dans ce cadre, les nano et pico satellites sont devenus de plus en plus attrayant pour les missions scientifiques dans l'espace, en raison de leurs caractéristiques de design et conception relativement simples et basées sur composants commerciaux. Le standard CubeSat avec 1 Unité de volume, créé par la Californie Polytechnic State University en 1999, permet désormais la création de satellites avec des performances électriques, masse et intégration mécanique, comparables avec celles des satellites bien plus volumineux, pour des applications dans les domaine de la télécommunication, validation de technologie, sciences et observation de la terre, tout en gardant une très bonne polyvalence et avec des coûtes de conception très bas. Par ailleurs, les CubeSats peuvent être combinés en systèmes plus grands de 3 unités (3U), pour effectuer des tâches complexes en maintenant les avantages des économies de temps, au niveau de planning du projet, et de budget.

L'Université de Montpellier et son Centre Spatial Universitaire (CSU), soutiennent la recherche dans le domaine spatial et les projets conduits par les étudiants depuis le lancement, en 2007, du premier CubeSat français réalisé par des étudiants: ROBUSTA. Suite à la récente popularité du standard, la diffusion entre l'éducation et les secteurs commerciaux et la croissance rapide des petites satellites dans les différents domaines de recherche, le CERN a également commencé à montrer un intérêt vers les CubeSats, et en particulier sur le risque associé aux effets du rayonnement sur les composants électroniques embarqués. En Octobre 2014 CHARM, "CERN High Energy Accelerator Mixed-Field Facility"), nouvelle plateforme de test au CERN pour l'analyse des effets de rayonnement sur l'électronique en champs radiatifs mixtes, a été mise en service. CHARM offre la

possibilité de tester des composants ainsi que des équipements électroniques au niveau du système, dans un champ de particules mixte et avec une large gamme d'énergies, introduisant ainsi une nouvelle approche particulièrement appropriée pour les missions spatiales LEO.

Par conséquence, en 2014, le CERN et son département de transfert de connaissance, ont proposé et financé ce projet de thèse afin de lancer dans l'espace une nouveau CubeSat appelé CELESTA, CERN Latchup Experiment and STudent sAtellite. CELESTA est un CubeSat de 1 unité basé sur la technologie RadMon, la plateforme de test CHARM et la structure du satellite ROBUSTA déjà lancé avec succès dans l'espace. Les objectifs essentiels du projet CELESTA sont énumérés ci-dessous:

1. Le développement et le lancement en orbite basse d'une version de charge utile CubeSat RadMon V6, servant comme module autonome de surveillance de radiations pour des applications spatiales.

2. La vérification de la procédure de qualification du CubeSat à CHARM, avec démonstration que l' environnement spatial LEO peut être reproduit avec confiance dans CHARM.

3. L'ajout d'une expérience scientifique sur la charge utile, pour l'évaluation des effets Single Event Latchups (SEL) sur des mémoires SRAM, visant à une évaluation plus détaillée de l'environnement à différentes altitudes selon une orbite polaire.

4. La caractérisation sous radiation de composants commerciaux, à travers des campagnes de test avec protons focalisés et dans le champ mixte à CHARM, pour sélectionner les appareils avec les meilleures performances électriques. Ce dernier objectif contribue à la création d'une base de données des composants commerciaux utilisés tant pour le design du RadMon que pour sa version charge utile.

Pour ce qui concerne le travail effectué sur l'amélioration des capteurs du RadMon V6, le principal résultat s'agissait de l'étude et intégration sur FPGA d'un algorithme pour la correction en temps réel des événements "burst" des MCU, Multiple Cell Upset. Ce type d'événements se produisent sur les mémoires SRAM actuellement embarquées sur le RadMon V6 et utilisées comme capteurs de fluence des hadrons à haute énergie (HEH). Ce sujet est traité en détail dans le chapitre 3 de cette thèse. L'environnement radiatif et la structure du CERN sont présentées dans le deuxième chapitre, accompagné aussi par une description du RadMon V6, la plateforme CHARM et leur fonctionnement. Les chapitres 4, 5 et 6 décrivent le projet CELESTA et se concentrent sur la recherche et le développement de la charge utile. L'analyse de la mission spatiale est présentée au chapitre 4, fournissant des données obtenues à partir des simulations des orbites proposées, ainsi qu'une analyse des contraintes de la mission et les résultats du premier test à CHARM sur une carte prototype. Les résultats obtenus lors de ce première test ont permis une caractérisation plus approfondie des candidats SRAM et ils ont fourni la base pour l'étude d'un circuit de détection latchup adapté aux missions LEO CubeSat, qui fait

l'objet du chapitre 5. Le chapitre 6 traite de la structure complète du CubeSat, développé en partenariat avec le CSU de Montpellier: chaque sous système du satellite est détaillé en termes de fonctions, caractéristiques électriques, mécaniques et contraintes radiatifs. La conception de la charge utile finale est décrite ainsi que les résultats obtenus lors de l'irradiation à CHARM. Les conclusions de ce travail de thèse sont enfin énumérées au chapitre 7. Le RadMon V6 et son rôle essentiel dans le cadre des activités de recherche au CERN, est le sujet principal de ce travail de thèse. Le CubeSat CELESTA, avec sa charge utile scientifique, est le premier projet nano satellite géré par le CERN et le CSU. Il représente la première étape d'un intérêt croissant au CERN sur les études en champs mixte du matériel scientifique pour des applications spatiales en orbites basses.

Les composants commerciaux, "Commercial Off The Shelf " (COTS), sont largement utilisés au CERN à cause de leurs compromis entre performances électriques et coût. Plusieurs campagnes des tests ont été nécessaires pour sélectionner les meilleurs composants et évaluer leurs caractéristiques et fiabilités sous radiations, afin de choisir les composants pour le design du RadMon V6 et de sa version charge utile à embarquer sur CELESTA. Deux plateformes de tests ont été utilisées pour la qualification sous radiation: la "Proton Irradiation Facility" (PIF) du "Paul Scherrer Institut" (PSI) et CHARM. Au PSI, un faisceau de protons mono-énergétiques, ayant pour diamètre 5 cm, impacte les composants à tester. Le faisceau a une énergie de 230 MeV, qui peut être régulée avec un dégradeur, qui permet d'obtenir des énergies de faisceau plus basses. Le flux de faisceau est mesuré pour calculer précisément la section efficace du composant à tester ainsi que le transfert d'energie dans le composant ou "Linear Energy Transfer" (LET).

Les tests au niveau système dans un champ mixte nécessitent une installation complètement différente. CHARM a été conçu pour répondre à ce besoin: la plateforme a commencé sa phase de mise en service pour la première fois vers la fin de 2014 et il est en pleine activité depuis 2015. CHARM reçoit un faisceau de protons à 24 GeV provenant de la ligne d'extraction du PS: les particules frappent une cible métallique et un champ secondaire de rayonnement est généré. Ce champ irradie entièrement la salle de test. Ce type de test permit la caractérisation de larges systèmes, par opposition au tests traditionnels avec faisceaux focalisés. L'intensité du champ radiatif peut être modulée par le choix du matériel de la cible: Al ou Cu, ainsi que par l'utilisation de quatre plaques de blindage (deux en béton et deux autres en fer) qui peuvent être déplacés à l'intérieur de la salle de test. Les utilisateurs peuvent finalement choisir entre plusieurs emplacements numérotés pour placer les équipements à tester. Les spectres de particules dans la zone de rayonnement peuvent être sélectionnés en connaissant la configuration de CHARM en termes de matériel, cible, type de blindage et numéro d'emplacement.

Les différentes configurations de la plateforme sont pré-calculées par des simulations FLUKA et vérifiées lors des mesures effectués avec les RadMons. Par conséquence CHARM permet de répliquer un grand nombre d'environnements réels de rayonnement: espace en orbite terrestre basse, atmosphère, sol, avioniques et les environnements utiles pour les applications CERN: le tunnel du "Large Hadron Collider" (LHC), avec ses

zones adjacentes, ainsi que les zones couvertes par blindage sur tout le domaine des accélérateurs. Finalement CHARM est une moyen fiable pour s'assurer du fonctionnement correct des équipements électroniques dans un spectre de particules représentatif de l'environnement retrouvé dans l'application finale, et il représente la pierre angulaire de cette thèse.

Le complexe d'accélérateurs du CERN est divisé en deux zones: les tunnels, où se trouvent les lignes des faisceaux de particules, et les zones expérimentales, avec les détecteurs et les systèmes installées pour les différentes expériences. Le Large HadronCollider (LHC) est le plus grand et puissant accélérateur de particules du monde, le tunnel qui l'héberge a une longueur 27 km et il contient deux anneaux de faisceaux parallèles adjacents qui se croisent en quatre points, chacun contenant un expérience: ATLAS, CMS, LHCb et TOTEM. Avant d'être insérés dans le LHC, les faisceaux de protons sont accélérés initialement par un accélérateur linéaire, le LINAC2, puis par les synchrotrons PSB, PS et SPS.Par conséquence, les zones des tunnels et les zones des expériences sont caractérisées par des champs radiatifs très élevés. Plusieurs facteurs contribuent à la création de ces niveaux de rayonnement, notamment les fragments produits par les collisions entre faisceaux des protons, les pertes provenant naturellement du flux de particules, l'interaction entre le faisceau et les gaz résiduels ou finalement les interactions entre le faisceau et la matière qui se produisent inévitablement dans les systèmes consacrés aux diagnostiques. L'environnement radiatif est caractérisé par un champ mixte de particules comprenant des électrons, des photons, neutrons et hadrons chargés, avec énergies comprises entre le keV et le GeV.

Les effets des rayonnements dans un tel environnement représentent une énorme préoccupation pour le fonctionnement correct de l'ensemble des équipements électroniques installés. L'énergie cinétique des particules impactant les dispositifs de silicium peut créer des dommages dans la structure à semi-conducteurs des circuits intégrés. Par ailleurs la structure de certains composants peut se dégrader avec le dépôt d'énergie résultant du processus d'ionisation, responsable de l'accumulation des charges dans un matériau isolant, en particulier dans le dioxyde de silicium largement présent dans des dispositifs microélectroniques. Enfin les hadrons très énergiques sont capables de déposer de grandes quantités d'énergie par ionisation indirecte, générant ainsi des effets singuliers qui provoquent de graves échecs et forcent le remplacement précoce des composants, résultant des pertes de ressources de temps et de budget. Ces effets nécessitent une action de surveillance constante et efficace sur toutes les zones du CERN ayant un environnement radiatif, mission principale du système de monitoring RadMon.

Le système de surveillance RadMon a été proposé en 2005, dans le cadre du projet du CERN Radiation 2 Electronics (R2E), visant à la conception d'un système fiable, précis et distribué sur tout le réseau du CERN pour l'évaluation de effets des radiations sur l'électronique. Plusieurs campagnes de test ont été réalisées pour caractériser et qualifier des composants commerciaux sous radiations afin de sélectionner les plus appropriés et aboutir enfin à la version actuelle du système, conçue en gardant les aspects de longévité,

maintenabilité et la possibilité de futures mises à jour. Un total de 119 RadMon V6 ont été installés à partir de Juillet 2016 à travers le tunnel du CERN et les zones expérimentales.

Le RadMon V6 mesure les trois principaux effets du rayonnement sur l'électronique: la dose ionisante totale (TID), les dommages dus au déplacement ou "Displacement Damage" (DD) et les effets singulier (SEE). Pour ce qui concerne la TID il y a deux effets principaux qui affectent les appareils électroniques: la production de défauts dans des couches isolantes et l'accumulation des charges positive dans les couches isolantes. En raison de ces effets la structure électrique la plus affectée par les effets de dose est le MOSFET, à la base de la technologie CMOS, qui est devenu dominant sur les circuits intégrés caractérisées par une densité de portes logiques très élevé. Le capteur de TID embarqué sur le RadMon est un MOSFET très sensible à l'accumulation de charges dans le substrat de SiO_2: le RadFET. Dans le RadFET la tension de seuil V_{th}, nécessaire pour créer le canal actif entre "source" et "drain", est directement proportionnelle à la quantité des charges piégées dans le SiO_2, d'où la mesure de dose ionisante. Le DD est relié aux effets de radiation incident qui délogent les atomes dans le réseau cristallin des atomes. Le RadMon V6 utilise des diodes p-i-n pour mesurer le Displacement Damage et l'effet cumulatif de la dose équivalente aux neutrons 1MeV ("1MeV neutron equivalent dose"). Ce dernier effet ne concerne pas le sujet de cette thèse et n'a pas été détaillé dans ce travail de recherche.

Alors que la TID et le DD sont des effets cumulatifs, les effets singuliers ont une nature stochastique qui peut être caractérisée seulement en termes de probabilité des événement par rapport au flux de particules. Plusieurs zones dans le complexe d'accélérateurs du CERN sont caractérisées par des taux réduits en termes de dose et de dépôt d'énergie non ionisants, mais avec de très hauts niveaux de hadrons de haute énergie, au-dessus de 20 MeV, et donc suffisamment énergétiques pour générer une grande quantité des effets singuliers à travers une ionisation directe. À cet égard, les SEE représentent la principale source de défaillances dans l'environnement radiatif du CERN. La principale avancée du capteur du RadMon V6 par rapport à ses versions précédentes, était la nouvelle série de mémoires SRAM Cypress pour l'évaluation de la fluence des hadrons à haute énergie. Le RadMon embarque 4 mémoires SRAM CY62157EV30, réalisées avec technologie 90 nm, pour compter les Single Event Upsets (SEU) et mesurer la fluence des HEH en fonction de la section efficace des mémoires.

Suite à l'installations des premières unités du RadMon V6 en 2014, un grave problème a été observé se produisant sur la nouvelle mémoire Cypress SRAMs: un large nombre d'effets de type Multiple Cell Upset, appelé "burst", ont commencé à apparaître sur la structure des cellules de la mémoire, affectant fortement la précision de mesure de fluence des HEH. Cet effet a nécessité une solution immédiate et efficace, fournissant ainsi la base et la motivation initiale de ce travail de doctorat. La mémoire Cypress CY62157EV30 a été sélectionné en raison de sa haute section efficace avec protons et ses caractéristiques d'insensibilité aux neutrons thermiques, indépendance du niveau de tension d'alimentation et disponibilité sur le marché, caractéristiques ayant une grande

importance dans le contexte d'une application au CERN. Une première campagne de test à PSI a été effectué pour étudier le phénomène des burst sur ces mémoires. Deux lots différents de la CY62157EV30 ont été testés avec une tension d'alimentation de 3.3 V et une énergie de faisceau de 150 MeV.

Lors des tests à PSI un effet en particulier a été montré par l'analyse des résultats: le nombre des "burst" a été plus élevé en présence de hauts flux de particules et avec une période très courte entre chaque lecture/écriture dans la mémoire. Par ailleurs, des "bursts" de MCU affectant un large nombre de cellules et suivant les colonnes dans l'architecture interne de la mémoire, ont été observés lors d'accès aux différentes zones de la mémoire en suivant un adressage physique, i.e. défini par la structure des blocs dans la SRAM. Les résultats ont montré que ce type d'erreur était du à des micro-latchups entre les cellules de la mémoires, résultant en un nombre très élevé de bits d'erreur pendant l'écriture et la lecture de la SRAM. Une étude des paramètres impliqués dans la production de ces événements a permis la formulation d'un algorithme de détection en temps réel pour la correction de ces "bursts".

Compte tenu de la nature des latchups, des événements observés, et la relation entre les colonnes des cellules en erreur et l'architecture interne de la SRAM, un nouveau modèle d'adressage a été développé en accédant aux différents blocs de la SRAM de manière alternative. La mémoire a été séparé en deux zones, situées dans les parties gauche et droite de la mémoire, en mettant en œuvre deux fenêtres de détection et en lisant les cellules de la mémoire sur chaque ligne dans chaque bloc. Avec une alternance entre les blocs de mémoire accédés, le stress électrique sur les cellules actives situées sur la même colonne a été réduite, et aucune erreur a été observée. Cette technique a permis d'être plus rapide et moins chère par rapport aux algorithmes software de post-traitement des données, et a permis la reconnaissance des "bursts" en présence de flux de particules très élevés. Suivant ce résultat, l'algorithme a été mis en œuvre sur le FPGA du RadMon V6 et il a été évalué a PSI ainsi qu'à CHARM dans un champ radiatif mixte, représentatif des zones des tunnels. Les résultats ont prouvé l'efficacité de cette technique de détection et correction des MCU, ce qui a conduit à la conception d'un nouveau firmware pour le RadMon V6 incluant la solution proposée.

Environ 74 unités RadMon V6 ont été reprogrammés ou nouvellement installés dans les tunnels du PSB et SPS, dans les expériences ALICE, HiRadMat et NA62, et dans la zone de test de CHARM. Les données expérimentales recueillies pendant l'opération de ce nouveau firmware, ont montré plusieurs événements "burst" détectés correctement et filtrés, permettant ainsi d'avoir des mesures corrigées des fluences HEH. Par ailleurs, la solution retenue a été particulièrement efficace à faible fluence, où un seul événement observé peut être suffisant pour obtenir 60% d'erreur sur la mesure.

De futures optimisations de l'algorithme ont été prévues pour améliorer la précision de la mesure et réduire la probabilité des MCU, telles que la taille des fenêtres de détection ou une meilleure fractionnement des zones physiques dans la mémoire.

Le deuxième but de ce travail de thèse, le développement d'un RadMon charge utile pour des applications CubeSat en LEO, a été conduit en parallèle avec l'analyse des "burst" sur les mémoires Cypress, les tests sur les différents composants commerciaux à PSI, et la mise à jour des RadMon V6 avec le nouveau firmware.

La stratégie de conception a fait suite à une première étude des paramètres de la mission, conduit afin d'étudier la faisabilité de l'adaptation du RadMon V6 à un module charge utile CubeSat 1U. Les paramètres de mission ont été étudiés par rapport à deux orbites polaires différents: la première circulaire avec apogée et périgée à 600 km, la deuxième elliptique avec apogée 1400 km et périgée 300 km. Les effets des rayonnements sur l'électronique ont été simulé par moyen des logiciels OMERE, STELA, CREME et FASTRAD. La TID par rapport au blindage et structure du satellite a été étudiée avec STELA, CREME et, dans un deuxième temps, avec FASTRAD sur un modèle 3D du CubeSat. OMERE a été utilisé pour estimer les effets singulier par rapport aux capteurs SRAM déjà utilisés sur le RadMon.

Une étude de fiabilité a été conduit à partir d'une carte de test prototype développée sur la base des composants COTS et capteurs du RadMon. Un RadFET avec 100 nm d'épaisseur et une mémoire Cypress CY62157EV30 SRAM ont été embarqués sur le module pour mesurer respectivement la dose ionisante et la fluence des hadrons à haute énergie. Une autre mémoire SRAM, la Brilliance BS62LV1600, a été embarqué pour analyser les effets de Single Event Latchup. Ce type de mémoire a été choisi comme premier candidat pour l'objectif scientifique secondaire de la charge utile, visant une cartographie des événements SEL à différentes altitudes sur une orbite polaire, particulièrement lors de la traversée de l' Anomalie du Atlantique du Sud (SAA) et lorsque le satellite passe à travers les cuspides polaires.

La carte de test a été irradiée à CHARM, avec une cible de cuivre et sans blindage, dans un emplacement de test représentatif de l' environnement LEO. Le test a été conçu pour obtenir une meilleure compréhension des paramètres du système, tels que la consommation de courant, la dégradation par rapport au TID, la caractérisation et calcul des événements et la sensibilité à la température par rapport aux exigences de mission.

Les essais expérimentaux ont montré une dépendance entre les valeurs de tension seuil du RadFET et la température de la carte, en mettant en avant la nécessité d'une caractérisation plus approfondie des effets des basses températures sur le capteur. Un des amplificateurs opérationnels est tombé en panne en raison d'un latchup et l'ADC a fonctionné jusqu'à un TID de 250 Gy. Les résultats expérimentaux ont permis la vérification de la procédure de qualification en champ mixte et l'évaluation d'une première carte prototype, des capteurs et leur fiabilité sous rayonnement, en fournissant une base pour des futures tests sur composants commerciaux et une meilleure compréhension des contraintes de mission. Par ailleurs, la nécessité d'une caractérisation plus détaillée de la mémoire SRAM pour l'expérience latchup a été mis en évidence. L'utilisation d'un ADC dans la chaîne des composants pour la détection des latchup a été inefficace par rapport au consommation de puissance, et une autre solution, ainsi qu'une meilleure compréhension des paramètres pour une détection des SEL efficace, a été nécessaire.

Suivant ce résultat, la section efficace de trois mémoires SRAM, réalisées par Issi, Samsung et Brilliance, a été vérifiée à PSI. Pour ce type de test, les mémoires ont été positionnées comme cible face au faisceau de protons, ayant différentes énergies: 30, 60, 100 et 200 MeV. Les SEL ont été enregistrés en utilisant une configuration de contrôle simple de la tension d'alimentation, ainsi que deux systèmes d'acquisition très rapides développés précisément pour la détection des latchups: le système GUARD de TRAD et le LatMon, réalisé au CERN. L'analyse des données a permis le choix du lot numéro I de la mémoire Brilliance comme meilleure candidate pour la mission CELESTA, en raison de sa section efficace des SEL très élevée avec des protons et de sa faible consommation de courant.

Dans un deuxième temps, une autre carte de test a été réalisé en utilisant uniquement des composants COTS précédemment caractérisée à PSI. Cette carte a été fabriquée pour proposer un nouveau circuit de détection de latchups afin de vérifier sa fonctionnalité à CHARM avec les mémoires SRAM candidats pour l'expérience latchup de la mission.

Les circuits intégrés embarqués sur la carte ont été choisis pour réduire au maximum la consommation d'énergie et la probabilité des événements SET, tout en fonctionnant jusqu'à un maximum de 32 krad (Si). Les deux Lots I et II de la SRAM Brilliance BS62LV1600, ainsi que la SRAM Issi IS61LV5128AL, ont été irradiés à CHARM avec le circuit de détection des latchups dans un emplacement représentatif du spectre de particules LEO.

Les résultats ont montré une grande variation entre les lots I et II de la SRAM Brilliance. Par ailleurs, une diminution progressive de la section efficace du Lot II de la SRAM Brilliance a été observé, ce qui suggère des dommages dans la structure du composant. Ce dernier effet nécessitait une investigation plus approfondie et il sera l'objet des études futures. Les résultats obtenus avec la SRAM Brilliance et ses propriétés électriques en termes de consommation de courant et de niveau du courant maximum lors d'une latchup, ont confirmé la choix comme candidat pour la mission. La carte de test a été irradiée jusqu'à une fluence totale de $5.76{\cdot}10^{11}$ heh/cm^2 et une dose cumulés de 37.8 krad (Si). Aucun SET avec période supérieure à 20μs a été observé sur la tension de sortie du LM124, un des amplificateurs opérationnels embarqués. Le slew rate du LM124 et la consommation de courant totale du circuit n'ont pas montré de dégradation a cause du TID. Suivant ces résultats, le circuit de détection des latchups a été choisi pour être embarqué sur le module charge utile. De plus, ce type de circuit et ses composants peuvent être utilisés aussi pour fournir détection ainsi que protection anti-latchups, en particulier sur des dispositifs conçus pour des missions spatiales en orbite LEO et applications avec niveaux de TID et fluence similaires.

Les résultats retournés par les simulations des champs radiatifs, l'analyse des effets de radiation dans l'environnement des orbites proposées, les résultats des tests sur les cartes prototypes à CHARM, la caractérisation des composants commerciaux et des mémoires SRAM et la vérification du circuit de détection des latchups, ont finalement abouti à la conception de la charge utile dans une version définitive. Les composants commerciaux ont été sélectionnés selon les caractéristiques de température de fonctionnement,

entre -20° et 80° C, la consommation de courant, le type de package et la fiabilité sous radiations. Le CubeSat CELESTA est basé sur la plateforme ROBUSTA, et donc il est caractérisé par les mêmes contraintes mécaniques et énergétiques, et il utilise le même protocole de communication. Par conséquence, les spécifications pour la charge utile en termes de masse, puissance et géométrie pour les cartes de chaque sous-système, sont celles imposées par la structure de ROBUSTA. La charge utile finale de CELESTA a été conçue en respectant les exigences de son intégration sur le satellite: le poids de la charge utile est de 60 g, elle consomme en moyenne 162 mW de puissance, 300 mW au maximum, et utilise la géométrie des cartes CubeSat développées par le CSU. Les autres sous-systèmes sur le satellite sont: le module de communication et de gestion des télémétries (TTC), le module de gestion de la puissance et de lancement des antennes (EPS), et le contrôleur de la communication entre les différents systèmes (ODBH).

Le protocole de communication utilisé est le bus CAN, développé par BOSCH. Toutes les cartes utilisent un contrôleur CAN pour envoyer des messages à l'OBDH et finalement interagir avec la station sol, localisé à Montpellier dans le bâtiment du CSU. L'interface CAN de la charge utile RadMon a été intégrée dans le firmware du FPGA, en suivant la structure de gestion des messages et des trames CAN utilisée sur ROBUSTA. Tous le firmware de la charge utile, comme pour le RadMon, a été durci en utilisant la triplication des registres (TMR).

La charge utile a été divisée en deux cartes: une carte mère, avec l'FPGA, l'ADC et les régulateurs de tension, et une carte "mezzanine", avec les capteurs, notamment un RadFET 100 nm, une lot II Cypress CY62157EV30 pour la mesure de fluence HEH, et deux BS62LV1600 Brilliance SRAM pour l'expérience latchup. Les simulations FASTRAD effectuées par le CSU de Montpellier ont montré une dose totale estimée à 84 Gy, dans le pire cas pour la mission CELESTA en orbite elliptique, d'où cette valeur a été prise comme valeur TID critique à atteindre lors de la qualification a CHARM en champ mixte.

Une configuration du CubeSat CELESTA partiellement assemblé a été réalisée en utilisant le fond de panier principal du CubeSat, une module charge utile et un module OBDH, visant à une vérification sous radiations de l'ensemble du satellite, le fonctionnement du protocole de communication et de l'interface CAN, l'évaluation des latchups et des événements destructifs et l'observation de la consommation de courant en fonction de la TID. Le CubeSat partiel a été placé à CHARM et a été irradié pendant 6 jours, en utilisant trois configurations de CHARM avec des niveaux de fluence des particules de plus en plus élevés. Le niveau de TID critique a été atteint, et tout le système, OBDH et module charge utile, a fonctionné sans défaillance majeure jusqu'à 140 Gy et une fluence totale de $3.5{\cdot}10^{11}$ heh/cm^2, bien au dessus des niveaux prévus pour la mission. Plusieurs événements se sont produits sur l' OBDH qui ont nécessité un reset général du satellite. Par ailleurs, un des convertisseurs de tension sur la charge utile, le TPS62125, est tombé en panne juste au dessus des niveaux de TID et de fluence finales, résultant en un perte des données et de communication par la carte mère de la charge utile. À cet égard le test a été très effectif: il a mis en évidence les points faibles du design, les composant commerciaux critiques et la nécessité d'un watchdog pour les resets, finalement en montrant

l'efficacité de la procédure de test en champ radiatif mixte. La communication avec le bus CAN et la fonctionnalité de la charge utile ont été vérifiées. Le FPGA a été programmé en utilisant 50% de sa capacité disponible, donc plus d'espace sera disponible pour des améliorations futures, comme l'inclusion de l'algorithme de détection des "burst" ou le conditionnement des autres capteurs, par exemple des capteurs de TID de type "floating gate".

Le test a CHARM avec les deux modules a complété l'étude des faiblesses du système en termes des effets de radiation sur les composants électroniques et au niveau système. Le lancement de CELESTA dans l'espace est prévu pour le 2018, et un test final avec le satellite complet est prévu en 2017 à CHARM, avec le bût de vérifier entièrement la fonctionnalité du satellite dans un environnement radiatif mixte.

Mots clefs: Surveillance des radiation, Qualification Composants Electroniques, Dosimetrie, CubeSat, Environnement Radiatif.

Contents

Contents xv

List of Figures xvii

List of Tables xxiii

1 Introduction 1

2 The Radiation Environment and Monitoring at CERN 7

2.1 | **The CERN Radiation Environment and its Related Effects** 7

2.2 | **Radiation Effects on Electronics** 12

2.2.1 | Total Ionization Dose Effects 12

2.2.2 | Single Event Effects: Description and Mechanisms 14

2.2.3 | Displacement Damage Effects 17

2.3 | **Radiation Monitoring at CERN: State of the Art** 17

2.3.1 | The Radiation Monitor (RadMon) V6 19

2.3.2 | RadMon V6 Installations in the CERN Areas 23

2.4 | **The CHARM Mixed-Field Facility** 25

2.5 | **Testing at the PSI-PIF Facility** 28

2.6 | **Conclusions** 28

3 Burst Detection and Correction on the RadMon V6 HEH Fluence Sensors 31

3.1 | **The Problem: Multiple Cell Upset Burst Events** 31

3.1.1 | SRAM Memories Characterization at PSI-PIF 33

3.2 | **The Proposed Algorithm for Burst Detection on CY62157EV30 SRAM Memories** 36

3.2.1 | Tests in Dynamic Mode on Lots I And II of Cypress CY62157EV30 . 39

3.2.2 | Burst Detection Through a Statistical Approach 43

3.2.3 | Burst Detection With Alternate Block Addressing 43

3.2.4 | Evaluation of the Corrected Cross-Section 46

3.3 | **2016 Results of the Upgraded RadMONs in the Tunnel and Experimental Areas** 48

3.3.1 | Validation of the Algorithm on a RadMon V6 Unit 48

3.3.2 | Results in the SPS Tunnel 50

3.3.3 | Results in the Experimental Areas ... 52
3.3.4 | Future Optimizations of the RadMon V6 Sensors ... 54
3.4 | Conclusions ... **55**

4 A Qualification Procedure For Nanosatellites At CHARM ... **57**
4.1 | The CELESTA Mission ... **57**
4.1.1 | The Space and Low Earth Orbit Environment ... 59
4.2 | Mission Constraints Analysis ... **61**
4.2.1 | Evaluation of the Orbits ... 61
4.3 | The CELESTA Test Board ... **67**
4.4 | Experimental Setup and CHARM Configuration ... **70**
4.5 | Test Board Experimental Results ... **73**
4.6 | Conclusions ... **76**

5 Single Event Latchup Detection on Commercial SRAMs ... **79**
5.1 | Single Event Latchup Detection Techniques ... **79**
5.1.1 | Current Monitoring Setup ... 80
5.1.2 | The CERN LatMon System ... 81
5.1.3 | The Proposed Circuit for SEL Detection ... 82
5.2 | SEL Test Strategy in a Mixed-Field ... **83**
5.3 | Results of the SRAM Experimental Tests ... **86**
5.3.1 | PSI Results with a Proton Mono-Energetic Beam ... 86
5.3.2 | SRAM Test Results at CHARM ... 88
5.4 | Conclusions ... **92**

6 The CELESTA 1U CubeSat Radiation Qualification ... **95**
6.1 | The CELESTA CubeSat Structure ... **95**
6.1.1 | The Final CELESTA Payload ... 99
6.2 | Experimental Tests Of The CELESTA Payload ... **105**
6.2.1 | The Payload Setup At CHARM ... 105
6.2.2 | Test Results Of The CELESTA Payload And OBDH Modules ... 109
6.3 | Conclusions ... **114**

7 Conclusions ... **117**

A Overview of the MCU burst events shapes **123**

B Compendium of experimental tests on candidate COTS devices **129**

Bibliography ... **143**

LIST OF FIGURES

1.1 The CERN complex with its particle accelerators and experimental areas.[**source**: https://home.cern/] 4

2.1 CERN radiation levels per year expressed in terms of TID, HEH and 1-MeV neutron equivalent fuences. The International Space Station HEH yearly fluence is indicated as a figure of merit [**source** [1]]. 9
2.2 FLUKA simulated lethargy spectra for hadrons at an LHC tunnel location. The different shaded regions represent approximately thermal neutrons (gray), intermediate neutrons (blue) and HEH fluxes (red).[**source** [2]]. 10
2.3 The LHC areas and the associated impact of radiation effects on the installed electronics. 11
2.4 Energy band diagram of a MOS system on a p-substrate, biased at a positive voltage. [**source** [3]]. 13
2.5 Schematic of two cross-coupled inverters in CMOS technology, a red bolt highlights a sensitive node of the structure. 15
2.6 Scheme of a p-n-p-n parasitic structure in an N-well bulk CMOS Inverter (a), and the corresponding SCR bipolar network (b). **[source]**: https://en.wikipedia.org. . 17
2.7 The three boards making up the RadMon V6 System: Power, Main and Sensor boards. 20
2.8 The fully assembled Radiation Monitoring V6 System. 21
2.9 Functional structure of the RadMon V6. 21
2.10 The RadMon V6 system sensors and its deported module. 22
2.11 Schematic of the RadFET sensor acquisition network. 23
2.12 RadMon V6 modules installed in the PSB (a), PS (b) and SPS (c) tunnel areas. . . . 24
2.13 The CHARM Irradiation Area, showing the beam injection line, the four movable shieldings and the numbered test locations in the access corridor and irradiation area. 25
2.14 View of the inside of the CHARM irradiation area. The movable shieldings, test locations and AVT path are indicated. 26
2.15 A plot of the reverse integral spectra for several test configurations at CHARM (grey shaded area), compared with different radiation environments, normalised to 1 at 20 MeV. **[source]**: [4]. 27

3.1 Integrated SEU counts (top) and SEU rate (bottom) measured by one RadMon V6 (labelled "SIMA.LI04S") during operation in the SPS from April 1st 2015 to December 12th 2015. The red areas correspond to large MCU events involving high quantity of bit flips. 33

3.2 Setup used during test campaigns at PSI. An Agilent Power supply and an FPGA ProASIC3 tester board are connected to the DUT. 34
3.3 Examples of a small cluster of bit upsets (a) and a burst event characterized by several single bit upsets following a rectangular geometrical shape (b). 36
3.4 Analysis of the number of bit upsets (on the left) and rows (on the right) affected per MCU event (both types A and B). 37
3.5 The detection window size is 64 bits x 10 rows. It moves by steps of one row within the same physical block. When the number of SEUs in the window is above Th_{SEU} a burst is detected. 38
3.6 Example of a burst event involving several bit upsets on adjacent rows and error bits located on the same column arrays. Memory blocks are highlighted with different shades of grey. 41
3.7 Number of bit upsets per SRAM block, SEU_{block} (green) and SEU_{burst} per SRAM block (red) in one example run. All SEU recorded during irradiation are shown. . 44
3.8 Scheme of the alternated addressing pattern: two rectangular filters move sequentially following the block lines (from top to bottom in the higher half, and from bottom to top in the lower half), while alternating the addressed cells between the left and right sectors of the memory. 45
3.9 SEU map of the SRAM during irradiation with an alternate blocks algorithm. The rectangles correspond to the detection window at the location where a burst event was recognized. 46
3.10 cross-sections σ (blue) and σ_{corr} (red) vs particle fluence (top plot). SEU_{TOT} (blue) and $SEU_{TOT} - SEU_{burst}$ (red) evaluated at every read cycle of the memory (bottom plot). Fluence is measured in particles (pp) over cm^2. 47
3.11 Percentage error vs particle fluence calculated between σ and σ_{corr} with σ_{corr} as reference in a chosen run. At lower fluence values the occurrence of burst events correspond to large errors on the cross-section measurement. Fluence is measured in particles (pp) over cm^2. 47
3.12 Two RadMon V6 units, labelled CHARM-B3 and CHARM-B7, installed in the CHARM irradiation area at position G0. 49
3.13 Total number of SEU recorded by RadMons B3 and B7 during three weeks of irradiation (top), and the SEU rate showing corrected VS not corrected SEU readings (bottom). 49
3.14 SEU rate of the RadMon "1RI01S" in the period April-November 2016. The corrected (blue) and uncorrected SEUs (red) are shown for the period with firmware V2. When firmware V1 was used, no correction was applied and only uncorrected SEU data are given (in blue colour). 50
3.15 The corrected (blue) and uncorrected (red) integrated SEUs between April-November 2016 for RadMon "2LI04S" upgraded with firmware V2 (top), along with the SEU rate (middle) and relative percentage error (bottom). At low fluence levels, a burst event yields a 15% error on the HEH fluence measurement. 51

3.16 The corrected (blue) and uncorrected (red) SEUs between April-November 2016 for RadMon "6RI05S" upgraded with firmware V2 (top), along with the SEU rate (middle) and relative percentage error (bottom). The first burst occurred is enough to yield an error on the fluence measurement of 60%. The filtering algorithm is valid also in the presence of fast varying flux values. 52
3.17 The corrected (blue) and uncorrected (red) SEUs between April-November 2016 for RadMon "4RI05S" upgraded with firmware V2 (top), along with the SEU rate (middle) and relative percentage error (bottom). In presence of higher flux levels, the detection algorithm applies a constant correction reaching in this case up to 34% of the HEH measurement. 53
3.18 The corrected (blue) and uncorrected (red) SEUs of RadMon "B6" upgraded with firmware V2 and located in CHARM position 1 (top), and their relative SEU rates displayed with the facility SEC1 counts (black) VS time (bottom). One large MCU burst (circled in orange) fell out of the filtering action. 54

4.1 Radiation effects on electronics as caused by the three sources of energetic particles in space.[**source**: [1]] 60
4.2 STELA simulation results for the polar circular orbit. 63
4.3 STELA simulation results for the polar elliptical orbit. 63
4.4 Dose rate along the proposed circular orbit. The dose rate values reach a maximum of 10 mrad/sec in the colour scale. 64
4.5 Dose rate along the proposed elliptical orbit. The dose rate values reach a maximum of 100 mrad/sec in the colour scale. 64
4.6 Proton contribution to SEU occurrences simulated with OMERE, considering a Cypress CY62157EV30 SRAM flying in a circular polar orbit. 66
4.7 Heavy Ion contribution to SEU occurrences simulated with OMERE, considering a Cypress CY62157EV30 SRAM flying in a circular polar orbit. 66
4.8 Layout of the first payload test board, with sensors of TID, HEH flux and a latchup experiment. 67
4.9 The hold time, cut time and current threshold quantities involved in the recognition of an SEL event. 69
4.10 Normalized Reversed HEH integral flux for both circular and elliptical orbits, and for test locations 2, 3 and 4 at CHARM. A copper target with "OOOO" shielding were set. 71
4.11 Normalised reverse integral of the HEH spectrum calculated with FLUKA for the PROBA II orbit and three CHARM configurations: copper and aluminium target materials with "CIOO" and "OOOO" shieldings. Test positions R2, R3 and R10 are taken into account. 72
4.12 HEH flux levels in the CHARM irradiation area using a copper target and no shieldings. Test location number 3 is evidenced with a red square. 72
4.13 The test setup in the CHARM irradiation area: the payload module is positioned in location 3 with a RadMon unit installed right above. 73

4.14 Measurement of the TID recorded by the module and the RadMon installed right above. Temperature values are given by the on-board sensor. 74
4.15 ADC voltage reference and TID measured by the RadMon over time. The dose values take into account annealing effects. The periods with no irradiation are discarded. 74
4.16 Measurements of the HEH fluence over TID and HEH flux over time. The dose values are given by the RadMon. The periods in which the beam was stopped are discarded in the analysis. 75
4.17 I_{cc} current consumed by the Brilliance SRAM over time. Several current pulses, even below the set threshold, are visible. 76

5.1 A typical system setup for latchup events detection. 80
5.2 The CERN Latchup Monitoring System (LatMon) board. 81
5.3 Hardware architecture of the LatMon. 82
5.4 The proposed circuit for latchup detection and protection. 83
5.5 CHARM HEH flux normalized at 100 MeV for test locations "4" (or "R4") and "G0", and the expected HEH flux for a 600 km circular LEO orbit with 98° inclination. . 84
5.6 The test setup positioned over test location "R4". The SEL detection board is set over two PCBs connected to an external Power Supply unit. 85
5.7 Results of the SRAM candidates Single Event Latchup cross-section VS energy with a focused proton beam. Values have ≈10% confidence due to count statistics and facility dosimetry. 86
5.8 Examples of SEL events current profiles for each memory under test. 88
5.9 SRAM B latchup events detected on the V_{LAT} signal (grey) and the V_{out} output signal from the LM124 (red). 89
5.10 DUT current waveforms recorded by the power supply control setup for SRAM B, Lot II, #3 (top) and SRAM A #1 (bottom). The current thresholds were set at 10 mA and 50 mA respectively. 90
5.11 Results of tests at CHARM in a mixed-field environment at position 4. Confidence intervals are set at 20% due to the estimation of the fluence values from the proton hit counts on the beam target. 91

6.1 Mechanical structure of the satellite. 96
6.2 Signal connections between each sub-system on the CELESTA CubeSat. 98
6.3 Payload size specification and mechanical constraints. 102
6.4 The CELESTA payload mother board. The FPGA, ADC and mezzanine connectors are highlighted. 103
6.5 The CELESTA full payload module: motherboard and mezzanine boards are attached together. 104
6.6 CAD model of the fully assembled CELESTA CubeSat. The Payload can be located at different positions in front of the EPS. 105
6.7 The CELESTA satellite used during tests at CHARM. The PL and ribbon cable are highlighted in (a), the DOSI area and OBDH module are pointed out in (b). 107

6.8 Example of a "TM Data Transfer" request initiated by the PL. 108
6.9 CHARM setup showing the CELESTA structure with a nearby RadMon (a) and the full rack on position "R5" (b). 109
6.10 The temperature (top left), TID (top right), SEU (bottom left) and SEL (bottom right) recorded by the payload sensors during the test. Red vertical lines point out the times in which the facility was reconfigured, whereas magenta ones the request of a general RESET following an error. 110
6.11 Current consumed by the OBDH during the test. The zoomed area in the purple rectangle shows the current when the OBDH became unresponsive, requiring a general reset. 112
6.12 Current consumed by the PL during the test. Between October 9^{th} and 10^{th} the current raised quickly due to a hardware failure. 113
6.13 The latchup counts (bottom) and calculated cross-sections (top) over the measured fluence for BSI1 and BSI2 SRAMs. The SEL saturation is clearly visible. . . . 114

A.1 caption 125
A.2 Map of the bit upsets on a Lot I CY62157EV30, accessed with physical addressing. Large vertical upset involving several columns in a block were observed. 126
A.3 SRAM map of a Lot II CY62157EV30, accessed using the alternate addressing pattern. Smaller MCU burst clusters are circled in red. 127

B.1 Current consumption measured on the +5V supply of one MAX11046 unit under test. 130
B.2 Voltage acquired on channel 0 by one MAX11046 unit under test. 131
B.3 The test board used for the AD8029/AD8030 tests. A total of 18 units were exposed to the beam while 3 were kept out as reference. 132
B.4 Input bias current of both the AD8029 and AD8030 with a 100 kΩ resistor on the positive input. Chips 15 and 5 were the reference devices. 133
B.5 Current consumption of all the irradiated devices, measured on the +5 V and -5 V supply rails. 133
B.6 Voltage output drift ΔV_{out} of the AD8029/AD803 over TID. Chips 21 and 5 were the reference devices. The input was set at 1 V. 134
B.7 Current consumption measured on the +18 V positive rail of the OPA227 under test. 135

List of Tables

2.1 HEH annual fluxes for different radiation environments. 9
2.2 Expected worst-case annual radiation levels to electronics for nominal LHC operation conditions. [**source**: [5]] 11

3.1 DUT Identification and operating conditions 34
3.2 Results of proton tests in static and dynamic modes of the IS61WV5128 SRAM Memory. 34
3.3 Results of proton tests in static mode of the CYLE1049DV3 SRAM Memory. 35
3.4 Results of proton tests in static and dynamic mode of the CY7C1059DV33 SRAM Memory. 35
3.5 Results of proton tests in static mode of the KM684000BLT SRAM Memory. 35
3.6 Test results on CY62157EV30 Lots I and II - SRAM rewriting disabled 40
3.7 Test Results with Dynamic Mode on Lot II 42
3.8 Test Results on Lot II and initial pattern 0xFFFF 42
3.9 Test Results on Lot II and alternate blocks addressing 46

4.1 Parameters of the two selected polar orbits. 62
4.2 STELA simulation parameters 62
4.3 Summary of the radiative environment predicted dose and flux levels. 65
4.4 TID, power and temperature characteristics of the payload test board components 68
4.5 Summary of the timing signals on the Payload Test Board. 70
4.6 HEH flux and CHARM test accelerator factor for positions 2, 3 and 4. 71

5.1 SRAM memory candidates 84
5.2 Four-Parameter Weibull fit to the SEL cross sections for SRAM A, B and C, performed using a non-linear least squares fit. 87
5.3 Predicted in-flight SEL counts for SRAM A, B and C in a 2 year mission in LEO orbit. 87
5.4 Cross-section σ results of tests at location 4 90
5.5 Predicted in-flight SEL counts for SRAM A #1 and SRAM B Lot II #3 in a 2 year mission in LEO orbit. 91
5.6 Cross-section results for SRAM A tested at location "G0". 92

6.1 FASTRAD results on the CELESTA full satellite CAD model. Dose calculation with solid sphere dose curve. 105
6.2 Fluence and dose results returned from the facility measurements. 112

B.1 Parameters of the ADC MAX11046 test at PSI. 130
B.2 Parameters of the OPA227 test at PSI. 135

B.3 Beam parameters, total fluence and TID results of CAN transceiver SN65HVD233DG4 tests. 136
B.4 Events recorded on the CAN transceiver SN65HVD233DG4 test boards. 136
B.5 Results of the CY62167GE30 SRAM PSI test in static mode. 138

ACRONYMS

ALICE A Large Ion Collider Experiment

CELESTA CErn Latchup Experiment and STudent sAtellite

CERN European Organization for Nuclear Research

CHARM CErn High energy AcceleRator and Mixed-field facility

CMOS Complementary Metal-Oxide Semiconductor

CMS Compact Muon Solenoid

COTS Commercial Off The Shelf

CSU Centre Spatial Universitaire

EPS Electrical Power Subsystem

FLUKA Fluktuierende Kaskade

HEH High Energy Hadrons

LEO Low Earth Orbit

LEP Large Electron Positron

LET Linear Energy Transfer

LHC Large Hadron Collider

LHCb LHC beauty

MBU Multiple Bit Upsets

MCU Multiple Cell Upsets

OBDH On Board Data Handling

PL PayLoad

POT Protons On Target

PS Proton Synchrotron

PSB Proton Synchrotron Booster

PSI Paul Scherrer Institut

R2E Radiation To Electronics

RadMon Radiation Monitoring System

ROBUSTA Radiation On Bipolar University Satellite Test Application

SEC1 Secondary Emission Counter 1

SEE Single Event Effect

SEL Single Event Latchup

SET Sigle Event Transient

SEU Single Event Upset

SPS Super Proton Synchrotron

TID Total Ionizing Dose

TTC Tracking, Telemetry and Command

1

First Chapter

Introduction

Scientific Background and Overview

The research work and the scientific objectives presented in this thesis are in the field of the effects of radiation on electronics, with focus on high radiation monitoring and small satellite applications. The research activity was carried out at CERN, the European Organization for Nuclear Research, and it was organised in two parallel lines of research: (i) the follow-up, optimization and upgrade of the new Radiation Monitors (RadMons) recently deployed in the CERN accelerator complex, and (ii) the feasibility study, development and test of a version of the CERN RadMon adapted to function as a scientific payload on a small satellite, a 1 Unit (1U) CubeSat. Both tasks involved a thorough characterization of the radiation sensors and a full qualification of several commercial electronics components against radiation, ultimately converging on an optimized version of the CERN RadMon, in terms of hardware and sensors conditioning, and its design as a payload-like stand-alone module for radiation measurement in Low Earth Orbit (LEO) space. In this regard, nano and pico satellites have recently become more and more attractive for scientific missions in space, due to their innovative, relatively simple and cheap design. On the other hand CubeSat based projects often requires a greater than desirable amount of risk associated with the effect of radiation on electronics. Spacecrafts at LEO altitudes are subject to interaction with geomagnetically trapped protons and electrons, thus resulting in the need of testing design components at several ground facilities, a process both expensive and time consuming. In 2014 CERN commissioned the CERN High Energy Accelerator Facility (CHARM), a new facility for the evaluation of small components and large systems in high radiation. CHARM provides the possibility to test at system level in a mixed particle field and within a broad range of energies, thus introducing a new approach in terms of radiation qualification of electronics, particularly fitting for LEO space missions. This research work was carried out in partnership with the University of Montpellier within the "Institut d'Electronique et des Systèmes" (IES)

Laboratory and the "Centre Spatiale Universitaire" (CSU), the University Space Center of Montpellier. The main upgrade of the CERN RadMon, in its latest version, consisted in the study and integration on the system main FPGA of an algorithm for the real-time correction of Multiple Cell Upset "burst" events occurring on the High Energy Hadron (HEH) fluence sensors (i.e. SRAM memories), a major problem diagnosed in the deployment and early operation phase of the device. Further on, the design of the RadMon CubeSat payload started out with the support of the CERN Knowledge Transfer in the framework of the CERN Latchup Experiment and STudent sAtellite (CELESTA) project, a collaboration between the CSU, the University of Montpellier and CERN. The essential goals of the project are listed in the following:

1. The development and launch in LEO of a CubeSat payload version of the CERN RadMon, serving as a stand-alone radiation monitoring module for future small satellites applications.
2. The qualification of the CubeSat at CHARM, hence the demonstration that LEO space radiation environment can be reproduced at the CHARM facility.
3. The addition of an SRAM based Single Event Latchup scientific experiment on the payload, aiming at a further evaluation of the LEO radiation environment at different altitudes along a polar orbit.
4. The radiation characterization of commercial components, through test campaigns with focused protons and in the CHARM mixed-field, to select the devices with the best electrical performances and contribute to build-up a database of qualified commercial components for both the RadMon and its payload version.

The thesis Chapters present the approaches adopted and report experimental results following the structure given below:

Chapter 2 presents the unique radiation environment of the CERN accelerator complex, in particular in the scope of the risks associated to radiation effects on electronics, the main ones being, in the context of this work, Total Ionizing Dose, Single Event Upsets and Single Event Latchups. The most recent version of the Radiation Monitors, the "RadMon V6", is described with the motivations for its design choices in terms of hardware components and radiation sensors. Finally the CHARM facility, the main platform used for experimental tests at the core of this research, is presented.

Chapter 3 addresses the main upgrade of the RadMon V6. The latter is equipped with previously characterized SRAMs as High Energy Hadron fluence monitors. Multiple Cell Upsets arising as "bursts" of Single Event Upset events were observed during early operation of the device. This effect was found to be related to the electrical properties of the chosen components rather than to the physics of particle interactions. An MCU detection and correction algorithm was embedded in the RadMon FPGA to alter the conditioning of the sensors and provide corrected values of the measured particle fluences.

Experimental results of the approach followed and the SRAM candidates analysed are reported. Results from the operation of the upgraded devices in the experimental and accelerator areas are discussed.

Chapter 4, 5 and 6 focus on the research and development of the payload for the CELESTA mission. The space mission analysis is presented in Chapter 4, providing data resulting from simulations of the proposed orbits and the associated foreseen radiation environment. Mission constraints are analysed and discussed, the first prototype test board is described together with the procedure followed for the qualification of electronics at CHARM. Results obtained lead to a deeper characterization of the candidate SRAM components and the proposal of a latchup detection circuit tailored to LEO CubeSat missions, which is the subject of Chapter 5.

Chapter 6 addresses the full satellite structure, developed in partnership with the CSU. Each module of the spacecraft is detailed in terms of its functions and electrical, mechanical and radiation related constraints. The design of the final payload is reported, together with results obtained during irradiation at CHARM. Finally conclusions are listed in Chapter 7.

The CERN RadMon, and its essential role in the framework of the CERN research activities, is the main subject of this work. The launch of CELESTA is foreseen in 2018. The CubeSat, with its scientific payload, is the first small satellite project in which CERN actively took part, and it represents the initial step of a growing interest into radiation testing for space applications at the CERN facilities.

The CERN Accelerator Complex

A particle accelerator is a complex system which uses electromagnetic fields to focus, steer and accelerate elementary particles in order to deliver them to specific experimental areas, or to create collisions that ultimately yield particle fragments captured and analysed by detectors. Electrons and protons are first separated from their atoms and used as a source to form the beam, in particular protons are usually produced starting from hydrogen gas. The energy an electron gains travelling through a potential difference of 1 Volt is defined as 1 electron-Volt (eV, equivalent to $1.6 \cdot 10^{19}$ Joules), which is the standard unit of measurement for the beam energy. An electrical field is applied to the particles of the source in order to guide them towards the first stage of acceleration. Accelerators can be linear (LINAC) or circular, where the accelerator elements are placed as a ring storing one or two beams and allowing their repeated circulation through the structure. Colliders are circular accelerators where two beams travel in opposite directions and then collide at specific points where the two rings meet. The Large Hadron

Collider (LHC) is the world's largest and highest-energy particle accelerator. It was built by the European Organization for Nuclear Research (CERN) near Geneva, across the French-Swiss border. The LHC was completed on July 2008 and tested for the first time on September the 10^{th} 2008 with its first circulating beam [6]. The LHC tunnel contains two adjacent parallel beam rings that intersect at four points, each containing a proton beam. Dipole magnets keep the beams on their circular path, while quadrupole magnets are used to keep the beams focused. Prior to being injected into the main accelerator, particles pass through a series of systems that successively increase their energy. The first stage is the linear particle accelerator LINAC 2, which generates 50 MeV protons and feeds the Proton Synchrotron Booster (PSB), the second stage. From there, protons are accelerated to 1.4 GeV and injected into the Proton Synchrotron (PS), where they reach the extraction energy of 24 GeV. Finally the Super Proton Synchrotron (SPS) is used to further increase the beam energy to 450 GeV, before injecting the beam into the main LHC ring and ultimately reach 7 TeV.

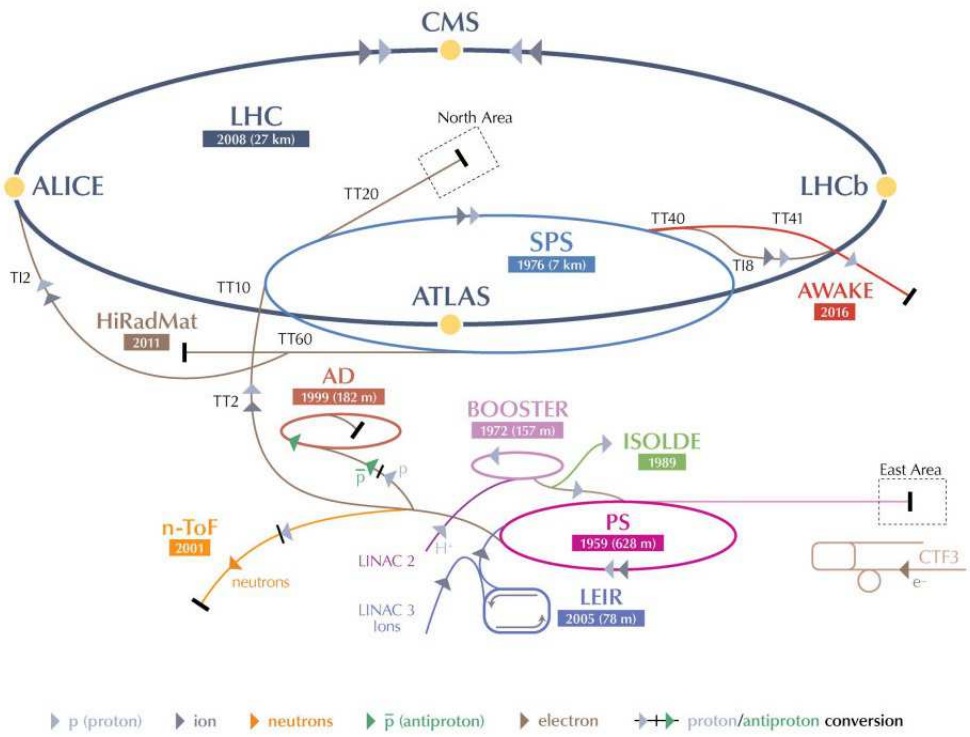

Fig. 1.1: The CERN complex with its particle accelerators and experimental areas.[**source**: https://home.cern/]

Figure 1.1 shows a scheme of the CERN accelerator complex: six detectors were built around the LHC and located in large underground caverns at the interaction points. Two of them, the ATLAS experiment and the Compact Muon Solenoid (CMS), are large,

general purpose particle detectors, devoted to the Higgs boson research. The other experiments, "ALICE", "LHCb", "TOTEM" and "LHCf", are much smaller and pursue other research subjects. On July the 4^{th} 2012, ATLAS and CMS announced separately the discovery of a new particle at the energy of 125 GeV, with a local significance of 5 sigma [7]. Later on, in 2013, the LHC produced data with enough confidence for the publication of the Higgs Boson discovery, the last unobserved particle among those predicted by the Standard Model, thus setting a milestone in the understanding of the Standard Model of Physics and starting new challenges for its confirmation and investigation. A continuous effort for the optimization of the LHC is currently ongoing as part of the "High Luminosity" project: a machine upgrade planned until 2025, aiming at an increase of the integrated luminosity (i.e. the number of collisions over cm^2 that can be produced, a figure of merit of the collider performance) by a factor 10 [8]. In 2016 the LHC beams reached 13 TeV of energy, thus enabling physicists to dig deeper into the study of the Standard Model processes and the understanding of the Higgs boson characteristics [9]. The Radiation Monitoring systems, distributed along the whole CERN tunnel and experimental areas, ultimately play a significant role in the context of the machine performance. This subject will be addressed in detail in the following Chapter.

The Era of Small Satellites

The CubeSat standard for small satellites was created by the California Polytechnic State University in 1999 [10], [11]. A CubeSat spacecraft has limitations of volume, mass and power which are more extreme when compared to larger, more conventional vessels. A 1 Unit CubeSat has the shape of a cube with dimensions 10 cm x 10 cm x 10 cm, a maximum mass of roughly one kilogram and an available power approximately 1 to 2 Watt, provided by solar cells mounted on the structure. On the other hand CubeSats are characterized by a simple modular design, they have shorter project planning schedules, lower costs and less risks, while keeping very good versatility and technical performances for space missions in Low Earth Orbit.

Nowadays most of the demand for small satellites concerns four activities: technology validation, telecommunication, Earth science and Earth observation. Technological demonstration is widespread: CubeSats provide a more suitable and much cheaper solution for short missions targeting the validation of new technologies. Small satellites have a design based on commercial components, rather than space grade ones, hence the associated low costs, moreover they can be combined to form 3 Unit (3U) CubeSats, to carry out complex tasks while holding the advantages of time and budget savings.

A recent trend in the small satellites community involves covering of a large low orbit area with entire networks of CubeSats, called "constellations". The number of CubeSats constellation projects is constantly increasing, examples are the Flock-1 project [12], to create a constellation of over one hundred nanosatellites, or QB50 [13] with fifty

nanosatellites flying in LEO. CubeSats started out in the University field with the purpose to increase the interest into space science, but they are now rapidly assuming a vast commercial aspect. Space agencies (e.g. NASA and ESA) and governmental enterprises are not anymore the only key players, several private companies, such as Clyde Space [14], Kosmotras [15] and 4Skies [16], to name a few, are now providing technology solutions and contributing to the growth of the market. The launch of satellites is not anymore a prerogative of governmental enterprises, but other private institutions have started offering rides into space, for instance SpaceX [17] and RocketLab [18], thus the commercial potential of CubeSats is increasingly exploited and the satellite market is rapidly changing.

Between 2004 and 2013, 75 nanosatellites were launched into space, other 94 only in the three months between November 2013 and January 2014. Starting from June 2014, more than a thousand nanosatellites were scheduled to be launched within the next five years, and as of 2016 a number of 3600 small satellites are expected to be launched over the next ten years. The total market value of these satellites is anticipated to be $22 billion, a 76% increase over that of 2006-2015 [19].

The University of Montpellier, and its Space Center, constantly support student research projects oriented to space science [20]. In January 2007 the ROBUSTA ("Radiation On Bipolar University Satellite Test Application") team took part in the first workshop on small satellites organized at ESA-ESTEC in Noordwijk, Netherlands, among 22 other participants.

ROBUSTA was selected together with 8 CubeSats from other European Universities, with the purpose to carry out several scientific and technological validation missions in space. As a result the ROBUSTA 1U CubeSat was part of the ESA scientific program called "CubeSats for the Vega Maiden Flight" [21], and it was launched on a VEGA rocket on 13th February 2012, from the launching station of Kourou in the French Guiana. In 2016 the Small Systems and Satellites Symposium organised by ESA held a special session called "Small Satellites Go Viral!" [22], arising the question whether small satellites are in fact spreading among the education and commercial sectors similarly to consumer products. Following the evolution of space science and the rapid growth of nano satellites, CERN also started holding an interest in the field. Consequently the CELESTA project was proposed as a scientific payload based on the RadMon technology to be integrated on the same structure used for ROBUSTA, already successfully launched into space.

2

Second Chapter

The Radiation Environment and Monitoring at CERN

2.1 The CERN Radiation Environment and its Related Effects

The CERN accelerator complex is characterized by strong radiation fields both in the tunnel and the experimental areas. Several factors contribute to the creation of high radiation levels, such as the fragments produced by proton on proton collisions, beam losses naturally coming from the stream of particles, the interaction between the beam and the residual gasses, or the collision beam-matter inevitably occurring in systems devoted to diagnostics (e.g. beam screens and scrapers) or collimation along the beam line. The radiation environment generated in such applications is very different than the one encountered for instance into space or medical applications: a mixed-field of particles including electrons, photons, neutrons and charged hadrons is found within the Large Hadron Collider tunnel, in the experiment caverns and in the whole underground areas in general.

Radiation effects on electronic equipments installed in such an environment represent a huge concern. The kinetic energy of particles impinging on silicon devices induce damages within the semiconductor structure of the integrated circuits, causing severe failures and forcing early replacement of components. A secondary effect is generated by the energy deposition deriving from the ionization process, responsible for the accumulation of charges in insulator material, in particular in the silicon dioxide largely present in microelectronics devices. Finally highly energetic hadrons are capable of depositing large amounts of energy through indirect ionization, thus inducing single event phenomena which can severely affect the well functioning of digital circuits, for instance in SRAM memories or in analog to digital converters.

The rare nature of the reaction products that are of interest to high-energy particle physics is due to the high quantity of interactions needed to produce them. The number of interactions per unit surface and time is known as luminosity, and the performance of a collider can be qualified by its ability to deliver integrated luminosity. This parameter is increased through technological enhancements such as more powerful magnets or superconducting links and/or by increasing the operational time, also referred to as availability [23]. Given the large amount of electronics being installed in areas affected by high radiation fields, a CERN wide project called "Radiation To Electronics" (R2E) [24] was initiated to quantify the danger of radiation induced failures, and to mitigate the risk with the goal of less than one failure a week.

The effects of radiation on electronics and the related performance degradation are dependent on several factors: the type of radiation, the rate of the energy deposition in the material, the various types of material present in the device, the contribution to the specific device function and the physical layout or internal structure of the irradiated component. The complex radiation fields involved were simulated using the FLUKA framework [25]. The latter consists in a general purpose Monte Carlo code for the calculation of particle transport and interaction with matter, covering an extended range of applications: from proton and electron accelerator shielding to target design, calorimetry, dosimetry and detector design [26], [27]. The interaction and propagation in matter of photons, electrons, neutrinos, muons and hadrons with energies from 1 keV up to TeV can be estimated on complex geometries using FLUKA code. In this regard FLUKA represents a powerful tool, largely used in this work to benchmark results of measurements retrieved by radiation sensors and provide an estimation of the particle spectra at a specific location.

The proportion of the different particle species, for instance within the LHC fields, depends on the distance and on the angle of interaction, together with the shielding material installed (if present). Electronic components and systems exposed to mixed radiation are subject to three different types of radiation damages: displacement damage (DD), damage from the Total Ionising Dose (TID) and Single Event Effects (SEEs), further detailed in section 2.2. The radiation levels per year, in the injector and tunnel areas, are highlighted in Figure 2.1 in relation to the main agents of radiation damage to electronics. The expected radiation levels drive the choice of electronics used in the hardware design, i.e. COTS or hardened and military/industrial grade components. An example of failure induced by high radiation occurred in 2007 in the CNGS (CERN Neutrinos to Gran Sasso) facility. The failure was caused by high-energy hadrons on the programmable logic controller of the ventilation control system, forcing the experiment to be stopped for 5 days. The successive counter measurements consisted in moving most of the electronics out of CNGS tunnel, creating a radiation safe area and adding shielding.

In terms of Single Event Effects, hadrons are the types of particles most responsible

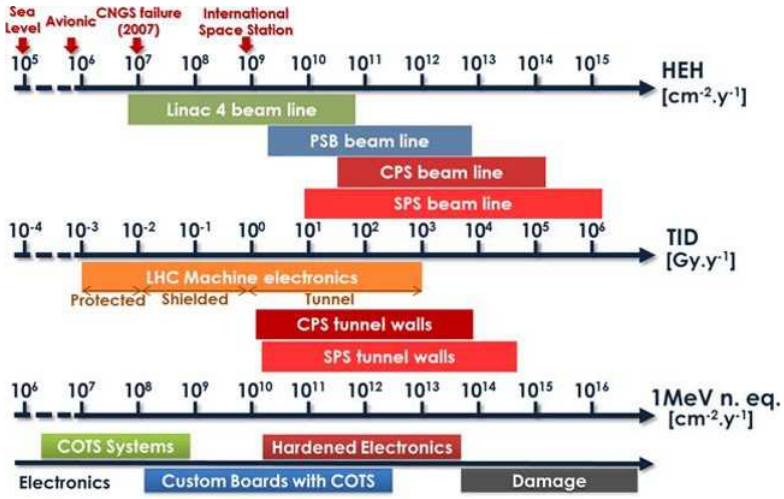

Fig. 2.1: CERN radiation levels per year expressed in terms of TID, HEH and 1-MeV neutron equivalent fuences. The International Space Station HEH yearly fluence is indicated as a figure of merit [**source** [1]].

of inducing SEE within the CERN radiation environment, in particular protons, neutrons, charged pions and kaons. Charged hadrons are mostly found with energies in the MeV range, neutrons instead can extend down to thermal energies, (keV). A typical LHC particle energy spectra can be seen in Figure 2.2 expressed in lethargy form VS energy intervals measured in GeV.

In first approximation the SEE rate can be assumed as proportional to the High Energy Hadron (HEH) flux, defined as the integral hadron flux above 20 MeV. Table 2.1 reports the approximate annual HEH flux values for different radiation environments. HEH flux levels found in ground and avionics environments have orders of magnitudes much lower compared to the ones obtained for the International Space Station (ISS) Orbit or in typical Low Earth Orbit missions. The LHC environment instead is characterized by a large range of HEH fluxes, between 10^6 and 10^{12} highly energetic hadrons per cm^2 per year (heh·cm^{-2}·yr^{-1}). Radiation monitors installed in such areas must then operate with HEH sensors characterized by a high sensitivity in order to measure a wide range of hadron fluxes and energies.

Table 2.1: HEH annual fluxes for different radiation environments.

Spectrum	ϕ_{HEH} **[/cm^2/yr]**
Ground Level	$\approx 2 \cdot 10^5$
Avionics	$\approx 2 \cdot 10^7$
ISS Orbit	$\approx 7 \cdot 10^8$
Polar LEO Orbit (800 km)	$\approx 3 \cdot 10^9$
LHC	$\approx 10^6 - 10^{12}$

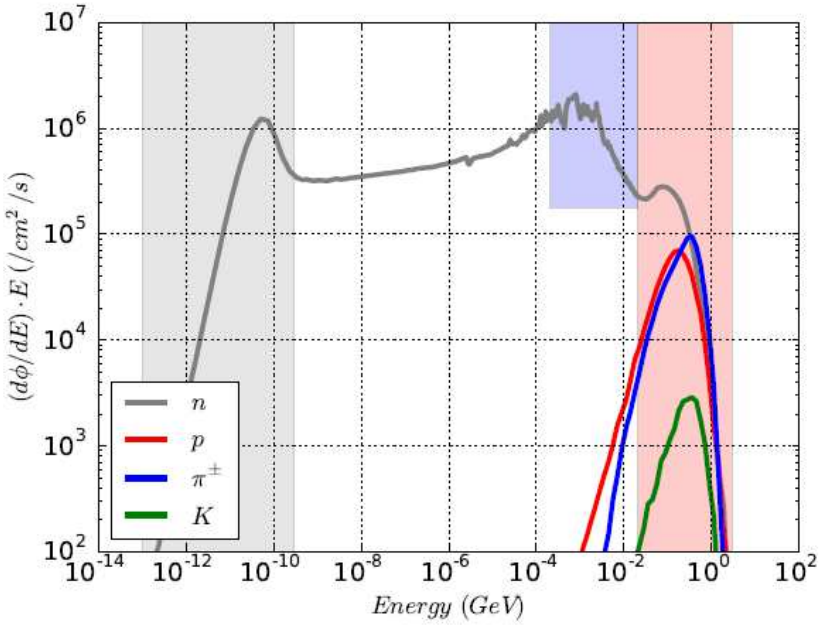

Fig. 2.2: FLUKA simulated lethargy spectra for hadrons at an LHC tunnel location. The different shaded regions represent approximately thermal neutrons (gray), intermediate neutrons (blue) and HEH fluxes (red).[**source** [2]].

Where Total Ionizing Dose and Displacement Damage are cumulative effects, Single Events have a stochastic nature that can be characterized only in terms of probability to occur as a function of accumulated High Energy Hadron Fluence for particles holding enough energy, normally above 20 MeV, to induce direct ionization. The areas adjacent to the accelerator tunnels have dedicated shielded alcoves where electronics equipment can be located occupying several square meters of floor space. These locations are characterized by reduced rates in terms of dose and non-ionizing energy deposition, but large gradients of high energy hadrons (> 20 MeV) are still present. In this regard SEE represent the major source of failures within the CERN radiation environment [24], in particular affecting commercial components or "COTS" (Commercial Off The Shelf), largely used in the design of electronics targeted for installation in high radiation areas [28], [29].

The LHC layout has eight arcs, (ARC), and eight Long Straight Sections, (LSS). In addition, 16 Dispersion Suppressors (DS) are located between the arcs and the LSS zones, aiming at reducing the machine dispersion inside the insertions. In summary the areas exposed to radiation in the LHC ring can be divided into two main categories:

1. The tunnel areas (the ARC and DS).

2. The shielded areas (in the LSS).

Table 2.2: Expected worst-case annual radiation levels to electronics for nominal LHC operation conditions. [**source**: [5]]

Area		ϕ_{HEH} [cm^{-2}·yr^{-1}]	**TID** [Gy·yr^{-1}]
Tunnel	DS	$5 \cdot 10^9$	10
	ARC	$5 \cdot 10^8$	1
Alcoves	UJ	$1 \cdot 10^9$	1
	RR	$1.5 \cdot 10^8$	0.1

The tunnel areas are commonly affected by very high radiation levels, the shielded zones, also referred to as alcoves, can be further subdivided into heavily shielded areas close to the interaction points (UJ areas) and lightly shielded areas (RR areas). Figure 2.3 shows the LHC areas with the associated level of risk of radiation effects on electronics. Table 2.2 shows the expected annual HEH fluences and doses for nominal LHC conditions in the tunnel and alcoves.

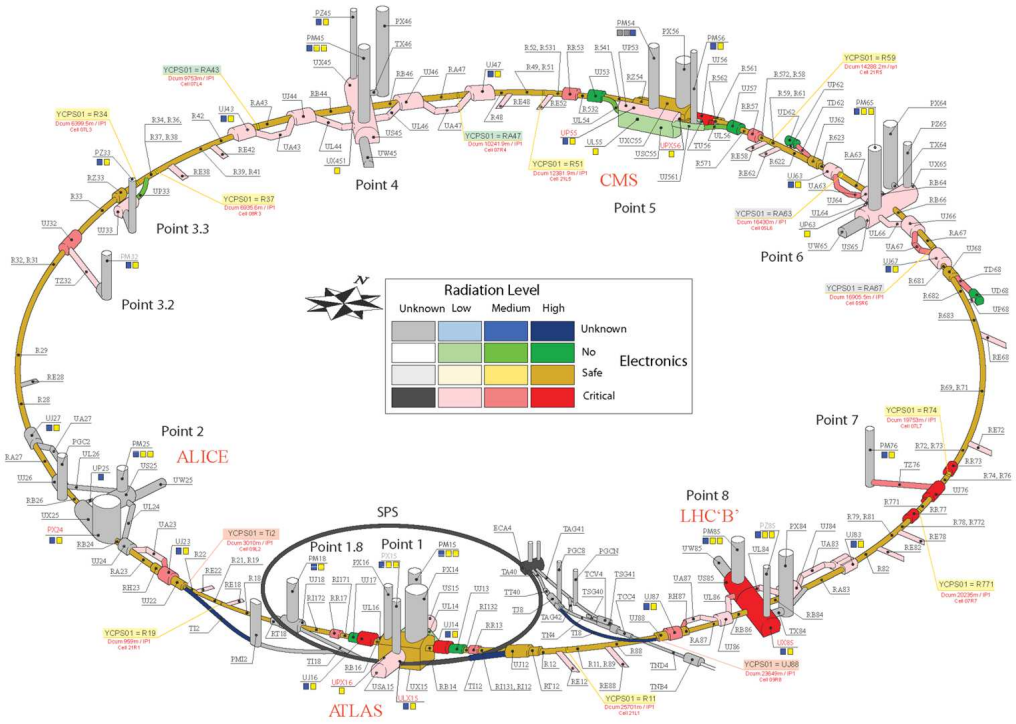

Fig. 2.3: The LHC areas and the associated impact of radiation effects on the installed electronics.

High HEH flux levels up to an order of magnitude of 10^9 cm^{-2}·yr^{-1} are present in the shielded areas along the LHC ring. Neutrons were reported to be the dominating particle in these areas, representing up to 98% of the spectra of the HEH fluence for the

UJ alcoves and 70% to 90% of the spectra for the RR alcoves, [30]. In particular, the radiation environment close to the interaction points of the four main experiments along the LHC, (ALICE, LHCb, CMS and ATLAS), is extremely hostile and a full characterisation of the detectors required to monitor radiation in these areas was carried out in [31]. The radiation fields found at CERN, and described so far, provide the background for the need of a Radiation Monitor deployable in harsh environments, capable of measuring the main agents in terms of radiation damage to electronics in a complex mixed-field. Details of these effects and the relative design choices for the radiation monitor system currently in operation at CERN are given in the following.

2.2 Radiation Effects on Electronics

2.2.1 | Total Ionization Dose Effects

High-energy photons and particles, such as electrons and positrons, are able to deposit large amount of their energy in the material they are interacting with, thus inducing an ionization process. This energy deposition is conventionally defined as Total Ionizing Dose (TID) and measured in Gray (Gy) or rad. 1 Gy corresponds to 100 rad, which is the energy of 1 Joule released in 1 Kg of matter. There are two main effects of TID on electronic devices:

1. The generation of defects in insulating layers.
2. The build up of positive trapped charge in the insulating layers.

The electrical structure most affected by TID is the MOSFET, at the basis of the CMOS (complementary MOS) technology, which has become dominant in the area of digital integrated circuits due to its use in designs characterized by very high gates density and low power. The way ionizing radiation affects MOS devices is mainly related to build up of oxide trapped charge and the increased amount of density of interface states at the oxide boundaries. Figure 2.4 shows a representation of the ionizing radiation damage in SiO_2. When ionizing radiation passes through the oxide, the energy deposited creates electron/hole pairs. After a few picoseconds the generated carriers thermalize, losing much of their energy. Some of the electrons undergo recombination with holes, but the majority are swept quickly out of the oxide by the applied potential, thanks to their high mobility, whereas the heavier and slower holes move inside the oxide in the opposite direction.

The amount of recombination is given by the charge yield, which depends on the electric field, and the type and energy of the incident radiation. A final positive charge is then observed into the oxide, resulting from the unrecombined holes that remained trapped in the strained areas of the oxide close to the interfaces with Si or the gate. This happens because hole transport occurs by hopping through localized states, and

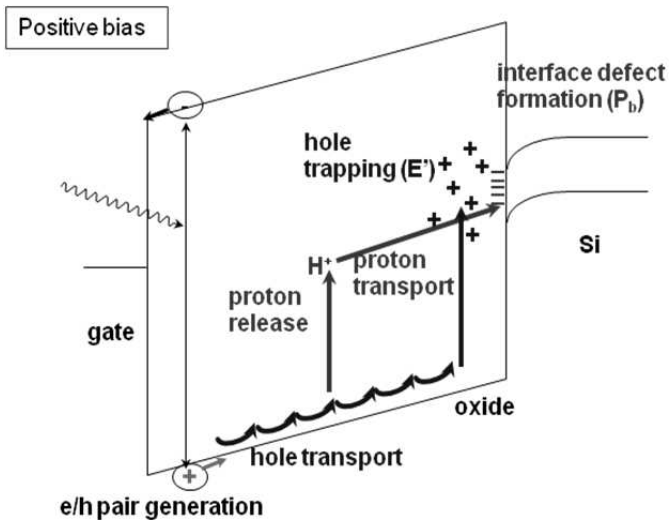

Fig. 2.4: Energy band diagram of a MOS system on a p-substrate, biased at a positive voltage. [**source** [3]].

since holes are positively charged, they are pushed towards the Silicon/Silicon Oxide (Si/SiO_2) or the gate SiO_2 interface depending on the sign of the electric field. Since the number of electron-hole pairs is proportional to the deposited energy, the total damage is also roughly proportional to the total absorbed dose. In particular, in the case of heavy ion irradiation, the incident particles may have enough energy to create a dense cloud of electron-hole pairs in the SiO_2, thus generating very intense transient currents that may result in serious damage of the device itself.

While the net charge trapped in the oxide is always positive, charge balance at the interface depends on the type of MOSFET, whether it is an N- or a P- MOS. When the channel is formed (thus when the gate to source voltage V_{GS} is above the threshold voltage V_{th}), the interface traps are mostly positively charged in a P-MOS and negatively in an N-MOS. Positive charge trapping and generation of interface states can severely affect the behaviour of a MOSFET [32]. Technology evolution, in particular thinning of the gate oxide, has been beneficial for total dose issues in low-voltage CMOS electronics. The effects and the amount of charge trapping are less and less severe as the oxide thickness is scaled down. The dependence of the threshold voltage shift ΔV_{th} on the oxide thickness t_{ox} is expressed in first approximation by the following formula, valid for relatively thick oxides:

$$\Delta V_{th} = -\frac{Q_{ox}}{C_{ox}} \propto t_{ox}^2, \tag{2.1}$$

where C_{ox} is the specific capacitance of the MOS (measured in F/m^2), and Q_{ox} is the trapped charge, which is proportional to the elementary charge q ($1.6 \cdot 10^{-19}$ C), the oxide thickness and the density of oxide trapped holes per unit of area (measured in m^{-2}), [33]. Total dose has a negative impact on bipolar junction transistors (BJT) as

well, but the impact on MOSFET devices is of particular interest for the purpose of this work, since the relation between the absorbed dose and the voltage threshold shift is at the basis of the RadFETs [34], the TID radiation sensors currently equipped and most commonly used on the CERN Radiation Monitors.

2.2.2 | Single Event Effects: Description and Mechanisms

Single Event Effects (SEE) are generally induced by the interaction of an ionizing particle with a sensitive node of an electrical component. Ionizing particles can be primary (such as heavy ions in space environment or alpha particles produced by radioactive isotopes contained in the die or its packaging), or secondary (recoils) created by the nuclear interaction of a particle, like a neutron or a proton with silicon, oxygen or any other atom of the die. SEE occur when the charge resulting from the carriers liberated by the ionizing particle, and collected at the junction or contact, is greater than the charge carrying an elementary information in the component. The Linear Energy Transfer (LET) is an important parameter to quantify the sensitivity of devices in terms of SEE. The energy transfer is the energy deposited per unit length given in MeV·cm^2/mg, and it describes the average energy loss by the ion per unit length of the transverse material. The LET depends on the impinging particle and its kinetic energy, as well as the target material. As a result, the energy of the incident particles must be carefully taken into account when characterizing components against radiation.

Some Single Event Effects are classified as "soft", since they do not induce any physical damage, but only loss of information, such as a bit flip in a memory cell. Other events are defined "hard", since they are capable to induce permanent damage, such as the gate oxide rupture following the strike of a heavy ion. The main classes of soft effects are:

1. Single Event Upset (SEU): the corruption of a single bit in a memory array.
2. Multiple Bit Upset (MBU): the corruption of multiple bits due to a single particle.
3. Single Event Transient (SET): a transient signal induced by an ionizing particle in a combinatorial or analog part of a circuit.

The main classes of hard effects are:

1. Single Event Gate Rupture (SEGR): the rupture of gate oxide, occurring especially in power MOSFETs.
2. Single Event Burnout (SEB): the burnout of a power device.
3. Single Event Latchup (SEL): the activation of parasitic bipolar structures leading to a sudden increase of the supply current.

SEE are generally characterized by their cross-section σ, described as the total area sensitive to the considered effect, independently on how the area is distributed on the sample. The cross-section σ_{SEE} of a component, relative to SEE, is given as

$$\sigma = \frac{number\ of\ events}{particle\ fluence}. \tag{2.2}$$

This relation ties together the number of recorded SEE and the measured particle fluence, and it was widely used in this work, especially in Chapter 3 and Chapter 5, for the calculation of the SEU and SEL cross-sections in SRAM devices. A large literature has been developed around the study of SEE, their mechanism, prediction models and mitigation techniques. The physics and characteristics of each of these effects involve many aspects belonging from different science domains. The work presented in this thesis was focused principally on Single Event Upsets and Single Event Latchups, thus a brief description of these particular effects is given in the following.

Single Event Upsets

The charge released in an SEU event is collected through the so-called funneling mechanism [35], [36]: most of the charge is channelled in at the struck junction, generating a deformation of the junction potential which extends into the substrate. The remaining charges diffuse in the substrate and may undergo recombination. An ionizing particle impinging on a MOSFET structure may alter the internal device field and create a conductive channel between the source and drain terminals. In this case the potential barrier between source and drain would collapse due to funneling, thus generating a transient short circuit current.

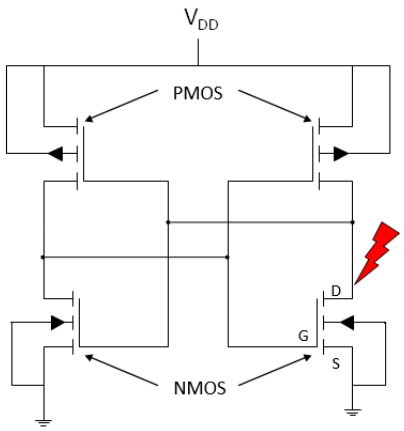

Fig. 2.5: Schematic of two cross-coupled inverters in CMOS technology, a red bolt highlights a sensitive node of the structure.

Figure 2.5 shows the schematic of a general static RAM cell, featuring two cross-coupled inverters in CMOS technology. When a particle strikes the drain electrode of the off N-MOSFET, the released current might decrease the potential at the drain to a level below the switching voltage, hence generating a change of the initial state. Following the recent trends of technology scaling in advanced CMOS technologies, the perturbation of the potential due to a particle strike may cover source, drain and substrate contacts (or even more than a single transistor). Multiple Bits Upsets might be generated by one single hit on the sensitive volume of components, such as in four transistor (4T) or six transistor (6T) SRAM architectures. Higher robustness can be achieved by physically separating the nodes of the single cell at enough distance to prevent a single particle to affect many of them. Memories affected by Single Event Upsets show several bit flips, which are directly related to the flux of ionizing radiation passing through the sensitive area of the die. SRAM memories can therefore be used in mixed-field environments as monitors of the particle fluence, using the relation given in equation 2.2 combined with the knowledge of the component cross-section. This subject will be further described in Chapter 3 in relation to recent upgrades of the CERN HEH fluence monitors.

Single Event Latchups

Bulk CMOS structures contain parasitic bipolar p-n-p and n-p-n transistors. In a typical p-well technology these parasitic transistors can form a p-n-p-n thyristor, also called silicon-controlled rectifier (SCR), in which the base-collector junctions of the bipolars are common, as shown in Figure 2.6. During normal operation the SCR is not active, but an external excitation, such as a pulse of radiation or an electrical condition, may trigger on the thyristor network and force into conduction one of the BJT transistors. As a result a self-maintained low-impedance path is generated between the supply terminal and the ground terminal of the CMOS cell, ultimately yielding a sudden increase of the current consumed by the device.

For the Single Event Latchup to occur, the power supply level must be able to sink or source a current greater than the holding one required to maintain the latch. If no protection mechanism is applied, such as promptly powering down the component, the SEL may end up damaging or completely destroying the MOS device. Several techniques have been studied in order to mitigate this kind of effects at fabrication process, for instance through the reduction of the spreading resistance in the well and in the substrate, or introducing a lightly doped epitaxial layer with a heavily doped substrate instead of using bulk CMOS [37]. A more detailed description of SEL characterization, the systems adopted to detect them and the solutions applied to protect sensitive equipment will be given in Chapter 5. Single Event Latchups, and more in general Single Event Effects, have become more complex to study as the feature size of CMOS processes (the minimum length that can be obtained by the lithography) has been scaled down to sub-

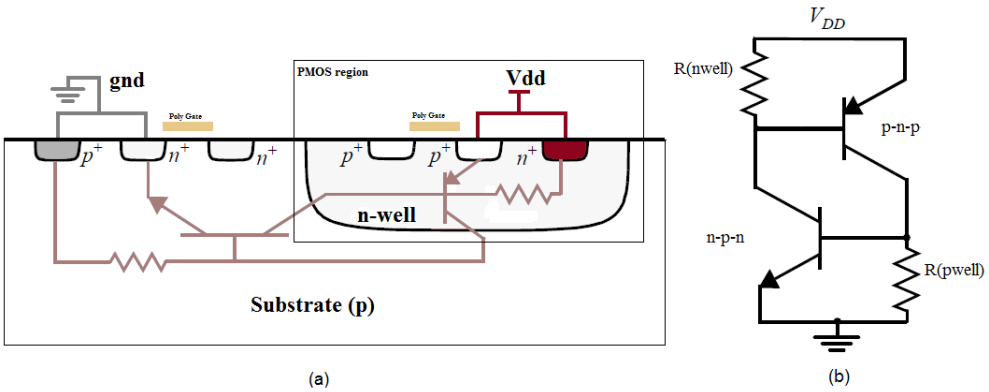

Fig. 2.6: Scheme of a p-n-p-n parasitic structure in an N-well bulk CMOS Inverter (a), and the corresponding SCR bipolar network (b). **[source]**: https://en.wikipedia.org.

micron level.

2.2.3 | Displacement Damage Effects

Displacement Damage occur when incident radiation dislodges atoms from their lattice site. The defects resulting from this process induce a modification of the electronic properties of the component. Neutrons colliding with the atoms of crystalline materials, can lose part of their energy displacing a primary atom out of its lattice site resulting in a silicon interstitial and left over vacancy (the Frenkel pairs) [38]. This pair can migrate through the material and thus provide the building block for extended defects [39]. Displacement Damage is the primary mechanism of device degradation for high energy neutron irradiation, although a certain amount of atomic displacement may be determined by charged particles. The CERN radiation monitors measure the 1 MeV neutron equivalent fluence per cm^2 by means of p-i-n diodes sensors, characterised by a wide undoped intrinsic semiconductor region between a p-type and an n-type semiconductor areas. Displacement effects can highly damage devices based on bulk conduction, such as particle detectors, charged-coupled devices or solar cells. Details of the phenomena involved and their effect on electronics in particle accelerator applications will not be treated further, as they are not the primary focus in this work.

2.3 Radiation Monitoring at CERN: State of the Art

The availability of the Large Hadron Collider (LHC) machine is limited by its operation cycle, where protons needs to be injected and accelerated to their collision energy. After this time the beam is used for physics production in what is known as stable beam

conditions. The duration of an uninterrupted stable beam cycle is roughly 10 to 15 hours after which the beam is dumped due to its loss of intensity in the collision points and other locations in the accelerator. As already discussed in section 2.1, a large amount of equipment highly based on commercial components is installed in the LHC tunnel, in its adjacent areas as well as in the CERN galleries and experimental caverns. During 2011 13 beam dumps per fb^{-1} were attributed to radiation effects on electronics. This number was reduced to roughly 3 radiation dumps per fb^{-1} in 2013 and ultimately to 2 dumps per fb^{-1} in 2015, [5]. This improvement was achieved in the scope of the R2E project through short-term measures such as relocation, shielding reinforcement and replacing of sensitive equipment with more robust versions. In this regard an accurate on-line monitoring of the radiation levels is essential for the early recognition of failures and the study of long-term equipment degradations.

Monitoring systems for accelerators, such as beam loss or beam position monitors, are conceived and designed to provide data for beam steering and beam loss detection, with limited performance for the measurement of the radiation fields and quantities related to damage on electronics. The LHC tunnel and its adjacent areas required a more robust solution, easily deployable and enabling on-line measurements of radiation, hence the rise of the Radiation Monitoring System, referred to as "RadMon". Monitoring radiation levels allows to anticipate possible device degradation and identify instantaneous failures of electronic equipment caused by radiations. In addition, RadMons can be used to verify the shielding efficiency and benchmark FLUKA results. In this regard the RadMons can be used for calibration within test facilities for radiation measurements and quality assurance purposes, for instance they are deployed within the CHARM test facility irradiation area, detailed further in section 2.4. The RadMon project started in 2005 with the first proposal of a Radiation Monitor system within the R2E project framework. In 2007 the RadMon version 5 (V5) was conceived and first installed in the CERN tunnels [40]. Feedback from the on-field usage of the monitor in the first period of LHC operation (2010-2012), and especially new monitoring requirements, lead to the launch of a new design of the RadMon, the version 6 (V6). The RadMon V6 design aimed at an enhanced radiation measurement capability together with an increased longevity and maintainability. Radiation monitors similar to the CERN RadMon are also used in the space community [41],[42]. The RadMon V6 was designed specifically with commercial components, due to their performance, low price and availability, and for the purpose of creating a large distributed network of on-line radiation measurements around the whole complex. Since electronic components exposed to radiation at CERN experience all three types of radiation damages, the RadMon V6 was designed in order to measure TID, the 1 MeV neutron equivalent fluence and the High Energy Hadron fluence. In terms of Single Event Effects, which represented the major threat especially in the shielded areas, the SEU cross-section measurement together with the knowledge of the expected radiation levels provide a good indication in terms of mean time between failures (MTBF) of the system. The upgrades of the SEU sensors of the RadMon V6 and their characterization

will be addressed in detail in chapter 3.

As a system installed in radioactive areas and fully designed with COTS, the RadMon components and its sensors needed a strict process of radiation hardness assurance (RHA) involving characterization and qualification of each device under radiation. A complete and exhaustive specification of the RadMon V6 and characterization of the system is described in [43] and [44]. In order to research suitable components to be included within design of systems deployed in high radiation environments, a database of devices has been build up at CERN throughout several campaigns at different test facilities within the Radiation Working Group [45]. Other sources of data regarding radiation tests on commercial components can be found on the NASA database [46], on the ESA European Space Components Information Exchange System [47] or on specific pages provided by the component manufacturers [48]. The test facilities most used for test campaigns carried out in this work were the Paul Scherrer Institut (PSI) Proton Irradiation Facility (PIF) and the CERN High Energy Accelerator Mixed-field facility (CHARM). PSI is located near Villigen, in Switzerland, and it is used for focused mono energetic tests. The CHARM mixed-field facility is located at CERN and it is further described in section 2.4.

2.3.1 | The Radiation Monitor (RadMon) V6

The RadMon V6 design required an improvement on four different features with respect to the older version V5:

1. A modular architecture for an easy replacement and easy integration of new sensors.
2. Higher radiation tolerant design ($>$ 200 Gy).
3. Remote reconfigurability.
4. Improved measurement accuracy, with particular emphasis on the SEE measurement.

The modular design was achieved breaking down the system into three different printed circuit boards (PCB), each with a different task: a main board, for the monitoring of the current and reference voltages in the sensitive nodes of the electrical networks; a power board, for the distribution of the required voltage supply levels directly from the 220 V plug, and finally a sensor board, for the installation and easy replacement of the radiation sensors. Figure 2.7 shows the three PCB modules of the system and Figure 2.8 shows the fully mounted RadMon V6 device.

The radiation tolerance of the device, up to 200 Gy, was achieved through a full set of test campaigns dedicated to the qualification of each single component included in the

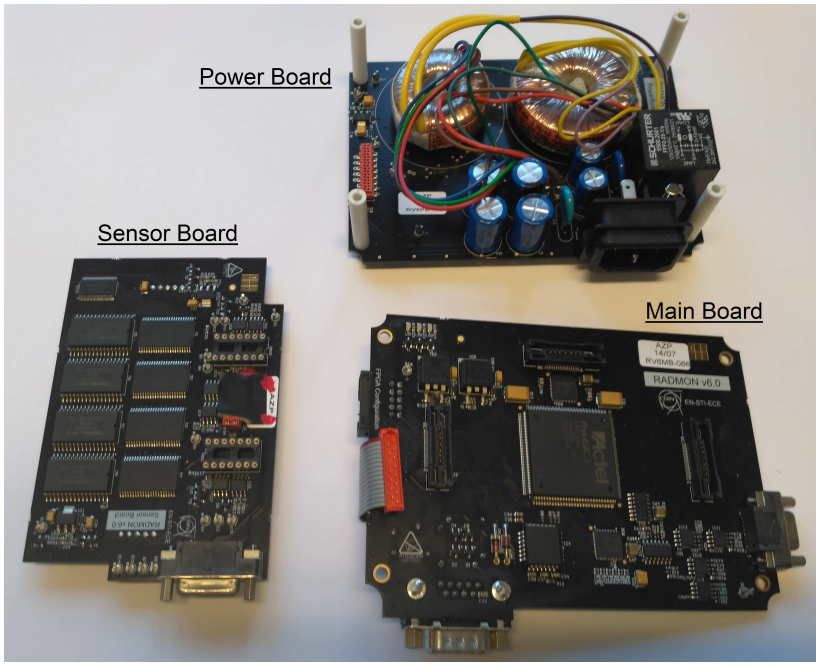

Fig. 2.7: The three boards making up the RadMon V6 System: Power, Main and Sensor boards.

electrical design. The power board is equipped with toroid transformers, passive components and linear regulators providing positive and negative supplies. These components were qualified with care towards Single Event Burnout and Single Event Latchup. Considering all outputs, the power board is capable of supplying a total power of 7 Watts to the whole system. The Main board hosts a ProASIC3 A3P1000 FPGA manufactured by Microsemi and it functions as the driving core. Figure 2.9 shows the interconnections between the three modules and the functional structure of the system. The ProASIC3 is a FLASH based FPGA family largely used in space as well as in avionics and particle accelerator applications for its low susceptibility to SEE. The communication protocol of the RadMon V6 is the WorldFIP, whose interface is embedded in the FPGA, a significant change respect to the RadMon V5, where a MicroFip device was used instead. The Main board also features the FIP driver (the World FIP physical interface), a 16-bit analog-to-digital converter (ADC) and temperature sensors.

The voltage regulators, the current sources, the signal amplifiers and the ADC are the main components, and thus were tested using 230 MeV protons (up to 6-8 $\cdot 10^{11}$ p/cm^2) and 1 MeV neutrons (up to $4 \cdot 10^{12}$ n/cm^2) [49], to verify their robustness against TID, soft and hard SEEs, and DD effects. The ADC plays a fundamental role in the RadMon architecture, and it will be subject of study also in relation to the RadMon adaptation to a 1U CubeSat payload, discussed in Chapters 4, 5 and 6. In particular the 200 Gy TID limit of the RadMon V6 is given by the ADC tolerance to absorbed dose. Two ADC units of the same device, a Maxim MAX11046, were installed: one dedicated to the health monitoring of the system and the second one for the acquisition of the signals coming

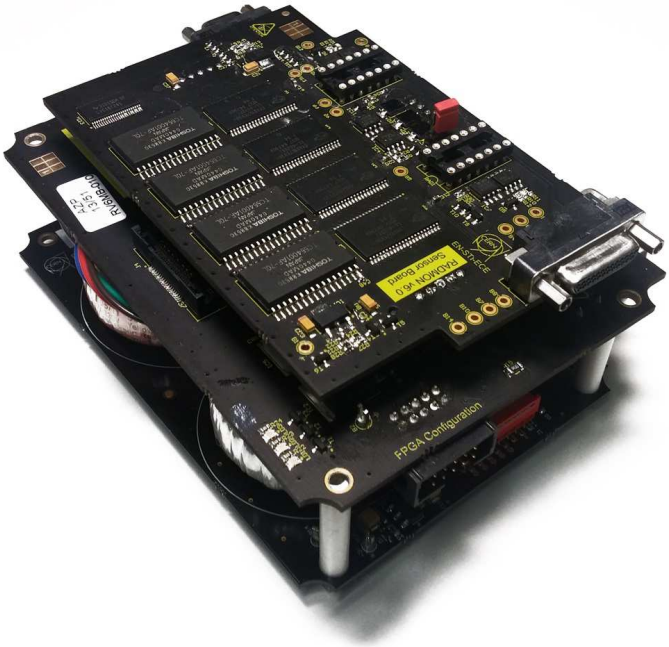

Fig. 2.8: The fully assembled Radiation Monitoring V6 System.

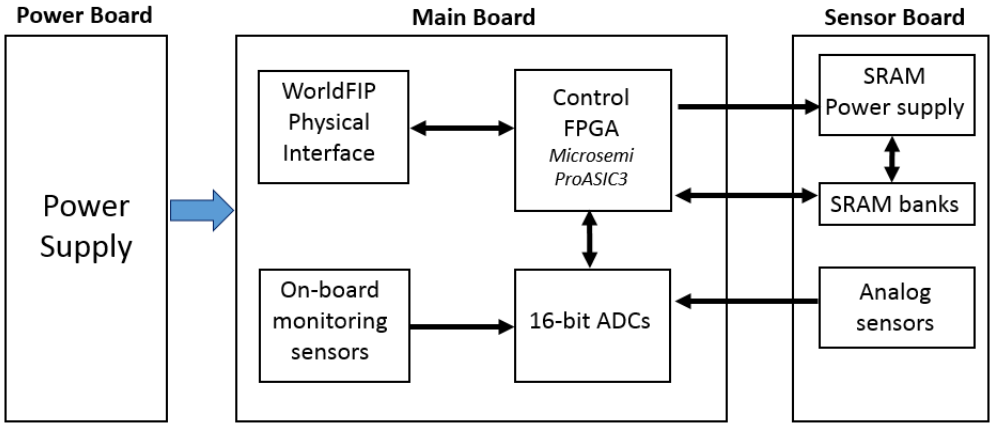

Fig. 2.9: Functional structure of the RadMon V6.

from the sensors. An 8-channels 16-bit ADC configurable with a sampling rate up to 250 kS/s was chosen. The device allows a full scale range of +/- 5V with 152 μV resolution, thus achieving a high precision recording the input levels, especially targeted to TID measurements.

The Sensor board is equipped with the following sensors: two RadFETs for TID, three p-i-n diodes for DD and two sets of four SRAM memories for the HEH fluence measurement. In addition, a dedicated PCB called "deported module" can be connected

via an up to 50 m long cable to the RadMon V6, forming a "mother-daughter" system. The deported module can host up to two RadFETs and two p-i-n diodes, together with a temperature sensor. This possibility was introduced to enable TID and DD measurements in zones with very high radiation levels, where a sensor module could reach the areas of interest to perform dosimetry measurements without exposing the main "mother" board of the RadMon. The RadMon sensors are highlighted in Figure 2.10 together with the deported module and its cable.

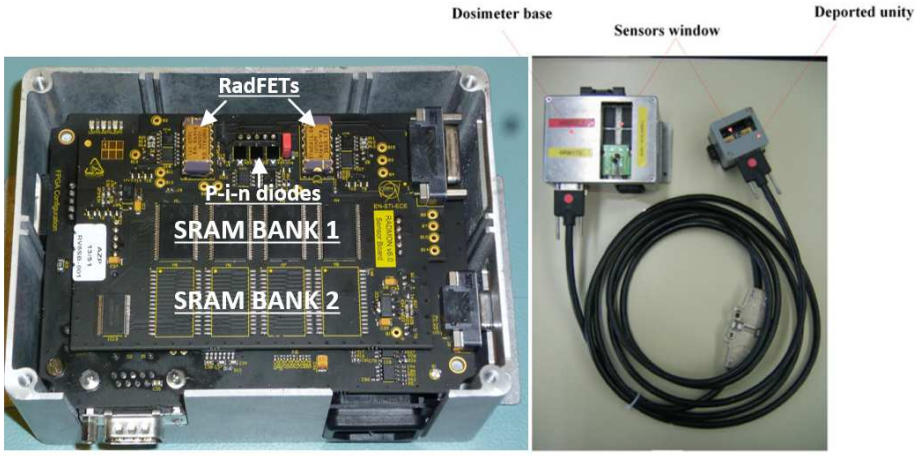

Fig. 2.10: The RadMon V6 system sensors and its deported module.

The voltage signal from the RadFETs corresponds to the Δ_{th} shift of the threshold voltage proportional to the absorbed dose. Figure 2.11 shows the schematic of the acquisition network implemented on the RadMon: a switch (Sw1) allows the user to set the gate contact of the RadFET either to ground (GND) or to a voltage bias (normally +5 V), the RadFET biasing conditions can therefore be configured if the specific environment requires a different sensitivity of the device. A second switch (Sw2) is included to ground the source pin during irradiation, the RadFET threshold voltage V_{th} is read after opening Sw2 and injecting a 10 μA current through the RadFET source. An operational amplifier is set as a buffer and can be configured with gains 1, 0.5 and 0.1, thus the user can choose a different value of gain to increase the dynamic range of the read by scaling the final voltage seen by the ADC. This choice is very important, since the trapped charge in the RadFET can lead to a V_{th} output that can saturate the ADC input. Similarly to the RadFET, the p-i-n diodes are read with a 1 mA current injected through the contacts of the device, with the output voltage being acquired by the ADC.

The main sensor advancement of the RadMon V6 with respect to its previous versions is given by the SRAM memories for the HEH fluence measurement. The device chosen for the first SRAM bank is the 400 nm Toshiba TC554001AF-70L 4 Mbit memory (512 Kbit x 8 bit). This SRAM was chosen due to its large fast neutron cross-section and its high thermal neutron cross-section [50]. Thermal neutrons represent a huge

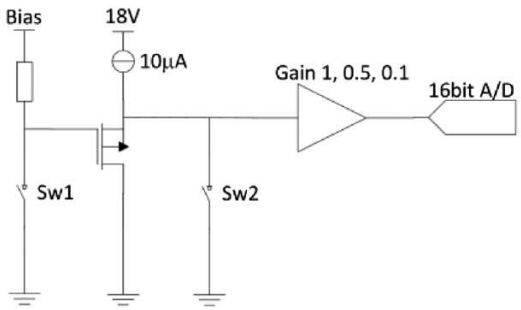

Fig. 2.11: Schematic of the RadFET sensor acquisition network.

threat to electronic devices: several components were included in the design of the installed systems since 1998, and therefore might contain implants with traces of ^{10}B. Thermal neutrons can induce a large number of Single Event Upset phenomena through the $^{10}B(n,\alpha)^{7}Li$ capture reaction [51], meaning their contribution to the SEE rate cannot be neglected. The second SRAM bank is based on an 8 Mbit SRAM (512 Kbit x 16 bit) built with a 90 nm process, the Cypress CY62157EV30. This device was chosen mainly for its high proton cross-section and low sensitivity to thermal neutrons after a full characterization campaign [52]. Nevertheless, during the RadMon V6 operation an issue related to the generation of multiple clusters of bit upsets highly compromised the reading from this SRAM component. A study of the CY62157EV30 as an HEH monitor, together with results from other memories and a full description of the method realised for the correction of the reading problem encountered is detailed in chapter 3. In total 16 Mbit from four Toshiba SRAMs can be addressed, together with 32 Mbit from four Cypress SRAMs. Both banks can be configured with different voltage levels, in order to adjust the sensitivity of each bank. RTD temperature sensors are placed on the Main board as well as on the sensor board, in proximity of the RadFET and p-i-n diodes, to record the temperature close to these devices. The temperature compensation for the RadMon V6 is performed in post-processing by the acquisition software.

2.3.2 | RadMon V6 Installations in the CERN Areas

The RadMon V6 was initially deployed in 2014 in the injector areas, and in 2015 the installation in the main tunnels and experimental areas was started. Wherever there was no possibility of having a fixed RadMon installation (mainly due to the FIP cabling), a "BatMon" was placed, consisting essentially in a battery operated version of the V6 monitor. BatMon have the same sensors of the RadMon V6 and follow the same design, but they acquire data locally and are read at each technical stop of the machines. In the tunnel areas, RadMon V6 were installed along the PS Booster, PS and SPS caverns, examples of such installations are highlighted in Figure 2.12.

In total, up to July 2016, 16 RadMon V6 units were installed in the PS, below the

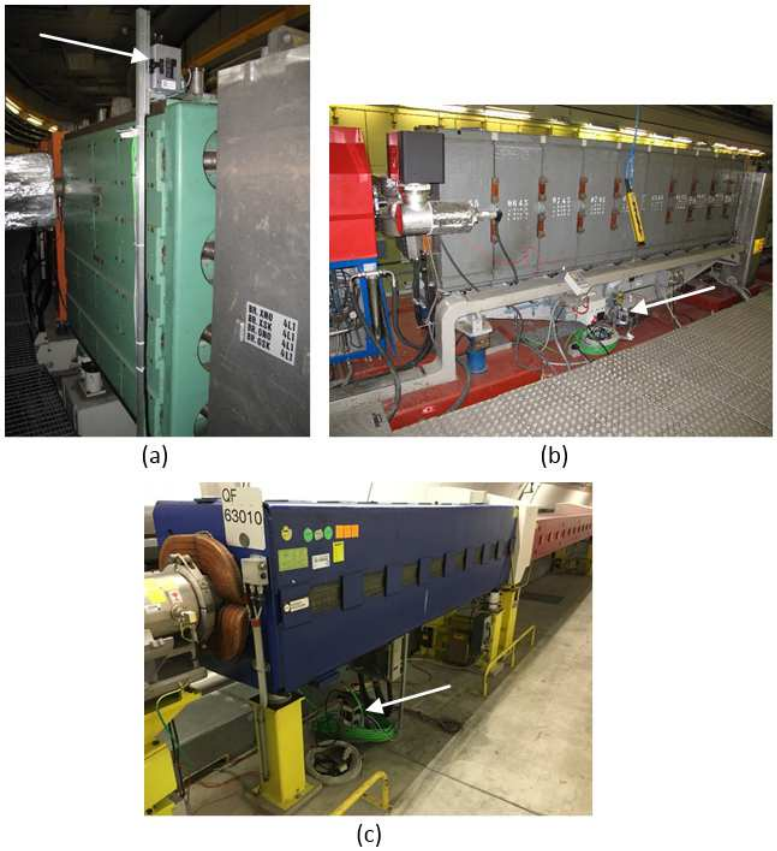

Fig. 2.12: RadMon V6 modules installed in the PSB (a), PS (b) and SPS (c) tunnel areas.

main dipoles and into the straight sections, 8 units were located along the PS Booster ring, and finally 59 V6 RadMons were placed in the SPS: 24 under the dipole magnets, 34 under the quadrupole magnets and 1 in the point 2 area. Within the experimental areas 13 units were installed in the UX25 cavern hosting the ALICE experiment, 11 were placed in the North Area for the NA62 experiment, 5 units were assigned to HiRadMat, and 7 were deployed and extensively used within the CHARM test facility irradiation area. In total 119 Radiation Monitors V6 were installed up to July 2016, adding up to the 379 units, between V4 and V5, already present in the whole complex. As already stated, RadMons are essential to limit beam dumps caused by radiation failures, in particular from high energetic hadrons, but their use is not limited to radiation monitoring along the tunnel lines. RadMons are used to benchmark predictions of the radiation levels calculated using FLUKA, in particular in relation to the imminent HI-LUMI upgrade of the LHC [53], moreover the RadMon V6 plays a major role in the calibration and operation of the CHARM facility, the main CERN cornerstone for the qualification of devices in a complex mixed-field environment.

2.4 The CHARM Mixed-Field Facility

Tests in a mixed-field, and on large systems, require a whole different facility and qualification process. The CERN High Energy Accelerator Mixed-field facility (CHARM) was built to provide an answer to this need. CHARM is situated in the Proton Synchrotron (PS) East Area hall. It started its commissioning phase for the first time in late 2014 and it has been in full operation since 2015. The facility is dedicated to the tests of electronics and systems in a well-characterised mixed-radiation field, which can replicate a wide number of real radiation environments, such as the Low Earth Orbit space, atmosphere, ground, avionic and all the environments of interest for CERN related applications: the LHC tunnel, adjacent shielded areas or its injector chain, [54].

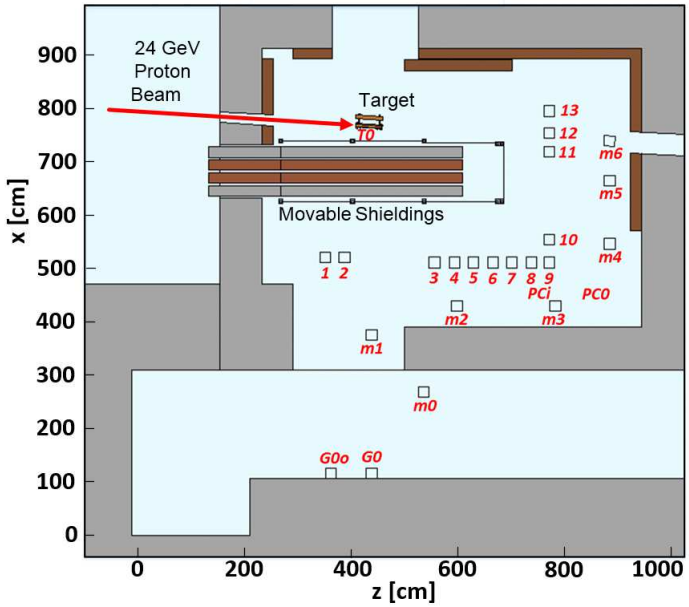

Fig. 2.13: The CHARM Irradiation Area, showing the beam injection line, the four movable shieldings and the numbered test locations in the access corridor and irradiation area.

The facility receives the 24 GeV proton beam coming from the PS extraction line of the East Irrad Area, located upstream. The beam impinges on a target, generating a secondary high-radiation field which pervades the whole area, as opposed to traditional focused beams steered directly on the tested target. The intensity of the radiation field can be modulated by the choice of target head, e.g. two massive ones (Al or Cu) or one with holes, such that only part of the primary beam interacts with the target. The field can be further modulated by setting four shielding plates that can be moved inside, two made of concrete and the other two made of iron. The various field configurations are pre-calculated by FLUKA simulations and constantly benchmarked through calibrated measurements performed using RadMon V6 devices deployed in specific test locations

within the facility [55]. Figure 2.13 shows the CHARM irradiation area: several numbered test locations are defined both inside the actual irradiation area and in the access corridor. Test locations ranging from "1" to "9" (also called "R1-R9") are referred to as "longitudinal", in parallel with the shieldings, whereas the ones from 10 to 13 ("R10-R13") are termed "lateral". Locations "G0o" and "G0" have lower spectra hardnesses and are sited inside the access corridor, in front of the area entrance, "m0" to "m6" instead follow the path of a Montrac rail system, a shuttle designed to carry tested equipment to additional test points.

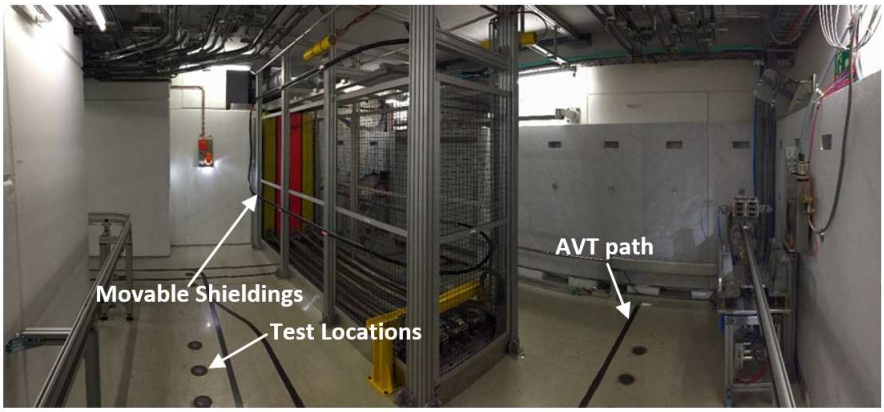

Fig. 2.14: View of the inside of the CHARM irradiation area. The movable shieldings, test locations and AVT path are indicated.

The users of the facility may perform tests on electronic cards, crates and racks, by choosing the test location and facility configuration that yield the best representative environment foreseen for the final application of the tested equipment. The size of the available test area was designed in order to ultimately allow the irradiation of large objects, even systems connected with complex services (power, cooling, etc.). Once the test location and CHARM configuration are chosen, the electronics under test is installed on a rack and moved to the test position using an automated conveyor system (AVT) or the Montrac shuttle rail system. A photo of the facility inside is given in Figure 2.14. The beam intensity is measured using either the Secondary Emission Counters, "SEC1" and "SEC2" or the ionisation chamber "IC", [4]. To determine the number of protons reaching the target, (Protons On Target or "POT"), the SEC1 detector is mostly generally used as reference. This detector is calibrated using a fast Beam Current Transformer (BCT) placed upstream, just after the point of extraction from the PS. A cross-check is also made using activation foils.

The particles generated at CHARM have energies ranging from keV (for instance, thermal neutrons) up to GeV. The characterization of electronics in a broad energy range is of particular interest in terms of Single Events Effects. Components with high-Z materials near their sensitive volume can have a very strong SEE cross-section dependence with energy, for instance testing with a 60 MeV proton beam could lead to a factor 100

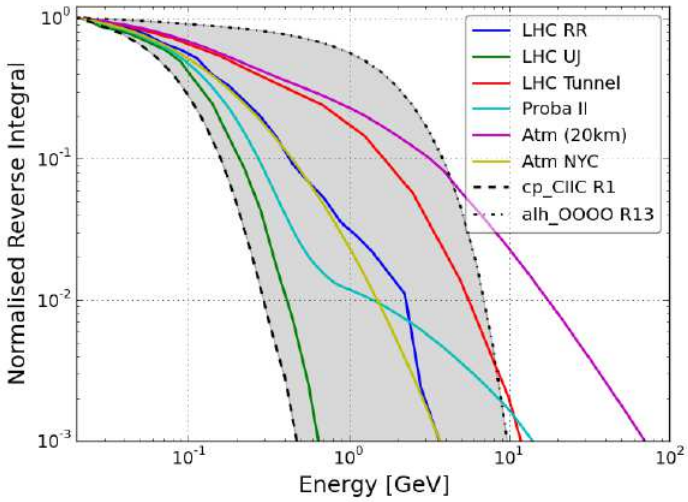

Fig. 2.15: A plot of the reverse integral spectra for several test configurations at CHARM (grey shaded area), compared with different radiation environments, normalised to 1 at 20 MeV. **[source]**: [4].

underestimation of the error rate [56].

Fluences of particles with different nature and energies have a different impact on the operation of electronics. In order to compare the mixed-radiation field at CHARM with other fields, a metric needs to be defined. In terms of SEE the key figure of merit is usually the minimum LET required to induce events. At CHARM the High Energy Hadrons, corresponding to all hadrons above an energy of 20 MeV, are taken in consideration. As a result, the metric used was defined as the spectra "hardness" (or "hardness factor"), which quantifies the range of energies of high energy hadrons in a radiation environment. To calculate this factor, one takes the simulated high energy hadron spectrum and makes a reverse integral, normalised to 1 at 20 MeV. Figure 2.15 shows a comparison between CHARM test configurations and a few example environments, in terms of the reverse integral spectra VS energy as returned by FLUKA simulations. The target material is defined as "cp", copper, or "alh", aluminium with holes. The shieldings settings in this case can be "CIIC" (Concrete, Iron, Iron, and Concrete, all inside) or "OOOO" (all open, no shielding inside). The spectra of the LHC tunnel and shielded areas environments are shown, together with the ones of the Low Earth Orbit mission Proba-II launched by ESA [41], the atmospheric at 20 km of altitude, and the one defined in New York City outdoors (NYC) at sea level at a time of average solar activity. The radiation fields reproduced at CHARM can be modulated within a wide range, the shaded area, which includes all the above mentioned environments, thus providing a unique test platform for several applications of interest. The measurement of the SEE cross-section, induced by highly energetic hadrons in an energy range representative of the final environment, results in a new radiation qualification process which allows a fast screening of the components SEE sensitivity. This approach stands at the basis of the radiation hardness assurance

and testing procedure applied in this work, with particular emphasis in the field of small satellites for Low Earth Orbit missions.

2.5 Testing at the PSI-PIF Facility

The PSI-PIF facility is the main proton accelerator used for tests with focused mono-energetic beams by the CERN radiation working group, the community based at CERN and actively using commercial components in the design of electronics for high radiation environments. The Proton Irradiation Facility was built in cooperation between PSI and ESA [57], and it is located in the experimental area of the superconducting cyclotron-type accelerator COMET dedicated to tumor therapy [58]. An initial 230 MeV proton beam is delivered to the users. A primary energy degrader, made of 7 Cu plates of different thicknesses, allows setting a few discrete beam energies in the range from 200 MeV down to 30 MeV. The beam is subsequently guided to the Experimental Area where the PIF facility is located. The beam flux is measured by means of two ionization chambers, "IC1" and "IC2", respectively placed upstream and downstream the main collimators. The countings of the IC1 and IC2 are calibrated to measure the beam flux at the position of the DUT, which is generally placed 5 cm away from IC2 (downstream). The DUT is fixed on an experimental bench consisting of an adjustable frame sitting over an XY-table. The maximum beam intensity allowed is 5 nA, whereas the minimum is ≈ 0.1 nA, both can be set by the users from the control room. A set of collimators can be placed right before the DUT for further beam focusing, a 5 cm collimator was always adopted for all tests carried out in this work. The beam profiles are measured by means of a scintillator detector. The TID and flux measurements are provided by the facility, nevertheless before starting irradiation a calibration phase was always performed for each beam energy set. The calibration was done measuring the proton flux with an ESA SEU monitor [59].

2.6 Conclusions

The CERN complex, and in particular the LHC accelerator, are characterized by a mixed-field environment of particles within a wide range of energies. Electronics equipments installed in such harsh radiation areas are subject to TID and DD effects as well as high fluences of particles, yielding large amounts of single events and ultimately affecting the systems operation.

The Radiation Monitoring system was proposed in 2005 in the framework of the CERN R2E project, aiming at the design of a reliable, precise and distributed on-line network of systems for the monitoring of radiation and the evaluation of its effects on electronics. Several test campaigns at PSI were carried out to research and characterize suitable commercial components, and finally the design culminated in the current ver-

sion 6 of the system, conceived to enhance longevity, maintainability and the possibility of future upgrades.

A total of 119 RadMon V6 were installed as of July 2016 throughout the CERN tunnel and experimental areas. In addition the device is of extreme importance for the measurement of radiation fields within the CHARM test facility, the new experimental area dedicated to tests of systems in a mixed-field radiation environment representative of the one foreseen in the final application.

The main sensor advancement of the RadMon V6, with respect to its previous versions, was the new set of Cypress SRAM memories for the evaluation of the High Energy Hadrons fluences. Early during operation of the first RadMon V6 units installed, in 2014, a serious problem was observed occurring on the new bank of Cypress SRAMs. Multiple Cell Upsets arising as large "bursts" of bit flips started showing up in large clusters on the die, hence strongly affecting the HEH fluence measurement. This effect required an immediate and effective solution, thus providing the basis and the initial motivation of this Ph.D work. The next Chapter focuses on the study of the burst effect on the RadMon V6 Cypress SRAM memories, the set of tests performed to understand their nature and the solution approaches proposed and finally adopted to retrieve corrected values of the particle fluence.

3

THIRD CHAPTER

BURST DETECTION AND CORRECTION ON THE RADMON V6 HEH FLUENCE SENSORS

The design of the RadMon V6 and its role in the context of the CERN radiation environment was extensively described in Chapter 2. This Chapter reports in detail all the research and development work, carried out by the author of this manuscript, to find a solution to the effect of MCU "bursts" observed during early operation of the new set of SRAM sensors equipped by the RadMon V6. This latter problem prompted an initial study of the "bursts" in terms of their nature and the extent of their negative action on the HEH fluence evaluation. Further on a dedicated hardware test setup was designed and a set of experimental test campaigns were carried out to find an effective and rapid solution to the problem.

3.1 The Problem: Multiple Cell Upset Burst Events

It was aforementioned how single event effects play a major role in terms of radiation induced failures of electronics. The precise measurement of Highly Energetic Hadrons is essential for prevention and recognition of SEE effects. Commercial SRAM memories are commonly used in many applications as HEH monitors, [60]. The particle fluence ϕ is calculated using the relation between the cross-section σ and the number of bits in the SRAM memory N, defined as

$$\sigma = \frac{SEU_{tot}}{N \cdot \phi}, \tag{3.1}$$

where SEU_{tot} is the total number of Single Event Upsets (SEUs) recorded throughout the whole irradiation time. Two factors are essential to retrieve precise measurements

of the particle fluence: the SRAM cross-section σ, whose value depends strictly on the SRAM operating voltage and the energy of particles crossing the memory, and the correct evaluation of the SEUs occurring within the memory. Several units of different lots of the Toshiba SRAM TC554001AF-70L equipped on the RadMon were characterized in [44]. The average proton cross-section value for lots analysed in 2014 was calculated as $\sigma_{toshiba} = 5.4 \cdot 10^{-14}$ cm^2/bit. The 8 Mbit, 90 nm, Cypress SRAM CY62157EV30 was characterized in [52]. This SRAM exhibited an HEH cross-section in the order of 10^{-13} cm^2/bit with no record of latchup events. In addition, the component was found to be insensitive to thermal neutrons, regardless of the operative voltage, thus allowing monitoring of HEH and thermal neutron fluences in combination with the TC554001AF, with one single measurement and without changing the voltage supply [61]. Considering the high proton cross-section, 10 times larger than $\sigma_{toshiba}$, and the availability of the component on the market, the Cypress CY62157EV30 was chosen as the SRAM equipped on the second SRAM bank of the RadMon V6.

During 2014 and 2015 the HEH fluence data from the RadMon V6 installed and in operation was analysed. Figure 3.1 shows an example of the cumulated SEU counts and SEU rate measured by one RadMon V6 unit in the SPS tunnel between April 1st 2015 to December 12th 2015. Data shows Multiple Cell Upset (MCU) events, characterised by a large number of error bits, not observed during previous test campaigns. This effect could have been related to the radiation environment of the particular location, but it was instead shared by several devices under operation in different areas.

The generation of these events, defined as “bursts”, is potentially harmful and may corrupt the measurement of SEU_{tot}, leading to false data readings and accuracy loss. This SEU burst effect was observed in previous works [62], and it is described as a single event inducing several bits in a chip to fail at the same time, with error bits located physically at very close distance, resulting from a micro-latchup event across the die [63]. Such events are very hard to detect, especially with high particle fluxes, where the SEU rate is in the same order of the total number of bit errors caused by bursts, thus hiding them within the repeatability of the fluence measurement. A solution to the problem was proposed in [52] with an algorithm for the post-processing correction of the returned SEU data, accounting for MCU events characterized by a high number of SEUs in nearby cells. This approach, though in principle effective, is not practical for the RadMon V6 application. Considering the number of devices to scan, the fast reading rate ($\simeq$1 sec) and the need to return the error bits physical locations from the RadMon control circuitry, the large dataset to be processed would result in a computationally very expensive solution. The nature of the problem required a deeper study of the SEU burst generation and the evaluation of other possible solutions for a rapid on-line correction.

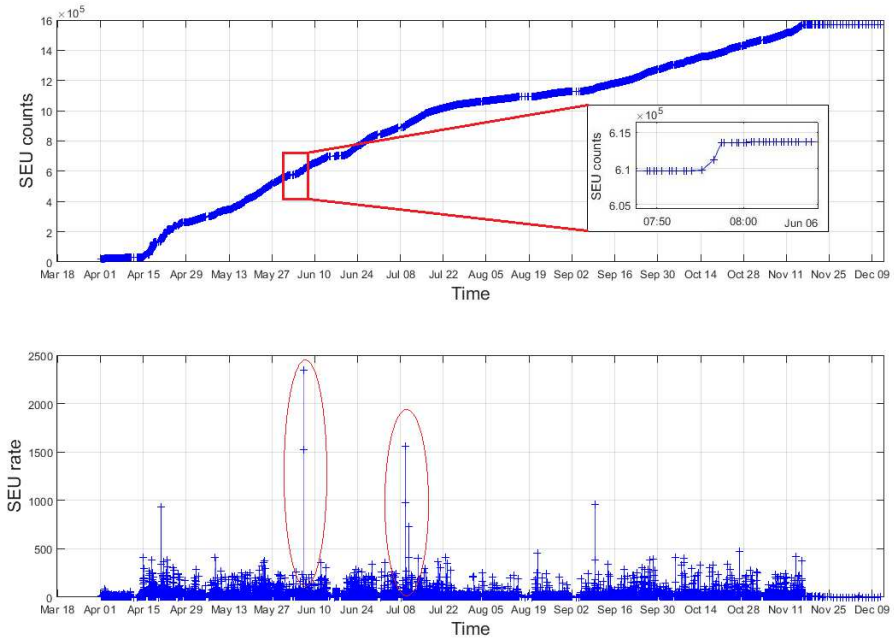

Fig. 3.1: Integrated SEU counts (top) and SEU rate (bottom) measured by one RadMon V6 (labelled "SIMA.LI04S") during operation in the SPS from April 1st 2015 to December 12th 2015. The red areas correspond to large MCU events involving high quantity of bit flips.

3.1.1 | SRAM Memories Characterization at PSI-PIF

Before researching methods for an embedded, on-line, correction of the MCU events on the CY62157EV30, several other SRAM candidates were characterized using focused proton beams. Irradiation tests were carried out at the PIF facility of the Paul Scherrer Institute with a proton beam set with several energies ranging from 30 MeV up to 150 MeV. A board hosting up to eight Device Under Test (DUT) SRAM targets was developed. The DUT board was connected with a micro-Coax cable to an FPGA tester board placed outside the beam. The tester was easily reprogrammable during irradiation: it provided the control signals for the DUT and it was interfaced via USB to a PC located in the control room of the facility. Figure 6.9 shows the setup of the test campaign.

There are two main methods to test memory components under radiation: static and dynamic, described in detail in the JEDEC standard [64]. In the static mode the DUT is initialized with a known pattern and then irradiated, the component state is read only at the end of irradiation and SEUs are counted comparing each bit word with the initial pattern. In the dynamic mode the DUT is continuously accessed with a period T_{read} during irradiation: the total number of SEUs are counted and the physical locations of the error bits are returned, the memory might be optionally reinitialized with the original

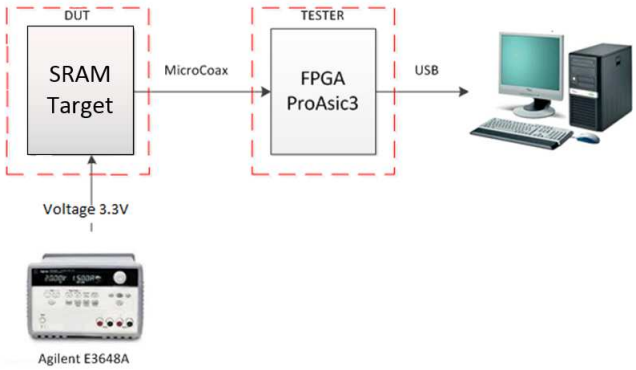

Fig. 3.2: Setup used during test campaigns at PSI. An Agilent Power supply and an FPGA ProASIC3 tester board are connected to the DUT.

bit pattern.

Table 3.1: DUT Identification and operating conditions

SRAM name	**Manufacturer**	**Voltage**	**size**	**Lot**
CY7C1059DV33	Cypress	3.3 V	8 Mbit	1331
IS61WV5128EDBLL	Issi	3.3 V	4 Mbit	1214
KM684000BLT	Samsung	5 V	4 Mbit	940
CYLE1049DV33	Cypress	3.3 V	4 Mbit	1205

Four SRAM candidates were considered during the tests: the Cypress CY7C1059DV33 and CYLE1049DV33, the Issi IS61WV5128EDBLL, and finally the Samsung KM684000BLT. Table 3.1 reports the Manufacturer, lot values, voltage levels and sizes of each selected component. Results for each one of the irradiated devices are summarized in the following tables. Tests were carried out both with the static and with the dynamic methods, in order to evaluate the cross-section using both types of addressing. The measurement results of the four SRAM target devices are reported in Tables 3.2, 3.3, 3.4 and 3.5.

Table 3.2: Results of proton tests in static and dynamic modes of the IS61WV5128 SRAM Memory.

Type of Test	**Fluence [p/cm^2]**	**# SEUs**	**σ [cm^2/bit]**	**Energy**	**Mean σ [cm^2/bit]**	**Std. Dev. σ [cm^2/bit]**
Static	$2.28{\cdot}10^{10}$	5	$5.23{\cdot}10^{-17}$	150		
Static	$1{\cdot}10^{11}$	173	$4.12{\cdot}10^{-16}$	150	$2.97{\cdot}10^{-16}$	$2.12{\cdot}10^{-16}$
Static	$1{\cdot}10^{11}$	179	$4.27{\cdot}10^{-16}$	150		
Dynamic	$1{\cdot}10^{11}$	160	$3.81{\cdot}10^{-16}$	150	-	-

Table 3.3: Results of proton tests in static mode of the CYLE1049DV3 SRAM Memory.

Type of Test	**Fluence [p/cm^2]**	**# SEUs**	**σ [cm^2/bit]**	**Energy**	**Mean σ [cm^2/bit]**	**Std. Dev. σ [cm^2/bit]**
Static	$1.0{\cdot}10^{10}$	590	$1.41{\cdot}10^{-14}$	150	$1.37{\cdot}10^{-14}$	$5.2{\cdot}10^{-16}$
Static	$1.11{\cdot}10^{10}$	619	$1.33{\cdot}10^{-14}$	150		
Static	$1.00{\cdot}10^{10}$	533	$1.27{\cdot}10^{-14}$	100	-	-
Static	$1.03{\cdot}10^{10}$	594	$1.37{\cdot}10^{-14}$	60	-	-
Static	$1.00{\cdot}10^{10}$	485	$1.16{\cdot}10^{-14}$	30	-	-

Table 3.4: Results of proton tests in static and dynamic mode of the CY7C1059DV33 SRAM Memory.

Type of Test	**Fluence [p/cm^2]**	**# SEUs**	**σ [cm^2/bit]**	**Energy**	**Mean σ [cm^2/bit]**	**Std. Dev. σ [cm^2/bit]**
Static	$1.0{\cdot}10^{10}$	1628	$1.94{\cdot}10^{-14}$	150	$1.96{\cdot}10^{-14}$	$3.22{\cdot}10^{-16}$
Static	$1.21{\cdot}10^{10}$	1982	$1.95{\cdot}10^{-14}$	150		
Static	$8.2{\cdot}10^{10}$	13768	$2.00{\cdot}10^{-14}$	150		
Static	$2.99{\cdot}10^{10}$	4616	$1.84{\cdot}10^{-14}$	100	-	-
Static	$2.51{\cdot}10^{10}$	4366	$2.07{\cdot}10^{-14}$	60	-	-
Static	$2.65{\cdot}10^{10}$	3142	$1.41{\cdot}10^{-14}$	30	-	-
Dynamic	$1.13{\cdot}10^{10}$	978	$1.03{\cdot}10^{-14}$	150	$1.39{\cdot}10^{-14}$	$5.44{\cdot}10^{-15}$
Dynamic	$4.01{\cdot}10^{10}$	3415	$1.01{\cdot}10^{-14}$	150		
Dynamic	$1{\cdot}10^{11}$	8635	$1.03{\cdot}10^{-14}$	150		
Dynamic	$1{\cdot}10^{11}$	8734	$1.04{\cdot}10^{-14}$	150		
Dynamic	$1{\cdot}10^{11}$	8798	$1.05{\cdot}10^{-14}$	150		
Dynamic	$7.47{\cdot}10^{10}$	6742	$1.08{\cdot}10^{-14}$	150		

Table 3.5: Results of proton tests in static mode of the KM684000BLT SRAM Memory.

Type of Test	**Fluence [p/cm^2]**	**# SEUs**	**σ [cm^2/bit]**	**Energy**	**Mean σ [cm^2/bit]**	**Std. Dev. σ [cm^2/bit]**
Static	$1.0{\cdot}10^{11}$	31482	$7.51{\cdot}10^{-14}$	150	$1.37{\cdot}10^{-14}$	$5.2{\cdot}10^{-16}$
Static	$1.0{\cdot}10^{11}$	31645	$7.54{\cdot}10^{-14}$	150		
Static	$5.48{\cdot}10^{9}$	1798	$7.82{\cdot}10^{-14}$	150		
Static	$5.0{\cdot}10^{9}$	1742	$8.31{\cdot}10^{-14}$	100	-	-
Static	$6.19{\cdot}10^{9}$	2284	$8.80{\cdot}10^{-14}$	60	-	-
Static	$8.80{\cdot}10^{9}$	2958	$8.01{\cdot}10^{-14}$	30	-	-

In all cases, results evidenced a proton cross-section at least one order of magnitude lower compared to the value obtained for the Cypress memory CY62157EV30 chosen for the RadMon V6, even for energies at 150 MeV and for the CY7C1059DV33, which has 8 Mbit instead of 4 Mbit compared to the other devices. Such measurements suggested that none of the tested SRAMs could replace the CY62157EV30, thus the operation of the RadMon units required a quick and exhaustive way to compensate the error introduced by the MCU events showing up on the second SRAM bank. For these reasons an algorithm for fast and direct detection and correction of SEU bursts was proposed and implemented on FPGA.

3.2 The Proposed Algorithm for Burst Detection on CY62157EV30 SRAM Memories

Data analysed in past test campaigns showed no record of SEU burst events when the DUT was tested in static mode, whereas in dynamic mode SEU burst events started to show up [65]. In the dynamic mode the peripheral circuits of the memory are more sensitive to upsets due to the read/write accesses on the memory array, therefore burst events are more likely to arise in this configuration.

Two lots, referred to as I and II, of the chosen DUT were tested. The functionality of the detection algorithm was tested along with a systematic analysis of the parameters involved in the generation of burst events on the chosen target [66]. The SRAM was tested in dynamic mode and the parameters of initial pattern, reading period, particle flux, and memory rewriting after full read were systematically changed during irradiation. The cross-section values were evaluated after each run and compared to the reference value of the cross-section calculated in static mode. The objective was to analyse the impact of each parameter on the SEU burst generation while testing the efficiency of the detection algorithm.

MCU events may show-up with different shapes and numbers of bits affected, therefore they can be classified in different categories [67]. The mechanisms at the source of these events was simulated in other works [68], [69]. Data collected in previous test campaigns on the chosen target [70] showed the presence of burst events characterized by a rather rectangular shape, as shown in Figure 3.3b, involving several bit upsets located in adjacent rows along the full width of a memory block (64 bits). This kind of MCU will be referred to as type *B*. In addition to type *B* MCU shapes, clusters with fewer cell upsets involved were also observed, as reported in Figure 3.3a: these events, referred to as type *A*, are caused by particles crossing the volume of the memory die and inducing currents in nearby cells, as opposed to type *B* burst events caused by micro-latchups in the address part. Type *A* MCUs were observed also in static mode, and they were taken into account when calculating the memory cross-section, whereas type *B* burst events were detected and excluded from the cross-section calculation.

(a) (b)

Fig. 3.3: Examples of a small cluster of bit upsets (a) and a burst event characterized by several single bit upsets following a rectangular geometrical shape (b).

The shape of type *B* MCUs, the number of bits involved and their distribution is connected to their latchup nature and the particular layout structure of the SRAM. The cells are electrically connected in rectangular blocks defined by the well taps of the memory internal architecture, [63], [71], [72], thus the parasitic currents generated by a micro-latchup are confined within a rectangular area.

The SRAM manufacturer applied a scrambled addressing scheme to access the SRAM cells. After decoding this scheme [1] it is possible to retrieve information on the physical location of the cells in the die and choose different addressing techniques. The proposed algorithm accesses the memory with a descrambled accessing scheme, called "physical", thus allowing to read address locations row-by-row and block-by-block, along the directions top-to-bottom and bottom-to-top of the die. This addressing scheme is opposed to a "linear" reading, where SRAM addresses are incremented linearly without any information on the physical location accessed.

The shape of the targeted type *B* burst events was investigated by processing a dataset of 137 previous runs in dynamic mode under protons. The SRAM bit map at the end of irradiation was evaluated and results are reported in Figure 3.4: the number of total Type *A* and Type *B* MCU events recorded is shown vs the number of bits and rows affected by each MCU. Single error bits represented about 51% of the total events and were excluded from the analysis. Results showed that the number of bit upsets involved in a burst event reached up to hundreds of error bits, extending over several consecutive rows.

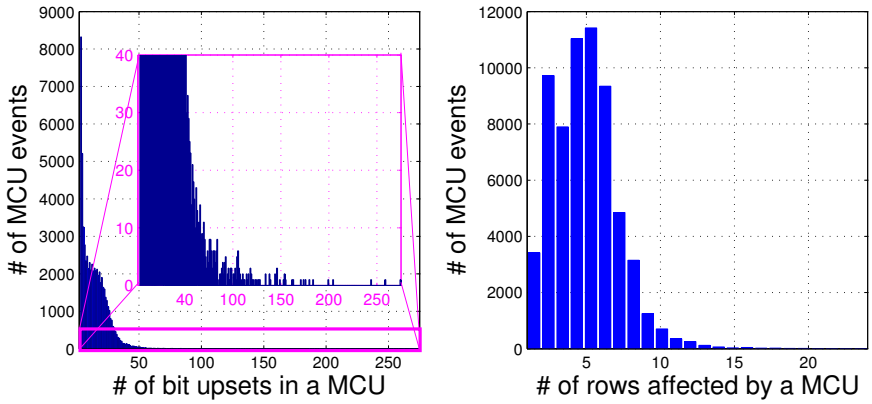

Fig. 3.4: Analysis of the number of bit upsets (on the left) and rows (on the right) affected per MCU event (both types *A* and *B*).

[1] The information on the SRAM internal layout was provided by Cypress through a strictly confidential communication. The manufacturer was aware of the research carried out and was notified of the results obtained.

Following these observations a detection window was implemented on an FPGA as a moving FIFO buffer and a "physical" addressing scheme was adopted. The detection window was designed with a width of 64 bits, the size of a block, and depth of 10 rows, as shown in Figure 3.5. The window dimensions were chosen as a first approach to fit the shape of the observed burst events while achieving a good trade off between the FPGA area and the latency, the period between two read operations, in view of its possible application on the RadMon system.

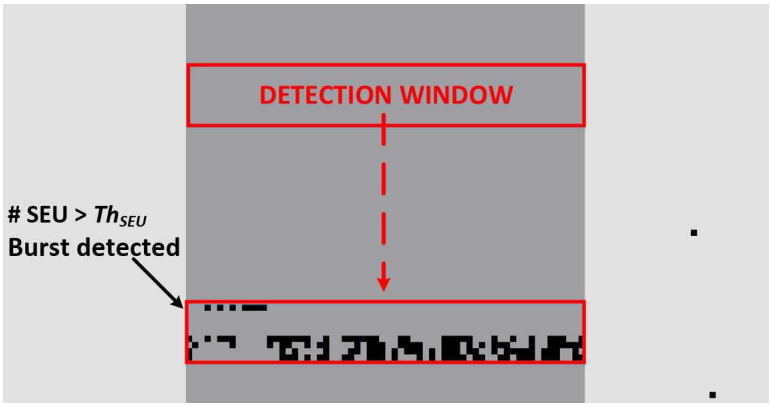

Fig. 3.5: The detection window size is 64 bits x 10 rows. It moves by steps of one row within the same physical block. When the number of SEUs in the window is above Th_{SEU} a burst is detected.

The window moves by steps of one row across each block of the SRAM, from top to bottom or vice versa. The number of error cells is counted at each step and stored in dedicated registers associated to each row of the window: the total number of SEUs located in the window is calculated as the sum of the error bit counts stored in each register. This value is then compared to a user set threshold value Th_{SEU}: when the value of Th_{SEU} is exceeded, a burst event is detected and the number of SEUs counted within the window, SEU_{burst}, is returned together with the row and block positions.

In order to prevent the algorithm from detecting several times the same event, the burst detection is disabled right upon recognition of a burst and 16 rows of the memory are read before enabling it again: 10 rows of the window size plus 6 rows to ensure enough margin. These parameters were set as a first step, assuming the detection would stop at the most twice when more than 16 rows were involved. In a first step, a post-processing software version of the algorithm was used to process previous data showing evidence of burst events, to determine the optimum value for Th_{SEU}. Values of $Th_{SEU} < 20$ were too low, as they lead to the detection of many type A MCUs. On the other hand, with $Th_{SEU} > 70$, several type B bursts were not recognized. A good trade off was found with a value of Th_{SEU} in the range of 30 to 40; in particular $Th_{SEU} = 40$ was set for burst recognition in all experimental tests at PSI. The equation 3.1 may be rewritten to

account for the bit errors detected in each burst. The corrected cross-section σ_{corr} was evaluated as

$$\sigma_{corr} = \frac{SEU_{tot} - SEU_{burst}}{N \cdot \phi}. \tag{3.2}$$

Experimental tests were run in dynamic mode and the address of each array containing error bits was returned, allowing to plot a map of the SEU physical location within the SRAM at the end of each irradiation. The software version of the algorithm was used to process the SEU map at the end of each run. The output was benchmarked with the results of the burst detection code embedded on the FPGA, to verify its correctness. When the memory was not rewritten with its original pattern, only results from the software implementation were used for the evaluation of σ_{corr}. In this case the FPGA detection algorithm can not be effective, since detected burst events are not cleared from the memory and thus the same event is reported more than once.

3.2.1 | Tests in Dynamic Mode on Lots I And II of Cypress CY62157EV30

A proton beam focused with a 5 cm collimator on the DUT was used in the tests carried out at the PSI-PIF facility, as already described in section 2.5. All tests were run at the beam energy of 150 MeV. The voltage applied to the chip was 3.3 V, this value was kept constant in order to compare cross-section results for the CY62157EV30 corrected by the algorithm, with the ones obtained earlier on the other SRAM candidates discussed in section 3.1.1. The voltage and beam energy were kept constant as they highly impact the cross-section evaluation. Values of TID and flux were provided by the facility. The parameters of T_{read}, the initial pattern, the memory rewriting option, the addressing scheme and the beam flux were systematically modified and their impact on the SEU generation was investigated. Chips were irradiated reaching only low doses (< 100 Gy), in order to exclude any cross-section dependency on the TID [73]. A total of one chip for Lot I and three chips belonging to Lot II were tested. The reference σ was reported for each component. Table 3.6 reports the results of tests with the memory not rewritten after each read access. The initial pattern was all zeros (0x0000) and σ_{corr} was evaluated in post analysis through the software implementation of the detection algorithm. The flux was fixed at a value $4.1 \cdot 10^7$ pp/(cm^2·s). The static cross-section reference values were $\sigma_I = 1.62 \cdot 10^{-13}$ cm^2/bit and $\sigma_{II} = 4.76 \cdot 10^{-13}$ cm^2/bit with standard deviation, calculated over 4 measurements, of $6.9 \cdot 10^{-14}$ cm^2/bit and $1.37 \cdot 10^{-14}$ cm^2/bit for Lots I and II, respectively.

The number of read accesses to the SRAM is given by the ratio between the total irradiation time and the period T_{read} between each full memory scan. In the case of T_{read} = 10 s the cross-section σ is within the repeatability of the reference and only a few SEUs are counted in SEU_{burst}. Instead, the cross-sections in the case of T_{read} = 3 s were

Table 3.6: Test results on CY62157EV30 Lots I and II - SRAM rewriting disabled

Test Method	T_{read} [sec]	Irrad time [sec]	$\sigma \cdot 10^{13}$ [cm^2/bit]	$\sigma_{corr} \cdot 10^{13}$ [cm^2/bit]	SEU_{tot}	SEU_{burst}	Fluence [10^9·pp/cm^2]
				Lot I			
Static	-	-	1.62	-	-	-	-
Dynamic	10	45	2.16	2.15	6770	45	1.86
Dynamic	3	602	3.03	1.79	126502	51649	24.8
Dynamic	3	692	3.90	1.88	183444	94782	28
				Lot II			
Static	-	-	4.76	-	-	-	-
Dynamic	1	367	19.2	4.60	241330	183424	15
Dynamic	40	367	4.99	4.46	63421	6727	15.2

higher than a factor 2 with respect to the reference values, with an elevated number of error bits both in SEU_{tot} and SEU_{burst}. Since the fluence values were all different in each run of Lot I, the irradiation time was fixed to achieve the same amount of fluence in runs over Lot II, while the value of T_{read} was varied to change the amount of read cycles per run. Two cases with T_{read} = 1 s, (367 read cycles), and T_{read} = 40 s (9 read cycles) were compared: the cross-section in the first case was a factor 4 higher compared to the latter and a large number of events were detected as bursts. As a result at low T_{read} values corresponded to an increased number of events. This is explained by the increase of the effective time in which the peripheral circuits of the SRAM are driven, due to the enhanced number of read cycles, hence the higher probability of burst events occurrence. In all cases the calculated values of σ_{corr} were within the repeatability of the reference.

In addition to type *B* burst events, another effect was observed while analysing the error bits location, for both Lots, in runs with T_{read} = 3 s and 1 s. Several bit upsets were found on the same column array, following the direction of the address reading right after a large cell upset. Figure 3.6 shows an example: a large burst of error bits showed up spanning over two nearby blocks. In this case the reading direction is bottom towards top and several columns of the memory are upset right above the main SEU burst.

This effect suggested that the burst event, together with the chosen reading direction and a fast reading period, might have been responsible of these column upsets. A more detailed plot of the SRAM map, showing several vertical and type *B* bursts, is reported in the Appendix A. A similar error pattern was observed in [67] and associated to Single Event Functional Interrupts (SEFI) occurring on the peripheral circuitry of the memory. This kind of MCU was reported as affecting all the bits in a data word and characterized by a very low cross-section, whereas the observed data showed a large count of such events, with different bit word values, in the majority of cases associated with a type *B* burst induced by micro-latchup. In Figure 3.6 a few column upsets are located below the burst event, and the MCU cluster extends to the nearby block. Therefore this column upset effect might be associated to the electrical connections of the sensitive nodes of

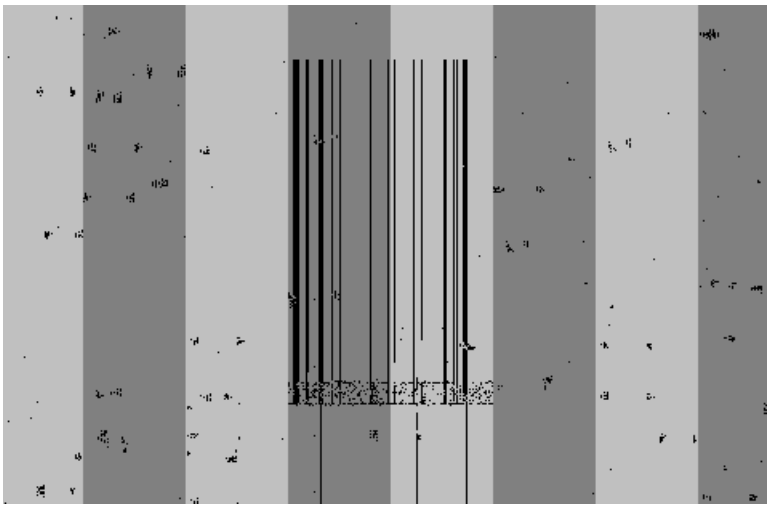

Fig. 3.6: Example of a burst event involving several bit upsets on adjacent rows and error bits located on the same column arrays. Memory blocks are highlighted with different shades of grey.

the SRAMs: for instance the currents induced by micro-latchups might drift from the inverted loops of the addressed cells and affect all the cells connected to the bit line of a specific column. In addition, the column errors which extended vertically above the burst, following the read direction, stopped once the horizontal well gap between the upper and lower parts of the memory was reached. These observations lead to believe that the origin of these column errors would rather be a direct consequence of the micro-latchups, rather than a functional failure.

Experimental tests were run to further investigate this column upset effect and to validate the detection and correction algorithm. Results of irradiations in dynamic mode on lot II chips are reported in Table 3.7. Runs characterized by a high number of burst events are highlighted with bold σ values. The initial pattern was set at all zeros. The fluence was set constant at a value of 10^{10} pp/cm^2. The cross-section reference for this set of runs was $\sigma_B = 2.17 \cdot 10^{-13}$ cm^2/bit with standard deviation $2.2{\cdot}10^{-14}$ cm^2/bit. High cross section results were returned with $T_{read} = 3$ s and a physical addressing scheme, regardless of the memory rewriting option. A fast reading period coupled with a linear addressing scheme did not yield a high number of SEUs, but the analysis of the error bit locations showed evidence of burst events with no bit column arrays upsets. Runs with lower particle fluxes in several cases returned cross-section values comparable with the reference σ_B, which is explained by the increased probability of a particle strike to hit nodes sensitive to latchups and generate burst events.

Table 3.8 shows the result of runs in dynamic mode with initial pattern all ones (0xFFFF), the cross-section reference was $\sigma_{II} = 2.72 \cdot 10^{-13}$ cm^2/bit. Runs with $T_{read} =$

Table 3.7: Test Results with Dynamic Mode on Lot II

T_{read} [sec]	**Memory rewrite**	**Addressing scheme**	$\sigma \cdot 10^{13}$ [cm^2/bit]	**Flux** [pp/cm^2·s]
10	No	Physical	2.20	1.33·10^8
10	No	Physical	2.30	1.34·10^8
3	No	Physical	**3.76**	1.34·10^8
10	Yes	Linear	2.27	1.33·10^8
3	Yes	Linear	2.34	1.34·10^8
3	Yes	Linear	2.49	1.33·10^8
10	Yes	Physical	2.33	1.34·10^8
10	Yes	Physical	2.40	1.33·10^8
3	Yes	Physical	**3.19**	1.32·10^8
3	Yes	Physical	2.78	1.32·10^8
3	Yes	Physical	**4.47**	1.33·10^8
3	Yes	Physical	2.60	2.40·10^6
3	Yes	Physical	**3.14**	2.40·10^6
5	Yes	Physical	**3.62**	2.65·10^7
5	Yes	Physical	2.53	2.66·10^7
5	Yes	Physical	2.88	2.64·10^7

3 s and flux 1.33·10^8 pp/cm^2·s were characterized by several column errors and as a result the computed cross-section was more than a factor 2 higher than the reference σ measured in Static mode. Therefore the content of the SRAM cell did not have an impact on the generation of the bit column upsets.

Table 3.8: Test Results on Lot II and initial pattern 0xFFFF

Test Method	T_{read} [sec]	**Memory rewrite**	**Addressing scheme**	$\sigma \cdot 10^{13}$ [cm^2/bit]	**Flux** [pp/cm^2·s]	**Fluence**·10^{10} [pp/cm^2]
Static	-	No	-	2.72	1.33·10^8	-
Dynamic	3	Yes	Physical	**4.42**	1.33·10^8	2.65
Dynamic	3	No	Physical	**6.07**	1.33·10^8	4.66

Results showed that the physical addressing, though necessary to implement the burst detection algorithm, is also at the basis of the generation of the bit column upsets, which highly affect the evaluation of SEU_{burst} and consequently the corrected cross-section σ_{corr}. Since the micro-latchup events coupled with a physical addressing are assumed to be at the basis of the column upsets, an alternative addressing algorithm was required for the mitigation of this effect.

3.2.2 | Burst Detection Through a Statistical Approach

The output of the detection algorithm was evaluated during irradiations in dynamic mode with memory rewriting enabled. The returned SEU physical locations were processed with the software version of the algorithm and results were benchmarked with the FPGA output. In all cases the algorithm was able to detect MCUs in nearby rows classifying them as burst events. Both the corrected cross-sections, the one computed via software analysis of post irradiation data and the one calculated by the new detection firmware, were corresponding. On the other hand a direct comparison of σ_{corr} with the reference σ found in Static mode was not possible during these tests. The count of the SEUs belonging to the bit column errors must be excluded by SEU_{TOT}, but when their value was $< Th_{SEU}$ the algorithm was not effective in recognizing them. Moreover the algorithm was disabled right after detection of a burst for 16 rows, therefore in many cases some SEUs forming the column patterns were not taken into account as they occurred within the gaps in which the detection was disabled. As a result in many cases σ_{corr} obtained by the firmware detection algorithm did not yet provide the required performance, [66].

Since the observed bit column error events were highly affecting the count of cell upsets occurring within each SRAM block, a statistical approach to detect and correct burst events was suggested. The values of total bit upsets and bit upsets classified as bursts by the detection algorithm, were analysed for each block of the SRAM. The total number of SEUs within blocks affected by bit column errors was then highly above the expected average number of SEUs per block. Figure 3.7 reports the number of total SEU events occurred per SRAM block SEU_{block}, together with the SEU_{burst} value returned by the detection algorithm. The memory is divided in 64 blocks: the amount of SEUs within blocks 8 and 9 is highly over the mean of SEU per block $\overline{SEU_{block}}$.

In this case a possible solution to detect and correct SEU bursts was suggested by using the physical addressing of the memory combined with a periodic calculation of $\overline{SEU_{block}}$. For instance, when the total bit errors in a block is above $\overline{SEU_{block}}$ plus one standard deviation of SEU_{block}, the value of $\overline{SEU_{block}}$ would be added to SEU_{TOT} instead of counting all the bit upsets in that block. Considering that the $1-\sigma$ repeatability between samples of the same lot is $\simeq 20\%$, [52]. The error introduced by this method is acceptable, though requiring further investigation of its feasibility, especially with high SEU rates.

3.2.3 | Burst Detection With Alternate Block Addressing

Results provided so far evidenced the need to overcome the effect of the large vertical upsets while applying a fast correcting method to compensate for the error introduced

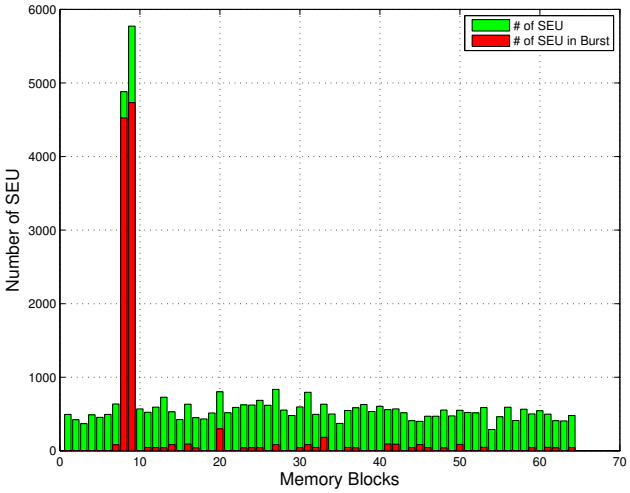

Fig. 3.7: Number of bit upsets per SRAM block, SEU_{block} (green) and SEU_{burst} per SRAM block (red) in one example run. All SEU recorded during irradiation are shown.

by burst events. Data recorded while using a linear addressing did not yield any bit column error, even though they revealed many type B MCUs. The pattern of the physical locations accessed with a linear addressing was analysed: in this configuration the same block was accessed twice at different rows before moving to another block, once the addresses of the second block were read, the previous block was accessed again. This pattern was repeated for all blocks until a full read cycle of the memory was obtained. It was then assumed that the straight lines of bit upsets were formed due to a constant electrical stress of SRAM cells within the same block, possibly enhanced by type B burst events and fast reading. When a location on the memory is addressed, the rest of the SRAM is kept in data retention, thus held at a lower voltage than the operating one. With a linear addressing, blocks are constantly switched, therefore memory cells are alternatively active and held at lower voltage for longer periods. This power cycle reduces the effective duration of micro-latchup events, thus explaining why column errors were not present when a linear scheme was adopted. Following these observations a new addressing technique was developed alternating block accesses. Assuming the set of SRAM blocks B_n, where $n = 0 \cdots 63$, the memory was divided into a left part, blocks in the range $n = [0-31]$, and a right part, blocks in the range $n = [32-63]$. Starting from the initial block B_0 the SRAM is accessed in blocks located alternatively in the left and right part of the memory, therefore implementing two detection windows: one for the right and one for the left part of the SRAM.

The same row and column positions are alternatively read in blocks of the two sides, and increased following the direction top to bottom or bottom to top, as in the physical addressing. Figure 3.8 shows the SRAM split in four areas, the top and bottom parts, given by the intrinsic structure of the device, and the left/right parts, as seen by the addressing pattern implemented in the FPGA firmware. The addition of the burst detec-

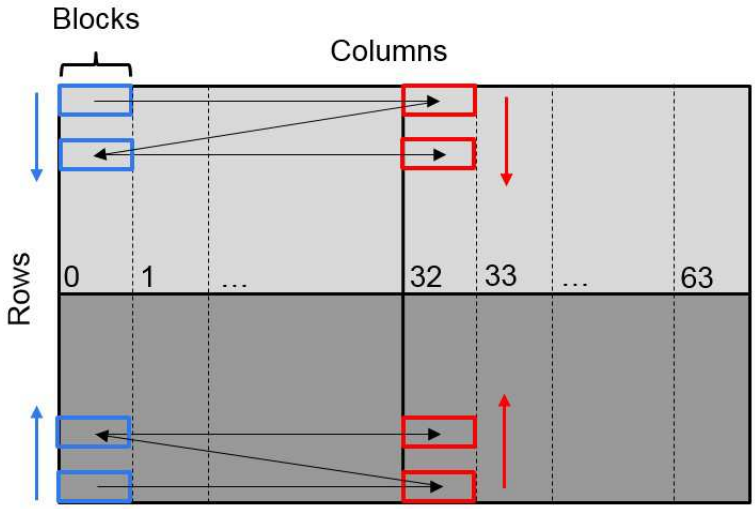

Fig. 3.8: Scheme of the alternated addressing pattern: two rectangular filters move sequentially following the block lines (from top to bottom in the higher half, and from bottom to top in the lower half), while alternating the addressed cells between the left and right sectors of the memory.

tion core on the RadMon V6 FPGA corresponds to an acceptable increase of 5% of the FPGA area. The rows in which the burst detection is disabled were set to 10, keeping a window depth size of 10 rows, thus allowing a full scan of the memory without any gaps between detected bursts. Further tests were carried out at CHARM, in this case the DUT was no longer irradiated with a focused beam, but placed inside the irradiation area in a dedicated test location. Test location 10 was chosen in order to achieve a low value of TID (<100 Gy) while collecting enough statistics of burst events and ensuring a high energy hadron flux sufficiently high in order to cover the RadMon application areas. In particular the chosen test location is within the positions providing spectra representative of the tunnel areas, which are of particular interest for the RadMon V6 operation. A copper target was used and no shielding was applied. The electronics test setup was the same used in PSI proton tests, with the exception that the FPGA tester was placed far from the target, out of the irradiation area, and a 40 m long micro-Coax cable was used to connect the two boards. The timings were adjusted to be comparable to the ones in PSI accounting for long cables. Two Lot II targets were irradiated for more than two weeks. In all runs with an alternate blocks addressing no bit column errors were observed. Figure 3.9 shows the SEU map of the die during one of the irradiations: three type *B* MCUs are visible, the detection window stopped twice for each burst event and the number of bit upsets involved was reported. Results yielded by the software version of the algorithm were in perfect agreement with the output of the firmware detection, a more detailed plot of the SRAM map is reported in Appendix A in Figure A.3.

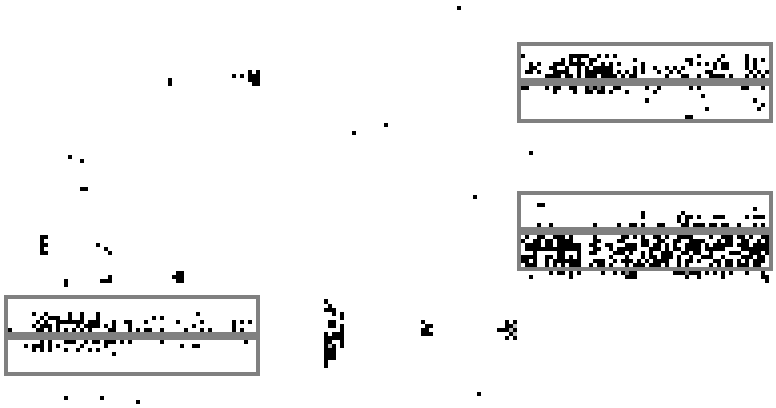

Fig. 3.9: SEU map of the SRAM during irradiation with an alternate blocks algorithm. The rectangles correspond to the detection window at the location where a burst event was recognized.

3.2.4 | Evaluation of the Corrected Cross-Section

Table 3.9 reports test results of runs using an alternate addressing pattern on an SRAM device within CHARM. The cross-section σ was compared with the corrected one σ_{corr}. At the end of irradiation the percentage error between σ and σ_{corr} was calculated using σ_{corr} as the reference value. The minimum correction applied on σ was 6.2%. Fluence values were returned by the analysis of FLUKA relative to the chosen test position [4]. The period between read operations over the same memory unit on the RadMon is $\simeq$ 8 sec, therefore T_{read} was set to a faster value of 5 sec to increase the statistic of burst events. The fluxes are reported in terms of their average values during irradiation.

Table 3.9: Test Results on Lot II and alternate blocks addressing

T_{read} [sec]	$\sigma \cdot 10^{13}$ [cm^2/bit]	$\sigma_{corr} \cdot 10^{13}$ [cm^2/bit]	**Percentage Error**	**Fluence**$\cdot 10^{10}$ [pp/cm^2]	**Flux** [pp/cm^2·s]
5	1.76	1.65	6.2%	4.22	$4.88 \cdot 10^5$
5	1.59	1.39	12%	1.58	$7.29 \cdot 10^5$
5	1.56	1.41	9.9%	4.15	$1.11 \cdot 10^6$

Figure 3.10 shows the evolution of σ and σ_{corr} and the values of SEU_{TOT} and $SEU_{TOT} - SEU_{burst}$ per SRAM read cycle over particle fluence during one of the tests. The repeatability of the corrected SEU values is lower compared to the uncorrected ones: each peak of SEU_{TOT} was related to a burst event. At higher SEU rates the bursts are more and more hidden within the repeatability of the measurement, therefore an accurate correction is needed to retrieve the correct σ_{corr} value.

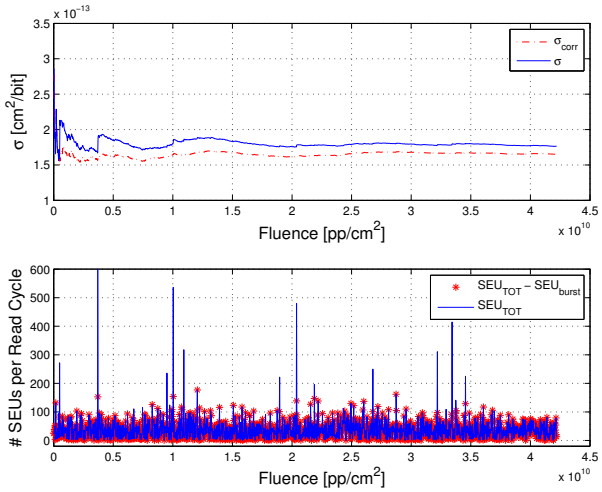

Fig. 3.10: cross-sections σ (blue) and σ_{corr} (red) vs particle fluence (top plot). SEU_{TOT} (blue) and $SEU_{TOT} - SEU_{burst}$ (red) evaluated at every read cycle of the memory (bottom plot). Fluence is measured in particles (pp) over cm^2.

Figure 3.11 shows the percentage error calculated between σ and σ_{corr} reported in the top plot of Figure 3.10, using σ_{corr} as reference. At low fluence values, σ is characterized by large fluctuations, due to burst events involving many bit upsets. As a result the error respect to σ_{corr} can be higher than 30%. For higher fluence values the cross-section becomes more stable and the error committed in the estimation of σ is within 5% to 10%.

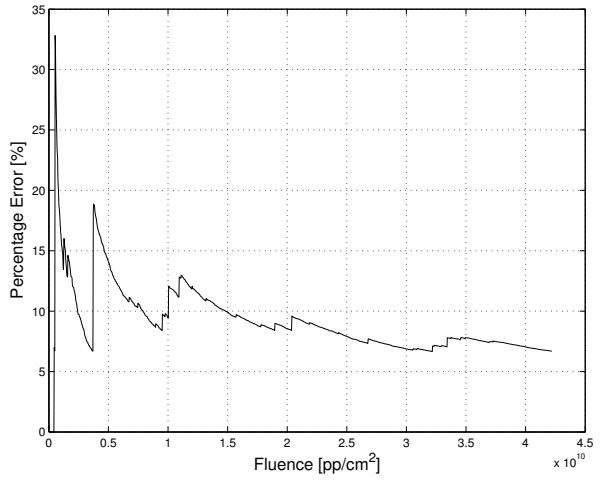

Fig. 3.11: Percentage error vs particle fluence calculated between σ and σ_{corr} with σ_{corr} as reference in a chosen run. At lower fluence values the occurrence of burst events correspond to large errors on the cross-section measurement. Fluence is measured in particles (pp) over cm^2.

The alternate blocks memory accessing technique proved to be highly effective in relieving the electrical stress on the active cells positioned on the same column, since no bit column errors were observed in all runs [74]. The evolution of the cross-section σ and the corrected one σ_{corr} showed, in summary, that at low fluence values, burst events yield large errors in the evaluation of the cross-section, due to the high ratio between SEU_{burst} and SEU_{TOT}, whereas at higher fluence levels the error in the calculation of σ depends on the cumulated number of SEUs coupled with the probability of a burst event given by the environment. Given the promising results, the algorithm was implemented on a RadMon device, tested at CHARM, and finally, in early 2016, deployed on the RadMon V6 units installed in the SPS, ALICE, CHARM, HiRadMat and NA62 areas.

3.3 2016 Results of the Upgraded RadMONs in the Tunnel and Experimental Areas

3.3.1 | Validation of the Algorithm on a RadMon V6 Unit

Data in the previous sections evidenced the sensitivity of burst events to high particle fluxes and fast reading times. The algorithm proved to be effective on the SRAM device irradiated at CHARM, therefore it was implemented on a RadMon V6 unit for a final qualification of its performance. A burst detection core was added within the main firmware of the RadMon V6 system, from hereafter referred to as "firmware V2" as opposed to the older version with a simple linear addressing "firmware V1". In the new implementation, both the bit upsets corrected by the algorithm, SEU_{TOT} - SEU_{burst}, and the bit upsets not corrected, SEU_{TOT}, were returned on the FIP network by the RadMon unit. Two RadMon V6 were placed in position G0 inside CHARM, close to the entrance area of the facility, both mounting four Lot II CY62157EV30 in the SRAM bank 2. The two devices were labelled "CHARM-B3" and "CHARM-B7", and they were attached close to each other at 1.20 m of height, as shown in Figure 3.12.

The "B7" unit was programmed with the old firmware V1, as opposed to B3 which was upgraded to firmware V2 with an SEU threshold of $Th_{SEU} = 30$, in order to evaluate the difference between the two versions and quantify the efficiency of the SEU correction. The two RadMons were irradiated for 21 days with the configuration of copper target with no shielding, reaching an estimated fluence of $\approx 9.1 \cdot 10^{10}$ heh/cm^2. Figure 3.13 shows the total number of SEU recorded by RadMons B3 and B7, and the SEU rate, measured in SEU counts per RadMon read, resulting from the four Cypress memories in the SRAM bank. No burst events occurred on the B3 corrected data, whereas several MCU events were spotted both in the uncorrected SEUs of B3 and B7. The maximum percentage error between the B3 total corrected upsets over the uncorrected ones was 15%. The calculated cross-section was $\sigma = 2.31 \cdot 10^{-13}$ cm^2/bit, assuming a 20% error in

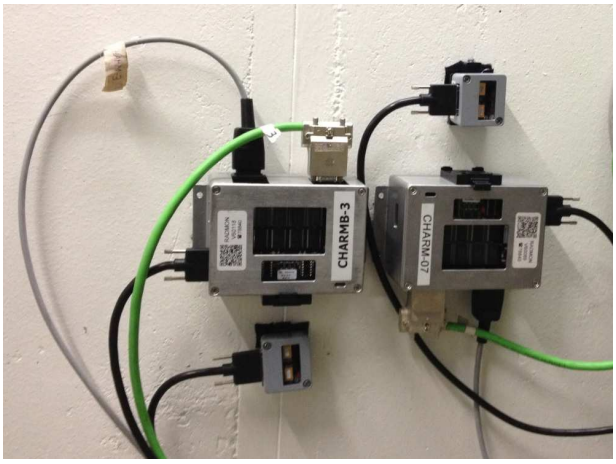

Fig. 3.12: Two RadMon V6 units, labelled CHARM-B3 and CHARM-B7, installed in the CHARM irradiation area at position G0.

the fluence estimation returned by the facility, which is compatible with the σ reference values previously obtained at PSI and in [52].

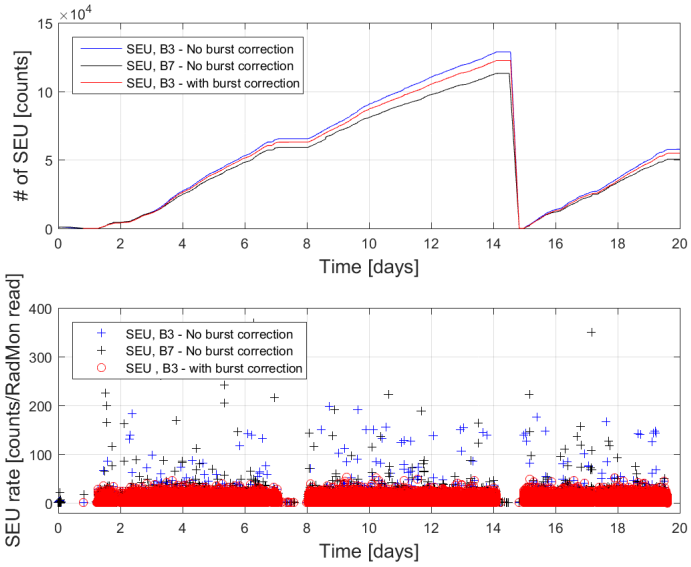

Fig. 3.13: Total number of SEU recorded by RadMons B3 and B7 during three weeks of irradiation (top), and the SEU rate showing corrected VS not corrected SEU readings (bottom).

Since no large vertical upsets were observed and the burst detection and correction algorithm proved to be efficient on a V6 Radiation Monitor, several devices were progressively installed and/or programmed with firmware V2 in early 2016. Results of data from operation of the upgraded devices are discussed in the following section.

3.3.2 | Results in the SPS Tunnel

During the Technical Stop 1 (TS1) of the CERN machines, in April 2016, up to 30 RadMon V6 units were reprogrammed or newly installed with the upgraded firmware V2 inside the SPS tunnel. Data showing results from April until November 2016 are hereby presented. Figure 3.14 reports the SEU rate, measured in counts per RadMon read, of the RadMon device labelled "1RI01S". In the time segment with firmware V2, the SEUs corrected by the algorithm are given in blue colour, whereas the uncorrected ones are given in red, when the unit was programmed with firmware V1, no correction was applied and the only SEUs in output are displayed in blue. A clear difference is visible in the transition of the HEH monitors between the two firmware versions: several burst events with amplitude up to ≈300 upsets were occurring during the whole operational period. When the RadMon was reprogrammed with the correction method, all MCU events were correctly filtered.

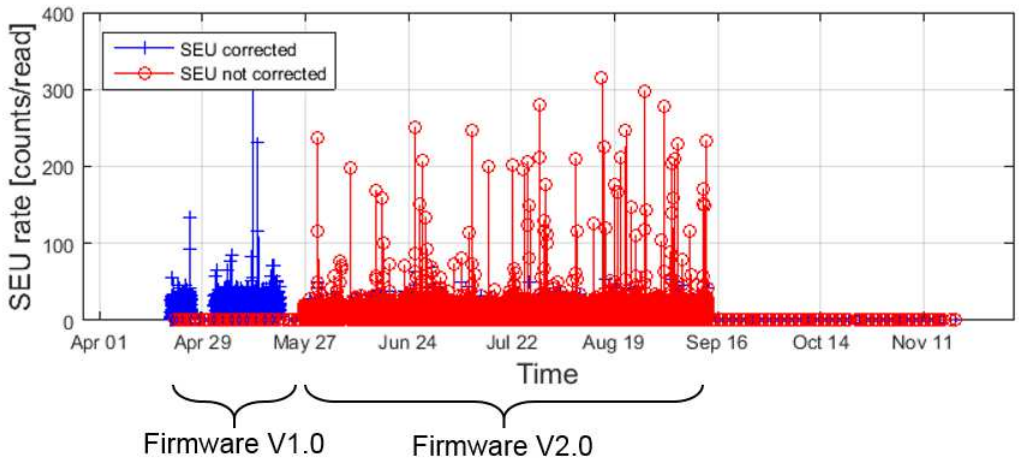

Fig. 3.14: SEU rate of the RadMon "1RI01S" in the period April-November 2016. The corrected (blue) and uncorrected SEUs (red) are shown for the period with firmware V2. When firmware V1 was used, no correction was applied and only uncorrected SEU data are given (in blue colour).

All data from the SPS RadMon V6 systems were analysed to evaluate results of the new firmware and checked for large vertical upsets which might have potentially corrupted the efficiency of the correction method. Figure 3.15 and 3.16 refer to data from RadMons "2LI04S" and "6RI05S" respectively. The flux levels recorded by the two devices corresponded to average SEU rates of ≈ 15 SEUs per read. In the case of RadMon "2LI04S", in Figure 3.15, only five bursts occurred in the time span of eight months. These events were corrected and their impact on the fluence calculation resulted in a maximum error of ≈ 15%. This result strongly highlights how at low flux, and thus with a lower probability of MCU bursts, HEH fluence results can still be highly affected by even

one single event corrupting the SEU counting, hence the need of an efficient correction filter independent of the flux levels. This latter observation is even more stressed out by results shown in Figure 3.16 for RadMon "6RI05S": the first burst detected caused a reading error of ≈ 60% of the measurement, and the algorithm was efficiently filtering out MCU events even when the SEU rate increased, such as during November month. This result is of especially high relevance, since it stressed out the importance of a method based on the topological representation of the MCUs in the SRAM layout, as opposed to the application in post processing of a fixed threshold on the SEU rate. This latter method would not be a solution to the burst problem in the context of the RadMon monitors, since the tunnel environment is characterized by strong varying flux levels, and consequentially by highly different SEU rates.

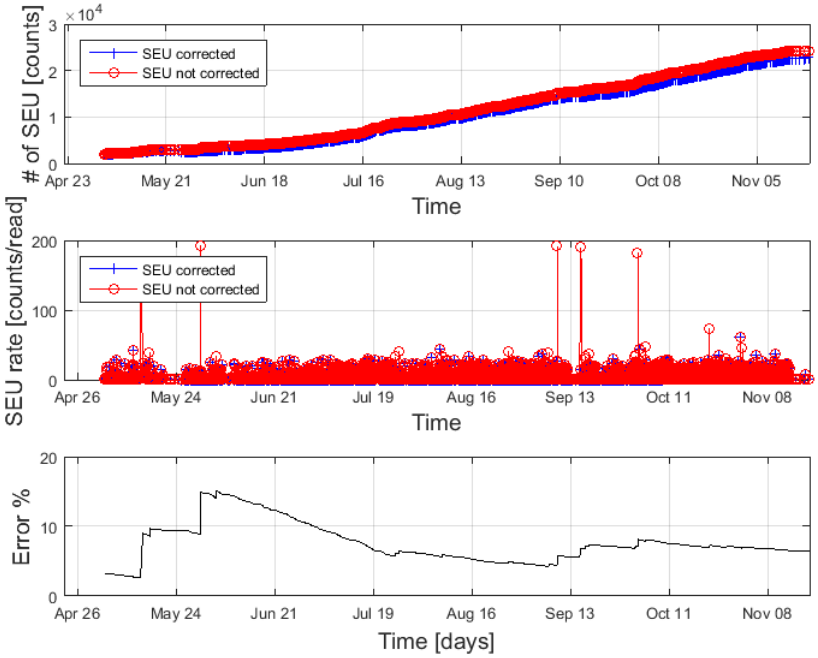

Fig. 3.15: The corrected (blue) and uncorrected (red) integrated SEUs between April-November 2016 for RadMon "2LI04S" upgraded with firmware V2 (top), along with the SEU rate (middle) and relative percentage error (bottom). At low fluence levels, a burst event yields a 15% error on the HEH fluence measurement.

Higher HEH flux levels were monitored by RadMon "4RI05S", in Figure 3.17. In this case average SEU rates of ≈ 100 SEUs per read were measured during the whole time period. A constant percentage error of up to 34% was estimated on the HEH fluence measurement.

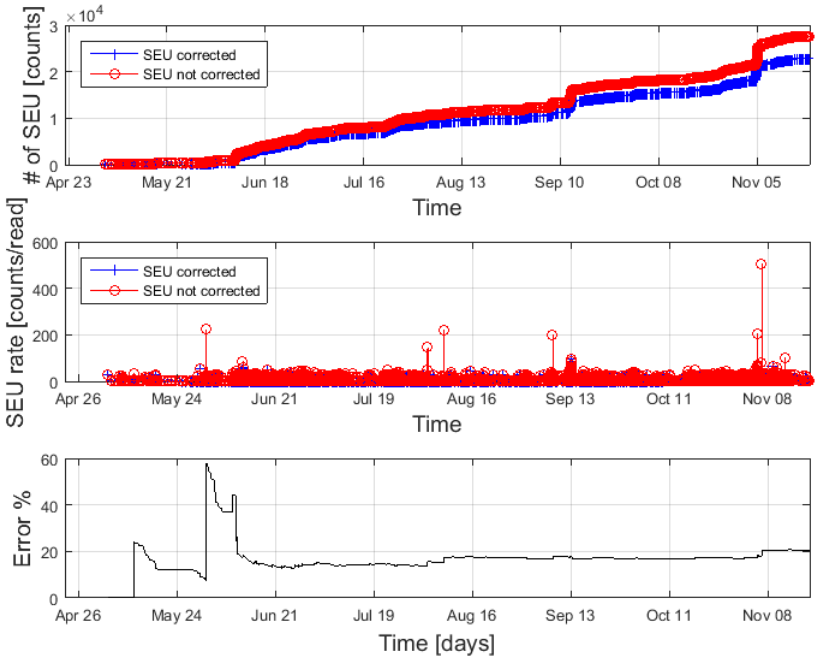

Fig. 3.16: The corrected (blue) and uncorrected (red) SEUs between April-November 2016 for RadMon "6RI05S" upgraded with firmware V2 (top), along with the SEU rate (middle) and relative percentage error (bottom). The first burst occurred is enough to yield an error on the fluence measurement of 60%. The filtering algorithm is valid also in the presence of fast varying flux values.

3.3.3 | Results in the Experimental Areas

Several RadMon V6 units were upgraded with the new firmware and installed also in the experimental areas. During the Year End Technical Stop (YETS) 2015-2016, 5 RadMon V6 were installed in the HiRadMat facility. In April 2016, 11 RadMons were deployed in the NA62 experimental area and other 7 were placed inside the CHARM facility. During the second Technical Stop (TS2), in September 2016, the 13 RadMons located in ALICE cavern and the 8 RadMons inside the PSB tunnel were reprogrammed with firmware V2. Data from operation of the ALICE, PSB, NA62 and HiRadMat units did not show any evidence of burst events: the fluxes recorded were very low, in particular for NA62 and ALICE RadMons. One RadMon in HiRadMat, labelled "Hiradmat-3" experienced a hardware failure caused by radiation in May 2016, and therefore it was replaced. A particular care was given to the monitors located inside the CHARM facility: these systems hold the double function of monitoring the radiation levels at the different positions, and calibrating the facility through benchmarking of data with values returned by FLUKA. The CHARM facility started to be back in operation in April 2016, after 2015-2016 winter shut down. During the commissioning, each test position was calibrated

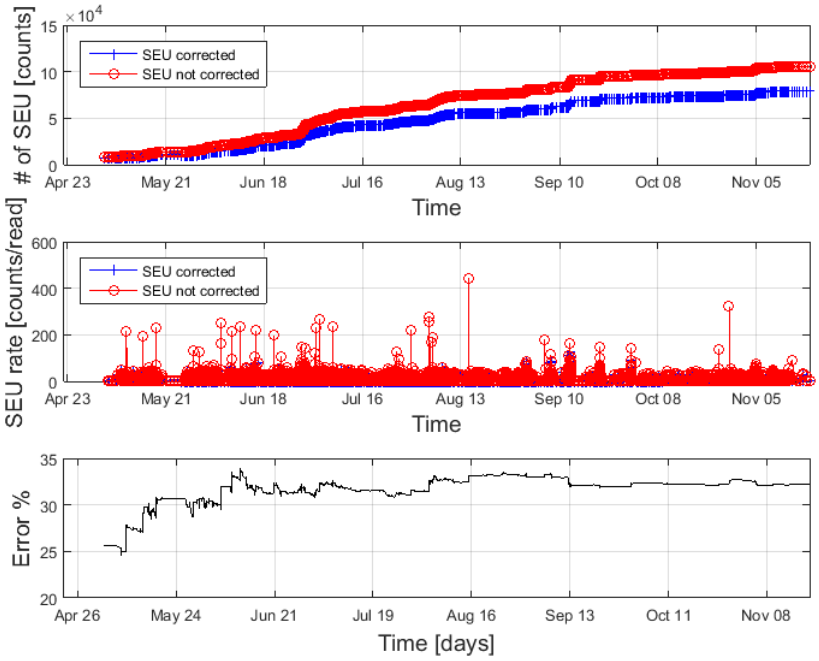

Fig. 3.17: The corrected (blue) and uncorrected (red) SEUs between April-November 2016 for RadMon "4RI05S" upgraded with firmware V2 (top), along with the SEU rate (middle) and relative percentage error (bottom). In presence of higher flux levels, the detection algorithm applies a constant correction reaching in this case up to 34% of the HEH measurement.

using the 7 RadMon units, referred to as "B1","B2", "B3", "B4", "B5", "B6" and "B7", re-programmed with firmware V2. Several facility configurations of target and shieldings were set, in order to measure particle spectra for each settings at different test locations. This process of calibration of the facility is essential to ensure the correct operation and retrieval of the HEH fluences and TID values for CHARM users, [55]. Figure 3.18 shows the corrected and uncorrected SEUs recorded by RadMon "B3".

The SEU rates are plot together with the counts coming from the SEC1, which gives indication of the beam intensity and operation. One large MCU burst involving more than 1500 cells was observed. This event was not filtered by the correction algorithm, hence the final HEH fluence relative error was only 4% respect to the corrected SEU values. This event might have been related to vertical upsets and it is the only case observed in 2016 in which a burst was not detected. The SEC1 data did not show any modification of the beam intensity, therefore the event is not related to a sudden variation of the beam parameters. On the other hand, this burst showed up similarly on three other RadMon units deployed on different test locations at the same time, suggesting the cause might have been of different nature, such as a failure on the electrical network shared by the systems. Nevertheless, this episode provided fruitful information for future improvements of the correction algorithm.

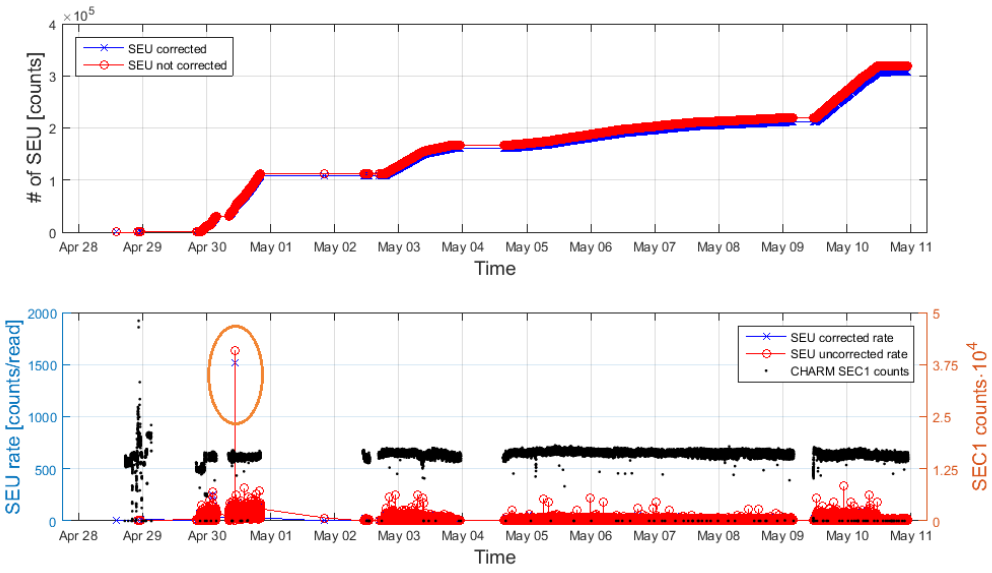

Fig. 3.18: The corrected (blue) and uncorrected (red) SEUs of RadMon "B6" upgraded with firmware V2 and located in CHARM position 1 (top), and their relative SEU rates displayed with the facility SEC1 counts (black) VS time (bottom). One large MCU burst (circled in orange) fell out of the filtering action.

3.3.4 | Future Optimizations of the RadMon V6 Sensors

The results obtained by the monitors upgraded with the new firmware in 2016 proved the efficiency of the algorithm detecting and correcting MCU burst events on the Cypress CY62157EV30 SRAM used as HEH monitor. For future optimized versions of the RadMon, the algorithm can be further improved: for instance alternating read operations to SRAM blocks over more than 2 parts of the memory has the effect of decreasing the period between accesses to addresses of the same block, thus mitigating the column error effect and lowering the probability of events such as the one observed during the commissioning of CHARM in April 2016. A lower Th_{SEU} value can also be a good solution to account for error bits eventually excluded by the detection, provided an acceptable error would be introduced to the SEU count. Nevertheless, the algorithm technique was developed in response to the burst problem encountered on the CY62157EV30 device while in operation. More SRAM candidates will be the object of study in order to find other suitable candidates not affected by the burst effect. In particular, preliminary results on the Cypress CY62167GE30-45ZXIE 65 nm SRAM showed a proton cross-section comparable with the CY62157EV30, making it a possible valid candidate for HEH fluence measurements, preliminary results of static tests carried out at PSI are reported in Appendix B. Concerning the TID sensors, a future improvement may include the combined use of RadFETs with a Floating Gate dosimeter (FGDOS), [75]. This latter device shows characteristics of high dose sensitivity and it is of particular interest especially consider-

ing the adaptation of the RadMon V6 to a CubeSat payload for radiation monitoring in Low Earth Orbit Space, which is the main subject of this work.

3.4 Conclusions

The 90 nm 8 Mbit Cypress SRAM memory CY62157EV30 was chosen as the new HEH fluence monitor in the recently upgraded RadMon V6 System. The component was selected due to its high proton cross-section, insensitivity to thermal neutrons, independence from the operating voltage and availability on the market, characteristics of extreme relevance in the context of a radiation monitoring application within the CERN tunnels and experimental areas. Multiple Cell Upsets, induced by micro-latchups and arising as bursts of a high number of error bits, were reported during operation in dynamic mode of the memory. A study of the parameters involved in the generation of these events was carried out at the PIF facility at PSI, using a focused proton beam. An algorithm for on-line fast detection and correction of these bursts was implemented on FPGA and evaluated. Two lots of the chosen DUT were tested with a 3.3 V voltage supply and a beam energy of 150 MeV.

Several test parameters were systematically changed during each run and the SRAM cross-sections were evaluated. The reading period and the particle flux resulted the parameters most involved in the generation of bursts: with fast reading values and high particle fluxes the probability of burst events arising on the memory was increased. The use of a physical addressing scheme, where addresses are read across SRAM blocks within the internal architecture of the memory, resulted in a high number of bit upsets located in the same column array of the die. These events were highly affecting the algorithm, thus a direct comparison of the final cross-section σ and the corrected one σ_{corr} was not possible using a physical addressing scheme. For this reason a statistical solution to the problem was considered and investigated. In this latter technique, error bits counted within blocks affected by a large number of SEU would be replaced by the expected value of the mean of the SEU occurring in each block. Although this method represented a valuable option, a better approach for the mitigation of column errors was required. Given the latchup nature of the observed events and the relation of the column errors to the internal layout architecture of the SRAM, a new addressing pattern was developed accessing alternate blocks located in the left and right parts of the memory, while implementing two detection windows and incrementing rows and columns within each block. Tests with this addressing scheme were performed at the CHARM mixed field facility at CERN: with an alternate blocks memory accessing, the electrical stress on the active cells positioned on the same column was reduced and no bit column errors were observed in all runs. This technique resulted to be faster and less computationally expensive compared to post-processing algorithms, and it allowed burst recognition with high fluxes (i.e. with high SEU rates), where burst events are hidden within the repeatability of the

measurements, as well as in areas with lower flux levels.

Further on the algorithm was implemented on a RadMon V6 unit and verified at CHARM during three weeks of irradiation. Results proved the efficiency of the MCU detection and correction algorithm, leading to the design of a new firmware for the RadMon V6, including the proposed technique. Around 74 RadMon V6 units were upgraded or newly installed within the PSB and SPS tunnels and the ALICE, HiRadMat, NA62 and CHARM areas. Experimental data collected from operation of the devices mounting the new firmware showed several burst events correctly detected and filtered out, hence retrieving corrected measurements of the HEH fluences. The solution adopted resulted particularly effective at low fluence and flux values, where one single event was observed to be enough to yield 60% of error on the measurement. A failed burst correction attempt occurred only once: one large burst event was observed and undetected at the same time on three RadMon units during the commissioning of the CHARM facility, in April 2016. This latter observation provided useful grounds for future optimizations of the algorithm, such as exploiting different Th_{SEU} values, adjusting the detection window size or using alternative addressing patterns (e.g. further splitting of the SRAM area).

The following Chapters will focus on the effort carried out in this work towards the adaptation of the RadMon V6 to a 1U CubeSat scientific payload. In particular, the next Chapter will present the motivations that led to the start of the research project CELESTA, the investigation of the radiation environment encountered during the proposed mission and the analysis of the associated design constraints.

4

FOURTH CHAPTER

A QUALIFICATION PROCEDURE FOR NANOSATELLITES AT CHARM

4.1 The CELESTA Mission

In the previous chapters the CERN Radiation Monitor V6 was introduced, along with its most recent upgrades, in relation to its use as an on-line tool for distributed measuring of the radiation fields. As already given in the Introduction, one of the main scopes of the research presented in this work concerns the application of the RadMon V6 as a satellite payload for space science. The use of Nano and Pico satellites for scientific research in space missions is constantly and rapidly growing in both the industrial and academic sectors. Their design and small dimensions lead to a huge saving in terms of budget, time and resources for a space mission, when compared with larger, more conventional satellites. CubeSats are commonly designed with an extensive use of Commercial Off The Shelf (COTS) components, due to their availability in the market and overall good electrical performances in a radiation environment over an average mission timeframe of two years. Nevertheless the choice of each candidate device to be embarked on a CubeSat mission undergoes a strict process of radiation qualification which is time-consuming and expensive, [76], [77]. Therefore a huge testing effort is often dedicated to characterize every single component and assess parameters such as its degradation over TID and sensitivity to Single Event Effects, using different sources at various terrestrial facilities. The same approach is followed in the framework of the Radiation-to-Electronics project at CERN, where design requirements of scalability, low cost and high electrical performances make COTS components the first choice at the basis of systems located in high radiation areas [28]. Testing at CHARM is therefore essential for radiation hardness assurance of large systems and small commercial components, moreover the use of the facility can be also extended to systems designed for space applications. In this

context the CERN Latchup Experiment and STudent sAtellite (CELESTA) was recently proposed. CELESTA is the first CERN-driven nanosatellite, developed in collaboration with the University of Montpellier and the Centre Spatiale Universitaire of Montpellier, in the framework of a collaboration agreement defined and signed in 2015 [78] with the support of the CERN Knowledge Transfer Fund. The project has two main objectives:

1. Develop and launch into space a CubeSat payload version of the CERN radiation monitor V6, coupled with a Single Event Latchup experiment.

2. Demonstrate that the space radiation environment of Low Earth Orbit can be reproduced at the CHARM facility.

Concerning the first objective, CELESTA has been designed as a 1U CubeSat based on the ROBUSTA platform [79] and the CERN Radiation Monitors. The RadMon V6 components and sensors were adapted to a new design tailored to comply with CubeSats requirements and ultimately forming a stand-alone radiation monitor for Low Earth Orbit missions. In addition, a Single Event Latchup experiment based on SRAM memories was proposed as a secondary scientific objective to be embarked on the payload. The goal is to map SEL occurrences at different orbit altitudes within the Low Earth Orbit. The aim is to differentiate the protons and heavy ions contributions within the radiation environment, especially when crossing the South Atlantic Anomaly (SAA, described in the next section), and at polar latitudes, when the satellite passes through polar cusps. Regarding the second objective, tests of the system in the CHARM irradiation area allow the benchmarking of results in terms of the predicted SEL rate, HEH fluence and TID values. Although CHARM and LEO environments cannot be compared through individual particle spectra, they are comparable through the hadron spectra and the energy deposition distribution in a representative geometry. The equivalence between the CHARM and LEO environments would open the facility for space systems characterization activities, as well as validating the radiation qualification procedure adopted for small satellites and COTS components.

The design strategy followed an initial study of the mission parameters in order to investigate the feasibility of the adaptation of the CERN RadMon to a CubeSat payload module. As a second step a payload test board was developed starting from the COTS components in the RadMon design. The module was integrated with a 100 nm RadFET for Total Ionizing Dose (TID) and the 90 nm Cypress CY62157EV30 SRAM memory for the High Energy Hadron (HEH) fluence measurements. The test board was irradiated at CHARM in a test location representative of the LEO environment, to get a better understanding of system parameters such as current consumption, degradation over TID, characterization of single events and sensitivity to temperature in relation to mission requirements.

4.1.1 | The Space and Low Earth Orbit Environment

At the early beginning of a space mission, a special care must be given to the analysis of system constraints and requirements in relation to the foreseen mission radiation environment. When particles reach the earth's atmosphere, they collide with the nuclei of nitrogen and oxygen atoms and create cascades of secondary radiation of different kinds, including leptons, photons, and hadrons. Radiation is present in the natural environment: the flux of particles varies with altitude, latitude, and to a lesser extent with longitude. Neutrons, protons and pions can induce SEEs and originate failures in the electrical design of a satellite. Similar to the environment encountered in the CERN accelerator tunnels, particles may have a broad energy spectrum and present several interaction mechanisms that result in energy deposition in the materials. The radiation environment found in space is characterized by three main sources of energetic particles which can yield effects on electronics components:

1. Radiation belts, such as the the Earth's so called Van Allen belts, or the planetary ones, for instance in the case of Jupiter for the JUICE mission [80].

2. Solar energetic particles events, more commonly refered to as solar flares.

3. Galactic Cosmic Rays (GCR).

The Earth's radiation belts are mainly populated by energetic protons and electrons, trapped inside the Earth's magnetic field. There are two belts, the inner belt, closer to the Earth up to ≈ 3 Earth radii at the magnetic equator, and the outer belt from 4 to 7 Earth radii. The inner belt is made of electrons and highly energetic protons, instead the outer belt is mostly made of energetic electrons. Particle energies in the radiation belts vary from several keV up to hundreds of MeV for protons, and from several eV to ≈ 10 MeV for electrons. Particles trapped in the belts are subject to different movements, such as gyration or bouncing around the magnetic field line, and drift around the planet. The Earth's magnetic field is a dipole tilted by approximately 11° from the rotation axis of the Earth, the center of the field is not at the center of the Earth, but it is offset by more than 500 km towards South-eastern Asia. As a consequence, a low magnetic intensity region forms at the South Atlantic region, called South Atlantic Anomaly (SAA). In this region trapped particles can access lower altitudes creating a hazard zone for LEO missions, in particular concerning single events induced by high energy protons. The second source of energetic particles are solar events caused by eruptions on the sun corona. Those events, commonly called solar flares, accelerate protons and ions in the interplanetary medium. Protons can reach energies up to 500 MeV and ions more than 100 MeV/nuc. Galactic cosmic rays are the final source of radiation in space: they are generally made of ions and include also protons. In particular ions with atomic number Z up to $Z = 30$ can be largely found in the composition of GCR [81]. Cosmic rays cover a large spectrum of energies, with a comparatively high flux in the 100 MeV to 10 GeV range and a peak corresponding to ≈300 MeV/nuc. Cosmic particles collide with the nuclei of atoms making

up the Earth atmosphere and initiate the so-called air showers, producing particles such as neutrons, protons, muons, pions, electrons and gamma-rays. All three energetic particle populations present a long-term variation with the solar cycle. The solar cycle has a duration of approximately 11 years: 4 years from solar minimum to solar maximum and 7 years from solar maximum back to solar minimum. The majority of the very high intensity solar events occur at the solar maximum, whereas at the solar minimum GCR may easily penetrate the Heliosphere and thus contribute to higher flux values of ions. The solar cycle must be then taken into consideration when preparing a space mission and planning the orbit parameters. The space radiation environment interacts with matter and causes the various types of radiation effects on electronics components already described in the previous chapters. Figure 4.1 shows the connection between the three sources of energetic particles and the major relative effects on electronic devices.

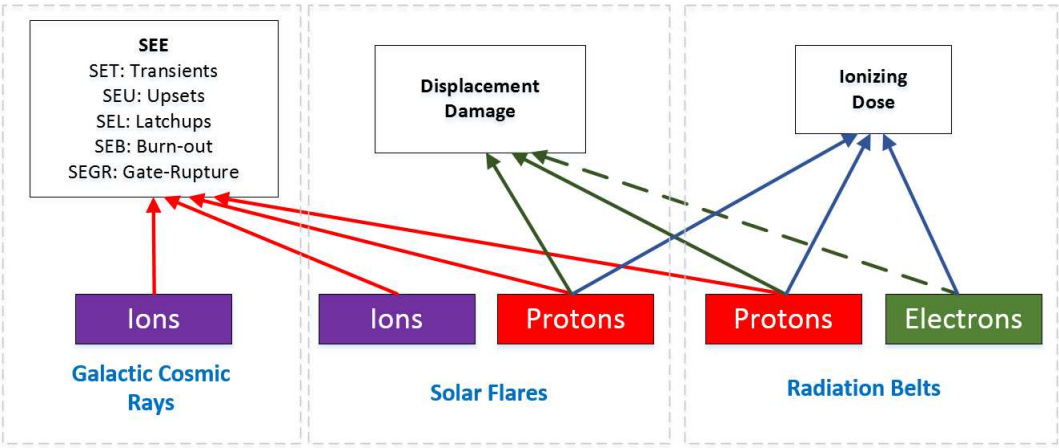

Fig. 4.1: Radiation effects on electronics as caused by the three sources of energetic particles in space.[**source**: [1]]

Single Event Effects occur when an ion deposits more charge than a critical charge value in the silicon layer, or in the case of protons when the recoil atom deposits the charge. Interplanetary missions such as JUICE must also take into account the SEE cross-section caused by the high quantity of energetic electrons found in the planet surrounding belts [82]. Ionising dose is a cumulative effect which can originate from both electrons and protons. Both types of particles from different sources may cause charge trapping in the silicon oxide. Similarly, atomic displacement is due to electrons and protons in space, and may affect the electrical performance of electronic devices as well as the materials forming the satellite (e.g. solar panels).

In the context of Low Earth Orbit CubeSat missions, the Earth's inner proton radiation belt is the main concerned environment. Charged hadrons dominate the inner belt, thus contributing to high SEE cross-sections created by indirect ionization, and ultimately resulting in particle spectra highly comparable to the ones found in particle accelerators.

In particular, the following conclusions can be extracted when comparing the proton belt environment with the accelerator context:

1. High Energy Hadrons fluxes in the proton belt are similar to those in the shielded LHC locations.

2. The accelerator field is typically composed of protons, charged pions and neutrons, whereas protons are the only relevant hadron type for the inner belt case inducing SEEs through indirect ionization.

3. Spectra are generally harder (more energetic) in the accelerator case, except for the negligible contribution from Galactic Cosmic Ray protons which correspond to ≈1% of the spectra at energies above 1 GeV.

These observations highlight the relevance of the CHARM facility in the context of radiation testing of systems designed for space applications, and in particular of CubeSats. Inside the mixed-field produced at CHARM, the contribution to TID is roughly equally divided between charged hadrons, photons and electrons/positrons. The HEH contribution is approximately ≈40% of pions, ≈35% of neutrons and ≈25% of protons. Assuming that SEEs are mainly induced by indirect energy deposition, hadrons may be considered, in first approximation, as identical particles, thus validating the use of CHARM to obtain predictions of the in-flight trapped proton SEE rates and the estimation of the devices' HEH cross-sections. The space environment is at the core of the activity in the SEE analysis domain: detailed and accurate models of the space radiation environment are available, as well as a wide range of space borne detectors (and even full missions) specifically designed to study the radiation effects on electronics. Space environment standards are provided by ESA-ECSS (European Co-operation for Space Standardization) as well as NASA, in order to help engineers in the process of studying the environment parameters that need to be taken into account for the assessment of radiation effects for a specific mission, [83]. In particular, the guidelines address orbit analysis, the prediction of energetic particle fluxes (electrons, protons, ions) and more in general the radiation effects input parameters: the dose-depth curve for Total Ionising Dose, the equivalent fluence depth curve for Total Non-Ionising Dose and the LET Spectrum for SEE.

4.2 Mission Constraints Analysis

4.2.1 | Evaluation of the Orbits

The CELESTA mission is scheduled to last approximately two years, a nominal time duration for a CubeSatellite deployed in LEO orbit. The analysis of mission constraints begins with the investigation of possible orbits and the study of the expected radiation

fields. Different LEO polar orbits were considered and in particular two were selected for further characterization: one circular, with apogee and perigee at 600 km and 97.8° inclination, and one elliptical, with apogee at 1400 km and perigee at 300 km and 98.83° inclination. The orbital parameters are reported in Table 4.1 and they were kept for all simulations performed. Only quasi-polar orbits were taken into account: this aspect is of extreme importance for the mission, as a polar orbit crosses highly different areas in terms of particle spectra, thus allowing to effectively differentiate the protons and the heavy ions contributions to the measured SEE occurrences.

Table 4.1: Parameters of the two selected polar orbits.

Orbit	**Apogee** [km]	**Perigee** [km]	**Inclination** [°]
Circular	600	600	97.8
Elliptical	1400	300	98.83

Low Earth Orbits range between 200 km and 2000 km from the Earth surface, this orbit range is common among CubeSat missions and for other spacecrafts such as the International Space Station (ISS). The ROBUSTA radio-communication subsystem was designed specifically for typical LEO link budgets. The mission environment was simulated with different tools: the orbit decay was simulated with the Semi-analytic Tool for End of Life Analysis (STELA) [84], a tool developed by CNES, the French National Space Agency ("Centre National des Etudes Spatiales"). STELA allows to effectively propagate LEO orbits as well as geo-stationary (GEO) and geo-stationary-tracking (GTO) orbits. The mission lifetime is calculated while verifying that the protected zones of the atmosphere, where satellites are restricted, are respected. Simulation parameters of the reflecting and drag area, drag coefficient "Cd"[85], satellite mass and solar activity are given in Table 4.2.

Table 4.2: STELA simulation parameters

Space Object						**Solar Activity**
Reflectivity Coefficient	**Reflecting Area** [m^2]	**Drag Area** [m^2]	**Drag Coefficient**	**Cd**	**Mass** [kg]	Mean Constant
1.5	0.015	0.015	Constant	2.2	1.0	

Figure 4.2 and 4.3 show STELA simulation results for the 600 x 600 km circular orbit and the 300 x 1400 km elliptical orbit, respectively. Both orbits have a lifetime of two years, following project requirements and complying with French Laws on Space Operations (LOS), which state that the spacecraft must re-enter the atmosphere within twenty-five years after the mission end. In the case of an elliptical shape, the apogee is subject to a larger decay effect over time.

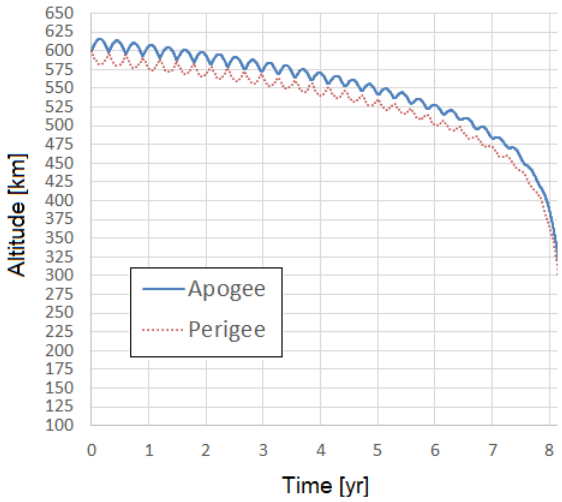

Fig. 4.2: STELA simulation results for the polar circular orbit.

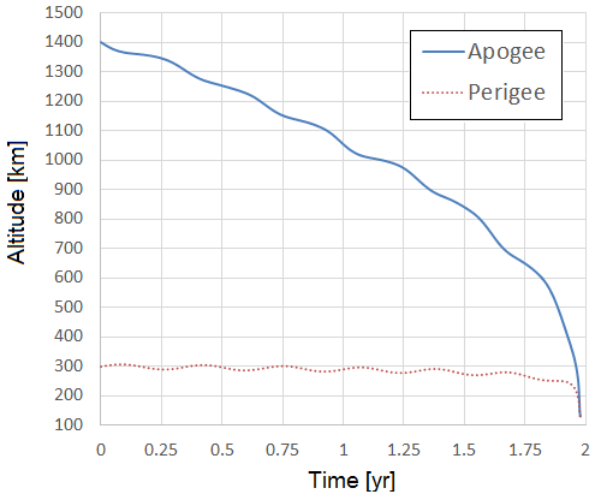

Fig. 4.3: STELA simulation results for the polar elliptical orbit.

The wavelet observed on the orbit shape is due to the choice of drag parameters, which account for the atmosphere affecting the trajectory of the satellite. The orbital decay must be carefully examined: high altitude levels correspond to higher dose rates. As a consequence, the calculation of the final total dose absorbed during the mission is subject to large variations depending on the amount of time spent by the satellite at high altitudes. In order to have a clearer picture of the dose and flux rates expected during the mission, simulations were performed using the OMERE tool, a modelling tool for external radiative environments [86] developed by the company TRAD. Figure 4.4 shows the dose rate evaluation obtained by OMERE simulations in the case of the proposed circular orbit, Figure 4.5 in the case of the elliptical one. In both cases 1 mm

of Aluminium shielding was assumed around the spacecraft and a solid sphere model was adopted. High dose values were obtained when the satellite passed through the polar cusps or in the SAA, which was an expected result. For the elliptical orbit, the rate increases considerably with the altitude and when the spacecraft gets deeper into the Van Allen belts, consequently the maximum dose rate value reached along the elliptical orbit is a factor 10 higher compared to the circular one.

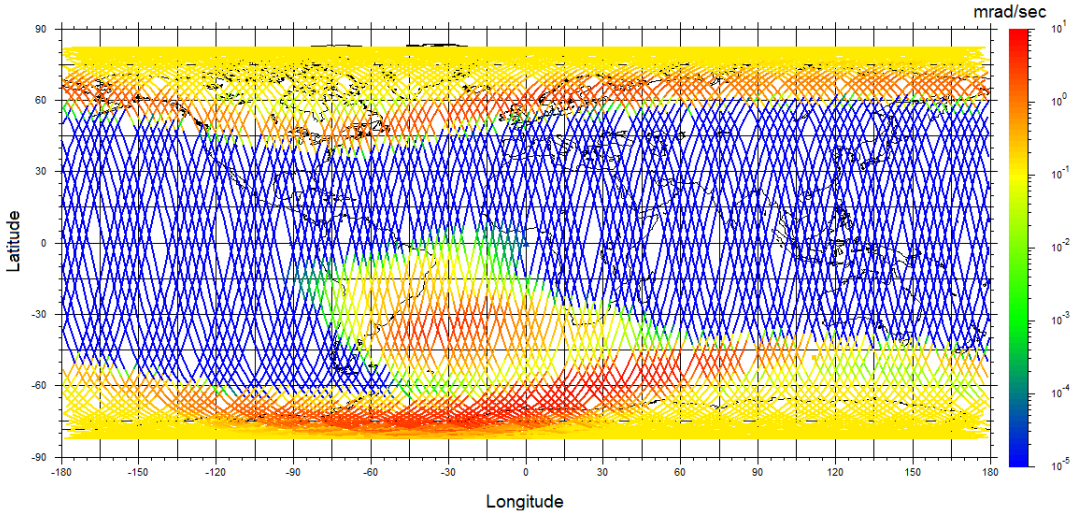

Fig. 4.4: Dose rate along the proposed circular orbit. The dose rate values reach a maximum of 10 mrad/sec in the colour scale.

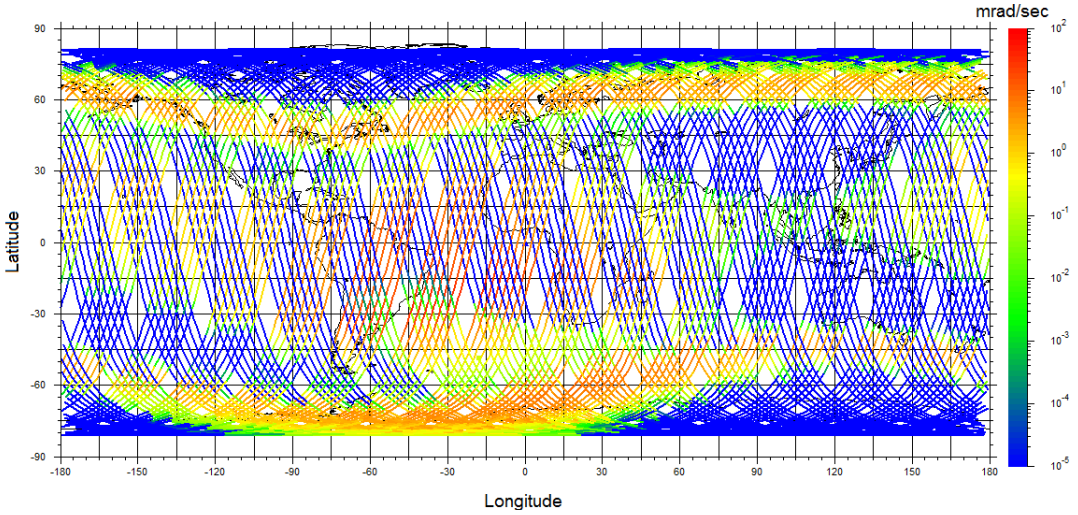

Fig. 4.5: Dose rate along the proposed elliptical orbit. The dose rate values reach a maximum of 100 mrad/sec in the colour scale.

A summary of simulation results in terms of expected TID and energetic proton fluxes

is reported in Table 4.3. A final TID value of 160 Gy (16 krad(Si)) is expected for the simulated circular orbit and 290 Gy (29 krad(Si)) for the elliptical one. Proton fluxes reach levels in the order of $10^{\cdot 5}$ p·cm^{-2}·h^{-1} and $10^{\cdot 6}$ p·cm^{-2}·h^{-1} for the circular and elliptical orbits, respectively. These values were essential for the choice of components to be included in the design of the payload electronics, as they represent the first constraint to be evaluated in terms of tolerance to radiation effects. The estimation of the proton fluxes was necessary to obtain a prediction of the number of events expected in flight. Using Equation 3.1 described in chapter 3, the number of Single Events Upsets expected during flight on an SRAM device can be calculated using the cross-section σ and the estimated proton flux values for each orbit.

Table 4.3: Summary of the radiative environment predicted dose and flux levels.

	Dose		**Protons Flux**
	Dose rate [mGy·/h]	**TID** [Gy]	[protons·cm^{-2}·h^{-1}]
Circular	9.06	160	$1.93 \cdot 10^5$
Elliptical	16.55	290	$2.41 \cdot 10^6$

Considering the circular orbit, OMERE simulation results of the SEU occurrence rate using a Cypress CY62157EV30 memory are reported in Figure 4.6, for the proton contribution, and Figure 4.7 for the heavy ion one. The SEU rate resulting from trapped protons is higher with respect to the one calculated for HI. Although essentially concentrated in the SAA, HI instead are present mostly in the polar cusps. The values of the Cypress SRAM cross-section VS energy, obtained during test campaigns [87], were convoluted with the environment spectra in order to calculate an estimation of the predicted total SEU mission values, the approach followed is fully described in [56]. As a preliminary result, 2500 SEU were calculated for the circular orbit and 14000 for the elliptical with 2 years of mission lifetime [88].

The satellite is composed of several subsystem modules, connected inside a mechanical structure in the shape of a cube with ≈ 10 cm of side length. A more detailed description of the CELESTA structure, subsystems and their functions is addressed in chapter 6. A study of the displacement damage in a 2 year mission in LEO orbit was carried out in [89], simulation results estimated a 1 MeV neutron fluence below $2 \cdot 10^{11}$ cm^{-2}, too low to be considered for in-flight measurement. As a consequence the estimation of DD using p-i-n diodes was excluded from the CELESTA payload sensors. A maximum total dose value of TID_{max} = 290 Gy, (29 krad(Si)), was calculated for a 2 years elliptical polar orbit. This value was used in the experimental tests as the maximum target TID level for the qualification and choice of the COTS components. The expected temperature range during the mission is ≈ -20 °C to 80 °C. The power budget constraints are set by the CubeSat platform: the maximum total satellite power consumption is P_{tot} = 1 W, while the average power allowed for the payload is 600 mW. Results of mission orbit and environment analyses, together with the temperature and electrical constraints imposed by the satellite platform, led to the design of a test board for the proof of principle

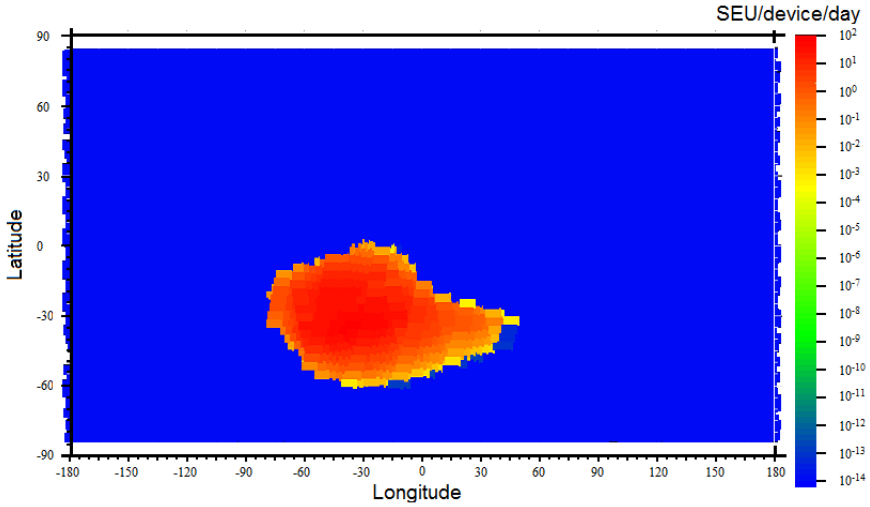

Fig. 4.6: Proton contribution to SEU occurrences simulated with OMERE, considering a Cypress CY62157EV30 SRAM flying in a circular polar orbit.

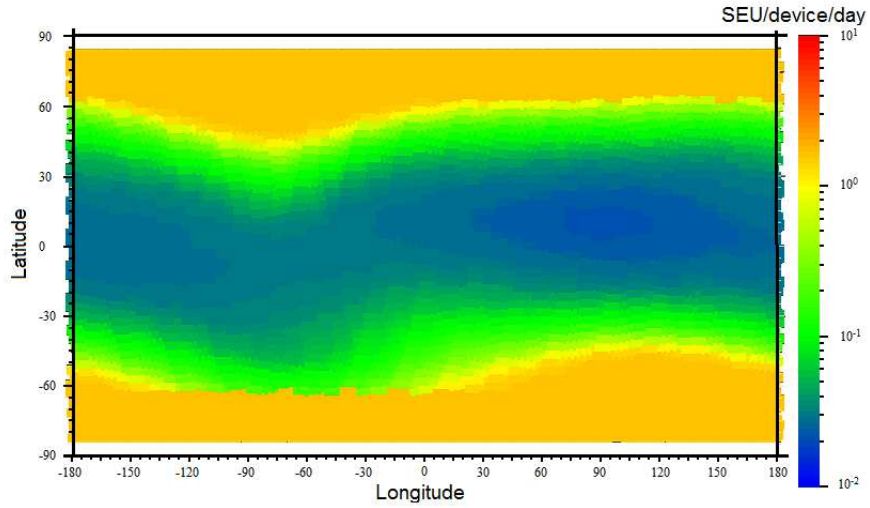

Fig. 4.7: Heavy Ion contribution to SEU occurrences simulated with OMERE, considering a Cypress CY62157EV30 SRAM flying in a circular polar orbit.

study of the payload concept, the radiation characterization of the selected commercial components and the evaluation of results in the mixed-field provided by CHARM. The components qualification over radiation is focused only on the payload design, assuming mission requirements hold valid for the full platform layout.

4.3 The CELESTA Test Board

Following results obtained through simulations during the initial phase of mission analysis and constraints evaluation, an experimental verification of the RadMon V6 adaptation to a 1U CubeSat payload was required. In this context, the author of this work took on the process of defining the strategy for the electronics test setup, the design of the electrical circuits, their layout on dedicated Printed Circuit Boards and finally the development of the FPGA digital firmware (similarly to the process of burst analysis, test strategy and hardware development already described in Chapter 3). As a result, a preliminary test board for the analysis of the payload requirements and constraints was developed. The board size did not follow the standard 1U CubeSat dimensions, as the qualification and testing of the chosen hardware had higher priority over the board size definitions. One Cypress memory was chosen as candidate for the HEH fluence measurement, given its low neutron cross-section and high proton cross-section over a broad range of energies. If required, the SRAM can be optionally conditioned using the burst detection with alternate addressing accessing. One RadFET was included in the test board, the unit with 100 nm thickness was preferred over the 400 nm due to its higher linear response to radiation [75]. For the latchup experiment the Brilliance BS62LV1600 SRAM was chosen as a first candidate for the latchup experiment due to its high SEL cross-section and low nominal power consumption [90]. Further details on the characterization of the latchup detection approach and characterization of this component are given in Chapter 5. The final layout of the payload test board is shown in Figure 4.8.

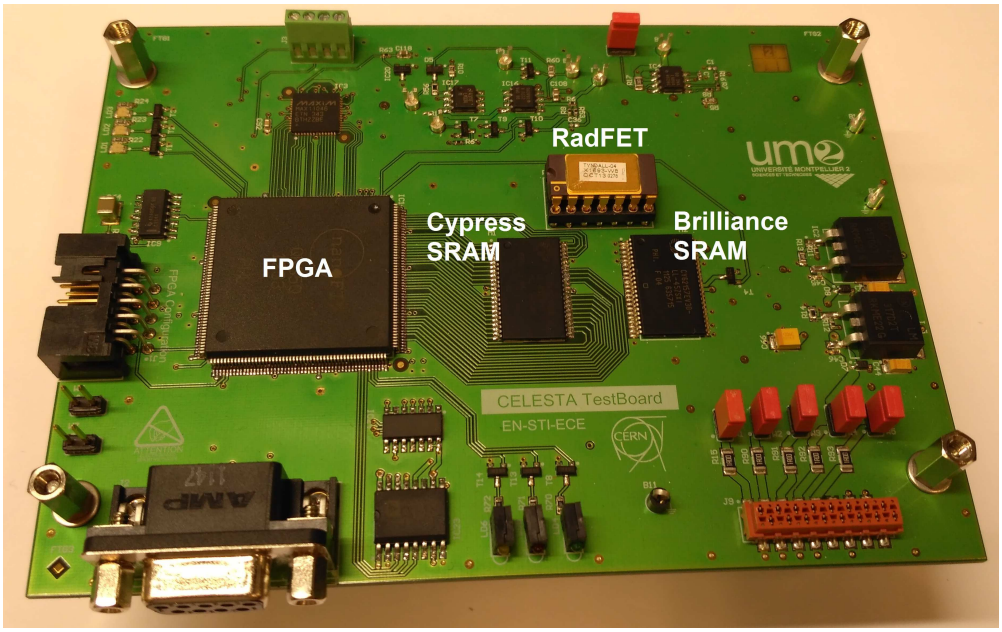

Fig. 4.8: Layout of the first payload test board, with sensors of TID, HEH flux and a latchup experiment.

Table 4.4: TID, power and temperature characteristics of the payload test board components

Reference	Function	Supply Voltage [V]	Average Power [mW]	Quantity	TIDmax [krad (Si)]	Temperature Range
Sensors						
CY62157EV30LL	HEH flux measurement	3.3	0.0049	1	-	-
RadFET	TID measurement	$V_{th} \approx 2.2$ V	0.020	1	-	-
BS62LV1600EIP55	Latchup Experiment	3.3	0.033	1	-	-
Main IC components						
LM317D2TG	Voltage Regulator	+8	15	2	50	-65 °C to 125 °C
LM134M	Current source	+8	1	1	40	-55 °C to 125 °C
LM45CIM3	Temperature sensor	+5	50	1	68	-65 °C to 150 °C
INA146UA	Difference amplifier	+5/-5	3	1	24 (32)	-55 °C to 125 °C
OPA2227	Operational amplifier	+8/-5	90	2	40	-55 °C to 125 °C
MAX3491ESD	RS-422 Transceiver	+3.3	10	1	65	0 °C to 70 °C
MAX11046ETN	ADC	+5/+3.3	240	1	20	-40 °C to 85 °C
ProASIC3 A3P400	FPGA	+1.5/+3.3	168	1	39	-40 °C to 85 °C

The COTS components integrated on the board were chosen with respect to constraints of temperature range of operation, maximum TID tolerance and average power consumption [91]. These parameters are reported in Table 4.4 for each integrated circuit included in the final design of the board. The sensors' temperature of operation is within the target range and TID effects are assumed having no impact on the SEL and SEU cross-sections up to TID_{max}. The contribution of the sensors to the overall power consumption of the module is very low: both the Cypress and the Brilliance memories have ultra-low power nominal currents, the RadFET V_{th} is read for a sweep time of 100 ms, after which the gate terminal is tied to ground. Given the dose rate previewed for the mission, the period between two RadFET readings is in the order of hours, thus the sensor consumption is negligible. The FPGA candidate is an Actel ProASIC3 A3P400. This component was tested with a proton beam and results are reported in [92]: no latchup events were observed with no degradation up to ≈ 39 krad(Si). The industrial version of the FPGA is used in order to satisfy the target temperature requirements and all the registers are triplicated to enhance reliability under radiation. Results of the device's degradation over TID and SEE characterization are found in [93] and [49]. The INA146 difference amplifier passed all tests up to a TID of 24 krad(Si) but with a lower gain configuration it reached up to 32 krad(Si). This result was taken into consideration in the circuit design. The 16-bit ADC passed all tests up to 20 krad(Si) [43]. This component is the most critical in the design in terms of power consumption and TID_{MAX}, nevertheless it was integrated in the design to evaluate its performance in a mixed field before possibly choosing a different candidate. The aim of the first tests was to evaluate the overall performance of the payload test board and qualify the sensors and the chosen components. For this reason a robust communication protocol and physical layer were necessary. The final CELESTA payload board will use a CAN bus protocol for the communication between the payload board and the On-Board-Data-Handling (OBDH) module. For the purpose of a preliminary test a Modbus protocol with serial RS-422 UART com-

munication was adopted since it proved to be reliable and radiation tolerant up to 45 krad(Si) [92]. The total power consumed by the payload test board was ≈ 800 mW. This result is calculated with an average estimation of the power consumed by each device on the board, without considering the duty cycle of operation of each component. For instance, the ADC device is run with a fast sampling rate due to the latchup detection functionality, but the TID measurement can be performed with a much slower reading period, in the order of hours, given the mission requirements. Therefore, the ADC can be held in stand-by and operated with a much shorter duty cycle, leading to a high reduction of the total average power consumption. The payload module is powered by 4 voltage supply lines: +5V dedicated to the ADC, -5V and +8V for the negative and positive rails of the operational amplifiers, and +8V for the voltage regulators required to produce other lower voltage values. The current consumed on each power line is monitored during the test to verify the functionality of the components. The ADC monitors its internal voltage reference, the RadFET threshold voltage V_{th} and the output of the temperature sensor integrated on the board. In addition, the ADC acquires a voltage signal proportional to the I_{cc} current consumed by the Brilliance SRAM, for the detection and counting of latchups. This represents a common technique for latchup detection. The parasitic thyristor structure induced by charge collection due to a particle hit, typical of latchups in CMOS devices, generates high current levels of the DUT consumed current which are strongly dependent on parameters such as the operative voltage value of the DUT and its underlying layout structure. In some cases short current transients are detected, where a temporary increase of the supplied current and rapid restoration to its nominal value is observed.

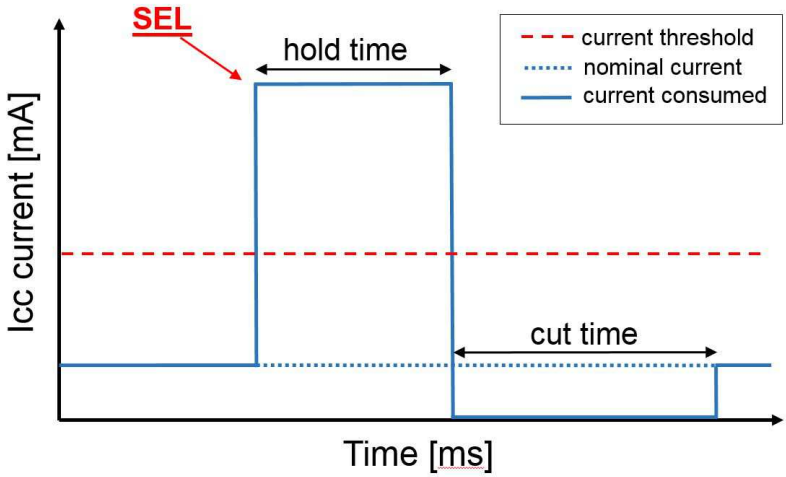

Fig. 4.9: The hold time, cut time and current threshold quantities involved in the recognition of an SEL event.

A common technique for SEL detection is shown in Figure 4.9. The DUT I_{cc} supply current is monitored: once the I_{cc} arises and sets to a level higher than a predefined

threshold value for an amount of time t_{hold} an SEL is counted. The power of the device is then cycled for a period t_{cut} to prevent damages to the tested equipment, and then restored to the nominal value. The ADC sampling frequency is set to $f_{sample} = 1$ kHz. When I_{cc} is found over a pre-set threshold value for a period t_{hold} the V_{cc} memory power is disconnected for a cut-time t_{cut}= 2 ms, and then restored. The hold-time t_{hold} was set to the order of μs. The voltages applied to the power rails of the operational amplifiers take into account the expected maximum latchup current levels for the chosen SRAM [94], as well as the maximum TID levels measurable by the RadFET sensor.

The HEH flux measurement is performed through the reading of the bit flips occurring on the 8 Mbit Cypress CY62157EV30 SRAM. The memory is initialized with a pattern "all zeros" and afterwards each address is read and the total SEUs are counted. The time for a full read operation is about 1.2 seconds. According to mission constraints a reading period T_{read}= 2 minutes is sufficient to retrieve significant data of the HEH fluxes, [95]. Each measured quantity is stored on registers implemented with Triple Modular Redundancy within the FPGA. The maximum data transfer rate is f_{data}= 50 Hz, thus the period of the data acquired is T_{data}= 20 ms. A summary of the timing signals is given in table 4.5. These settings are required for the test in order to store enough samples for the analysis, in the final application the reading time of the RadFET V_{th} and the Cypress SRAM will be in the order of hours, considering the dose rate and HEH flux levels expected during the mission, (for instance in the case of TID the measurement can be performed even every 10 hours).

Table 4.5: Summary of the timing signals on the Payload Test Board.

Device	Action	Timing
Cypress	pattern filling	≈131 ms
	reading period	2 min
	memory full scan	≈1 s
RadFET	reading period	2 min
Brilliance	ADC period	1 ms
	t_{cut}	2 ms
	t_{hold}	≈ 1μ s

4.4 Experimental Setup and CHARM Configuration

The CHARM facility and its environment were described in detail in section 2.4 of Chapter 2. The first step in the qualification of the test board is the definition of the test location and the facility configuration desired to achieve the particle spectra of the Low Earth Orbit. The proton spectrum for the proposed orbits has been extracted using the CREME on-line tool [96]. CHARM provides a mixed-field which includes electrons, photons and HEH, with a broad energy range. Figure 4.10 shows the normalized Re-

versed HEH integral flux for both circular and elliptical orbit at test locations "R2", "R3" and "R4". The contribution from the galactic cosmic-rays causes the deviation at high energy which moves away from the spectra seen at the CHARM test positions, however, as already mentioned, this only represents less then 1% of the total spectrum and can therefore be neglected. The annual space fluxes can be obtained at CHARM in few hours, since the facility provides a mean of accelerated ground testing. The HEH flux and the ground test accelerator factor are reported in table 4.6.

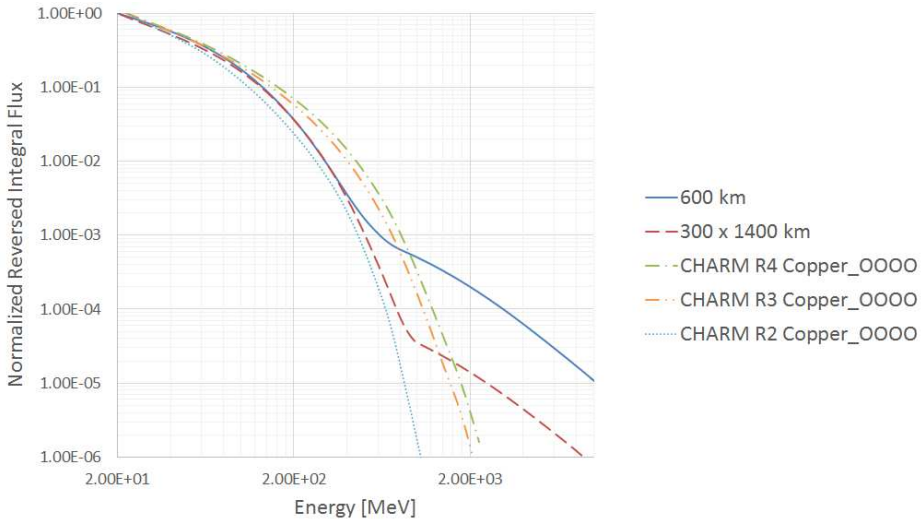

Fig. 4.10: Normalized Reversed HEH integral flux for both circular and elliptical orbits, and for test locations 2, 3 and 4 at CHARM. A copper target with "OOOO" shielding were set.

Table 4.6: HEH flux and CHARM test accelerator factor for positions 2, 3 and 4.

position	**HEH flux**	**Test Accelerator Factor**	
	[HEH·cm^{-2}·day^{-1}]	**circular orbit**	**elliptical orbit**
R2	$3.14 \cdot 10^{10}$	$1.52 \cdot 10^{4}$	$1.06 \cdot 10^{3}$
R3	$5.36 \cdot 10^{10}$	$1.25 \cdot 10^{4}$	$8.81 \cdot 10^{2}$
R4	$5.49 \cdot 10^{10}$	$1.37 \cdot 10^{5}$	$7.49 \cdot 10^{3}$

Similar results are yielded when comparing CHARM spectra with the PROBA-II mission orbit [97]. Figure 4.11 shows the reverse integral of the HEH spectrum of the proton belts along PROBA-II orbit, together with three CHARM test configurations with close matches calculated with FLUKA. The radiation fields of PROBA-II are very similar to the ones resulting from simulations performed for CELESTA. Simulation results using CREME and FLUKA frameworks led to the choice of test location 3 with no shieldings and a copper target as the closest match between the mission and the test location HEH spectra. Figure 4.12 shows FLUKA results of HEH flux levels expected for such configuration.

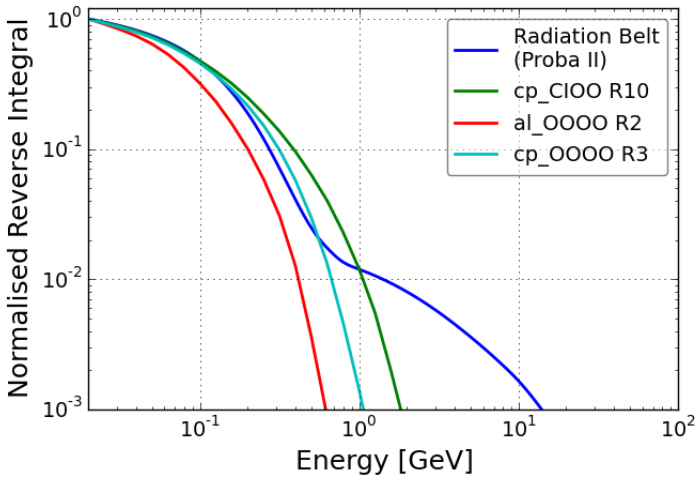

Fig. 4.11: Normalised reverse integral of the HEH spectrum calculated with FLUKA for the PROBA II orbit and three CHARM configurations: copper and aluminium target materials with "CIOO" and "OOOO" shieldings. Test positions R2, R3 and R10 are taken into account.

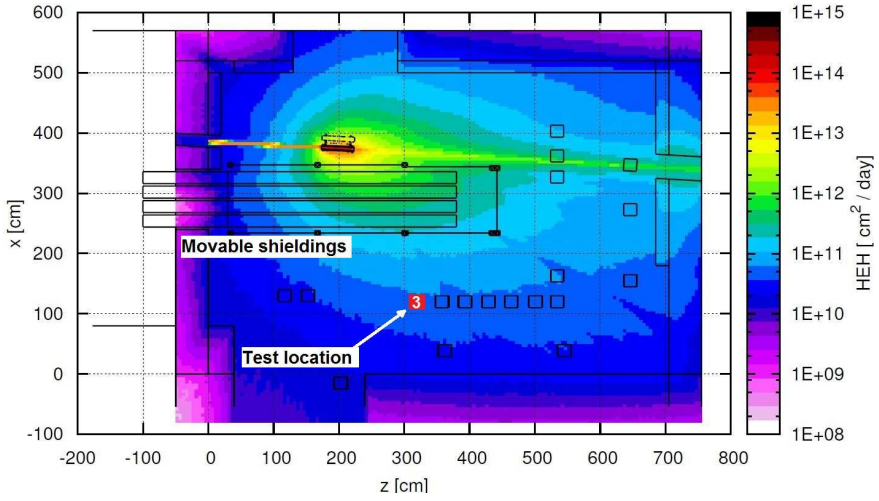

Fig. 4.12: HEH flux levels in the CHARM irradiation area using a copper target and no shieldings. Test location number 3 is evidenced with a red square.

The equipment dimensions, height from ground, beam parameters and facility geometry were taken into account in the calculation of the spectra. During the test, the board was placed in the CHARM area while power supplies and laptop were located in the control room in order to keep them safe from radiation exposure. The test approach in CHARM allows the radiation qualification of the chosen design components together with the assessment of the overall functionality of the module. Critical components can be identified and further tested, thus obtaining a first important screening of each device

and relative lots. The test setup in the CHARM irradiation area is shown in Figure 4.13, a RadMon V6 unit was installed right above the board, to compare recorded data from the sensors.

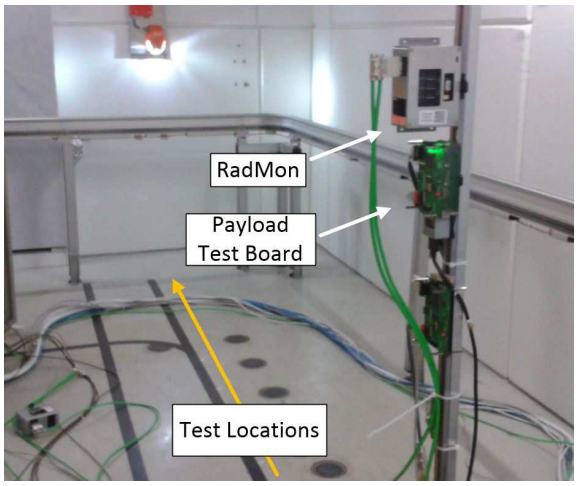

Fig. 4.13: The test setup in the CHARM irradiation area: the payload module is positioned in location 3 with a RadMon unit installed right above.

4.5 Test Board Experimental Results

Tests were carried out during the commissioning period of the facility, in November 2014. Figure 4.14 shows the measurement of the TID in Gy units provided by the board RadFET and the RadMon installed, together with the on-board temperature.

The dose rate measured was ≈ 2 Gy/h. The data acquisition was taken with T_{data} = 120 s over 8 days of irradiation, during which the beam was stopped twice and the test area was accessed by the users. The test board and the RadMon TID values are in close agreement up to ≈ 80 Gy, afterwards the two quantities diverge by ≈ 30%. The measurement was performed during the commissioning period of the facility, thus this result is compatible with the error committed in the estimation of the predicted dose rates, the beam intensity and the dose gradient due to the position of the RadMon respect to the tested module. The TID measurement was also affected by temperature: when the irradiation area was accessed, fast variations of the temperature on board corresponded with peaks in the measured TID. In this regard a temperature compensation was not included on the payload module design, whereas it was present on the RadMon. Following these considerations the dose values recorded by the board were assumed as more representative of the dose absorbed by the module respect to the RadMon ones. In addition, the board RadFET was subject to a lower annealing effect compared to the one installed on the RadMon unit, as showed by the decreasing TID values during the periods with no beam. The board RadFET reached 240 Gy of accumulated dose. At ≈ 200 Gy the board

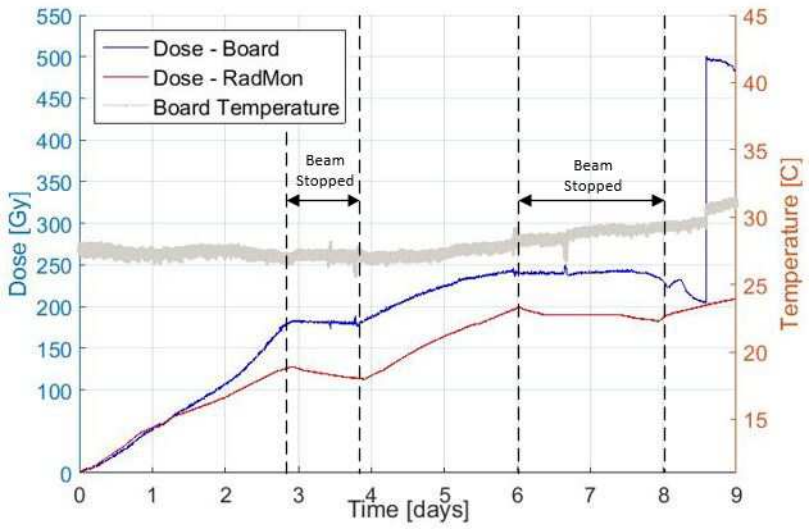

Fig. 4.14: Measurement of the TID recorded by the module and the RadMon installed right above. Temperature values are given by the on-board sensor.

temperature started rising monotonically and after the second beam stop the recorded V_{th} voltage values were subject to a large increase that was not recoverable by cycling the power of the module. This effect was found to be the result of a latchup of the operational amplifier "OPA2227" connected to the RadFET output.

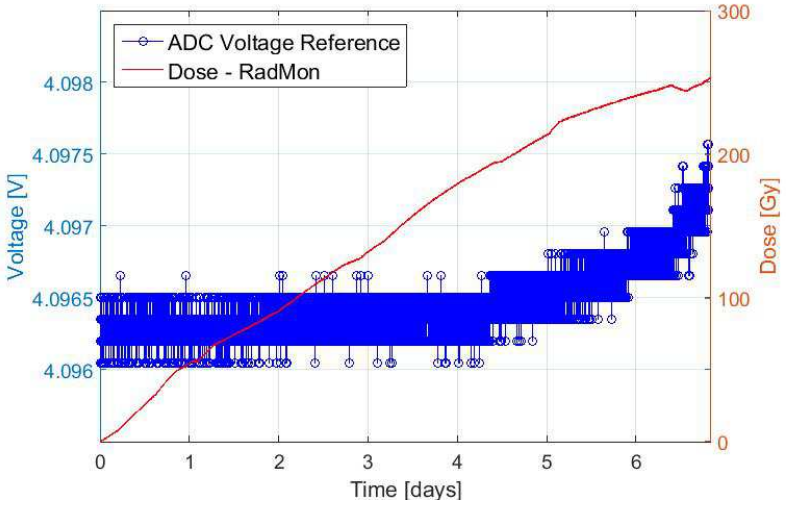

Fig. 4.15: ADC voltage reference and TID measured by the RadMon over time. The dose values take into account annealing effects. The periods with no irradiation are discarded.

The component resulted to be sensitive to Lot variations, thus the radiation test evidenced a fault in the component choice. The voltage reference of the ADC is reported

in Figure 4.15. In this case the TID measured by the RadMon is considered, to account for dose values recorded after failure of the board TID acquisition. When the ADC approached 200 Gy of accumulated dose, the voltage reference started increasing. At 250 Gy the reference was still within the component datasheet tolerance parameters, but the device current consumption had increased by a factor 2 and the functionality was compromised. Considering the 30% error between the TID measured by the RadMon and the actual dose absorbed by the payload test board, the TID value reached by the ADC before total degradation can be assumed higher. These values were larger than the ADC maximum TID of 200 Gy (20 krad(Si)), suggesting the component showed a better response to radiation due to the annealing in the periods without beam. This observation will be the object of future verifications. The HEH flux was stable during the measurement. The values of HEH fluence over TID and HEH flux over time are reported in Figure 4.16. A total fluence of $1.2{\cdot}10^{12}$ heh/cm^2 was reached during 20 days of irradiation. The SEU count was still valid at 386 Gy of TID, according to the dose provided by the RadMon. This result is compatible with the TID tolerance expected for the FPGA driving the SRAM. The final flux value was $\approx 6 \cdot 10^{10}$ heh/(cm^2·day), which is in agreement with the expected HEH flux rates, between $5{\cdot}10^{10}$ and $1{\cdot}10^{11}$ heh/(cm^2·day), reported in Figure 4.12 for test location number 3.

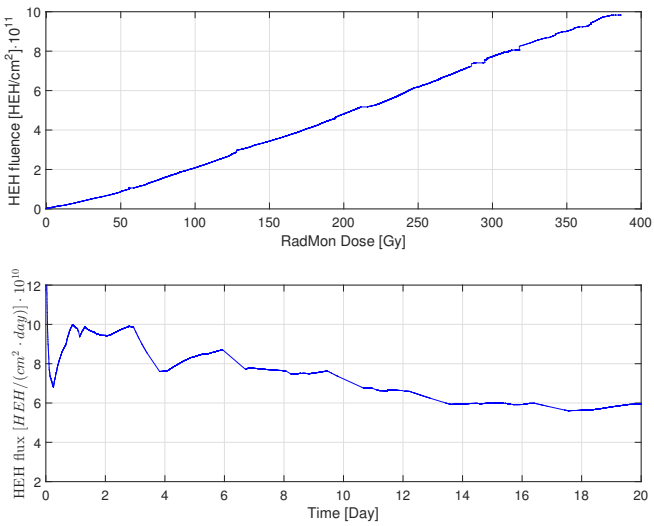

Fig. 4.16: Measurements of the HEH fluence over TID and HEH flux over time. The dose values are given by the RadMon. The periods in which the beam was stopped are discarded in the analysis.

The current threshold set for the latchup measurement was 15 mA, following data recorded during previous tests [90]. The ADC monitored the I_{cc} current of the memory with a 1 ms period, according to f_{sample}, but T_{read} was set to the maximum allowed data transfer period $T_{read} = 20$ ms. Figure 4.17 shows the measured current values over time

during a time frame of 30 hours of irradiation. Several current peaks are visible even below the set threshold, meaning they were not the result of a power cycle after cut-time t_{cut}, but were most likely the result of a current transient or a very short self recovered micro-latchup. With these observations the choice of cut-time, hold-time and threshold was crucial in order to discriminate the latchup events from the current pulses. A higher f_{read} value was required to evaluate with increased accuracy the current waveforms, thus only data recorded by the FPGA were taken into account. A total of 5500 SEL were recorded over a fluence of $8.5{\cdot}10^{10}$ heh/cm^2, yielding a final SEL cross-section of $6.47{\cdot}10^{-8}$ cm^2. Since the count of SEL recorded was affected by the high rate of events not physically recognizable as latchups, the calculated cross-section is at least a factor 3 higher compared to the one found in [56] for the same component under the same bias conditions. The test evidenced the need of a more consistent choice of t_{hold}, t_{cut} and current threshold in relation to the radiation levels of the chosen DUT location.

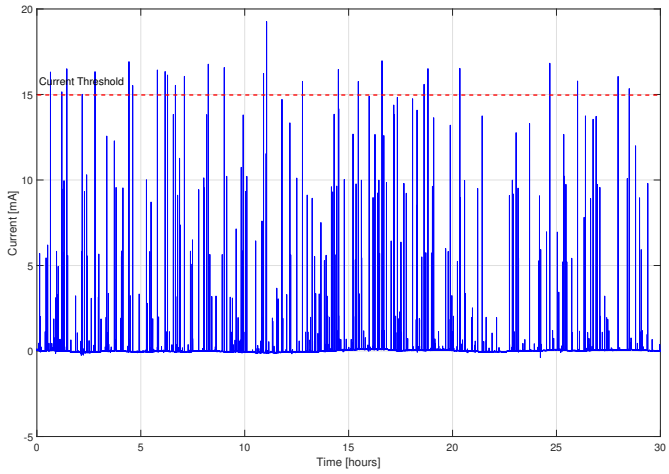

Fig. 4.17: I_{cc} current consumed by the Brilliance SRAM over time. Several current pulses, even below the set threshold, are visible.

4.6 Conclusions

In the framework of the CELESTA project, a qualification procedure for nanosatellites and systems deployed in high radiation environments was presented. The validation method was based on the CHARM mixed field facility, which provides dedicated test locations with particle spectra representative of various environments including the Low Earth Orbit (LEO). In the initial phase the research activities focused on the study of mission requirements and the radiation environment encountered along two proposed

polar orbits. Further on a test board was developed as a payload demonstrator, based on the CERN RadMon technology and coupled with an SRAM latchup experiment. The test board was designed for the verification of the overall system functionality, the evaluation of the CHARM representative environment and the qualification of the chosen commercial components. The test location within the irradiation area was chosen following FLUKA analysis of the CHARM HEH spectra, comparing results with the ones foreseen for the chosen LEO elliptical polar orbit. Experimental tests at CHARM showed a dependency between the RadFET voltage threshold values and the board temperature, in addition one of the operational amplifiers failed due to a latchup event, thus starting up the research for new candidates. The ADC showed degradation after 200 Gy, but the component was still functioning up to a TID of ≈250 Gy, an effect which required a deeper investigation. The qualification procedure allowed to assess the payload test board sensitivity to TID effects while analysing the components functionality under radiation. Results provided a valuable ground for future modifications of the board layout, identifying the weak points and steering design choices towards an optimized CubeSat-like version of the payload.

The measured HEH flux was compatible with the one predicted by FLUKA for the chosen test location, hence validating the SRAM sensor chosen for the SEU count. The current consumed by the SRAM selected for the latchup experiment revealed several short transients below the set current threshold, not directly recognizable as Single Event Latchups. Moreover, the ADC operation resulted in an overall high current consumption, thus evidencing the need of an alternative solution for SEL monitoring. These observations required further research towards a deeper understanding of the SRAM response to SEL events, and highlighted the need of latchup detection excluding the ADC functionality. Such thematics are fully described in the following Chapter, which will focus on the proposed technique for latchup detection on the final payload and the characterization of SRAM components carried out to select the best one for the CELESTA mission.

5

Fifth Chapter

Single Event Latchup Detection on Commercial SRAMs

The CELESTA test board experimental results evidenced the need of a more detailed characterization of the SRAM targets required for the CELESTA Single Event Latchup experiment. The use of the ADC for latchup detection proved to be inefficient in terms of power consumption, moreover a better characterization of the current threshold level, the values of T_{cut} and T_{hold}, and particular care with respect to the wiring of the component were required. In this chapter the electronics setups used for the detection of SELs are described. Results of radiation tests on several SRAM components are presented, together with the approach followed for the study of an effective latchup detection circuit suitable for a 1U CubeSat.

5.1 Single Event Latchup Detection Techniques

The mechanisms at the basis of Single Event Latchups (SEL), briefly described in Chapter 2, has been the object of deep study in the field of radiation effects on electronics [98]. The severe damage caused by latchup events on CMOS devices is enough to compromise the result of a space mission or the functioning of equipment placed in high radiation areas, such as in high energy accelerators [28]. It is therefore essential to qualify commercial components and evaluate their sensitivity to SEL before selecting the best candidates to be used in the application design, especially for spacecraft missions [76]. The scope of the CELESTA latchup experiment is the analysis of the in-flight SEL data recorded by a commercial SRAM at different geographical locations, and the benchmarking of the obtained results with the radiation response measured during

the characterization of the components at CHARM. A Brilliance SRAM component was used for the evaluation of the preliminary test board, but a larger set of components is required to be qualified in order to choose the best candidate. Several commercial SRAMs were tested using focused mono energetic proton beams at the PSI-PIF facility [57], to calculate the SEL cross-section of the tested devices, characterize their response to latchups, current levels and energy dependence. Once selected, the SRAM target was integrated in a dedicated PCB test board and irradiated in the CHARM mixed-field area. The SEL data of the SRAM memories irradiated with a mono energetic proton beam is reported in the following sections, discussing the techniques adopted to monitor the latchup currents and the electronics setups used. As a second step the proposed circuit for mixed-field tests is described in view of its use for detection of SEL on board of the CELESTA payload, thus considering requirements of current consumption and maximum Total Ionizing Dose (TID) of up to ≈ 32 krad(Si). The final aim of the tests corresponds to a full qualification of the proposed detection circuit, together with a more precise evaluation of the target SRAM cross-sections.

5.1.1 | Current Monitoring Setup

As aforementioned, in a typical system for latchup detection the Icc current levels of the DUT are acquired by an ADC with a fast sampling period and compared with a set current threshold level by the processing unit, as shown in Figure 5.1. A current switch is controlled to cut off the Vcc power of the target. The simplest implementation of this setup is the direct control of a power supply unit (PS): the instrument can be set configuring hold and cut times, but the sampling frequency and the recovery time of the system following an SEL event are usually very slow, in the order of seconds. For faster acquisition and recovery settings a more complex device is needed, such as the GUARD System [99] provided by TRAD.

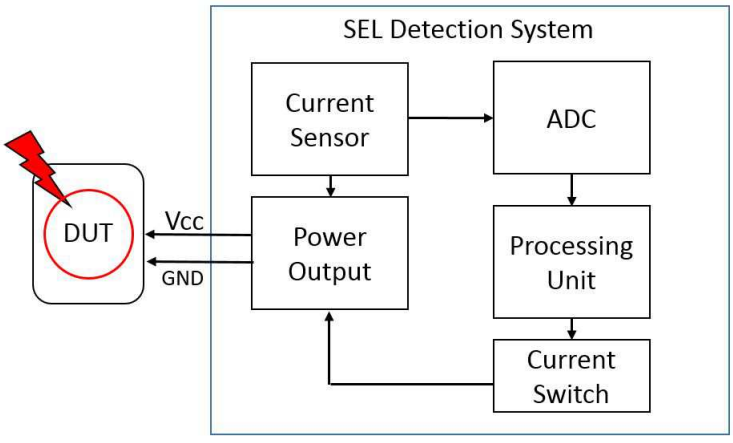

Fig. 5.1: A typical system setup for latchup events detection.

At CERN a Latchup Monitoring System (LatMon) was developed as a dedicated PCB for fast current sampling, high resolution and direct memory transfer of the SEL data, allowing real time recording of the DUT latchup current waveforms. Equipments such as the LatMon and GUARD are needed to collect enough statistic counts when the particle flux is high, and consequently when a short beam time is available to achieve the target fluence level. Both the GUARD and LatMon systems were used to characterize the target SRAM components, but a simpler circuit design, with components qualified over radiation and characteristics of low power, was required for mixed-field tests.

5.1.2 | The CERN LatMon System

The LatMon board is shown in Figure 5.2. The PCB features two separated voltage outputs, a positive one which can provide up to +15 V, and a negative for up to -15 V. The maximum sourced current is 3 A. The LatMon is designed to be compliant with the standard National Instrument PXI crate modules, it is directly powered by the PCI connector and it has also an isolated 24 V power input. The main core of the system is a Xilinx Spartan 6 FPGA.

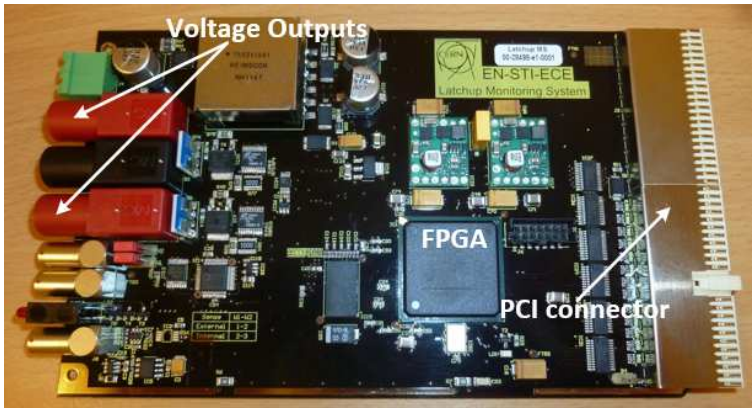

Fig. 5.2: The CERN Latchup Monitoring System (LatMon) board.

The hardware architecture of the LatMon is represented in the scheme of Figure 5.3. Two 16-bit ADCs and one 16 bit DAC are equipped, in order to select the voltage sourced and acquire the DUT current with a resolution of 100 μA. A PT100 sensor can be set to monitor the DUT temperature. The recorded latchup current shape is stored in a 128 Mb DDR3 memory with a fast interface. Data on the DDR3 is flushed to the PC using Direct Memory Access. As an additional feature the LatMon allows the setting of a current profile, this capability was introduced in order to perform latchup detection and protection of equipment with a known specific pattern of the current sunk. The LatMon was developed in order to provide a solution for latchup monitoring with characteristics of fast sampling, programmability of the latchup detection parameters, high current resolution, current profile recognition and PCI/PXI compliant. These features are not easily found

on market solutions provided by manufacturers such as National Instruments, Thermo or Geotest [100].

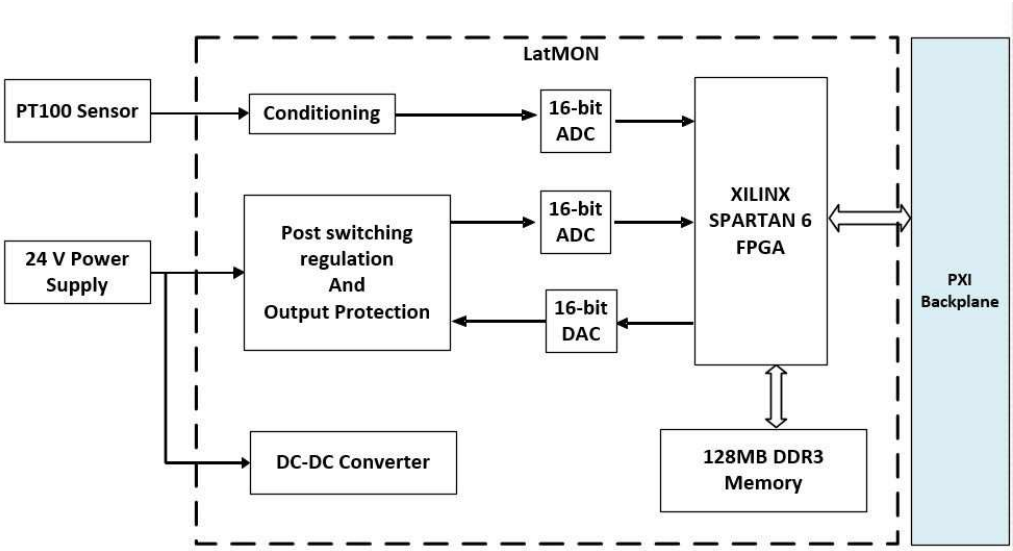

Fig. 5.3: Hardware architecture of the LatMon.

5.1.3 | The Proposed Circuit for SEL Detection

The use of an ADC component for constant monitoring of the current levels, as in the GUARD and LatMon units, results in an increased power consumption of the system, (e.g. hundreds of mW), not often affordable on small spacecrafts such as nanosatellites. Moreover, ADC devices show degradation over TID depending on technology and bit resolution, making the selection of the component quite challenging for latchup monitoring applications[101]. Devices radiation hardened against latchups are also available on the market: for instance ICs manufactured with silicon on sapphire (SOS) or silicon on insulator (SOI) technologies [102] and chips with anti-latchup circuitry integrated within the IC or package [103]. Such devices cannot be used when budget resources are limited, therefore the use of fully characterized standard commercial components is a more efficient solution. The circuit proposed for the detection of SELs in a mixed-field environment is shown in Figure 5.4. A resistor element R is placed in series with the DUT power supply V_{DUT}. The I_{cc} current is monitored using the INA146 difference amplifier. A low resistance value was chosen for R, to reduce the impact that the voltage drop over the resistor would have on the biasing of the component, and therefore on its latchup sensitivity. The output V_{LAT} is compared with a voltage reference V_{REF} using an LM124 operational amplifier in a voltage comparator configuration. The final output V_{out} is sent to the processing unit which records the latchup event and eventually cycles the DUT power, sending a switch control signal to a BST82 power MOSFET which cuts the DUT

ground connection.

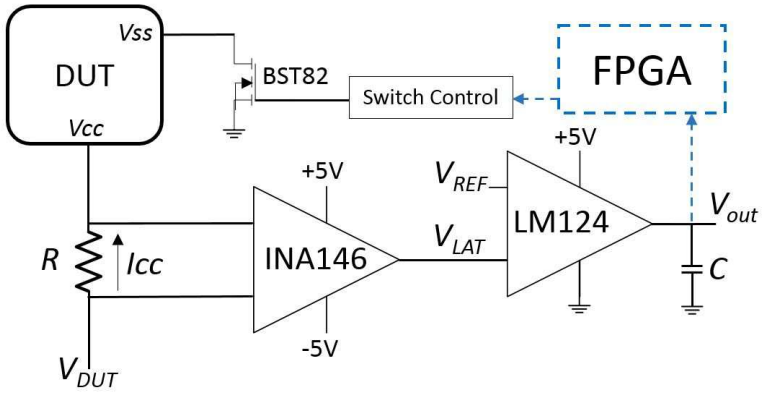

Fig. 5.4: The proposed circuit for latchup detection and protection.

The processing unit is the Microsemi ProASCIC3 FPGA already used in the RadMon and the CELESTA test board designs, which has TID degradation up to 39 krad(Si) and $3.9{\cdot}10^{11}$ p/cm^2 and it is not latchup sensitive. The INA146 was characterized and results are reported in [93]: the component passed all tests up to a TID of 24 krad(Si) and with a lower gain configuration reached up to 50 krad(Si). The BST82 showed no degradation up to 32 krad(Si) [93]. Given its bipolar technology the LM124 is not affected by latchup events, but SET events might show up on the output stage [104]. For this reason a capacitor C has been placed on the device output to filter out SET with time duration in the order of μs, as suggested in [105]. In addition the FPGA SEL count can be affected only by SET pulses with time duration in the order of ms and higher than t_{hold}, which is hardly observed. The LM124 has wide variability in terms of TID sensitivity depending on the manufacturer, therefore the LM124-B characterized in [106] was chosen in the circuit design, given its stable test results up to 50 krad(Si).

5.2 SEL Test Strategy in a Mixed-Field

Several publications focus on SEE in-flight data recorded during space missions, but a full characterization of the sensor components is required before choosing the optimal device, such as in the latchup experiment embarked on the PROBA-II mission [107]. Tests were initially performed at PSI with a focused proton beam. The SRAMs were positioned vertically in front of the beam, at room temperature and with bias V_{DUT} = 3.3 V on all devices. These parameters were kept constant since they are known to be highly affecting the final cross-section results [108]. Tests were run at the beam energies of 30, 60, 100, 150 and 200 MeV, where energies below 200 MeV were obtained through degradation of the primary beam in copper. Both the GUARD and the LatMon systems were used. Values of TID and flux were provided by the facility. Three SRAM candidates

were characterized, the DUT references are shown in Table 5.1: the SRAMs were named A, B and C. Two different Lots of SRAM B, indicated as I and II, were used during the tests.

Table 5.1: SRAM memory candidates

DUT label	Reference	Manufacturer
SRAM A	IS61LV5128AL-10TLI	Issi
SRAM B	BS62LV1600EIP55	Brilliance
SRAM C	AS7C34098A-10TNC	Alliance

Following the characterization using a mono energetic proton beam, mixed-field tests were carried out at CHARM on a dedicated PCB with the proposed circuit topology. Testing in a broad energy spectrum at a location with particle spectra representative of the final application environment is essential to correctly evaluate the effective target cross-section, [109], [110]. Test locations "R4" and "G0" were considered for the DUT placement within the facility. Figure 5.5 shows the HEH fluxes, normalized at 100 MeV, at positions "R4" and "G0", together with the flux expected in the proposed 600 km circular LEO orbit with 98° inclination. Position "R4" was selected instead of position "R3" used for the CELESTA test board experiments due to its higher accelerator test factor, position "G0" instead was chosen given its accessibility and for the purpose of recording a larger data set. The particle spectra at both test locations are well representing the Low Earth Orbit environment.

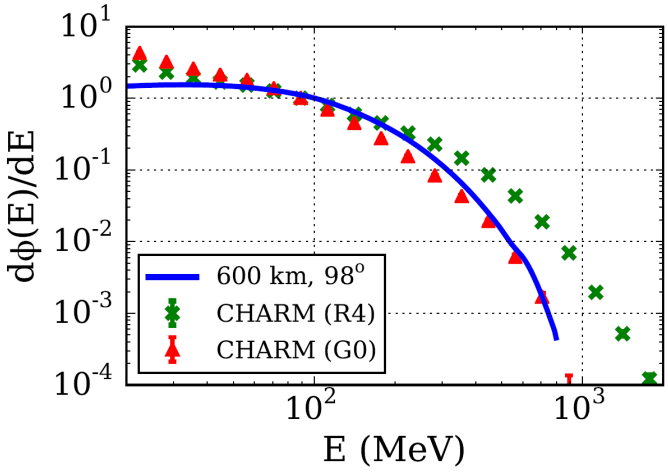

Fig. 5.5: CHARM HEH flux normalized at 100 MeV for test locations "4" (or "R4") and "G0", and the expected HEH flux for a 600 km circular LEO orbit with 98° inclination.

During the tests a configuration with a copper target and no shielding was set. Under these conditions the average HEH fluxes were $8.7{\cdot}10^5$ $cm^{-2}{\cdot}s^{-1}$ and $6.6{\cdot}10^4$ $cm^{-2}{\cdot}s^{-1}$ at location "R4" and "G0" respectively. Fluence values were returned by the analysis of FLUKA relative to the chosen test position together with the number of proton hit counts on the copper target. The parameters of bias, orientation, wiring of the components and temperature were the same set during PSI tests. The setup in the CHARM irradiation area is shown in Figure 5.6.

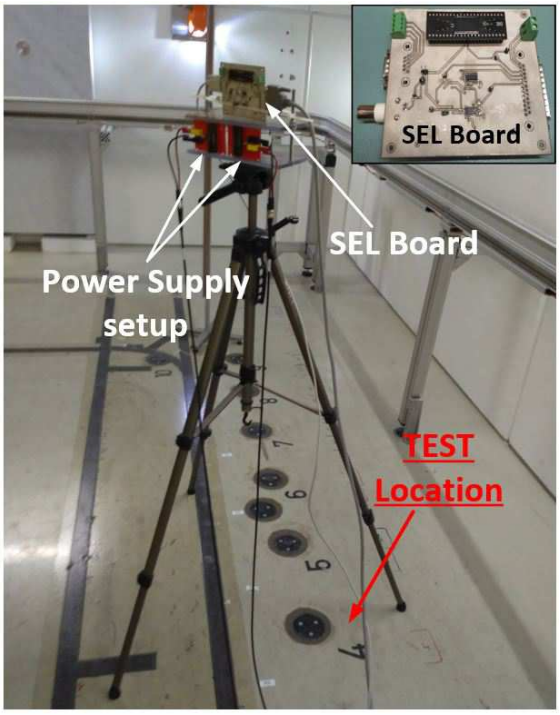

Fig. 5.6: The test setup positioned over test location "R4". The SEL detection board is set over two PCBs connected to an external Power Supply unit.

The SEL detection board was placed on a tripod above the chosen location at 1.20 m of height. To acquire a larger data record and cross-check the well functioning of the board, two simple PCBs, each carrying an SRAM adapter, were connected to an external power supply unit and placed right below the SEL board. The SRAM targets were soldered on the adapters, this way they were easily plugged and switched between the SEL board and the PCBs controlled by the power supply, in order to compare cross-section results yielded by the two setups.

5.3 Results of the SRAM Experimental Tests

5.3.1 | PSI Results with a Proton Mono-Energetic Beam

Tests were carried out with a constant flux of $6.4 \cdot 10^7$ $cm^{-2} \cdot s^{-1}$ up to a total fluence of $1 \cdot 10^{10}$ p/cm^2, with $t_{hold} = 10$ ms and $t_{cut} = 70$ ms. The current threshold was set at 50 mA for SRAM A and C and at 10 mA for SRAM B. The cross sections calculated for each candidate device are reported in Figure 5.7. SRAM A was tested with both the GUARD and the LatMon setups and the cross sections calculated were compatible. Lot I of SRAM B showed the highest cross-section results, compatible also with the SEL characterization carried out in [2] and the mixed-field tests performed in [56]. A preliminary result, obtained with a simple power supply control using quasi-monoenergectic 300 MeV neutron beam at the RCNP [111] cyclotron facility in Japan, is additionally reported for further confirmation of the SRAM B Lot I SEL cross-section result and data agreement. The maximum SEL current level of SRAM B was ≈ 20 mA, whereas both SRAM A and SRAM C showed current values in the order of hundreds of mA, meaning their use in an application with tight power constraints would require the addition of a current limiting element in the circuit.

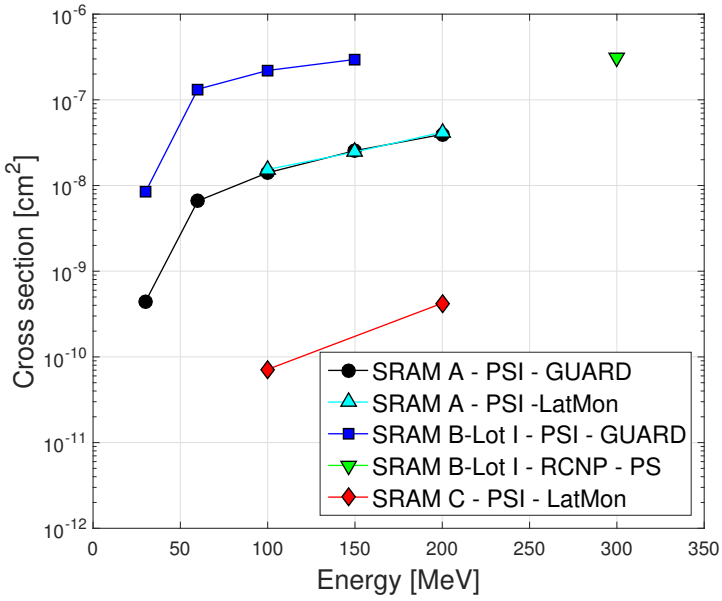

Fig. 5.7: Results of the SRAM candidates Single Event Latchup cross-section VS energy with a focused proton beam. Values have ≈10% confidence due to count statistics and facility dosimetry.

Following the JEDEC standard [112], a fit of the raw data to a four parameter Weibull function was performed and convoluted with respect to the foreseen mission environment, to obtain an estimation of the predicted SEL counts during flight. This procedure

is detailed in [56], where the analytical expression used to fit the experimental data of the mono-energetic cross sections $\sigma(E)$ is shown in Equation 5.1:

$$\sigma(E) = \sigma_{sat} \cdot (1 - \exp(-(E - E_o)/W)^s) \tag{5.1}$$

and the four fit parameters used are given in Table 5.2 for each SRAM candidate.

Table 5.2: Four-Parameter Weibull fit to the SEL cross sections for SRAM A, B and C, performed using a non-linear least squares fit.

Parameter	**SRAM A**	**SRAM B**	**SRAM C**
E_o (MeV)	17	27	25
σ_{sat} (cm^2)	$3.1{\cdot}10^{-8}$	$3.1{\cdot}10^{-7}$	$7.5{\cdot}10^{-9}$
W (MeV)	139	57	156
s	1.36	1.16	1.93

Table 5.3: Predicted in-flight SEL counts for SRAM A, B and C in a 2 year mission in LEO orbit.

Orbit	**Fluence (2 yrs.) [p(>20MeV)/cm^2]**	**SRAM A** *#SEL*	**SRAM B - Lot I** *#SEL*	**SRAM C** *#SEL*
Circular	$2.71{\cdot}10^9$	34	515	0.35
Elliptical	$3.86{\cdot}10^{10}$	496	7446	5.21

Results of the predicted in-flight SEL counts are reported in Table 5.3. Fluence values of protons with energies above 20 MeV are used in the analysis, considering a 2 years mission with the two LEO orbits investigated in Chapter 4. The LatMon data showed different shapes of the latchup currents. An example of a recorded SEL profile for each tested memory is reported in Figure 5.8: the maximum SEL current level of SRAM B was ≈ 20 mA, whereas both SRAM A and SRAM C showed current values in the order of hundreds of mA, meaning their use in an application with tight power constraints would require the addition of a current limiting element in the circuit.

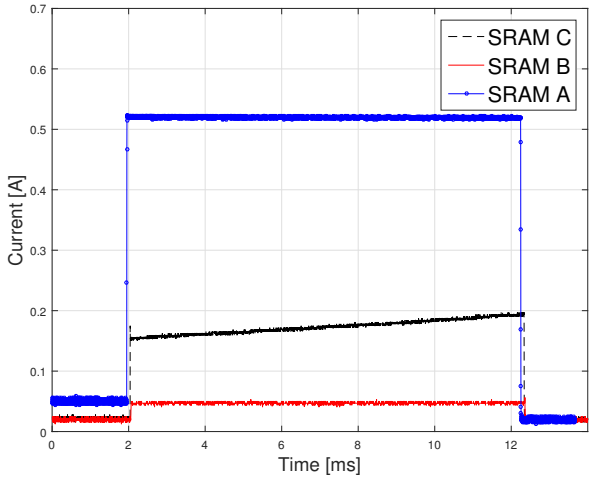

Fig. 5.8: Examples of SEL events current profiles for each memory under test.

The high proton cross-section calculated for SRAM B, and consequently the high number of SEL expected in orbit, together with its nominal current consumption, ≈ 30 μA, and relatively low SEL maximum current levels, made it a good candidate in terms of event statistics and operation on a spacecraft with limited power budget. Therefore SRAM B was selected as a potentially interesting candidate for SEL experimental tests at CHARM.

5.3.2 | SRAM Test Results at CHARM

The SEL board with the proposed circuit and the two PCBs controlled by a power supply were initially placed at location "R4". Another Lot of SRAM B, referred to as Lot II, was used during the tests, given the low availability of the component on the market. One sample of SRAM A, labelled #1, was also tested for data comparison with the results at PSI. The DUTs were irradiated up to a total high energy hadron fluence of $4.6{\cdot}10^{11}$ heh/cm^2. t_{hold} = 5 ms and t_{cut} = 50 ms were set for the SEL board, whereas t_{hold} = 2 s and t_{cut} = 2 s were set on the power supply setup, due to the slower acquisition and recovery time of the instrument. The current thresholds and all test parameters were the same used with the characterization under focused proton beams. The FPGA was located in the control room together with the power supply units and an oscilloscope connected to the DUT via long cables to capture V_{LAT} and V_{OUT} signals with 20 μs sampling resolution. Figure 5.9 shows an example of SRAM B latchup currents recorded together with the V_{out} detection signal from the LM124.

In Figure 5.10 is reported an example of the current waveforms recorded by the power supply setup for SRAM A and B. A resistor of value R was also placed in series with the Vcc of the targets controlled by the power supply setup, and no other resistor elements were added to limit the maximum SEL currents.

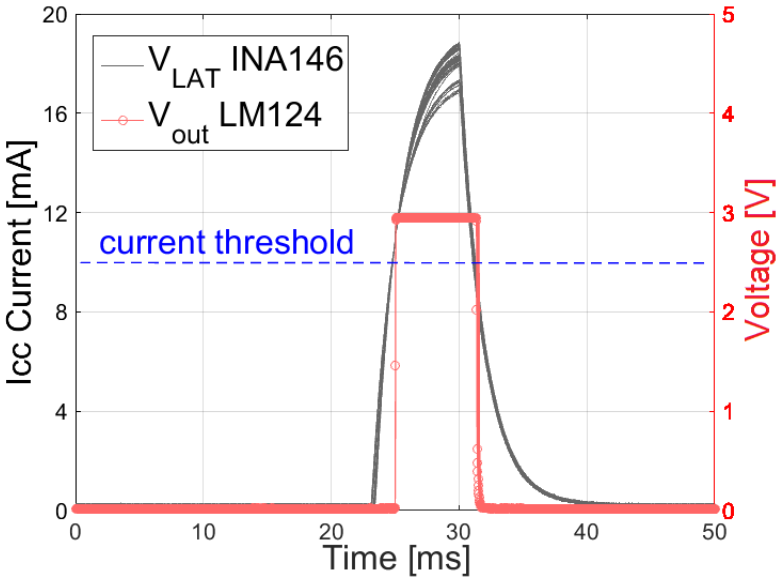

Fig. 5.9: SRAM B latchup events detected on the V_{LAT} signal (grey) and the V_{out} output signal from the LM124 (red).

Three SRAM B Lot II, labelled #1, #2 and #3 and one SRAM A, #1, were tested at location "R4". At the end of each irradiation step (i.e. when the beam provided by CHARM was interrupted), the DUT cross-sections were calculated. The targets were frequently switched between the power supply setup and the SEL board to compare results yielded by the different systems and evaluate the degradation of the SEL detection board. Figure 5.11 shows the cross-section results over HEH fluence, while table 5.4 reports the mean and the uncertainty, calculated as the standard deviation, of the cross-section σ for each one of the irradiated targets.

Results of SRAM B Lot II indicated an average cross-section value of $\approx 1.09 \cdot 10^{-8}$ cm^2, which is a factor 10 lower compared to σ calculated for Lot I tested with a focused proton beam, therefore the component SEL sensitivity resulted largely subject to Lot variations. SRAM A #1 showed a mean σ of $2.54 \cdot 10^{-8}$ cm^2, compatible with results found at PSI with both the GUARD and LatMon setups. Approximately 20% of the σ uncertainty is caused by the error in the estimation of the HEH fluence values due to the accuracy of the proton hit counts provided by the SEC1. SRAM B #1 and #2 showed values of the cross-section uncertainty above 40%, with σ results within a fluence of $1{\cdot}10^{10}$ heh/cm^2 in much better agreement compared to the ones calculated at higher fluence levels, although this result is expected due to the reduced number of events (i.e. statistic counts) at lower fluence values. SRAM B #2 and in particular #1 showed a progressive reduction of the calculated cross-section values over fluence. This effect was not due to a degradation of the SEL board circuit, since the σ of SRAM A evaluated at $4.6{\cdot}10^{11}$ heh/cm^2 was within the repeatability of the σ measurement expected for that device. SRAM B #1 and #2 were used in previous test campaigns, whereas SRAM B #3 and SRAM A #1 were irradiated for

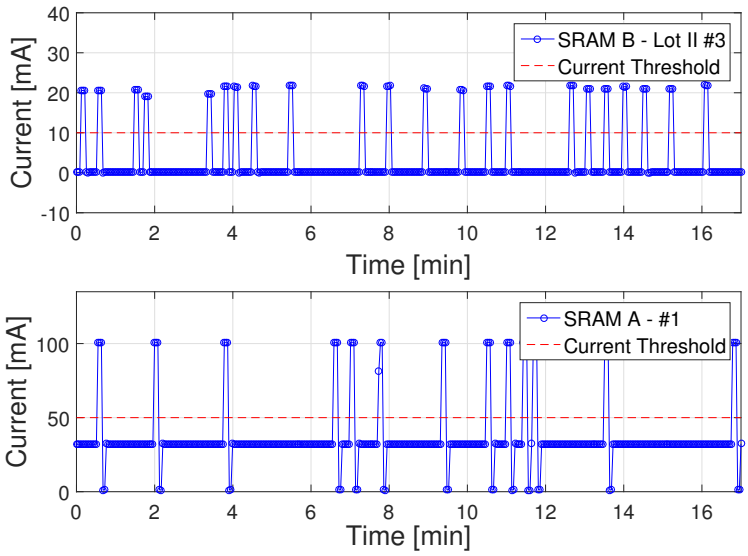

Fig. 5.10: DUT current waveforms recorded by the power supply control setup for SRAM B, Lot II, #3 (top) and SRAM A #1 (bottom). The current thresholds were set at 10 mA and 50 mA respectively.

the first time. In addition SRAM A #1 and SRAM B #3 showed cross-section uncertainties respectively of 36% and 19%, thus the decreasing effect on σ is less likely to be caused by the different t_{hold} and t_{cut} settings between the setups.

Table 5.4: Cross-section σ results of tests at location 4

DUT	σ **mean** [**cm**^{2}]	σ **uncertainty** [**cm**^{2}]	σ **uncertainty** [**%**]
SRAM A #1	$2.54{\cdot}10^{-8}$	$9.157{\cdot}10^{-9}$	36%
SRAM B #2	$4.31{\cdot}10^{-9}$	$1.80{\cdot}10^{-9}$	41%
SRAM B #1	$1.51{\cdot}10^{-8}$	$7.41{\cdot}10^{-9}$	49%
SRAM B #3	$1.33{\cdot}10^{-8}$	$4.62{\cdot}10^{-9}$	19%

Such observations suggested damage of the SRAM B #1 and #2 components due to the destructive nature of latchups [113]. An alteration of the SEL sensitivity over time was found on SRAM components of the same manufacturer in [114]. Another cause can be a synergistic effect due to the cumulated ionizing dose on the inner structure of the device. This result was not observed in previous tests and it will be the object of future research. Further data regarding SRAM B and the associated cross-section effect are described in Chapter 6. Considering the σ mean values obtained for SRAM A, $2.54 \cdot 10^{-8}$ cm^2, and for SRAM B Lot II #3, $1.33 \cdot 10^{-8}$ cm^2, values of the expected SEL counts during flight are calculated multiplying σ for the same orbit fluences given earlier in table 5.3.

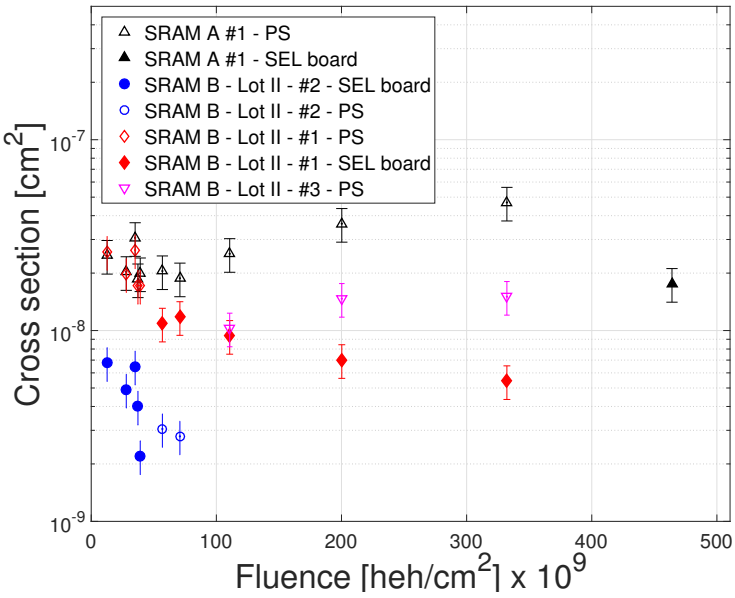

Fig. 5.11: Results of tests at CHARM in a mixed-field environment at position 4. Confidence intervals are set at 20% due to the estimation of the fluence values from the proton hit counts on the beam target.

Results are shown in table 5.5: the number of SEL in the case of SRAM A is in agreement with the values found at PSI, while for SRAM B Lot II it is more than a factor 10 lower compared to SRAM B Lot I. Both SRAM A and SRAM B Lot II showed results with similar order of magnitudes, and yielded enough statistic counts for the scientific scope of the mission. Despite the low availability of SRAM B Lots on the market, this component was still considered a better candidate choice compared to SRAM A, due to its electrical characteristics.

Table 5.5: Predicted in-flight SEL counts for SRAM A #1 and SRAM B Lot II #3 in a 2 year mission in LEO orbit.

Orbit	**Fluence (2 yrs.)** **[p(>20 MeV)/cm^2]**	**SRAM A** *#SEL*	**SRAM B - Lot II** #3 *#SEL*
Circular	$2.71 \cdot 10^9$	68	36
Elliptical	$3.86 \cdot 10^{10}$	980	513

To further qualify the latchup detection circuit, a set of experimental tests were carried out in position "G0". Given the results obtained at test location "R4", three new SRAM A devices, labelled #2, #3 and #4 were placed on the setup. Table 5.6 reports the results of SRAM A cross-section values calculated over three consecutive irradiation runs,

SRAM A #2 was positioned on the SEL board, while SRAM A #3 and #4 were controlled by the power supply setup.

Table 5.6: Cross-section results for SRAM A tested at location "G0".

Run	DUT	Test Setup	Fluence [heh/cm^2]	σ [cm^2]	# SEL
Run 1	#2	SEL board	6.38E+10	$7.46{\cdot}10^{-9}$	476
	#3	PS		$8.82{\cdot}10^{-9}$	559
Run 2	#2	SEL board	1.43E+10	$7.99{\cdot}10^{-9}$	114
	#4	PS		$6.80{\cdot}10^{-9}$	96
Run 3	#2	SEL board	3.87E+10	$7.67{\cdot}10^{-9}$	297
	#4	PS		$9.09{\cdot}10^{-9}$	350

The cross-section results between both setups were in good agreement. The mean of σ was $7.70{\cdot}10^{-9}$ cm^2 with an uncertainty of 3.4% for device #2 on the SEL board, and $8.23{\cdot}10^{-9}$ cm^2 with an uncertainty of 15% for devices #3 and #4 controlled by the power supply. The σ values calculated were $\approx 30\%$ lower compared to the ones obtained for SRAM A in position "R4". This result is explained by the higher percentage of hadrons with energies below 100 MeV at position "G0" with respect to position "R4". In total a cumulated dose of 37.8 krad(Si) and $5.76{\cdot}10^{11}$ heh/cm^2 fluence were reached on the SEL board during all irradiations in the mixed-field environment. No SET were observed on the V_{OUT} of the LM124, nor any build-up of the current consumed by the devices over TID. The overall circuit detection response to latchup was always within 50 μs, and no degradation of the LM124 slew rate was recorded up to the final fluence. These observations led to the integration of the SEL detection circuit components and design on the final CELESTA payload.

5.4 Conclusions

In the framework of the CELESTA project three commercial SRAM memories, labelled "SRAM A", "SRAM B" and "SRAM C", were characterized as possible candidates for a latchup experiment on board of a 1U CubeSat mission in Low Earth Orbit. The SEL cross-sections of the targets were initially evaluated using a mono energetic proton beam at the PSI-PIF facility. A simple power supply control setup, as well as the GUARD and CERN LatMon systems, were used to detect and record SEL events. The SRAM B was selected for the CELESTA mission, due to its low current consumption and high latchup cross-section results. As a second step, a dedicated PCB (referred to as "SEL board") was designed with a circuit developed using only COTS components previously characterized over radiation, choosing a circuit topology that minimized power consumption with no

SET occurrence nor degradation of the components up to a minimum of 32 krad(Si).

The SEL board with the selected device was irradiated at CHARM in a location with particle spectra representative of the LEO environment. Results showed a large Lot to Lot HEH cross-section variation for SRAM B. In addition, a progressive decrease of SRAM B #1 and #2 cross-sections over fluence was monitored, suggesting damage to the component structure. This effect required further investigation and it will be object of future study. A mean SEL cross-section of $1.33 \cdot 10^{-8}$ cm^2 was calculated on SRAM B Lot II #3, while SEL cross-section values obtained for SRAM A at position "G0" further confirmed the well functioning of the SEL detection circuit under radiation. The SEL cross-section results of SRAM B, for both Lots I and II, and its electrical properties in terms of current consumption and SEL maximum current levels, confirmed it as the best candidate, at the present, for CELESTA. Nevertheless other SRAM candidates with similar electrical characteristics will be researched and tested at CHARM.

The SEL board was irradiated up to a total fluence of $5.76 \cdot 10^{11}$ heh/cm^2 and a cumulated dose of 37.8 krad(Si). No SETs with period larger than 20 μs were observed on the V_{OUT} of the LM124. The slew rate of the LM124 and the current consumption of the circuit did not show any degradation over TID. Additionally the use of the proposed circuit can be extended for anti-latchup protection of devices in LEO space missions and in applications with similar TID and fluence levels.

Experimental results in a mixed-field provided a deeper insight in the characterization of the SRAM components, in particular for SRAM B, and were essential for the full radiation qualification of the SRAM target and the SEL board circuit. Results achieved in this Chapter, together with the ones obtained in the previous one, were combined to finally design a complete version of the CELESTA payload board, which is the subject of the next Chapter.

6

SIXTH CHAPTER

THE CELESTA 1U CUBESAT RADIATION QUALIFICATION

The test board qualification discussed in Chapter 4 provided the basic ground for the development of the final payload module. The analysis of mission constraints, the orbit evaluation and results returned by simulations of the radiation fields, provided a preliminary estimation of the expected TID and particle fluence values during the mission lifetime. The commercial components to be included in the payload design were selected according to characteristics of operational temperature range, power consumption, TID and fluence. Experimental results carried out at CHARM, and presented in Chapter 5, provided further insight on the characterization of the SRAM for the latchup experiment and the choice of SEL detection network. All of these results ultimately led to the design of the final payload board and its radiation qualification inside the CHARM mixed-field, which is the subject of this last Chapter.

6.1 The CELESTA CubeSat Structure

The ROBUSTA platform, the core design of CELESTA, is described in detail in [115]. ROBUSTA is compliant with the standard provided by the CubeSat Design Specification (CDS) [116], a document listing all mechanical and operational requirements to be met, the materials to be used, and the specific parts which need to be compatible with the orbital deployer. The ROBUSTA platform follows the specifications given below:

1. **Geometry:** the CubeSat platform has dimensions 100 x 100 x 113.5 mm^3, the gravity center is located within 2 cm from the geometric center. Maximum PCB size should not exceed **76 mm x 78 mm x 17.6 mm**.

2. **Mass:** the entire CubeSat (structure and electronics) does not weight more than 1.33 kg. No more than **200 g** are allowed for the payload module.

3. **Power:** the overall maximum power consumption can not exceed 1 W. A total **600 mW** average power consumption is allowed to the payload for one orbit, with a peak power of **610 mW**.

The mechanical structure is made of a mono-bloc support manufactured with aluminium alloy in the shape of a metallic cube, as reported in Figure 6.1. The rails of the structure host two deployment switches and two separation springs, this latter ones are used to provide adequate spacing between the different cubesats within the Poly Picosatellite Orbital Deployer (P-POD). A backplane mother board is attached with screws to the support. This latter one is equipped with vertical connectors of HARWIN type, one for each sub system board of the spacecraft, ultimately forming a comb shaped scheme where all PCBs are connected vertically to the backplane. The motherboard carries the communication and electrical interconnection signals between all the modules, thus minimizing the need of floating wires within the spacecraft.

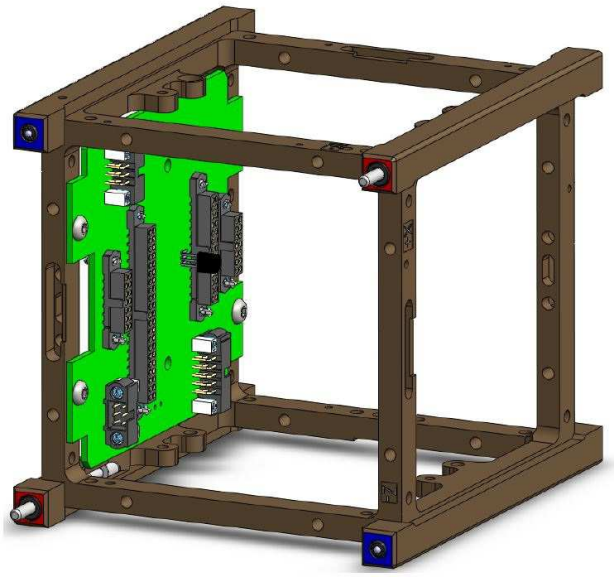

Fig. 6.1: Mechanical structure of the satellite.

The CELESTA CubeSat is composed of four sub-systems, described as follows:

Electrical Power Subsystem (EPS): devoted to the generation, storage, regulation and distribution of the electric power.

Tracking, Telemetry & Command (TT&C): the communication module, for data broadcasting with the ground station.

On Board Data Handling (OBDH): this unit processes and distributes commands, it holds the role of managing and processing the bus signals and optimize the spacecraft power consumption.

The Payload (PL): the board carrying the sensors and experiments to achieve the scientific goals of the mission.

CubeSats often carry an additional sub-system for the attitude control and orbit determination [117]. This latter module is necessary when a specific orientation of the CubeSat is required, for instance for Earth and space observation [118] or to maintain a precise orbit. In this case magnetic devices or thrusters are used as actuators to correct the satellite inclination and orbit. In the case of CELESTA the CubeSat will receive an initial rotation and momentum when deployed from the main rocket. Since measurements of the radiation fields do not require any specific satellite inclination, no attitude control sub-system is included in the spacecraft.

The Electrical Power Subsystem is directly linked to the solar panels of the satellite. The system converts the solar energy issued by six solar cells located each on one face of the cube, for the charging of the main battery. The battery is a Lithium-ion from Saft and the Solar cells are triple junction GaInP/GaAs/Ge on Ge substrate manufactured by Azurspace. The EPS hosts two DC/DC converters, four independent +6V power rails and one +5V power rail for the TTC. The EPS monitors and provides the power to all the other sub-systems. The management of power is essential since the total energy available, 1 W, does not allow a simultaneous supply to all the four integrated subsystems at the same time. For this reason a micro-controller unit is integrated on the EPS as the main core, whose functionalities include power diagnostics and communication with the OBDH for the transmission of the satellite health data. In addition, the EPS is in charge of the antenna deployment via Nichrome burn wire release [119].

The TTC module takes on the task of transmitting the telemetry (TM) data and receiving telecommands (TC) to and from the ground station, which will be located in Montpellier within the CSU infrastructure. The AX25 protocol was chosen for data encoding/decoding using AFSK modulation. The antennas are dipole-type, conceived with appropriate optimized lengths according to emission and reception frequencies [120]: the uplink reception frequency is 145.95 MHz, whereas 435.325 MHz is used for downlink communication (from satellite to ground station). In normal operation the TM are broadcast every three minutes, in particular the TTC is set to automatically broadcast a beacon frame of data (256 bytes), containing the sub-system statuses. The beacon frame is periodically refreshed by the OBDH. As a safety measure, a general reset signal connecting all boards is set: the TTC sends a hard satellite reset upon receiving a "Reset TC" command from the ground. This extra precaution allows the reset of the satellite bypassing the OBDH module, and it is implemented using a dual-tone system linked to a MOS-based switch.

The OBDH acts as the main processing unit which controls the data flow between each module. It has the role of managing the tasks performed by all the other sub-systems and optimize the power consumption. Each sub-system can be set by the OBDH in one of the following states:

1. **Off**: all the sub-system functionalities are shut down.
2. **Low-Power**: the sub-system carries only basic functionalities and it is kept to a minimal low power state.
3. **Commissioning**: the sub-system communication and main functionalities are active, in this state the module waits to be set in "Mission" mode.
4. **Mission**: the nominal operational state of the sub-system.

The main firmware of the CELESTA payload was developed taking into account the above configurations, in order to respond to the OBDH commands, set the power state according to needs and comply with the ROBUSTA specifications. The OBDH is equipped with a 18F46K80 PIC micro-controller, a real-time clock, a set of 8 Mbit FRAM memory units and an anti-latchup circuit. The on-board communications are performed using the Controller Area Network (CAN) bus protocol developed by BOSCH [121]. An extra dosimetry module named "DOSI" can be installed as a secondary payload on the OBDH PCB, it consists of an Optically Stimulated Luminescence sensor (OSL) [122] and a TRAD Space Dosimeter (TSD, manufactured by TRAD) for extra ionizing dose measurements. The DOSI can be installed for further benchmarking of the measured TID data. The interconnections between each sub-system are displayed in Figure 6.2.

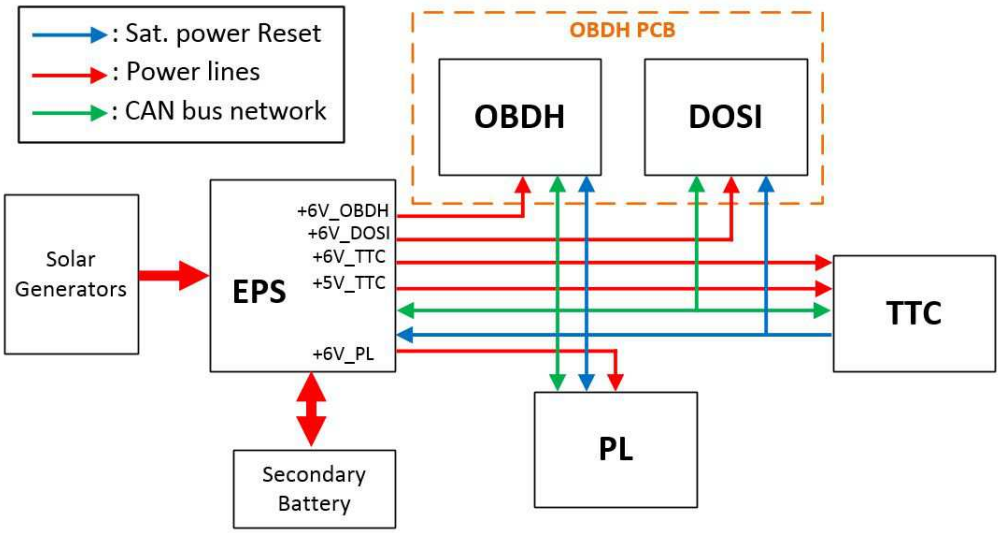

Fig. 6.2: Signal connections between each sub-system on the CELESTA CubeSat.

The OBDH is capable of reconfiguring each sub-system through the CAN network. The CAN bus is set with a bitrate of 125 kbit/s, and it follows the 29 bits extended ID protocol. The OBDH sends a periodical clock frame every 200 ms, in order to give the clock reference to the sub-systems. The real time clock is refreshed by a TC each time the satellite flies over the ground station. The telemetry raw data is stored on the OBDH FRAMs: these memory devices were chosen for their ease of use and relatively high tolerance to radiations. Finally the OBDH is responsible for the decodification and logging of the TC and the forwarding of the required actions to each TC recipient. The telemetry data cannot exceed 4 Mbits/day for one single ground station, the data is stored "as is" without any further processing, for instance the depth of charge of the EPS battery is included in each stored telemetry. The CubeSat is scheduled to remain "silent" in the period of approximately 1 hour after being deployed into orbit. Afterwards, the antennas are deployed and the beacon signal is broadcast to the ground station. Then the EPS, TTC and finally the PL are set in Mission mode and the CubeSat can start the measurements. The final payload design is discussed in the following section.

6.1.1 | The Final CELESTA Payload

The payload design derives from results obtained after the first feasibility tests and mission analysis, carried out in Chapter 4, together with the latch-up circuit discussed and characterized in Chapter 5 and the requirements imposed by the ROBUSTA platform. As already mentioned in the previous section, the payload requirements in terms of consumption, mass and geometry are: 600 mW average power, 610 mW peak power, 200 g maximum mass, 76 mm x 78 mm x 17.6 mm maximum PCB size. In addition, the 29 krad(Si) maximum TID value from preliminary simulations, and a temperature range of -20 °C to 80 °C are taken into account in the selection of commercial components, (as described in Chapter 4). Most of the COTS selected for the CELESTA test board were included also in the final payload design, although several tests at PSI were carried out in order to qualify new candidate components and assess their tolerance to radiations. A brief compendium of results obtained at PSI during test campaigns on different commercial components is reported in appendix B. The qualification of commercial components, the research of new candidates, the irradiation tests performed and the development of the required digital firmware for the conditioning of the electronics elements were all developed and carried out by the author of this work. Particular care was given to the choice of components in terms of power consumption. Devices such as the voltage regulators may consume large current amounts, dissipate energy through quick heating or be subject to large output variations over accumulated dose. Moreover a unique +6V power supply led to a challenging choice of the required components to achieve an efficient power management while minimizing the current consumed. Results of Chapter 4 evidenced the SEL sensitivity of OPA2227 depending on Lot and component type, this result was further confirmed by tests carried out at PSI and reported in appendix B. The

component was present in the RadFET acquisition chain already shown in Figure 2.11, and it was replaced by an AD8029 single rail-to-rail amplifier. This latter choice was driven by the need of a rail-to-rail amplifier to take advantage of a wider output range, while minimizing the need of providing larger voltage levels on the supply rails. The component allows to be operated with a single 10 V positive supply in a feedback configuration, for a total nominal current consumption of ≈ 3 mA. In addition an LP3990 linear voltage regulator was chosen as the main power switch of the latchup detection circuit. This choice was made to have further control on the power provided to the device under test, given the device has an "enable" signal for fast shut down of the supplied output. The CAN communication required a transceiver to convert the FPGA output into the CAN high and low signals travelling on the bus. The SN65HVD233DG4 transceiver manufactured by TI was used also in all the other CELESTA sub-systems, thus it was selected as the main CAN transceiver. The ADC MAX11046 showed good results in terms of performance, despite the component lower TID tolerance (with respect to the other chosen components) and high current consumed. The component was known to be subject to an increase of power over TID, possibly due to charge trapping in its BiCMOS structure [93]. This effect was further tested at PSI, in particular together with the shut down pin of the component, used to alternatively turn on and off the device. This latter characteristic is essential for the power efficiency of the satellite during the mission, since the ADC is one of the main and highest power consuming components of the payload. The device was kept in the payload design, but the 4-channel version was chosen, the MAX11044, due to its lower power consumption. Results of the characterization of the OPA2227, AD8029, LP3390, SN65HVD233DG4 and ADC MAX11046 are summarized in appendix B.

Not all components included in the design were subject to an earlier selection process through tests using focused protons. One of the main goals of the procedure for radiation qualification using mixed-fields at CHARM is the optimization of time and resources, ultimately converging on a radiation hardness assurance and functional characterization at system as well as component level of the tested equipment. As a result some commercial components, which were included in the other CELESTA sub-systems and which were never or partially tested before, were added to the payload design to be evaluated. An LM2681 voltage doubler manufactured by Texas Instruments was chosen to provide 10 V to the AD8029 positive rail on the payload RadFET acquisition chain, such component was found also in the EPS module and the same schematic network was adopted. The Texas Instrument TPS62125 buck converter was also included in the power managing part of the payload schematic. The TPS62125 was present on the OBDH module as well, and it was used to provide the 3.3 V and 1.2 V voltage supplies required by the CAN transceiver, oscillator, ADC and FPGA. All components were chosen using surface mounting packages, in some cases an extra glueing would be needed to comply with vibration test regulations for satellites depending on the package type [123], [124].

The PCB geometry for each sub-system must comply with the geometry requirement of 76 mm x 78 mm x 17.6 mm maximum PCB size. The CELESTA payload mechanical constraints in terms of geometry are summarized in the scheme of Figure 6.3: a maximum gap of 2 mm is allowed for components on the bottom side of the PCB, whereas 16 mm are allowed on the top side, the PCB thickness must not exceed 1.6 mm. COTS were chosen taking into account the size of the packages in order to fall within the mechanical specifications imposed by the platform. The final payload was designed following the modular principle at the basis of the RadMon V6. The payload was divided into two separate PCBs, a main or "mother" board and a mezzanine or "sensor" board, this decision was driven by the following advantages:

1. Further improvements of the sensors will require modifications of the sensor board only, thus reducing the time to design newer payload versions.

2. The sensor components, for instance the SRAMs used for fluence monitoring and more specifically for the SEL experiment, are subject to fast obsolescence. A modular design results in re-usability of the components, which is extremely helpful for radiation testing. As an example a failure occurring on the mother board might be resolved replacing the motherboard only, leaving the sensor part untouched.

3. Faster and easier identification of electrical failures, due to sensitive components being located on separate boards.

The CELESTA payload was ultimately designed respecting specifications of geometry and mass, following a careful selection process of several commercial components with respect to constraints of power consumption, size, maximum TID levels, latchup sensitivity, operational temperature range and electrical performance. The CELESTA payload mother board is shown in Figure 6.4. The ProASIC3-A3P1000 FPGA by Microsemi was chosen as the main core. The A3P1000 has the same electrical characteristics of the A3P400 used for the test board, but it is about a factor 3 larger in terms of FPGA gates area, therefore the A3P1000 was chosen in order to accommodate a larger design, possibly for future versions of the payload hosting more radiation sensors (i.e. a second RadFET and floating gate sensors [125]). In addition the voltage levels of the board were programmed to add the possibility of including the low power version of the FPGA, the Microsemi ProASIC3L-A3P1000, to further reduce dynamic power consumption and thus increase the payload adaptability to other spacecraft platforms. The connection to the mezzanine board was realized through two 120 pin FX8C-120S connectors manufactured by Hirose. These connectors were chosen for their robustness and accordance to mechanical specifications.

The sensor board was designed in the shape of a rectangle with dimensions: 70.08 mm x 53.02 mm. Following results of Chapters 3, 4 and 5, the sensors chosen where:

1. One 100 nm RadFET for TID.

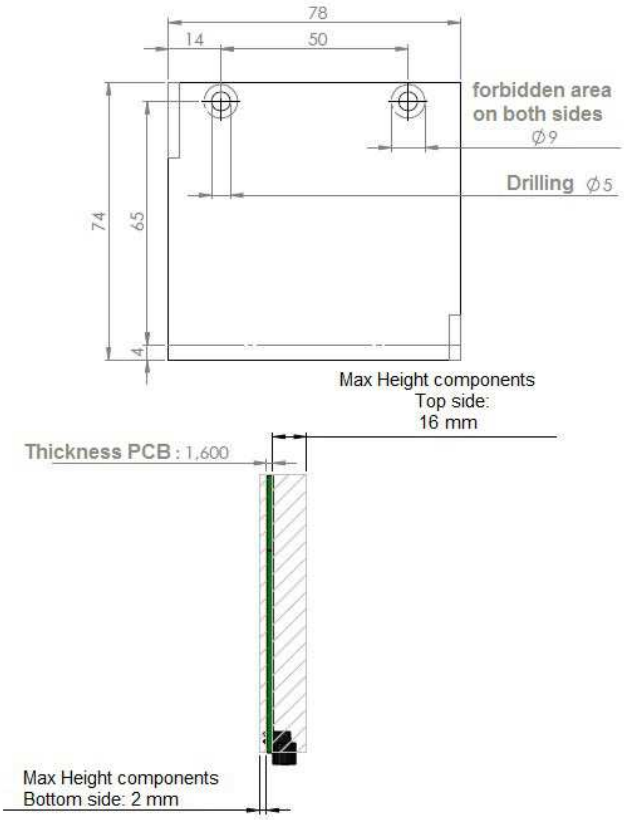

Fig. 6.3: Payload size specification and mechanical constraints.

2. One Lot II Cypress CY62157EV30 for HEH fluence measurements.

3. Two Brilliance SRAM BS62LV1600.

4. One LM45CIM3 temperature sensor.

The 100 nm RadFET is kept biased to ground on the gate pin and it follows the calibration performed in [44], similarly to the design of the RadMon V6 and the preliminary test board. The 90 nm Cypress CY62157EV30 was kept in the design, including the possibility of integrating in the FPGA the burst detection technique described in Chapter 3, future developments of the sensor payload may include a second SRAM unit to enhance the sensitivity of the HEH fluence measurements. The BS62LV1600 was kept due to its performances and ultra low power characteristics. Two units were included to further evaluate the effect of SEL cross-section saturation observed in Chapter 5. The full CELESTA payload, comprehensive of mother and sensor board connected, is reported in Figure 6.5. The temperature sensor was placed close to the RadFET to better evaluate the board temperature in proximity of the dose sensor. In addition the RadFET was connected through an adapter, to possibly change the component during the tests. The RadFET will be directly soldered to the PCB in the final payload scheduled to fly.

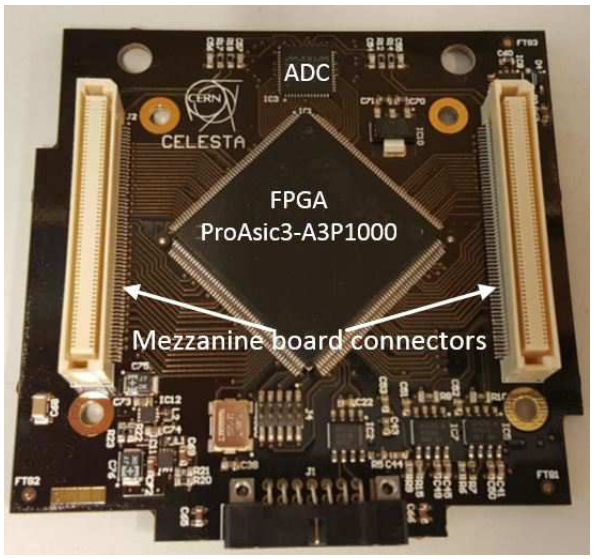

Fig. 6.4: The CELESTA payload mother board. The FPGA, ADC and mezzanine connectors are highlighted.

The final characteristics of the payload were measured and are given in the following:

Geometry: respected 76 mm x 78 mm x 17.6 mm maximum PCB size, total height of components less than 2 mm on bottom side and ≈ **15.46 mm** on top side (calculated at the top of the mezzanine board excluding the RadFET adapter).

Mass: approximately **60 g**.

Power consumption: average of **162 mW**, with **300 mW** of peak when enabling the acquisition of data via the ADC.

The main firmware takes charge of the sensors reading and conditioning, the timing of the variables involved and the communication with the OBDH. The communication was developed to comply with the protocol developed by the Centre Spatial Universitaire (CSU) of Montpellier and the CAN physical layer. The PL was set to transfer up to 32 bytes of data to the OBDH, further detailed in the next section.

Once the payload design was defined and completed, a more detailed analysis of the radiation levels within the satellite was performed. In Chapter 4 the environment outside the spacecraft was simulated and described to provide an overview of the expected TID and fluence levels, resulting in a valid input for further tests and calculations. The process of a detailed radiation effects calculation at component level involves simulations using a radiation model of the spacecraft, [126]. The CAD model of the fully assembled CELESTA CubeSat is reported in Figure 6.6. The fully assembled Payload can be plugged in front of the EPS at a variable distance.

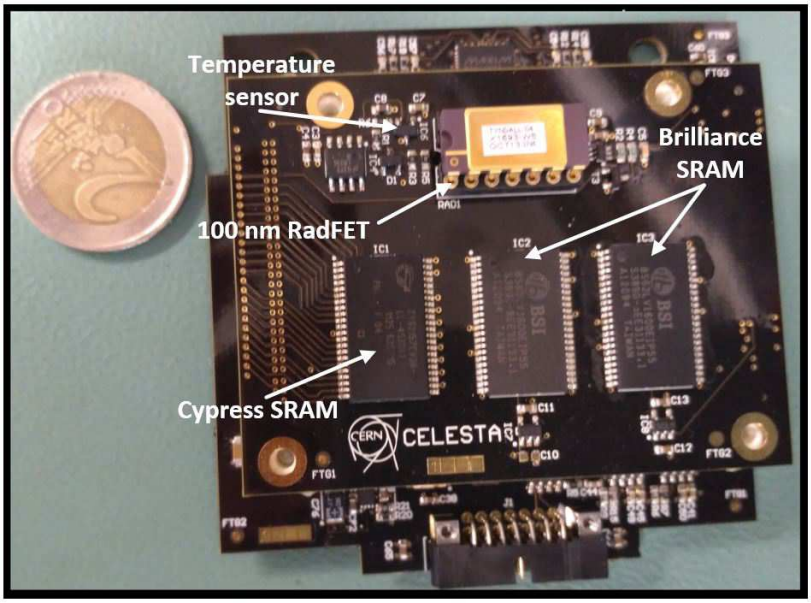

Fig. 6.5: The CELESTA full payload module: motherboard and mezzanine boards are attached together.

The model was imported into the FASTRAD tool [127] for radiation transport calculations. The software was provided by TRAD, simulations were performed by the University of Montpellier and the CSU. In general the first approach followed is the sector analysis using Ray Tracing (RT): such method consists in a worst case analysis and estimation of the TID levels, down to the detail of the electronic components packaging. The Ray Tracing analysis considers that particle paths follow straight lines, and it is used to identify components or zones of the spacecraft more sensitive or highly exposed to radiation. The inputs for a TID analysis using RT are the dose-depth curve [128], the number of sectors to be considered around the component and the calculation method. At each direction (sector of the spacecraft) the total Aluminium equivalent shielding is calculated, and the dose-depth curve resulted from OMERE simulations is read to define the expected dose at a specific coordinate point in the geometry. Finally the average dose at component level is estimated taking into account all sectors. The maximum TID values, in krad (Si), resulting from the worst case analysis within the CELESTA spacecraft are reported in Table 6.1 for each sub-system.

The highest amount of TID is expected on the EPS, up to 15.41 krad (Si) (154 Gy). The EPS, which includes the battery, is the largest module within the CubeSat. Results of FASTRAD simulations showed an extra shielding effect provided by the EPS on the payload located just in front of it. As a consequence the maximum TID value expected for the payload was **8.49 krad (Si)**, (84.9 Gy), which was the new maximum TID value set as mission constraint in terms of absorbed dose.

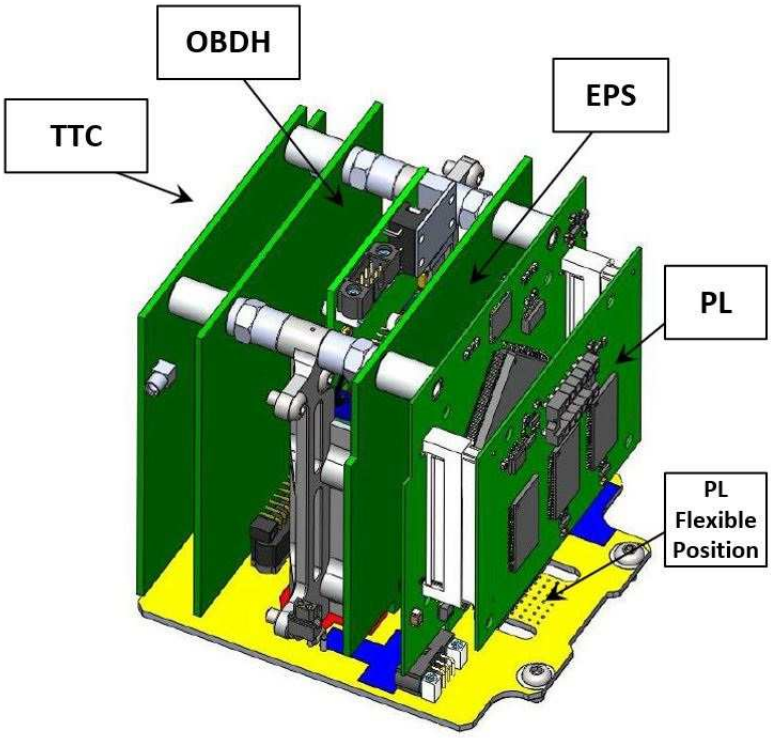

Fig. 6.6: CAD model of the fully assembled CELESTA CubeSat. The Payload can be located at different positions in front of the EPS.

Table 6.1: FASTRAD results on the CELESTA full satellite CAD model. Dose calculation with solid sphere dose curve.

Sub-System	**Max. Total Dose [krad (Si)]**
OBDH	12.76
PL	8.493
EPS	15.41
TTC	6.397

6.2 Experimental Tests Of The CELESTA Payload

6.2.1 | The Payload Setup At CHARM

An OBDH unit and a CELESTA mother board were manufactured. The OBDH was programmed following the specification and design of the ROBUSTA platform developed by the CSU. The OBDH integrates a PIC micro-controller which manages the CAN frames over the bus and controls the other sub units. The FPGA on the payload was programmed with a CAN core modified in order to comply with the ROBUSTA communication proto-

col and send/receive instructions to/from the OBDH. The core registers and FIFOs were implemented using TMR for higher tolerance to radiation. A predefined set of communication frames is exchanged between the payload and the OBDH. For instance the payload can be reset any time by a "Reset PL" command, and be set into "Mission" or "Low Power" states. The cause of a Reset is always reported and logged by the OBDH. To exchange data a "TM Data Transfer" request can be initiated by the PL: this command asks the OBDH for permission to broadcast new data and stock them in the board FRAM memories. Similarly the data transfer request may be initiated by the OBDH: in this case it's the OBDH to send an initial command to the PL and grant permission to transmit the information. Additionally the OBDH can be programmed to send a "Broadcast Frame" to each sub-system, requesting transmission of up to 48 bytes of valuable data, which are timestamped and stocked directly by the OBDH on the FRAM. The PL receives the periodical "Clock Frame" from the OBDH, which is used to timestamp the data. During the mission, the values of the recorded quantities are stocked in dedicated FPGA registers and then transferred to the OBDH. The latter is then responsible for the broadcasting to ground via the TTC unit. The main priorities of the satellite test at CHARM were:

1. The verification of the correct communication via CAN bus.
2. The verification of the payload power consumption over TID.
3. The qualification of the OBDH components in a mixed-field.
4. The measurement of radiation levels and further verification of the SEL detection circuit functionality.

A partial CELESTA unit was assembled using a mother board, a full payload and an OBDH module. The EPS and TTC modules were not included due to time constraints and to the priorities of the test, which involved mainly the OBDH and PL modules. The payload was programmed to transfer up to 32 bytes to the data handling system using a "TM Data Transfer" request. This operation was scheduled to be periodical with a period that could be set to minutes or hours. In the test the data transmission period was set to **1 minute**, this choice was driven by the need of a fast acquisition of the sensor quantities during the test: in the final application the sensor timings will be modified according to mission needs. The payload broadcasts to the OBDH the following 20 bytes of data:

1. 4 bytes of timestamp.
2. 2 bytes of temperature.
3. 2 bytes of the RadFET V_{th}
4. 3 bytes of SEU.
5. 3 bytes of MBU. Calculated as multiple bit upsets occurring on the same data row.

6. 3 bytes of SEL from brilliance number 1 (BSI1).

7. 3 bytes of SEL from brilliance number 2 (BSI2).

The timestamp frame is given periodically by the OBDH. The number of bytes allocated for each register was exaggerated on purpose, due to test requirements, in the final firmware the register size can be reduced. In particular the latchup detection can be modified in order to store a timestamped latchup count only whenever an SEL occurs, given the difference between the foreseen mission latchup rate and the one in the accelerated test. Figure 6.7 shows the PL and OBDH modules mounted on the mother board: a ribbon cable was plugged on the EPS connector and it was used to provide the required +6V main voltages to the units as well as to connect to the CAN network. The DOSI module was not included on the OBDH board, but it may optionally be integrated in future tests.

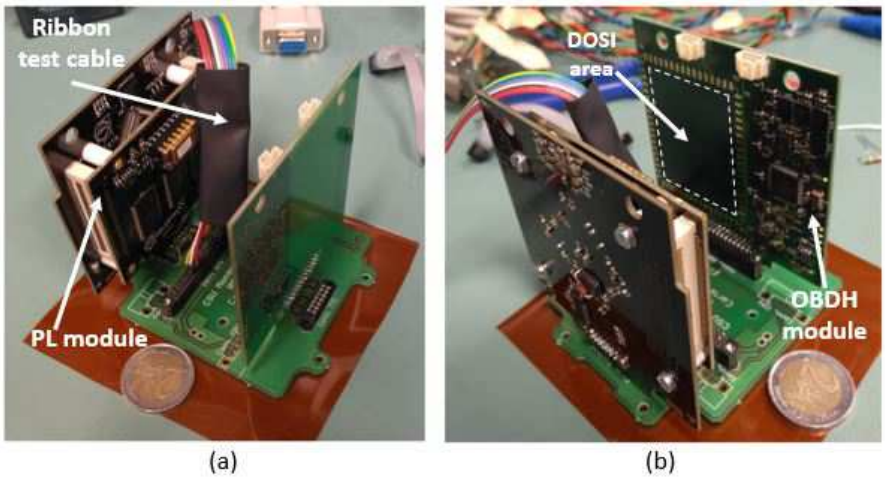

Fig. 6.7: The CELESTA satellite used during tests at CHARM. The PL and ribbon cable are highlighted in (a), the DOSI area and OBDH module are pointed out in (b).

The ribbon cable was linked to a 40 meters Sub-D 9 cable, connecting the satellite to a power supply and laptop which were located in the CHARM control room. The power supply provided the main +6V voltage and the laptop ran the controlling software. The latter consisted of a Labview program developed by the CSU to emulate the TTC and EPS sub-systems, thus controlling the satellite simulating the operations performed by the ground station. The laptop was connected to the CAN network using a CAN/USB adapter. All CAN frames travelling on the bus were logged and stored on the Laptop. Data was saved with the following format: "Data Timestamp, the 29 bit CAN Identifier in hexadecimal, data length field, data bytes (up to 8 bytes)".

A brief example of a TM transfer data request initiated by the PL is reported in Figure 6.8: the OBDH periodically sends a clock frame, at a given time the PL transmits a subsytem request, (coded as "SS_RQST"), to the OBDH, asking to start transmission. The

OBDH acknowledges the frame and thus grants permission to transmit the data. Four data frames, each carrying 8 bytes of data, are acknowledged and broadcast to the OBDH. The first two CAN data fields were fixed to the hexadecimal value "CA FE", the 20 data bytes relative to the sensors values were successively encoded in the other data fields. This scheme was adopted to have a simple implementation of the data transmission and quickly recognize eventual failures. Finally the PL notifies the OBDH of the end of the transmission with an "End Of Transfert" frame, acknowledged by the OBDH.

```
06/10/2016 22:47:49 - 000002F1 4 75 B8 F6 57 - OBDH -> ALL -
CLOCK_FRAME
06/10/2016 22:47:49 - 000002F1 4 75 B8 F6 57 - OBDH -> ALL -
CLOCK_FRAME
06/10/2016 22:47:49 - 0000131B 3 22 00 04 - PL -> OBDH - SS_RQST
06/10/2016 22:47:49 - 00000BB1 1 11 - OBDH -> PL - ACK_FRAME
06/10/2016 22:47:49 - 0000071B 8 CA FE 57 F6 B8 75 05 95 - PL ->
OBDH - DATA | 0 |
06/10/2016 22:47:49 - 00000BB1 1 11 - OBDH -> PL - ACK_FRAME
06/10/2016 22:47:49 - 0000271B 8 CA FE 23 1C 00 E1 A1 FF - PL ->
OBDH - DATA | 1 |
06/10/2016 22:47:49 - 00000BB1 1 11 - OBDH -> PL - ACK_FRAME
06/10/2016 22:47:49 - 0000471B 8 CA FE 00 00 7A 00 04 E2 - PL ->
OBDH - DATA | 2 |
06/10/2016 22:47:49 - 00000BB1 1 11 - OBDH -> PL - ACK_FRAME
06/10/2016 22:47:49 - 0000671B 8 CA FE 00 05 27 FF FF FF - PL ->
OBDH - DATA | 3 |
06/10/2016 22:47:49 - 00000BB1 1 11 - OBDH -> PL - ACK_FRAME
06/10/2016 22:47:49 - 0000041B 0 - PL -> OBDH - END_OF_TRANSFERT
06/10/2016 22:47:49 - 00000BB1 1 22 - OBDH -> PL - ACK_FRAME
06/10/2016 22:47:49 - 000002F1 4 75 B8 F6 57 - OBDH -> ALL -
CLOCK_FRAME
```

Fig. 6.8: Example of a "TM Data Transfer" request initiated by the PL.

In terms of timing of the sensor components, the ADC was turned off to save power and activated only for 10 seconds every minute. Therefore the RadFET V_{th} and temperature value were read once every minute. The Cypress memory was read every two minutes and each row was rewritten whenever an SEU was found. During the test the burst detection algorithm was not included in the firmware driving the Cypress memory, since no burst event was observed using a 2 minutes SRAM access period in previous tests presented in Chapter 4. Nevertheless in the future final version of the FPGA firmware, the code can be integrated with the burst algorithm to account for burst events occurring during flight. The registers storing the SEL counts were updated whenever an SEL was

recorded. Similarly to tests carried out in Chapter 4 and 5 the satellite was located in a test position representative of the LEO environment. In this case test location "R5" was selected. This choice was motivated by the higher flux and dose rates found at position "R5" when compared to locations "R4" and "R3", allowing for an even more accelerated test while sharing a very similar particle spectra relatively to the other two positions [55]. The CELESTA satellite setup in CHARM is shown in Figure 6.9: the CubeSat structure holding the mother board, PL and OBDH was installed on a movable rack at 1 m 29 cm of height from the ground. A RadMon V6 unit was located in proximity and the full rack was placed at test location "R5".

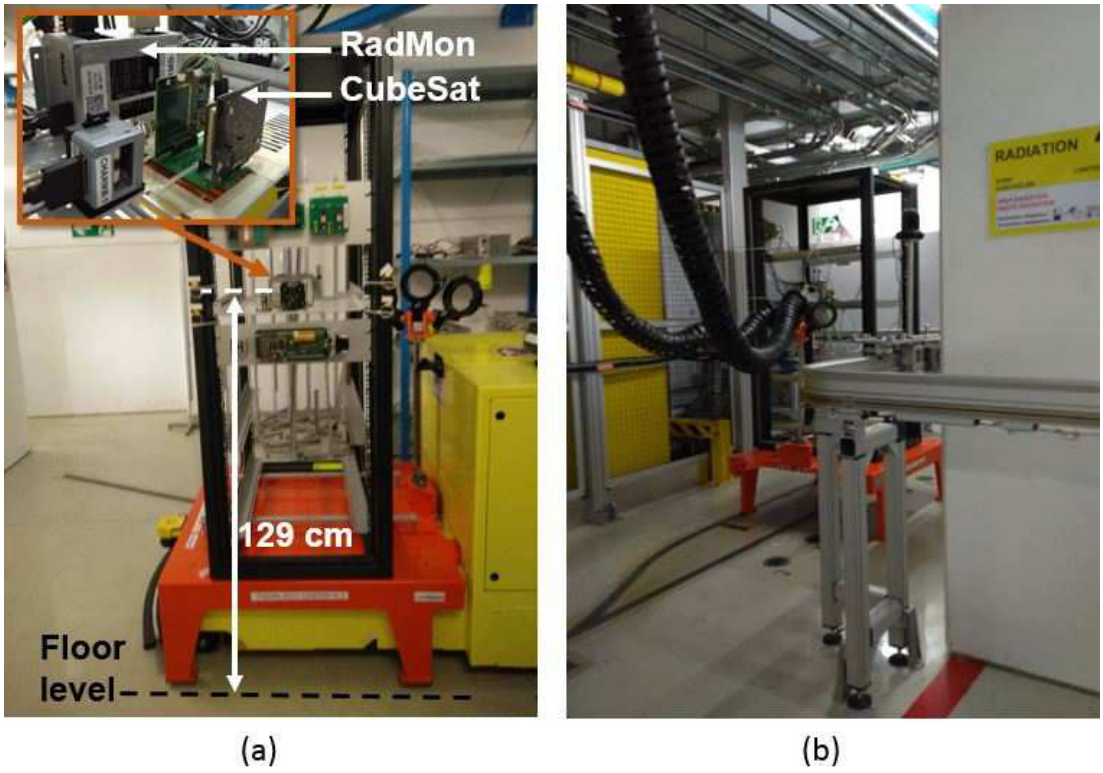

Fig. 6.9: CHARM setup showing the CELESTA structure with a nearby RadMon (a) and the full rack on position "R5" (b).

6.2.2 | Test Results Of The CELESTA Payload And OBDH Modules

The satellite was irradiated from the 5th to the 11th of October 2016, thus for about 6 days. The hardness of the mixed-field spectra was gradually increased in order to check the overall functioning of the setup in terms of electrical performances and communication. The copper target (Cu) and test location "R5" were fixed, the shieldings were set into three successive configurations: "CIIC", all slabs inside the area, "OOIC", only half

inside, and finally "OOOO", all shieldings out, which was kept for the majority of the test. The values recorded by the payload sensors are all summarized in Figure 6.10: the four plots report the temperature, TID, SEU and SEL recorded during the test. The "Cu_CIIC" configuration was kept for the first day of irradiation, during this period the temperature was constant around 21.25 C°, a low dose rate was recorded by the RadFET, reaching ≈ 2 Gy of TID, and similarly the SEU and SEL counts registered low rates. For a few hours half of the shielding was removed, in the plots it is possible to observe a sudden increase in the slope of the curves, which is even more marked when the final shieldings were removed and the final "Cu_OOOO" configuration was set. The beam was delivered constantly, except for a couple of hours on October 8th where it was stopped for technical reasons.

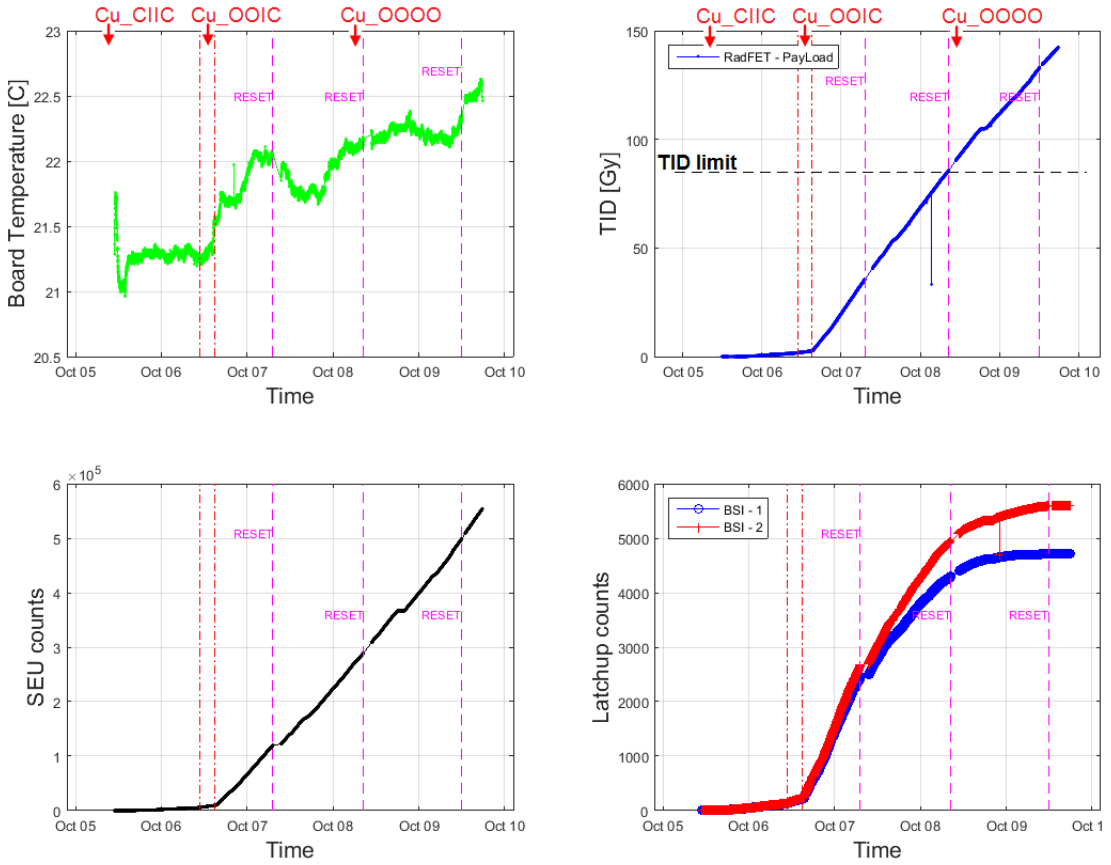

Fig. 6.10: The temperature (top left), TID (top right), SEU (bottom left) and SEL (bottom right) recorded by the payload sensors during the test. Red vertical lines point out the times in which the facility was reconfigured, whereas magenta ones the request of a general RESET following an error.

During the test the modules were set into "Mission" state. The CAN communication performed without any failure except for three events, highlighted in the plots by a verti-

cal line coloured in magenta. During each of these cases the OBDH failed responding to the payload data transfer requests and the communication was stuck. Setting the modules into "Commissioning" and then "Mission" mode was not sorting out any result. A "Send Reset TC" command was issued by the TTC, emulated via software, thus simulating a reset signal coming directly by the ground station and resetting the state of each module. This software reset had the effect of restarting the satellite and solving the communication failure. The current consumed by the OBDH was monitored and reported in Figure 6.11: the module consumed 18 mA on average, with a few peaks recorded over 25 mA. The area confined by the purple rectangle showed the behaviour of the current when the OBDH was unresponsive and a reset from the TTC was required: the current was held at a value approximately 1 mA lower than nominal, and only when the reset signal was sent the correct value was restored. Such behaviour might the consequence of a functional failure in one of the main registers of the micro controller, generating a "hang" state of the PIC, or a modification of one of the configuration registers of the device solved only by a direct reset to the initial state. Another failure occurred was the loss of the clock signal by the OBDH: the value of the RTC clock registered by the OBDH PIC was incorrect and the correct value needed to be restored by a TC command sent by the TTC, this error was not compromising the communication or the general functionalities of the satellite. In one case the OBDH was found accepting only the first PL data frame, rejecting the subsequent ones. This latter failure was again solved by resetting the OBDH status through a TTC command, directly sent from the ground (the controlling software).

The temperature increased monotonically up to 22.5 C°. The SEU counting was linear, with a mean SEU rate of 95 SEUs/min, no burst events were observed. The payload did not show any sign of degradation until 140 Gy. The measurement went over the TID limit set at 84.49 Gy, but at approximately 140 Gy the payload started being unresponsive and was not yielding any more data transfer requests. A closer look at the power consumption of the boards showed a failure in the system. Figure 6.11 and Figure 6.12 report the current consumption of the OBDH and PL respectively during the test. The payload consumes on average 27 mA, drawn from the unique +6V source, thus obtaining 162 mW average power consumption.

When the ADC is turned on, the consumed current reaches ≈50 mA, consequently the power raises at ≈300 mW. The maximum current peak was recorded at 70 mA, which was still within the range allowed by the platform for the maximum peak power. The PL experienced a hardware failure that led to large and quick current increase. The OBDH on the other hand became unresponsive to external commands. The power of the PL was cycled but the current kept increasing, thus excluding the possibility of a latchup event. The OBDH was shut down to prevent it from permanent damage, whereas the PL was kept on for several hours to monitor the current increase. The OBDH was restarted and the communication was restored but the PL was compromised after reaching 100 mA of consumed current. The system was irradiated until October 11th, the final fluence and

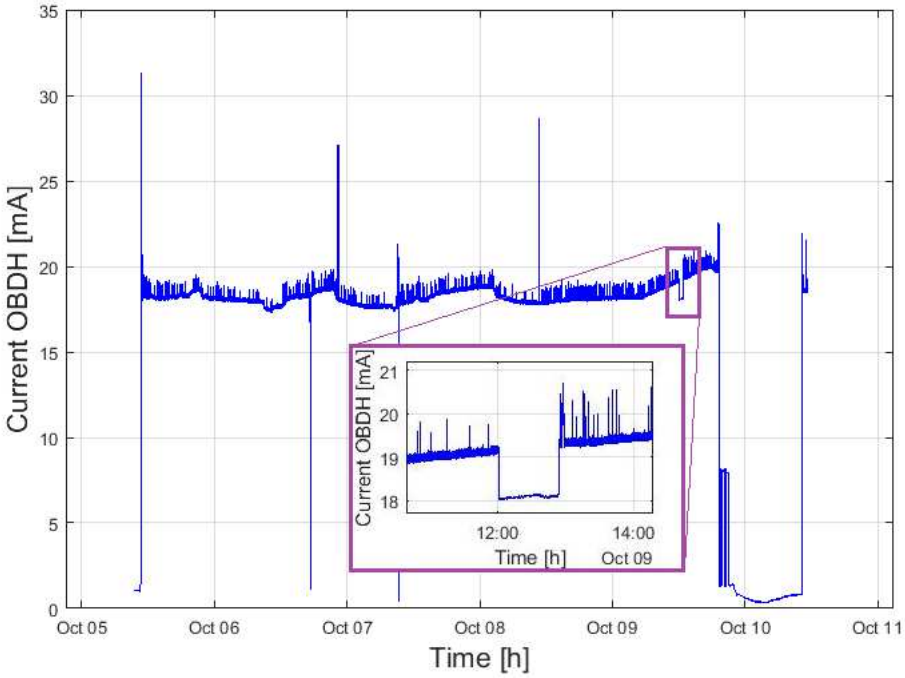

Fig. 6.11: Current consumed by the OBDH during the test. The zoomed area in the purple rectangle shows the current when the OBDH became unresponsive, requiring a general reset.

Table 6.2: Fluence and dose results returned from the facility measurements.

CHARM Configuration	**Fluence [heh/cm^2]**	**Dose [Gy]**
Cu_CIIC	$4.88{\cdot}10^{9}$	1.5
Cu_OOIC	$2.1{\cdot}10^{9}$	0.34
Cu_OOOO	$4.80{\cdot}10^{11}$	183.1
Total	$\mathbf{4.86{\cdot}10^{11}}$	**184.94**

dose values measured by the facility are reported in Table 6.2. In total 184.94 Gy of TID were reached, the OBDH was still broadcasting at the end of irradiation, whereas the PL had a failure at ≈ 140 Gy. The total fluence reached was $4.86{\cdot}10^{11}$ heh/cm^2.

The components on the PL mother and mezzanine boards were analysed after the test. The 3.3 V and 1.2 V rails needed for the FPGA and CAN transmitter were not sourcing the correct values, suggesting a failure of the TPS62125 voltage regulators, which were part of the selected COTS not previously characterized.

The SEL rate was on average 1.25 SEL/min on both BSI memories: the two curves showing the latchup counts over time overlap and follow the same slope. As the measurement continues though, the latchup counts diverge and eventually end up towards a

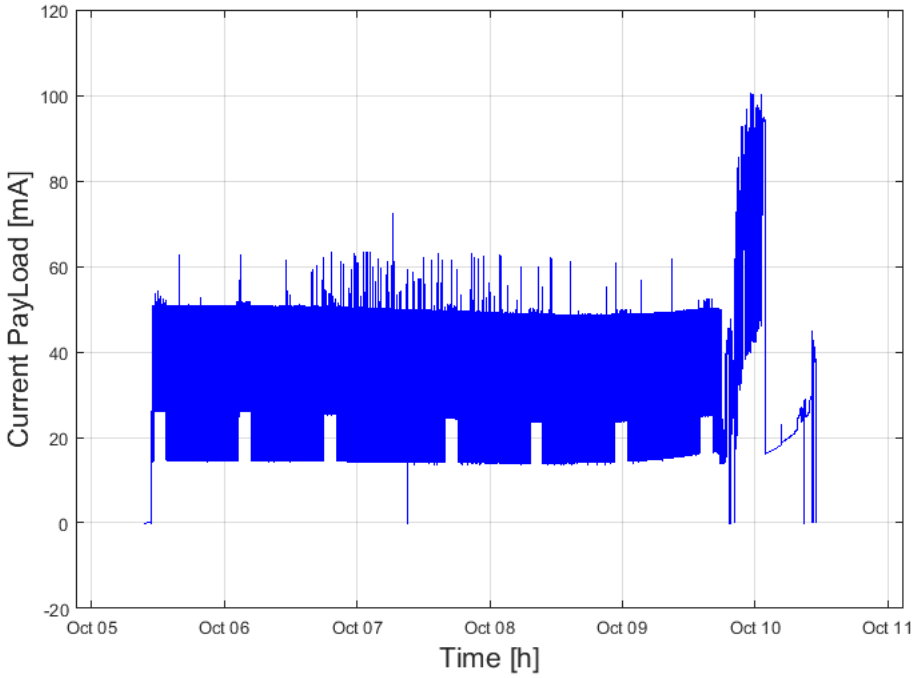

Fig. 6.12: Current consumed by the PL during the test. Between October 9th and 10th the current raised quickly due to a hardware failure.

saturation level, similarly to results obtained in Chapter 4. Figure 6.13 shows the latchup counts over fluence together with the calculated latchup cross-sections for BSI1 and BSI2, the fluence values were measured by the Cypress SRAM on the payload. Both memories belonged to Lot II and were never irradiated before, the curves show a smooth saturation of the recorded latchup counts starting over ≈3000 events. The initial cross sections were constant at $\approx 3.5 \cdot 10^{-8}$ cm^2 for both SRAMs, which was expected following results obtained in the analysis of Chapter 4. At approximately $5 \cdot 10^{10}$ heh/cm^2 the cross-section values decreased linearly, reaching $3.5 \cdot 10^{11}$, a factor 2 lower.

No SEL data was recorded afterwards, due to the hardware failure on the PL. This result confirmed the effect obtained while characterising the component with the SEL test board and the simple power supply setup, therefore it will be object of a deep study to investigate the reasons, at structural and layout level, which led to such a clear saturation of the recorded SELs. Nevertheless the fluence interval where the cross-sections values were constant, and the SEL count was accordingly linear, were well within the predicted target fluence levels for the CELESTA elliptical orbit. As a result the Lot II Brilliance devices are still considered to fly on board of the CELESTA payload, nevertheless other candidates will be characterized in order to find a second choice to replace, or to be joined to, the chosen SRAM.

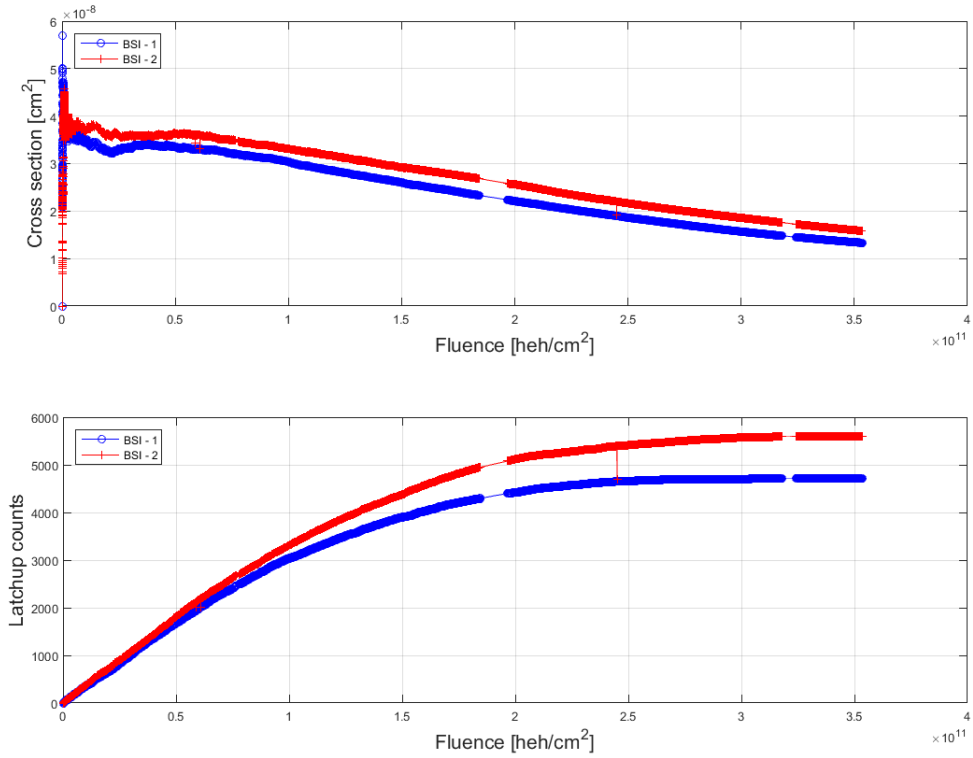

Fig. 6.13: The latchup counts (bottom) and calculated cross-sections (top) over the measured fluence for BSI1 and BSI2 SRAMs. The SEL saturation is clearly visible.

6.3 Conclusions

The CELESTA CubeSat is based upon the ROBUSTA platform developed by the CSU of Montpellier, thus the payload specifications in terms of mass, power and geometry are the ones imposed by the structure of ROBUSTA. The final CELESTA payload was designed respecting the requirements for its integration on the satellite. The payload weights 60 g, consumes 162 mW on average, 300 mW at peak, and it fits within the mechanical structure. The on-board communication was implemented using a CAN controller, embedded on the FPGA and hardened using TMR logic, combined with a transceiver element previously qualified at PSI. FASTRAD simulations, carried out by the CSU of Montpellier, showed an estimated total of 84 Gy as worst case TID limit for the mission, hence this value was assumed as critical TID value to be reached during the radiation qualification tests. The payload was equipped with one 100 nm RadFET for TID measurement, one Lot II Cypress CY62157EV30 for HEH fluence measurements and two BS62LV1600 Brilliance SRAMs for the latchup experiment.

A partially assembled CELESTA CubeSat setup was realized using one backplane board, one payload and one OBDH units. The setup was located at CHARM in test posi-

tion "R5", and it was irradiated for 6 days using three facility configurations of increasing HEH spectra hardnesses. Ultimately the satellite test was successful in the verification of the communication, the assessment of the payload functionality, the analysis of the radiation levels and the characterization of all the used COTS. The test evidenced a failure in the design, specifically in the selection of one of the components, the TPS62125 voltage regulator. This observation was of extreme importance also for the other sub-systems, since the TPS62125 was included in the design of the other modules. The firmware used 50% of the FPGA core cells and 28% of the embedded RAM, thus more space is available for the inclusion of the burst detection algorithm (another 5% more of the FPGA area) or the conditioning of other sensors (e.g. floating gate ones). The critical TID level obtained by FASTRAD simulations was reached and the whole system worked without any major failure up to 140 Gy. Several events occurred on the OBDH which required a general satellite reset. In this regard a test at CHARM of the full CELESTA satellite, (i.e. including the TTC and EPS modules), is planned in the future to complete the study of the system weaknesses in terms of radiation.

7

Seventh Chapter

Conclusions

The CERN accelerator complex is characterised by a high radiation environment made of mixed particles. The RadMon V6, the latest version of the CERN Radiation Monitor, plays an important role within the Radiation To Electronics project: it provides a precise on-line and distributed monitoring of the radiation levels, thus mitigating the risk of radiation induced failures on the electronics equipments installed in harsh areas, ultimately contributing to increase the availability of the beam to the experiments. This work focused on the follow-up and upgrade of the newly installed RadMon V6, together with its adaptation to a payload for a 1 Unit CubeSat dedicated to space missions in Low Earth Orbit. This latter research line was carried out in the framework of the CELESTA project, a collaboration between the CSU, the University of Montpellier and CERN, with the support of the CERN Knowledge Transfer. The mission aims at the development of a stand-alone radiation monitoring module for future small satellites applications, the demonstration of the LEO environment reproducibility at CHARM, the evaluation of the SEL occurrence on SRAM memories in low orbit as an added scientific experiment, and finally the radiation characterization of COTS components to select devices with the best performances for radiation monitoring in harsh environments. The two research lines were carried out in parallel and a full set of radiation tests were performed both with focused proton beams, at PSI, and in a mixed particle field, at the recently commissioned CHARM facility at CERN.

A study was carried out on the 90 nm 8 Mbit Cypress SRAM memory CY62157EV30. This component was chosen as HEH fluence monitor on the RadMon V6 due to its high proton cross-section, insensitivity to thermal neutrons, independence from the operating voltage and availability on the market, all key factors in an application requiring a large production of devices and with constraints such as the environment of the LHC. Multiple Cell Upsets, arising as bursts with a high number of error bits, were reported during

operation in dynamic mode of the chosen memory. This effect was found to be caused by micro-latchups occurring within the memory die. A study of the parameters involved in the generation of these events was carried out at the PIF facility at PSI, using a focused proton beam on the DUT. An algorithm for on-line fast detection and correction of these bursts was implemented on FPGA and evaluated. Two lots of the chosen DUT were tested with a 3.3 V voltage supply and a beam energy of 150 MeV. Several test parameters were systematically changed during each run and the SRAM cross sections were evaluated. The reading period T_{read} and the particle flux resulted to be the parameters most involved in the generation of bursts, as with fast reading values and high particle fluxes the probability of burst events arising on the memory increased. The initial bit pattern and memory rewriting during irradiation did not yield any relevant effect. The use of a physical addressing scheme, where addresses are read across SRAM blocks within the internal architecture of the memory, resulted in a high number of bit upsets located in the same column arrays of the die. Given the latchup nature of the observed events and the relation of the column errors to the internal layout architecture of the SRAM, a new addressing pattern was developed accessing alternate blocks located in the left and right parts of the memory, while implementing two detection windows and incrementing rows and columns within each block.

Further radiation tests were performed to validate the new addressing scheme at the CHARM mixed-field facility. With an alternate blocks memory accessing, the electrical stress on the active cells positioned on the same column was reduced and no bit column errors were observed in all runs. The algorithm was implemented on a RadMon V6 unit and verified at CHARM during three weeks of irradiation. Results showed an effective detection and correction of the MCU bursts, thus leading to the development of a new FPGA firmware for the RadMons based on the proposed technique. The new firmware was loaded on the units installed within the PSB and SPS tunnels, as well as in the ALICE, HiRadMat, NA62 and CHARM areas. The analysis of data collected in 2016 during operation of the newly programmed monitors showed several burst events correctly detected and filtered out. This approach resulted particularly effective at low fluence values, where one single event was observed to be enough to yield a large error of the HEH fluence measurement.

During the commissioning of the CHARM facility, in April 2016, one large burst event was not correctly detected. This observation provided useful data for future optimizations of the algorithm, such as exploiting different Th_{SEU} values, adjustments of the detection window size and the use of alternative addressing patterns (e.g. further splitting the memory die to decrease the access time to the same block). Ultimately the proposed method for fast on-line detection and correction of burst events proved to be effective, returning corrected values of the measured HEH fluence. Nevertheless, other latchup-free memory candidates are currently researched and considered for replacement of the chosen Cypress CY62157EV30 in future versions of the RadMon. The proposed correction technique is faster and less computationally expensive compared to software algorithms for the post-processing of data, in addition the method allows burst recognition

in presence of high fluxes, where burst events are hidden within the repeatability of the measurement, as well as in areas with lower flux levels. The approach followed can be used also for other SRAM memories sensitive to micro-latchups and showing evidence of SEU bursts with a similar rectangular shape.

In the context of the CELESTA project a qualification procedure for nanosatellites and systems deployed in high radiation environments was proposed and presented. The validation method is based on the CHARM mixed field facility, which provides dedicated test locations with particle spectra representative of various environments, including the Low Earth Orbit (LEO). A feasibility study was carried out using a test board, based on the CERN RadMon technology and equipped with an SRAM-based latchup experiment, evaluated in the CHARM mixed-field. Test locations within CHARM were selected following the analysis with FLUKA of the HEH spectra within the facility and their comparison with the ones expected for the chosen LEO orbit. Research activities focused on the study of the mission requirements, the qualification of the commercial components chosen for the hardware design and the overall evaluation of the payload test board functionality and reliability in the mission environment. During the first test, the acquisition of the ionizing dose evidenced a strong dependency on the board temperature, highlighting the need to compensate the measured data against temperature. This latter process is currently performed in post processing for the RadMon V6 devices, but other solutions, such as using two RadFET sensors operated at different bias voltages [129] will be object of study. In addition one of the operational amplifiers failed due to a latchup event, indicating a strong dependence on the manufacturer Lot number, a result that proved to be essential also for the RadMon V6 production. The HEH fluxes measured during the test at CHARM were compatible with the ones predicted by FLUKA for the chosen test location, hence validating the choice of the SRAM sensor for the SEU counting functionality. The current consumed by the SRAM selected for the latchup experiment revealed several short transients below the set current threshold, not directly recognizable as Single Event Latchups. This observation led to a deeper characterization of the chosen SRAM and the validation of a different latchup detection technique without ADC monitoring of the currents. As a result an SEL test board was designed with a circuit developed using only COTS components previously characterized over radiation, choosing a circuit topology that minimized power consumption with no SET occurrence nor degradation of the components up to a TID of 32 krad(Si). The SEL cross-sections of three commercial SRAM memories were evaluated at PSI, then the best candidate device, a Brilliance SRAM BS62LV1600 was selected for further qualification at CHARM. The SEL test board with the "SRAM B" (Brilliance) device was irradiated in the CHARM mixed-field facility at a location with particle spectra representative of the LEO environment. Results showed a large Lot to Lot HEH cross-section variation for this component, in addition a decrease of the cross-section over fluence was monitored on two tested units, suggesting a progressive damage on the component structure. Despite this result the high HEH cross-section of SRAM B, for both Lots I and II, together with its low nominal current

consumption and SEL maximum current levels, led to the final selection of this SRAM device as the candidate one for the CELESTA mission. Approximately 513 latchup events with a 2 years LEO mission were calculated, assuming an elliptical polar orbit up to a fluence $3.86{\cdot}10^{10}$ p(>20 MeV)/cm^2, with an SRAM B unit not previously irradiated. Other SRAM candidates with similar electrical characteristics will be examined to be eventually added on the final payload. The latchup detection circuit was irradiated up to a total fluence of $5.76{\cdot}10^{11}$ heh/cm^2 and a cumulated dose of 37.8 krad(Si). No SETs with period larger than 20 μs were observed on the output of the LM124 operational amplifier and the current consumption of the circuit did not show any degradation over TID.

Experimental results in a mixed-field provided a deeper insight of the functionality of the components and the characterization of the SRAMs, as a result the proposed circuit was integrated on the CELESTA payload design. The use of the proposed circuit can also be extended for anti-latchup protection of devices in LEO space missions and in applications with similar TID and fluence levels.

The initial feasibility study, together with the process of selection and test of the chosen devices, finally converged on the realisation of the payload module to be embarked on CELESTA. The payload has a modular design, made of a mother and a mezzanine sensor board, to facilitate possible future upgrades and adaptation to other payload designs. The design took into account the constraints imposed by the ROBUSTA platform, thus the final geometry of the PCBs respected the 76 mm x 78 mm x 17.6 mm maximum dimensions and height of components on the PCB top and bottom sides. The payload mass is ≈ 60 g and the average power consumption ≈ 162 mW, with ≈ 300 mW at peak when the ADC is enabled. Results of FASTRAD simulations showed an extra shielding effect on the payload (provided by the power system module), hence the maximum TID value calculated for an elliptical polar orbit in LEO was finally 8.49 krad (Si), (84.9 Gy). The satellite structure, holding one payload unit and one data handling system (OBDH), was irradiated for 6 days inside CHARM. During the test the OBDH was unresponsive several times, requiring a reset from the TTC. Other minor events occurred on the communication from the side of the OBDH, but they were always restored with a reset command. At ≈ 140 Gy the PL was subject to a current increase: this failure was believed to be induced by the TPS62125 voltage regulator, a component not previously characterized and included also in the design of the other CELESTA sub-systems. This result was extremely useful as it highlighted a possible weak point, in terms of radiation tolerance, in the electrical design of the modules. The total fluence reached during the test was $4.86{\cdot}10^{11}$ heh/cm^2. The two SRAMs of the latchup experiment registered a large number of events, but the SEL counting progressively saturated over a fixed value, a result similar to the one obtained in the tests with the SEL board. The cause of this progressive decrease of the SEL counts will be carefully examined, nevertheless the target fluence value, in the scope of the mission, was largely within the interval in which the SRAM cross-sections were constant.

Ultimately the PL test was successful in the verification of the communication, the

assessment of the payload functionality, the analysis of the radiation levels and the characterization of all the used COTS. The FPGA firmware used 50% of the core cells and 28% of the embedded RAM, therefore the inclusion of the burst detection algorithm or the conditioning of new floating gate sensors can be easily added in future upgrades. The TID level of 84 Gy, resulting from FASTRAD simulations, was reached and the whole system worked without any major failure up to 140 Gy. The events which required a general satellite reset highlighted the need for a future test of the whole satellite components, thus assessing the radiation tolerance of the EPS and in particular the TTC unit, which is responsible of sending the required reset command. Further tests of the full satellite including the payload are foreseen at the CSU laboratory facilities.

The CELESTA CubeSat is scheduled for flying in 2018. At the present, launching opportunities for student projects, such as the ESA "Fly Your Satellite!" program [130], are being considered. CELESTA is the first small satellite collaboration ever supported by CERN, and it certainly provided the grounds for other future collaborations, opening a new field of interest on space applications in the CERN radiation to electronics community.

A

Appendix A

Overview of the MCU burst events shapes

The analysis of the MCU burst effect on the Cypress CY62157EV30, used on the SRAM bank 2 of the RadMon V6, was the main subject of Chapter 3. The study of the burst shapes and their occurrence in terms of beam flux and reading period T_{read} lead to the development of a burst detection and correction algorithm based on a physical SRAM accessing scheme. The initial study of the large SEU clusters was carried out after a test campaign at PSI, whose results are reported in [70]. The SRAM cells were accessed using a linear algorithm, increasing the SRAM address counter linearly regardless of the pointed location. Figure A.1 shows the full memory map at the end of one beam run, each pixel corresponds to one SRAM cell, SEUs are highlighted in black, whereas blocks are depicted in shades of grey. In this case a Lot I CY62157EV30 was tested with the following test parameters: 3.3 V supply voltage, 230 MeV beam energy, $3.4{\cdot}10^{6}$ p·cm^{-2}·s^{-1} mean flux, reaching a total proton fluence of $5{\cdot}10^{9}$ p·cm^{-2} with a reading period $T_{read} \approx 4$ s. The zoomed rectangles highlight MCU events spanning over the full width of an SRAM block. The observation of such events led to the study of an effective, fast and easy to realize correction method.

In the subsequent set of PSI radiation test campaigns the SRAM was accessed using a physical pattern, following the direction of the SRAM blocks. Figure A.2 reports the SRAM map during a test in which the particle flux was increased by a factor 10 and the reading time was reduced, in order to observe a larger number of bursts. The target was a Lot I CY62157EV30, powered with 3.3 V. Test parameters were: 150 MeV beam energy, $4{\cdot}10^{7}$ p·cm^{-2}·s^{-1} mean flux, reaching a total fluence of $1.5{\cdot}10^{10}$ p·cm^{-2} with $T_{read} = 1$s. In the plot the rows are also marked in a different grey shade, to put in evidence the location of the bit cells on the rows. A large number of vertical bit upsets was observed. Most of

the time such events originated from or included a burst, characterized by a rectangular shape, and ended once the reading reached the end of the active block, located at the horizontal row in the middle of the SRAM. This result evidenced the latchup nature of the MCU events, thus leading to the formalization of the alternate addressing scheme.

Figure A.3 shows the final result of a Lot II CY62157EV30 tested at CHARM in position "R9" with "Cu_OOOO" setting. A fluence $7.7{\cdot}10^{10}$ p·cm^{-2} was reached, with a measured average flux of $8.9{\cdot}10^{5}$ p·cm^{-2}·s^{-1} and T_{read} =8 s, the nominal RadMon V6 SRAM reading period. The reduced accessing period and lower flux combined with the alternate block reading with $Th_{SEU} = 40$ resulted in no vertical upsets being observed. The zoomed areas in Figure A.3 show some MCU events falling within the rectangular window of the filter. In many cases small SEU clusters, circled in red, showed up in the nearby block close to an MCU burst. These bit upset clusters did not affect the estimation of the SRAM cross-section for two reasons: (i) most of the time their size was comparable with the dimensions of other MBUs caused by radiation, (ii) their dimensions were large enough to fall within the filtering action when using $Th_{SEU} = 30$, which was set in the algorithm verification at CHARM, described in section 3.3.1, and yielded a cross-section value comparable with the reference obtained during static tests.

Fig. A.1: SRAM map of a Lot I CY62157EV30, accessed with linear addressing. Two MCU burst events are highlighted by a close-up zoom.

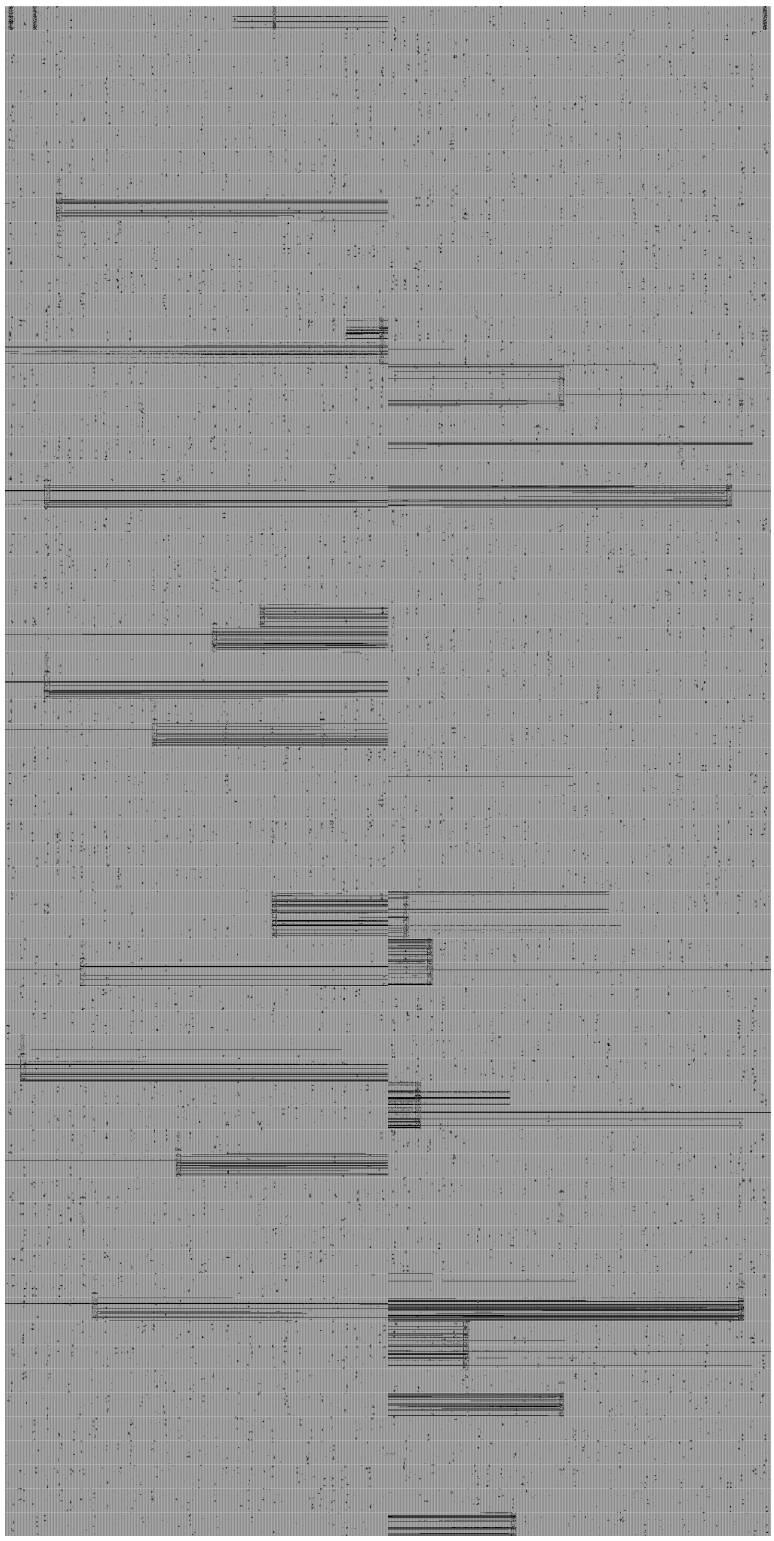

Fig. A.2: Map of the bit upsets on a Lot I CY62157EV30, accessed with physical addressing. Large vertical upset involving several columns in a block were observed.

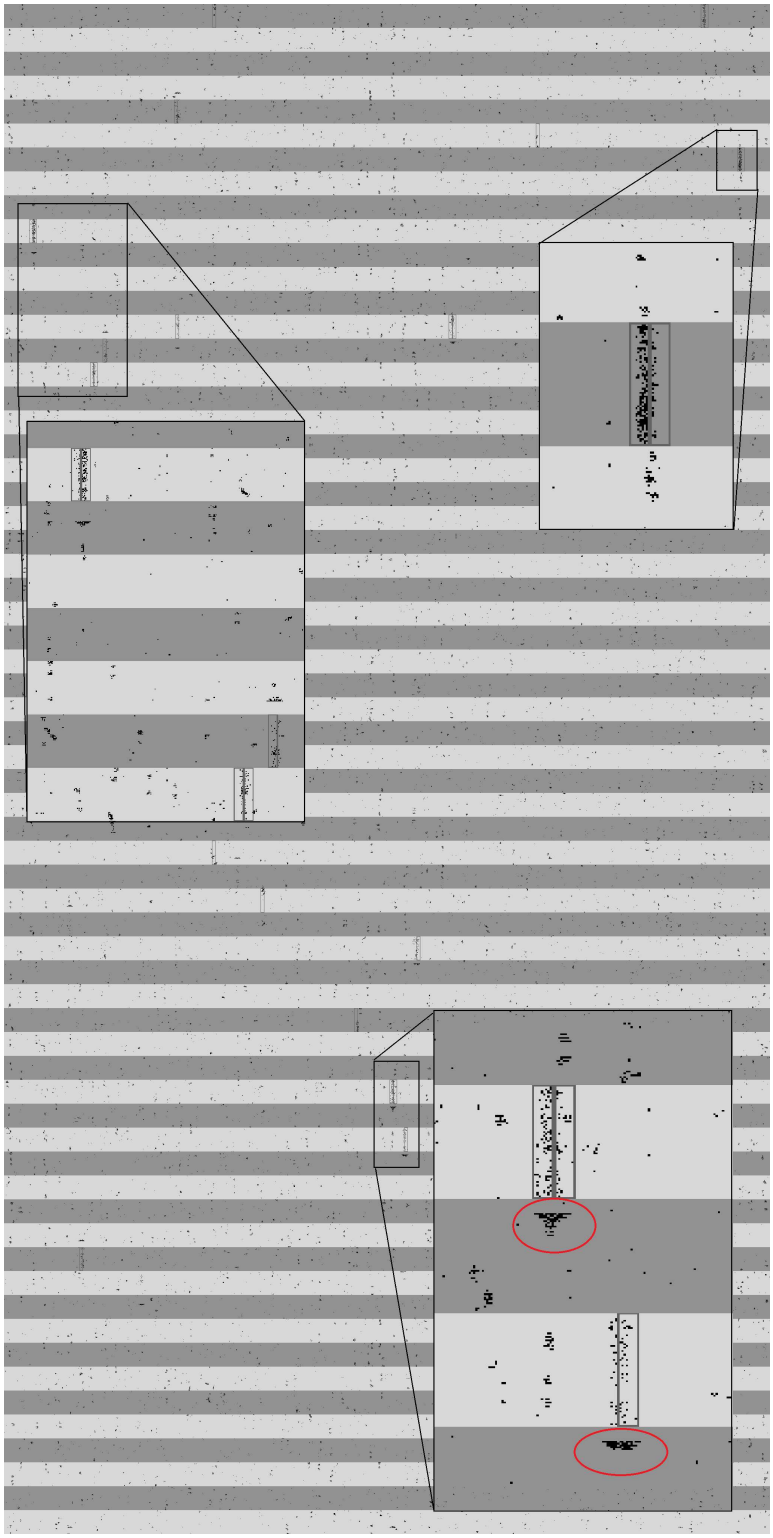

Fig. A.3: SRAM map of a Lot II CY62157EV30, accessed using the alternate addressing pattern. Smaller MCU burst clusters are circled in red.

B

APPENDIX B

COMPENDIUM OF EXPERIMENTAL TESTS ON CANDIDATE COTS DEVICES

Radiation tests using focused mono-energetic proton beams were carried out at the PSI-PIF facility, briefly described in section 2.5, to characterize several candidate COTS components used in the electronic system designs carried out in this work. Results of the characterisation of five most relevant components are given in the following.

Experimental Results of MAX11046 ADC

The MAX11046 is a 16-bit 6-channels ADC integrated in the RadMon V6 main and sensor boards. This component was characterized in previous test campaigns at PSI, results were described in [43] and commented in relation to its use for the acquisition of the sensor voltage signals. The device is based on BiCMOS technology, although the manufacturer does not provide any further detail on the component's layout, and it is powered by two voltage levels: +5 V and +3.3 V. The characteristics of high precision, electrical performance and tolerance to radiation made it a good candidate for the RadMon V6, thus this component was kept in the design of the CELESTA test board during the initial feasibility study. Results in a mixed-field, described in Chapter 4, showed an operational lifetime of the MAX11046 above 240 Gy (24 krad(Si)), nevertheless a more detailed radiation characterization of this component was necessary, oriented in particular towards the analysis of its power consumption within the final CELESTA payload design.

The MAX11046 nominally consumes ≈240 mW of power, divided as ≈40 mA over the +5 V rail and ≈12 mA over the +3.3 V rail. The component features a "shutdown" pin which, when enabled, powers off the +5V supply and sets the device in a low power

Table B.1: Parameters of the ADC MAX11046 test at PSI.

Beam energy	**Mean flux [p/(cm^2 ·]**	**Total Fluence [p/cm^2]**	**Mean Dose Rate [Gy/h]**	**Total Dose [Gy]**
200	$1.39{\cdot}10^8$	$3.61{\cdot}10^{12}$	$3.06{\cdot}10^2$	210

quiescent state. Two MAX11046 units were tested at PSI, reaching a fluence $3.61{\cdot}10^{12}$ p·cm^{-2} and a TID of 210 Gy. The parameters of the test are reported in Table B.1. During all runs the ADC was kept in low power and then periodically "switched on" using the shutdown pin functionality, in order to verify the use of this feature in the CELESTA application. The period was set at 2 minutes, with the ADC being turned on for 10 seconds, with 250 kS/s sampling frequency to acquire a +4 V voltage level on all channels. Figure B.1 shows the current consumed over the +5 V supply rail by one of the ADC under test, while Figure B.2 shows the +4 V voltage signal acquired by the tested unit on one of the channels (channel 0).

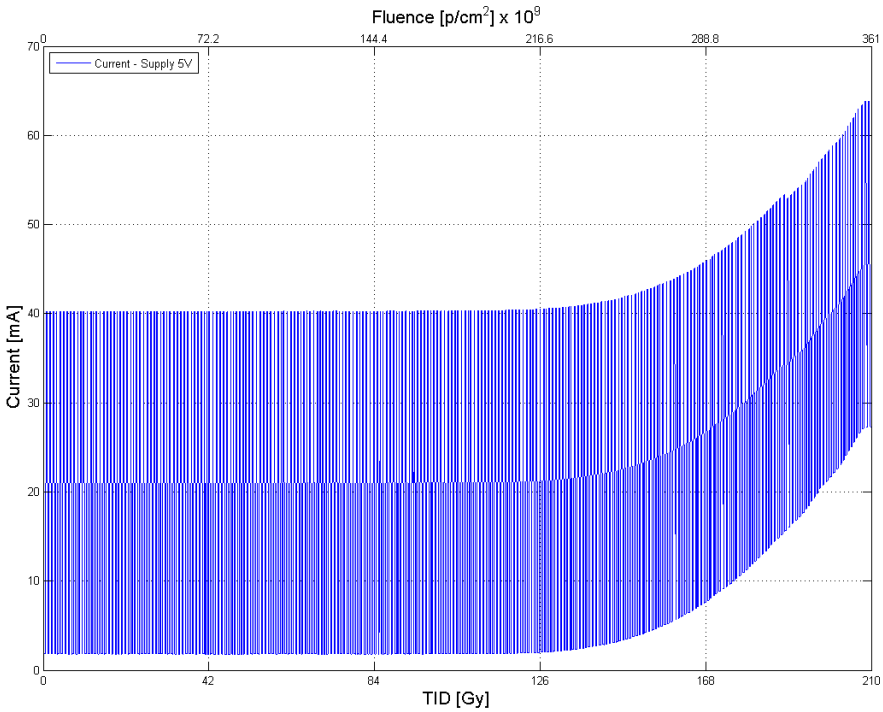

Fig. B.1: Current consumption measured on the +5V supply of one MAX11046 unit under test.

When powered off, the device current level was ≈1 mA. The ADC did not show any hardware failure or latchup event, but the current was subject to a slow build-up starting from ≈130 Gy of TID. The current progressively increased, reaching ≈65 mA at 210

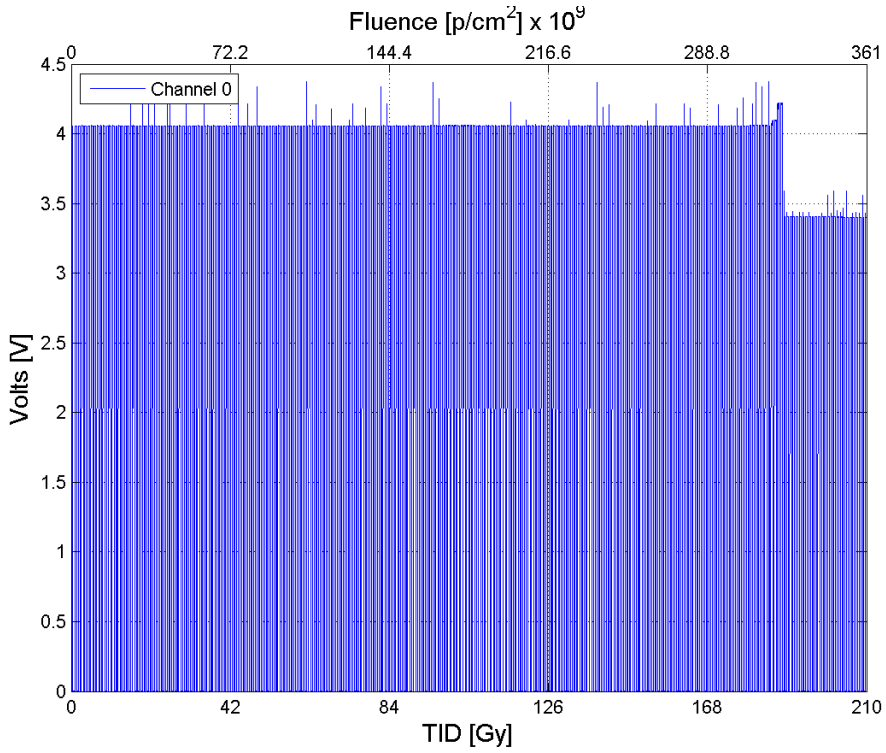

Fig. B.2: Voltage acquired on channel 0 by one MAX11046 unit under test.

Gy. The device was operative until ≈ 180 Gy, around this TID value the ADC failed in the acquisition of the input signal and never recovered. The ADC also failed in the conversion of the input quantity whenever the conversion process initiated right after powering on the device, as showed by the voltage "peaks" often raising above +4 V. A comparison between the above results and the performance observed in the test board evaluation suggested that the MAX11046 was sensitive to parameters such as the flux level and annealing. The component was held valid for the CELESTA payload design, especially considering the 84 Gy TID requirement resulting from FASTRAD simulations, although the 4-channels package version, the MAX11044, was finally included in the payload mother board given its reduced power consumption.

Experimental Results of AD8029/AD8030

The AD8029 (single) and AD8030 (dual) rail-to-rail high speed amplifiers manufactured by TI were tested as candidate devices for the CELESTA payload. Both components feature a quiescent current of 1.3 mA per amplifier, a 125 MHz small signal bandwidth and 60 V/μs slew rate. The rail-to-rail characteristic is of high importance in terms of the power management on board of a small satellite, as it implies lower voltage levels on the

device power rails while allowing a wide output range. The measurement focused on the input bias current "Ibias", measured with two different input resistor values: 100 kΩ and 10 kΩ, the output voltage drift ΔV_{out}, the voltage output V_{rail} when an input signal close to the positive rail value was applied, and finally the observation of SET events. A total of 18 components were placed in beam and tested in a feedback configuration to ensure a stable operation, the schematics were adjusted according to the specific measured quantities. A detailed report of the test planning and results is given in [131]. Figure B.3 shows the PCB designed for the radiation tests: 11 AD8029 and 7 AD8030 units were placed in a 5 cm area exposed to the beam, 2 AD8029 and 1 AD8030 were located outside as references.

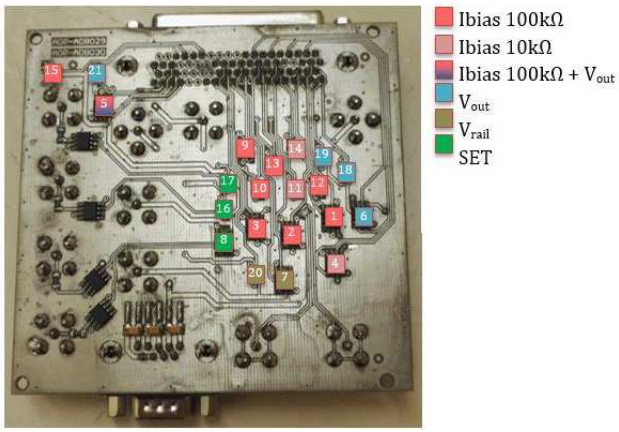

Fig. B.3: The test board used for the AD8029/AD8030 tests. A total of 18 units were exposed to the beam while 3 were kept out as reference.

The test was carried out with a 200 MeV beam, with an average flux $1.98{\cdot}10^{8}$ p·cm^{-2}, up to a fluence $1.29{\cdot}10^{12}$ p·cm^{-2} and a TID of 750 Gy. The devices were powered with +5 V and -5 V. Figure B.4 shows results of the bias current through an input 100 kΩ resistor. Amplifiers belonging to the AD8030 dual package were labelled as "A" and "B". The bias current was subject to a relatively small variation: in the worst case the current reached a ≈2.5% increase respect to the initial value at 0 Gy. The current levels were always comparable with the ones measured on the reference chips. A similar result was obtained also in the case of a 10 kΩ input resistor.

Figure B.6 shows the output drift voltage ΔV_{out}. In this case a 1 V signal was applied on the amplifiers input pin. A degradation of less than 1% was measured in the worst case, at the end of irradiation all voltage levels were comparable with the reference chips. The same results were observed while measuring the output with an input of ≈4.99 V, close to the positive supply voltage.

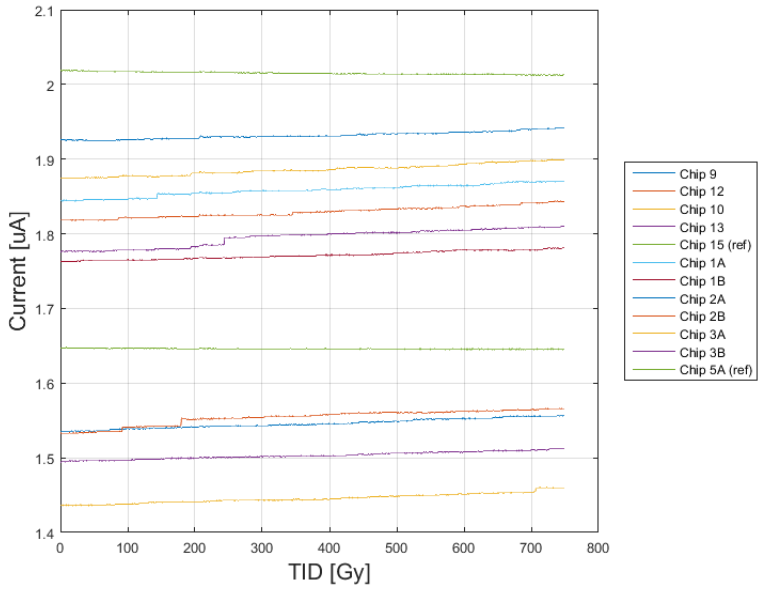

Fig. B.4: Input bias current of both the AD8029 and AD8030 with a 100 kΩ resistor on the positive input. Chips 15 and 5 were the reference devices.

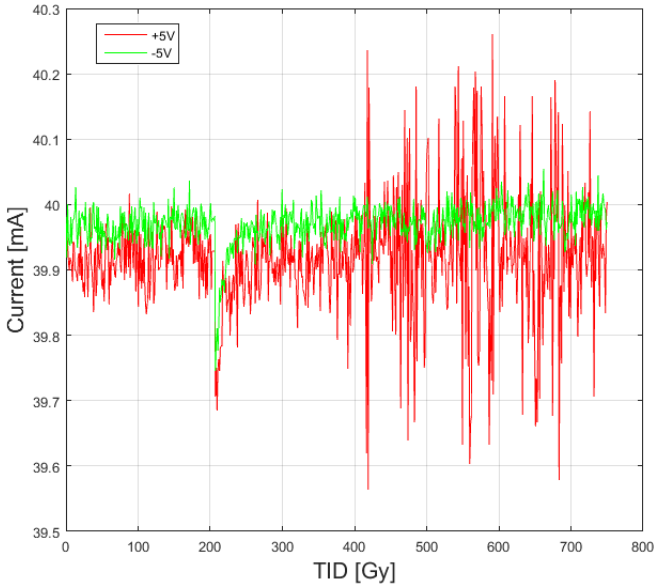

Fig. B.5: Current consumption of all the irradiated devices, measured on the +5 V and -5 V supply rails.

Finally Figure B.5 shows the current consumption of all the powered devices as a function of the absorbed dose. The current measured over the +5 V source started undergoing oscillations after reaching 400 Gy, although no large variation of the consumed currents was observed during the experimental tests and the current levels were

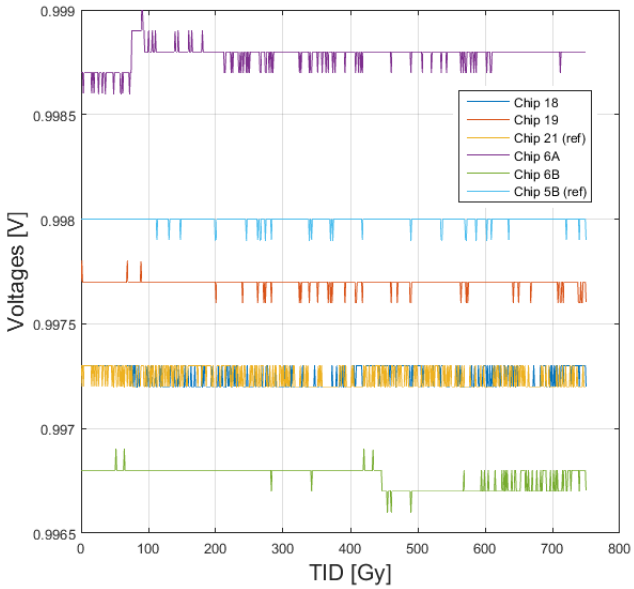

Fig. B.6: Voltage output drift ΔV_{out} of the AD8029/AD803 over TID. Chips 21 and 5 were the reference devices. The input was set at 1 V.

always within the parameters of nominal operation. No SELs were registered. A total of 29 SETs were recorded, thus obtaining a $5.62{\cdot}10^{-12}$ cm^{-2}/amplifier cross-section. The performance of this component under radiation made it a good candidate for both the RadMon and the CELESTA designs, therefore it was included in the schematics of the final payload.

Experimental Results of OPA227

The OPA2227 is a high precision, low noise dual operational amplifier manufactured by TI. The OPA227 is the single amplifier version of the same component. The device was characterized in [132], among other candidates, to assess its sensitivity to TID, SEE and DD. The component passed all tests and therefore it was included in the RadMon V6 design, both in its dual and single amplifier versions. Results in Chapter 4 showed a latchup event most likely generated by the OPA227, which was placed as part of the RadFET sensor acquisition network. A test on the specific component, using the same manufacturer and lot specifications, was carried out with the aim of understanding the source of failure and eventually excluding the device from future designs. The PSI test parameters are reported in Table B.2.

One unit of OPA227 was tested in feedback configuration, using +18 V and -5 V power supplies, as in the RadMon V6 design, and with the same network used on the CELESTA test board. A TID of 71 Gy was reached, no further testing was needed since the component resulted almost instantly highly sensitive to latchups. The events were

Table B.2: Parameters of the OPA227 test at PSI.

Beam energy	**Mean flux [p/(cm^2 ·]**	**Total Fluence [p/cm^2]**	**Mean Dose Rate [Gy/h]**	**Total Dose [Gy]**
200	$1.68{\cdot}10^{8}$	$1.2{\cdot}10^{11}$	$3.04{\cdot}10^{2}$	71

not destructive but clearly visible: Figure B.7 shows the OPA227 consumed current in an example time frame of the test. Several SELs showed up, reaching up to 18 mA from the nominal 2.2 mA level. The SEL were recovered cycling the power through the control setup. Following this analysis the OPA227 resulted highly dependent on the manufacturer and lot number, it was then replaced by the AD8029 single amplifier in the final CELESTA payload.

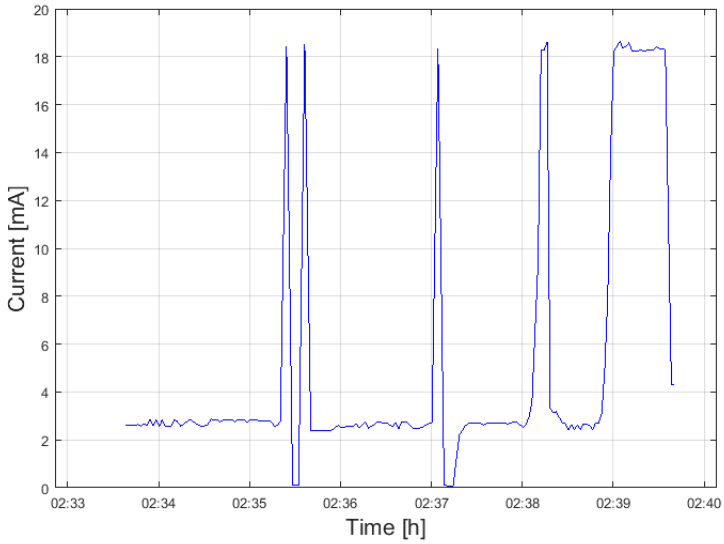

Fig. B.7: Current consumption measured on the +18 V positive rail of the OPA227 under test.

Experimental Results of SN65HVD233DG4

The SN65HVD233DG4 manufactured by Texas Instruments is the CAN transceiver adopted on the ROBUSTA platform. No previous radiation test record was found on the component during the early project design of the CELESTA payload, thus it was characterized against radiation at PSI. Two test boards were created, each carrying 4 transceiver units: 3 exposed to the beam and 1 placed outside as reference. The test parameters are reported in Table B.3: 750 Gy of TID and a fluence $1.29{\cdot}10^{12}$ p·cm^{-2} were reached at the end of irradiation.

Table B.3: Beam parameters, total fluence and TID results of CAN transceiver SN65HVD233DG4 tests.

Beam energy	**Mean flux [p/(cm^2 ·]**	**Total Fluence [p/cm^2]**	**Mean Dose Rate [Gy/h]**	**Total Dose [Gy]**
200	$2.11 \cdot 10^8$	$1.29 \cdot 10^{12}$	$4.42 \cdot 10^2$	750

Table B.4: Events recorded on the CAN transceiver SN65HVD233DG4 test boards.

Chips #	**Events**			
	Board #1		**Board #2**	
	time out	**wrong data received**	**time out**	**wrong data received**
Chip 1	4045	180	0	0
Chip 2	2	0	0	0
Chip 3	1	0	0	0
Chip 4	1	0	1	0

Each transceiver was connected to an RS-232 transceiver, forming a "loop back" configuration with the laptop located in the control room and running the controlling software. A data byte "0x55" was periodically sent, and transmitted back, with a baud rate of 115200 bps. The software was monitoring the devices current consumption and registering the events. Two kinds of errors were logged: "time out" events occurring when the transmitted signal was not received back, and "wrong data received", occurring when the received data did not correspond to the original one. The 4 chips were labelled "1", "2", "3" and "4", with Chip 1 being the reference one. Table B.4 reports the error events logged on the two boards during experimental tests.

On board #1 the reference Chip suffered a large number of time out and data errors, this behaviour was not due to radiation and a later check of the device revealed a soldering connection problem which triggered the high failure rate effect. Nevertheless 4 time out events were logged on the remaining chips and no wrong data was read back. On board #2 only Chip 4 had 1 time out error, whereas all the other components did not show any failure. The power consumption was stable and did not undergo any variation. No SEL event were reported. Excluding the reference Chip on board #1 the component showed very good performances. In a CAN network time out errors are easily eliminated by the communication protocol implemented on the FPGA, resending data whenever the CAN frame is not acknowledged, hence the adoption of this component on the CELESTA payload and all the other sub-systems.

Experimental Results at PSI of the CY62167GE30 Cypress SRAM.

The burst detection and correction method described in Chapter 3 was driven by the urgent need of an efficient way to compensate and correct the effect of MCU events showing up on the CY62157EV30 SRAM memories. The future versions of the RadMon will require a new SRAM memory, completely unaffected by latchups (to overcome the burst effect) and with similar, or improved, characteristics when compared to the CY62157EV30, namely a high HEH cross-section, insensitivity to thermal neutrons and availability on the market. Other SRAM candidates were tested and results were presented in Chapter 3. The 16 Mbit CY62167GE30 SRAM, manufactured by Cypress with 65 nm technology, was the subject of a PSI test campaign, since the component was used already in other SEU monitor applications [133] and the device showed promising results. The SRAM was powered with 3.3 V, the embedded ECC correction code was disabled and tests were run in static mode. Results of each beam irradiation are reported in Table B.5. Two sample units were irradiated at the energies of 200, 150, 100, 60 and 30 MeV for DUT 1 and at 200 and 100 MeV for DUT 2. Both samples exhibited a relatively constant cross-section value independent on the beam energy. Both samples showed a mean σ of $\approx 4 \cdot 10^{-14}$ cm^2/bit with uncertainty in the order of 10^{-15} cm^2/bit for DUT 1 and 10^{-16} cm^2/bit for DUT 2. This result was considered highly promising. Further tests will be carried out in dynamic mode to assess the other required characteristics and fully qualify the component for a future use on the CERN RadMons.

Table B.5: Results of the CY62167GE30 SRAM PSI test in static mode.

Device #	**Beam Energy**	**Total Fluence [p/cm^2]**	**SEUs**	**σ [cm^2/bit]**	**mean σ [cm^2/bit]**	**Std. Dev σ [cm^2/bit]**
DUT 1	200	$5.19\cdot10^9$	4238	$4.87\cdot10^{-14}$	$4.96\cdot10^{-14}$	$1.34\cdot10^{-15}$
	200	$5.13\cdot10^9$	4340	$5.04\cdot10^{-14}$		
	200	$5.00\cdot10^9$	4169	$4.97\cdot10^{-14}$		
	200	$5.07\cdot10^9$	4035	$4.74\cdot10^{-14}$		
	200	$5.08\cdot10^9$	4291	$5.03\cdot10^{-14}$		
	200	$5.05\cdot10^9$	4332	$5.11\cdot10^{-14}$		
	150	$5.03\cdot10^9$	3775	$4.47\cdot10^{-14}$	$4.15\cdot10^{-14}$	$5.42\cdot10^{-15}$
	150	$5.02\cdot10^9$	2602	$3.09\cdot10^{-14}$		
	150	$5.07\cdot10^9$	3900	$4.58\cdot10^{-14}$		
	150	$5.02\cdot10^9$	3508	$4.17\cdot10^{-14}$		
	150	$5.02\cdot10^9$	3604	$4.28\cdot10^{-14}$		
	150	$5.01\cdot10^9$	3636	$4.33\cdot10^{-14}$		
	100	$5.02\cdot10^9$	3757	$4.46\cdot10^{-14}$	$4.56\cdot10^{-14}$	$1.39\cdot10^{-15}$
	100	$5.00\cdot10^9$	3699	$4.41\cdot10^{-14}$		
	100	$5.01\cdot10^9$	3865	$4.59\cdot10^{-14}$		
	100	$5.00\cdot10^9$	3940	$4.69\cdot10^{-14}$		
	100	$5.00\cdot10^9$	3750	$4.47\cdot10^{-14}$		
	100	$5.00\cdot10^9$	3985	$4.75\cdot10^{-14}$		
	60	$5.00\cdot10^9$	4484	$5.34\cdot10^{-14}$	$5.15\cdot10^{-14}$	$1.45\cdot10^{-15}$
	60	$5.01\cdot10^9$	4228	$5.03\cdot10^{-14}$		
	60	$5.00\cdot10^9$	4245	$5.06\cdot10^{-14}$		
	60	$5.00\cdot10^9$	4245	$5.06\cdot10^{-14}$		
	60	$5.01\cdot10^9$	4436	$5.27\cdot10^{-14}$		
	30	$5.00\cdot10^9$	4157	$4.96\cdot10^{-14}$	$4.75\cdot10^{-14}$	$3.5\cdot10^{-15}$
	30	$5.00\cdot10^9$	4168	$4.97\cdot10^{-14}$		
	30	$5.00\cdot10^9$	3641	$4.34\cdot10^{-14}$		
DUT 2	200	$5.14\cdot10^9$	3814	$4.42\cdot10^{-14}$	$4.36\cdot10^{-14}$	$6.63\cdot10^{-16}$
	200	$5.16\cdot10^9$	3714	$4.29\cdot10^{-14}$		
	200	$5.10\cdot10^9$	3730	$4.36\cdot10^{-14}$		
	100	$5.00\cdot10^9$	3582	$4.27\cdot10^{-14}$	$4.23\cdot10^{-14}$	$6.74\cdot10^{-16}$
	100	$5.05\cdot10^9$	3514	$4.15\cdot10^{-14}$		
	100	$5.02\cdot10^9$	3586	$4.26\cdot10^{-14}$		

ACKNOWLEDGEMENTS

«Why doing a PhD?». I was addressed this questions several times. In my case I had the following three motivations: first because doing research is definitely fun, second because it gave me the opportunity to dedicate this work to the persons that most supported me in my life, and third because we all love hard challenges.

For these reasons I need to thank the people that took part in the realization of this research work and that gave me the opportunity to carry it on. I wish to thank my professor, Laurent Dusseau, for introducing me to the CubeSat world and letting me advance in my formation through a wonderful work experience. I thank the whole teams of the CSU of Montpellier and the IES Laboratory. My supervisor at CERN, Paul Peronnard, for his technical advice and always helpful support, and Markus Brugger, who started CELESTA and trusted me in the development of this project.

I thank Alessandro Masi, my section leader, and all the people who worked with me in the EN-STI-ECE, in particular the ones I worked with during the radiation test campaigns: Salvatore Danzeca, Gilles Foucard, Ruben Garcia Alia, Timothee Machlanski, Philippe Boisseaux-Bourgeois and Anne Sophie Merlenghi.

I give thanks to Enrico Chesta and the CERN Knowledge Transfer, for believing in this first small satellite project and supporting me throughout the development of the thesis.

Finally I thank Giulia, my brother Gabriele and his family, my great 17021 area supporters uncle Mimmo and aunt Anna, and my wonderful colleagues Pascal Oser, Alessandro Danisi and Ricardo Picatoste, their presence was essential for my personal and professional growth. To them I give my deepest thanks and most heart felt "It can only get better!".

List of Publications

- P. Oser, G. Spiezia, M. Brugger, S. Danzeca, E. Fadakis, G. Foucard, R. G. Alia, R. Losito, A. Masi, J. Mekki, P. Peronnard, G. Ruggiero, R. Secondo, K. Stachyra, and R. Gaillard, "*Compendium of Radiation-Induced Effects for Candidate Particle Accelerator Electronics*", 2014 IEEE Radiation Effects Data Workshop (REDW), 2014, pp. 1-8.

- G. Spiezia, M. Brugger, S. Danzeca, R. G. Alia, R. Gaillard, E. Fadakis, G. Foucard, R. Losito, A. Masi, J. Mekki, P. Oser, P. Peronnard, G. Ruggiero, and R. Secondo, "*Compendium of Radiation-Induced Effects for Candidate Particle Accelerator Electronics*", in 2013 IEEE Radiation Effects Data Workshop (REDW), 2013, pp. 1-7.

- R. Secondo, G. Foucard, S. Danzeca, R. Losito, P. Peronnard, A. Masi, M. Brugger, and L. Dusseau, "*Analysis and Detection of Multiple Cell Upsets in SRAM Memories Used as Particle Detectors*", 2015 15th European Conference on Radiation and Its Effects on Components and Systems (RADECS), 2015, pp. 1-4.

- R. Secondo, G. Foucard, S. Danzeca, R. Losito, P. Peronnard, A. Masi, M. Brugger and L. Dusseau, "*Embedded Detection and Correction of SEU Bursts in SRAM Memories Used as Radiation Detectors*", IEEE Transactions on Nuclear Science, vol. PP, no. 99, pp. 1–8, 2016.

- A. Merlenghi, M. Brugger, E. Chesta, S. Danzeca, R. Garcia Alia, A. Masi, P. Peronnard, R. Secondo, M. Bernard, L. Dusseau and J.R. Vaillé, "*The CELESTA CubeSat Radiation Monitoring Mission*", in ESA 4S Symposium 2016, Malta, 2016, pp. 1-14.

- R. Secondo, P. Peronnard, M. Brugger, S. Danzeca, E. Chesta, A. Masi, R. Garcia Alia, A. Merlenghi, L. Dusseau, M. Bernard, and J.R. Vaillé, "*A Nanosatellite Radiation Qualification Procedure At The CHARM Facility Based On The CELESTA Payload Demonstrator*", in ESA 4S Symposium 2016, Malta, 2016, pp. 1-11.

- R. Secondo, R. Garcia Alia, P. Peronnard, M. Brugger, A. Masi, S. Danzeca, A. Merlenghi, J.R. Vaillé and L. Dusseau, "*Analysis of SEL on Commercial SRAM Memories For Latchup Detection and Protection in LEO Space Applications*", 2016 16th European Conference on Radiation and Its Effects on Components and Systems (RADECS), 2016.

- R. Secondo, R. Garcia Alia, P. Peronnard, M. Brugger, A. Masi, S. Danzeca, R. Ferraro, A. Merlenghi, J.R. Vaillé and L. Dusseau, "*Analysis of SEL on Commercial SRAM Memories and Mixed-Field Characterization of a Latchup Detection Circuit For LEO Space Applications*", submitted to IEEE TNS 2016.

- Ruben Garcia Alia, Markus Brugger, Salvatore Danzeca, Francesco Cerutti, Joao Pedro de Carvalho Saraiva, Reiner Denz, Alfredo Ferrari, Lionel L. Foro, Paul Peronnard, Raffaello Secondo, Jens Steckert, Yves Thurel, Iacopo Toccafondo, Slawosz Uznanski, "*Single Event Effects in High-Energy Accelerators*", Semiconductor Science and Technology Special Issue, 2016.

BIBLIOGRAPHY

[1] R. Ecoffet, "Anomalies associated with radiation effects and the role of space agencies," CERN, 2014. [Online]. Available: http://www.slideserve.com/olisa/anomalies-associated-with-radiation-e-ffects-and-the-role-of-space-agencies

[2] R. Garcia Alia *et al.*, "Radiation Fields in High Energy Accelerators and their impact on Single Event Effects," 2014. [Online]. Available: https://cds.cern.ch/record/2012360?ln=en

[3] E. Verrelli and D. Tsoukalas, "Radiation Hardness of Flash and Nanoparticle Memories," 2011. [Online]. Available: http://www.intechopen.com/books/flash-memories/radiation-hardness-of-flash-and-nanoparticle-memories

[4] A. Thornton, "CHARM Facility Test Area Radiation Field," CERN, Tech. Rep., 2015. [Online]. Available: https://edms.cern.ch/document/1552117/1

[5] R. Garcia Alia, M. Brugger, S. Danzeca, F. Cerutti, J. d. C. Saraiva, R. Denz, A. Ferrari, L. L. Foro, P. Peronnard, R. Secondo, J. Steckert, Y. Thurel, I. Toccafondo, and S. Uznanski, "Single Event Effects in High-Energy Accelerators," *Semiconductor Science and Technology*, 2016.

[6] C. press release, "First Beam in the LHC - Accelerating Science," 2008. [Online]. Available: press.web.cern.ch

[7] G. Aad *et al.*, "Observation of a new particle in the search for the Standard Model Higgs boson with the ATLAS detector at the LHC," *Physics Letters B*, vol. 716, no. 1, pp. 1–29, Sep. 2012. [Online]. Available: http://www.sciencedirect.com/science/article/pii/S037026931200857X

[8] G. Apollinari, B. Alonso, O. Bruning, M. Lamont, and L. Rossi, "High-Luminosity Large Hadron Collider (HL-LHC)," 2015. [Online]. Available: http://cds.cern.ch/record/2116337

[9] C. press release, "Chicago sees floods of LHC data and new results at the ICHEP 2016 conference | Media and Press Relations," 2016. [Online]. Available: http://press.cern/press-releases/2016/08/chicago-sees-floods-lhc-data-and-new-results-ichep-2016-conference

[10] Keck CalTech, "Small Satellites: A Revolution in Space Science," California Institute of Technology, Pasadena, CA, Tech. Rep., 2014.

[11] M. H. Heidt, P. J. Puig-suari, P. Augustus, S. Moore, P. S. Nakasuka, P. Robert, and J. Twiggs, *SSC00-V-5 CubeSat: A new Generation of Picosatellite for Education and Industry Low-Cost Space Experimentation*, 2000.

[12] K. Rainey, "Largest Flock of Earth-Imaging Satellites Launch Into Orbit From Space," Sep. 2016. [Online]. Available: http://www.nasa.gov/mission_pages/station/research/news/flock_1

[13] "The QB50 Project," 2015. [Online]. Available: https://www.qb50.eu/index.php/community

[14] "ClydeSpace." [Online]. Available: https://www.clyde.space/

[15] "ISC Kosmotras." [Online]. Available: http://www.kosmotras.ru/en/company/

[16] "4skies." [Online]. Available: http://www.4skies.net/

[17] "Spacex." [Online]. Available: http://www.spacex.com/

[18] "RocketLab." [Online]. Available: https://www.rocketlabusa.com/

[19] Euroconsult Executive Report, "Prospects for the Small Satellite Market - Euroconsult Shop," 2016. [Online]. Available: http://www.euroconsult-ec.com/shop/space-industry/82-smallsats.html

[20] L. Dusseau, J. R. Vaille, F. Saigne, J. Gasiot, L. Cresciucci, D. Campillo, C. Chatry, U. Fink, J. Gruenenfelder, P. Calvel, and J. D. Gayrard, "CUBE SAT SACRED : a student project to investigate radiation effects," in *2005 8th European Conference on Radiation and Its Effects on Components and Systems*, Sep. 2005, pp. H2–1–H2–4.

[21] M. Bernard, L. Dusseau, and V. Muravyev, "Orbital Parameters Drift of Seven Vega Maiden Flight CubeSats," in *Proc. of the ESA 4S Symposium 2014*, 2014, pp. 1–2.

[22] "Esa 4s sympsoium 2016," 2016. [Online]. Available: http://esaconferencebureau.com/4S2016/home

[23] A. Apollonio *et al.*, "HL-LHC: Integrated Luminosity And Availability," in *Proceedings of IPAC2013*, vol. TUPFI012, Shanghai, China, 2013, pp. 1352–1354. [Online]. Available: http://accelconf.web.cern.ch/AccelConf/IPAC2013/papers/tupfi012.pdf

[24] M. Brugger and other, "Radiation Damage To Electronics At The LHC," in *Proceedings of IPAC2012*, vol. THPPP006, New Orleans, USA, 2012, pp. 3734–3736. [Online]. Available: http://accelconf.web.cern.ch/accelconf/IPAC2012/papers/thppp006.pdf

[25] M. Brugger *et al.*, "FLUKA Capabilities and CERN Applications for the Study of Radiation Damage to Electronics at High-Energy Hadron Accelerators," *Progress in NUCLEAR SCIENCE and TECHNOLOGY*, vol. 2, pp. 948–954, 2011.

[26] G. Battistoni, F. Cerutti, A. Fassò, A. Ferrari, S. Muraro, J. Ranft, S. Roesler, and P. R. Sala, "The FLUKA code: description and benchmarking," in *AIP Conference Proceedings*, vol. 896. AIP Publishing, Mar. 2007, pp. 31–49. [Online]. Available: http://scitation.aip.org/content/aip/proceeding/aipcp/10.1063/1.2720455

[27] T. Bohlen, F. Cerutti, M. Chin, A. Fasso, A. Ferrari, P. Ortega, A. Mairani, P. Sala, G. Smirnov, and V. Vlachoudis, "The FLUKA Code: Developments and Challenges for High Energy and Medical Applications," *Nuclear Data Sheets*, vol. 120, pp. 211–214, 2014.

[28] F. Faccio *et al.*, "COTS for the LHC radiation environment: the rules of the game," 2000.

[29] O. Flament, J. Baggio, S. Bazzoli, S. Girard, J. Raimbourg, J. E. Sauvestre, and J. L. Leray, "Challenges for embedded electronics in systems used in future facilities dedicated to international physics programs," in *2009 First International Conference on Advancements in Nuclear Instrumentation Measurement Methods and their Applications (ANIMMA)*, Jun. 2009, pp. 1–5.

[30] K. Roed, V. Boccone, M. Brugger, A. Ferrari, D. Kramer, E. Lebbos, R. Losito, A. Mereghetti, G. Spiezia, and R. Versaci, "FLUKA Simulations for SEE Studies of Critical LHC Underground Areas," *IEEE Transactions on Nuclear Science*, vol. 58, no. 3, pp. 932–938, Jun. 2011.

[31] F. Ravotti, "Development and Characterisation of Radiation Monitoring Sensors for the High Energy Physics Experiments of the CERN LHC Accelerator," CERN Thesis, 2006. [Online]. Available: http://cds.cern.ch/record/1014776

[32] H. L. Hughes and J. M. Benedetto, "Radiation effects and hardening of MOS technology: devices and circuits," *IEEE Transactions on Nuclear Science*, vol. 50, no. 3, pp. 500–521, Jun. 2003.

[33] M. Bagatin and S. Gerardin, Eds., *Ionizing Radiation Effects in Electronics: From Memories to Imagers*, 1st ed. Boca Raton ; London ; New York: CRC Press, Nov. 2015.

[34] "Tyndall Works P-Channel RADFET," 2013. [Online]. Available: http://www.tyndallworks.com/products-radfet.html

[35] A. Holmes-Siedle, *Handbook of radiation effects*. Oxford University Press, 2002.

[36] W. Dawes, "Radiation Effects Hardening Techniques," IEEE NSREC Short Course, Monterey, CA, 1985.

[37] G. F. E. Gene, N. C. Lee, T. K. Tong, and D. Sim, "Impact on Latchup Immunity due to the Switch From Epitaxial to Bulk Substrate," in *2006 IEEE International Symposium on Semiconductor Manufacturing*, Sep. 2006, pp. 156–159.

[38] R. Hull, *Properties of Crystalline Silicon*. The Institution of Engineering and Technology, Jan. 1999.

[39] M. Moll, "Radiation damage in silicon particle detectors: Microscopic defects and macroscopic properties," DESY-THESIS-1999-040, 1999.

[40] T. Wijnands *et al.*, "An on line radiation monitoring system for the LHC machine and experimental caverns," in *Proc. 12th Workshop Electron. LHC Future Exp.*, 2006, pp. 113–117. [Online]. Available: https://cds.cern.ch/record/1027423/files/p113.pdf

[41] A. Mohammadzadeh, H. Evans, P. Nieminen, E. Daly, P. Vuilleumier, P. Buhler, C. Eggel, W. Hajdas, N. Schlumpf, A. Zehnder, J. Schneider, and R. Fear, "The ESA Standard Radiation Environment Monitor program first results from PROBA-I and INTEGRAL," *IEEE Transactions on Nuclear Science*, vol. 50, no. 6, pp. 2272–2277, Dec. 2003.

[42] J. O. Goldsten, R. H. Maurer, P. N. Peplowski, A. G. Holmes-Siedle, C. C. Herrmann, and B. H. Mauk, "The Engineering Radiation Monitor for the Radiation Belt Storm Probes Mission," *Space Science Reviews*, vol. 179, no. 1-4, pp. 485–502, Nov. 2013. [Online]. Available: http://link.springer.com/article/10.1007/s11214-012-9917-x

[43] G. Spiezia, P. Peronnard, A. Masi, M. Brugger, M. Brucoli, S. Danzeca, R. Alia, R. Losito, J. Mekki, P. Oser, R. Gaillard, and L. Dusseau, "A New RadMon Version for the LHC and its Injection Lines," *IEEE Transactions on Nuclear Science*, vol. 61, no. 6, pp. 3424–3431, Dec. 2014.

[44] S. Danzeca, "The new version of the Radiation Monitor system for the electronics at CERN. Electronic components radiation hardness assurance and sensors qualification," CERN Thesis, 2014.

[45] "The CERN RadWG website," 2015. [Online]. Available: http://radwg.web.cern.ch/RadWG/

[46] "GSFC Radiation Data Base," 2016. [Online]. Available: http://radhome.gsfc.nasa.gov/radhome/raddatabase/raddatabase.html

[47] "ESCIES (European Space Components Information Exchange System)," 2016. [Online]. Available: https://escies.org/#&panel1-1

[48] "Rad Hard Space Products, Space & High Reliability," 2016. [Online]. Available: http://www.ti.com/lsds/ti/space-high-reliability/space.page#ampcomp

[49] G. Spiezia, M. Brugger, S. Danzeca, R. Alia, R. Gaillard, E. Fadakis, G. Foucard, R. Losito, A. Masi, J. Mekki, P. Oser, P. Peronnard, G. Ruggiero, and R. Secondo, "Compendium of Radiation-Induced Effects for Candidate Particle Accelerator Electronics," in *2013 IEEE Radiation Effects Data Workshop (REDW)*, Jul. 2013, pp. 1–7.

[50] C. S. Dyer, S. N. Clucas, C. Sanderson, A. D. Frydland, and R. T. Green, "An experimental study of single-event effects induced in commercial SRAMs by neutrons and protons from thermal energies to 500 MeV," *IEEE Transactions on Nuclear Science*, vol. 51, no. 5, pp. 2817–2824, Oct. 2004.

[51] R. C. Baumann *et al.*, "Radiation-induced soft errors in advanced semiconductor technologies," *IEEE Transactions on Device and Materials Reliability*, vol. 5, no. 3, pp. 305–316, Sep. 2005.

[52] S. Danzeca, G. Spiezia, M. Brugger, L. Dusseau, G. Foucard, R. Alia, P. Mala, A. Masi, P. Peronnard, J. Soltes, A. Thornton, and L. Viererbl, "Qualification and Characterization of SRAM Memories Used as Radiation Sensors in the LHC," *IEEE Transactions on Nuclear Science*, vol. 61, no. 6, pp. 3458–3465, Dec. 2014.

[53] "HL-LHC integration meeting n51: R2E," 5 August 2016. [Online]. Available: https://indico.cern.ch/event/559454/

[54] J. Mekki, M. Brugger, R. G. Alia, A. Thornton, N. C. D. S. Mota, and S. Danzeca, "A Mixed Field Facility at CERN for Radiation Test: CHARM," in *2015 15th European Conference on Radiation and Its Effects on Components and Systems (RADECS)*, Sep. 2015, pp. 1–4.

[55] S. Bonaldo, "CHARM - A New Mixed-field facility for Ionizing Radiation Test of Electronics at CERN," CERN Thesis, 2016.

[56] R. G. Alia, M. Brugger, S. Danzeca, V. Ferlet-Cavrois, C. Frost, R. Gaillard, J. Mekki, F. Saigné, A. Thornton, S. Uznanski, and F. Wrobel, "SEL Hardness Assurance in a Mixed Radiation Field," *IEEE Transactions on Nuclear Science*, vol. 62, no. 6, pp. 2555–2562, Dec. 2015.

[57] W. Hajdas, F. Burri, C. Eggel, R. Harboe-Sorensen, and R. d. Marino, "Radiation effects testing facilities in PSI during implementation of the Proscan project," in *2002 IEEE Radiation Effects Data Workshop*, 2002, pp. 160–164.

[58] M. Shippers, "First Year Of Operation Of PSI's New SC Cyclotron And Beam Lines For Proton Therapy," in *Cyclotrons and Their Applications 2007, Eighteenth International Conference*, 2007.

[59] Y. H. Luo, X. Q. Guo, G. Guo, H. Fan, and W. Hajdas, "Beam calibration verification of the Beijing HI-13 Tandem accelerator based on the ESA SEU Monitor," in *2013*

IEEE Nuclear Science Symposium and Medical Imaging Conference (2013 NSS/MIC), Oct. 2013, pp. 1–5.

[60] J. Barak, E. Adler, Y. Lifshitz, and J. Levinson, "Detecting heavy ions and protons in space: single-events monitor," in *, Eighteenth Convention of Electrical and Electronics Engineers in Israel, 1995*, Mar. 1995, pp. 5.5.1/1–5.5.1/3.

[61] D. Kramer, M. Brugger, V. Klupak, C. Pignard, K. Roeed, G. Spiezia, L. Viererbl, and T. Wijnands, "LHC RadMon SRAM Detectors Used at Different Voltages to Determine the Thermal Neutron to High Energy Hadron Fluence Ratio," *IEEE Transactions on Nuclear Science*, vol. 58, no. 3, pp. 1117–1122, 2011.

[62] N. Sukhaseum *et al.*, "Single event upset cross section dose dependence on 90 nm SRAM," in *RADECS 2012*, vol. DW-5, 2012.

[63] J. Tausch, D. Sleeter, D. Radaelli, and H. Puchner, "Neutron Induced Micro SEL Events in COTS SRAM Devices," in *2007 IEEE Radiation Effects Data Workshop*, vol. 0, Jul. 2007, pp. 185–188.

[64] J. S. S. T. Association, "Measurement and Reporting of Alpha Particle and Terrestrial Cosmic Ray-Induced Soft Errors in Semiconductor Devices," 2001.

[65] G. Tsiligiannis, L. Dilillo, A. Bosio, P. Girard, S. Pravossoudovitch, A. Todri, A. Virazel, J. Mekki, M. Brugger, F. Wrobel, and F. Saigne, "Evaluating a radiation monitor for mixed-field environments based on SRAM technology," *Journal of Instrumentation*, vol. 9, no. 05, p. C05052, May 2014. [Online]. Available: http://iopscience.iop.org/1748-0221/9/05/C05052

[66] R. Secondo, G. Foucard, S. Danzeca, R. Losito, P. Peronnard, A. Masi, M. Brugger, and L. Dusseau, "Analysis and Detection of Multiple Cell Upsets in SRAM Memories Used as Particle Detectors," in *2015 15th European Conference on Radiation and Its Effects on Components and Systems (RADECS)*, Sep. 2015, pp. 1–4.

[67] G. Tsiligiannis, L. Dilillo, A. Bosio, P. Girard, S. Pravossoudovitch, A. Todri, A. Virazel, H. Puchner, C. Frost, F. Wrobel, and F. Saigné, "Multiple Cell Upset Classification in Commercial SRAMs," *IEEE Transactions on Nuclear Science*, vol. 61, no. 4, pp. 1747–1754, Aug. 2014.

[68] F. Wrobel, J.-M. Palau, M.-C. Calvet, O. Bersillon, and H. Duarte, "Simulation of nucleon-induced nuclear reactions in a simplified SRAM structure: scaling effects on SEU and MBU cross sections," *IEEE Transactions on Nuclear Science*, vol. 48, no. 6, pp. 1946–1952, Dec. 2001.

[69] A. Tipton, J. Pellish, R. Reed, R. Schrimpf, R. Weller, M. Mendenhall, B. Sierawski, A. Sutton, R. Diestelhorst, G. Espinel, J. Cressler, P. Marshall, and G. Vizkelethy, "Multiple-Bit Upset in 130 nm CMOS Technology," *IEEE Transactions on Nuclear Science*, vol. 53, no. 6, pp. 3259–3264, Dec. 2006.

[70] G. Spiezia *et al.*, "PSI radiation test - CYPRESS 03.06.2011," CERN, Tech. Rep., 2011. [Online]. Available: https://edms.cern.ch/document/1219136/1

[71] H. Puchner, "Soft Errors - No Way To Escape," 2012. [Online]. Available: https://ewh.ieee.org/r6/scv/eds/slides/20081014-Helmut-Puchner-CypressSemi.pdf

[72] H. Puchner, R. Kapre, S. Sharifzadeh, J. Majjiga, R. Chao, D. Radaelli, and S. Wong, "Elimination of Single Event Latchup in 90nm SRAM Technologies," in *Reliability Physics Symposium Proceedings, 2006. 44th Annual., IEEE International*, Mar. 2006, pp. 721–722.

[73] J. R. Schwank, P. E. Dodd, M. R. Shaneyfelt, J. A. Felix, G. L. Hash, V. Ferlet-Cavrois, P. Paillet, J. Baggio, P. Tangyunyong, and E. Blackmore, "Issues for single-event proton testing of SRAMs," *IEEE Transactions on Nuclear Science*, vol. 51, no. 6, pp. 3692–3700, Dec. 2004.

[74] R. Secondo, G. Foucard, S. Danzeca, R. Losito, P. Peronnard, A. Masi, M. Brugger, and L. Dusseau, "Embedded Detection and Correction of SEU Bursts in SRAM Memories Used as Radiation Detectors," *IEEE Transactions on Nuclear Science*, vol. 63, no. 4, pp. 2168–2175, Aug. 2016.

[75] S. Danzeca, J. Cesari, M. Brugger, L. Dusseau, A. Masi, A. Pineda, and G. Spiezia, "Characterization and Modeling of a Floating Gate Dosimeter with Gamma and Protons at Various Energies," *IEEE Transactions on Nuclear Science*, vol. 61, no. 6, pp. 3451–3457, Dec. 2014.

[76] M. V. O Bryan, "Current Single Event Effects and Radiation Damage Results for Candidate Spacecraft Electronics," *NSREC*, 2002. [Online]. Available: http://radhome.gsfc.nasa.gov/radhome/papers/NSREC02_W16.pdf

[77] M. O Bryan, "Radiation Damage and Single Event Effect Results for Candidate Spacecraft Electronics," 2000. [Online]. Available: http://edge.rit.edu/edge/P13271/public/Datasheets/Radiation/nsrec00_W21.pdf

[78] "The CELESTA Mission," 2014. [Online]. Available: https://celesta.web.cern.ch/celesta/

[79] M. Guyot, S. Denise, L. Dusseau, F. Saigné, M. Bernard, P. Claudé, and M. Dudeck, "Electrostatic propulsion for satellites application to the Robusta-3 nanosatellite," *IEEE Transactions on Dielectrics and Electrical Insulation*, vol. 21, no. 3, pp. 1161–1165, Jun. 2014.

[80] "The JUICE Mission," 2015. [Online]. Available: http://sci.esa.int/juice/

[81] J. S. George, K. A. Lave, M. E. Wiedenbeck, W. R. Binns, A. C. Cummings, A. J. Davis, G. A. d. Nolfo, P. L. Hink, M. H. Israel, R. A. Leske, R. A. Mewaldt, L. M. Scott, E. C. Stone, T. T. v. Rosenvinge, and N. E. Yanasak, "Elemental

Composition and Energy Spectra of Galactic Cosmic Rays During Solar Cycle 23," *The Astrophysical Journal*, vol. 698, no. 2, p. 1666, 2009. [Online]. Available: http://stacks.iop.org/0004-637X/698/i=2/a=1666

[82] M. Tali *et al.*, "Mono energetic electron induced single event effects at the VESPER facility," in *Proc. of RADECS 2016*, 2016.

[83] S. E. Standard, "TEC-EES - ECSS Space Environment Standard," 2012. [Online]. Available: http://space-env.esa.int/index.php/ECSS-10-4.html

[84] "STELA Logiciels Gratuits," 2000. [Online]. Available: https://logiciels.cnes.fr/content/stela

[85] CNES, "STELA User's Guide," Oct. 2013. [Online]. Available: https://logiciels.cnes.fr/sites/default/files/Stela-User-Manual.pdf

[86] "OMERE Software TRAD," 2000. [Online]. Available: http://www.trad.fr/OMERE-Software.html

[87] G. Spiezia *et al.*, "IFE Radiation Test - Cypress Memory 12.05.2011," Tech. Rep., 2011. [Online]. Available: https://edms.cern.ch/document/1219128/1

[88] A. Merlenghi, M. Brugger, E. Chesta, S. Danzeca, R. Garcia Alia, A. Masi, P. Peronnard, R. Secondo, M. Bernard, L. Dusseau, and J. Vaille, "The CELESTA CubeSat Radiation Monitoring Mission," in *ESA 4S Symposium 2016*, Malta, Jun. 2016, pp. 1–14.

[89] A.-S. Merlenghi, "CELESTA (CERN Latchup STudent sAtellite) Project Pre-Study," Master Thesis, 2014.

[90] R. G. Alia *et al.*, "Radiation Fields in High Energy Accelerators and their impact on Single Event Effects." [Online]. Available: https://cds.cern.ch/record/2012360?ln=it

[91] K. Avery, J. Finchel, J. Mee, W. Kemp, R. Netzer, D. Elkins, B. Zufelt, and D. Alexander, "Total Dose Test Results for CubeSat Electronics," in *2011 IEEE Radiation Effects Data Workshop*, Jul. 2011, pp. 1–8.

[92] A. Masi, S. Danzeca, R. Losito, P. Peronnard, R. Secondo, and G. Spiezia, "A high precision radiation-tolerant LVDT conditioning module," *Nuclear Instruments and Methods in Physics Research Section A: Accelerators, Spectrometers, Detectors and Associated Equipment*, vol. 745, pp. 73–81, May 2014. [Online]. Available: http://www.sciencedirect.com/science/article/pii/S0168900214001053

[93] P. Oser, G. Spiezia, M. Brugger, S. Danzeca, E. Fadakis, G. Foucard, R. Alia, R. Losito, A. Masi, J. Mekki, P. Peronnard, G. Ruggiero, R. Secondo, K. Stachyra, and

R. Gaillard, "Compendium of Radiation-Induced Effects for Candidate Particle Accelerator Electronics," in *2014 IEEE Radiation Effects Data Workshop (REDW)*, Jul. 2014, pp. 1–8.

[94] R. Alia, M. Brugger, S. Danzeca, V. Ferlet-Cavrois, C. Poivey, K. Roed, F. Saigne, G. Spiezia, S. Uznanski, and F. Wrobel, "SEE Measurements and Simulations Using Mono-Energetic GeV-Energy Hadron Beams," *IEEE Transactions on Nuclear Science*, vol. 60, no. 6, pp. 4142–4149, Dec. 2013.

[95] R. Secondo, P. Peronnard, M. Brugger, S. Danzeca, E. Chesta, A. Masi, R. Garcia Alia, A. Merlenghi, L. Dusseau, M. Bernard, and J. Vaille, "A Nanosatellite Radiation Qualification Procedure At The CHARM Facility Based On The CELESTA Payload Demonstrator," in *ESA 4S Symposium 2016*, Malta, Jun. 2016, pp. 1–11.

[96] "Trapped Proton Models - CREME-MC," 2000. [Online]. Available: https://creme.isde.vanderbilt.edu/CREME-MC/help/ap8min-and-ap8max-trapped-proton-models

[97] R. Harboe-Sorensen, C. Poivey, A. Zadeh, A. Keating, N. Fleurinck, K. Puimege, F. X. Guerre, F. Lochon, M. Kaddour, L. Li, and D. Walter, "PROBA-II Technology Demonstration Module In-Flight Data Analysis," *IEEE Transactions on Nuclear Science*, vol. 59, no. 4, pp. 1086–1091, Aug. 2012.

[98] M. Shoga and D. Binder, "Theory of Single Event Latchup in Complementary Metal-Oxide Semiconductor Integrated Circuits," *IEEE Transactions on Nuclear Science*, vol. 33, no. 6, pp. 1714–1717, Dec. 1986.

[99] "The trad guard system," 2000. [Online]. Available: http://www.trad.fr/Guard-system.html

[100] "Geotest Test Solutions." [Online]. Available: http://www.marvintest.com/Newsletters/2011/November/solution_spotlight.html

[101] K. Chen, H. Chen, J. Kierstead, H. Takai, S. Rescia, X. Hu, H. Xu, J. Mead, F. Lanni, and M. Minelli, "Evaluation of commercial ADC radiation tolerance for accelerator experiments," Nov. Cornell University Library arXiv, 2014. [Online]. Available: https://arxiv.org/abs/1411.7027

[102] D. Truyen, E. Leduc, and F. Braud, "Elimination of Single Event Latch-Up in the ATMEL ATMX150rha Rad-Hard CMOS 150nm Cell-Based ASIC Family," in *2015 15th European Conference on Radiation and Its Effects on Components and Systems (RADECS)*, Sep. 2015, pp. 1–3.

[103] "Radiation induced single event latchup protection and recovery of integrated circuits," Patent, 2000, classificazione Stati Uniti 361/111, 257/E27.063, 257/E23.114; Classificazione internazionale H01L23/552, H01L27/092, H01L27/02;. [Online]. Available: http://www.google.com/patents/US6064555

[104] D. Chen, S. Buchner, A. Phan, H. Kim, A. Sternberg, D. McMorrow, and K. LaBel, "The Effects of Elevated Temperature on Pulsed-Laser-Induced Single Event Transients in Analog Devices," *IEEE Transactions on Nuclear Science*, vol. 56, no. 6, pp. 3138–3144, Dec. 2009.

[105] S. Larsson and S. Mattsson, "Heavy Ion Transients in Operational Amplifier of Type LM124, RH1014 and OP27," ESA/ESTEC, 2004.

[106] F. Roig, L. Dusseau, A. Khachatrian, N.-H. Roche, A. Privat, J.-R. Vaille, J. Boch, J. Warner, F. Saigne, S. Buchner, D. McMorrow, P. Ribeiro, G. Auriel, B. Azais, R. Marec, P. Calvel, F. Bezerra, and R. Ecoffet, "Modeling and Investigations on TID-ASETs Synergistic Effect in LM124 Operational Amplifier From Three Different Manufacturers," *IEEE Transactions on Nuclear Science*, vol. 60, no. 6, pp. 4430–4438, Dec. 2013.

[107] R. Harboe-Sorensen, C. Poivey, N. Fleurinck, K. Puimege, A. Zadeh, F. X. Guerre, F. Lochon, M. Kaddour, L. Li, D. Walter, A. Keating, A. Jaksic, and M. Poizat, "The Technology Demonstration Module On-Board PROBA-II," *IEEE Transactions on Nuclear Science*, vol. 58, no. 3, pp. 1001–1007, Jun. 2011.

[108] J. Felix, J. Schwank, M. Shaneyfelt, J. Baggio, P. Paillet, V. Ferlet-Cavrois, P. Dodd, S. Girard, and E. Blackmore, "Test procedures for proton-induced single event latchup in space environments," in *9th European Conference on Radiation and Its Effects on Components and Systems, 2007. RADECS 2007*, Sep. 2007, pp. 1–5.

[109] J. Schwank, M. Shaneyfelt, J. Baggio, P. Dodd, J. Felix, V. Ferlet-Cavrois, P. Paillet, D. Lambert, F. Sexton, G. Hash, and E. Blackmore, "Effects of particle energy on proton-induced single-event latchup," *IEEE Transactions on Nuclear Science*, vol. 52, no. 6, pp. 2622–2629, Dec. 2005.

[110] A. H. Johnson, G. M. Swift, and L. D. Edmonds, "Latchup in integrated circuits from energetic protons," *IEEE Transactions on Nuclear Science*, vol. 44, no. 6, pp. 2367–2377, Dec. 1997.

[111] Y. Iwamoto, M. Hagiwara, D. Satoh, S. Araki, H. Yashima, T. Sato, A. Masuda, T. Matsumoto, N. Nakao, T. Shima, T. Kin, Y. Watanabe, H. Iwase, and T. Nakamura, "Characterization of high-energy quasi-monoenergetic neutron energy spectra and ambient dose equivalents of 80–389 MeV 7 Li(p,n) reactions using a time-of-flight method," *Nucl.Instrum.Meth.*, vol. A804, pp. 50–58, Dec. 2015.

[112] J. S. JESD89A, "Measurement and Reporting Of Alpha Particle And Terrestrial Cosmic Ray Induced Soft Errors In Semiconductor Devices," 2006. [Online]. Available: https://www.jedec.org/standards-documents/docs/jesd-89a

[113] H. Becker, T. Miyahira, and A. Johnston, "Latent damage in CMOS devices from single-event latchup," *IEEE Transactions on Nuclear Science*, vol. 49, no. 6, pp. 3009–3015, Dec. 2002.

[114] F. Bezerra, "Evidence of Destructive Single Event Latch-Up on Various Devices Using TILU2 Test System," CNES-ESA Radiation Final Presentation days, Mar. 2015. [Online]. Available: https://escies.org/webdocument/showArticle?id=1009

[115] S. Perez, S. Jarrix, N. J.-H. Roche, J. Boch, J.-R. Vaillé, A. Pénarier, M. Saleman, and L. Dusseau, "ROBUSTA, a Student Satellite to Serve the Radiation Effects Community," *AIAA/USU Conference on Small Satellites*, Aug. 2009. [Online]. Available: http://digitalcommons.usu.edu/smallsat/2009/all2009/85

[116] T. C. Program, "CubeSat Design Specification Rev. 13," 2014. [Online]. Available: http://www.academia.edu/11525487/CubeSat_Design_Specification_Rev._13_The_CubeSat_Program_Cal_Poly_SLO_CubeSat_Design_Specification_CDS_REV_13_Document_Classification_X_Public_Domain_ITAR_Controlled_Internal_Only

[117] X. Sun and X. Wu, "A cubesat attitude control system with linear piezoelectric actuator," in *Proceedings of the 2014 Symposium on Piezoelectricity, Acoustic Waves, and Device Applications*, Oct. 2014, pp. 72–75.

[118] D. Selva and D. Krejci, "A survey and assessment of the capabilities of Cubesats for Earth observation," *Acta Astronautica*, vol. 74, pp. 50–68, May 2012. [Online]. Available: http://www.sciencedirect.com/science/article/pii/S0094576511003742

[119] A. Thurn, "A Nichrome Burn Wire Release Mechanism for CubeSats," in *Proceedings of the 41st Aerospace Mechanisms Symposium*, Jet Propulsion Laboratory, 2012. [Online]. Available: https://www.nrl.navy.mil/PressReleases/2014/AMS%20Paper%20-%20A%20Nichrome%20Burn%20Wire%20Release%20Mechanism%20for%20CubeSats%20-%20Final%20-%20Adam%20Thurn.pdf

[120] C. A. Balanis, *Antenna Theory: Analysis and Design, 3rd Edition*, 3rd ed. Hoboken, NJ: Wiley-Interscience, Apr. 2005.

[121] R. B. GmbH, "CAN Specification, Version 2.0," 1991. [Online]. Available: http://www.bosch-semiconductors.de/media/ubk_semiconductors/pdf_1/canliteratur/can2spec.pdf

[122] J. R. Vaille, F. Ravotti, P. Garcia, M. Glaser, S. Matias, K. Idri, J. Boch, E. Lorfevre, P. J. McNulty, F. Saigne, and L. Dusseau, "Online dosimetry based on optically stimulated luminescence materials," *IEEE Transactions on Nuclear Science*, vol. 52, no. 6, pp. 2578–2582, Dec. 2005.

[123] F. Yilmaz, O. O. Haktanir, and A. B. Uygur, "Quasi-static structural test of satellites," in *2015 7th International Conference on Recent Advances in Space Technologies (RAST)*, Jun. 2015, pp. 421–424.

[124] ECSS-E-HB-32-26A, *Spacecraft Mechanical Loads Analysis Handbook*. ECSS Secretariat ESA-ESTEC Noordwijk, Feb. 2013, vol. issue 1.

[125] M. Brucoli, "A complete qualification of Floating Gate Dosimeter for CERN applications," in *Proc. of RADECS16*, Bremen, 2016.

[126] J. Likar, S. Stone, R. Lombardi, and K. Long, "Novel Radiation Design Approach for CubeSat Based Missions," *AIAA/USU Conference on Small Satellites*, Aug. 2010. [Online]. Available: http://digitalcommons.usu.edu/smallsat/2010/all2010/15

[127] TRAD, "FASTRAD Software, the 3d CAD Tool For Radiation Shielding Analysis," 2016. [Online]. Available: http://www.fastrad.net/

[128] E. S. E. Standard, "ECSS-E-ST-10-12c - Methods for the calculation of radiation received and its effects, and a policy for design margins," Nov. 2008.

[129] M. Soubra, J. Cygler, and G. Mackay, "Evaluation of a dual bias dual metal oxide-silicon semiconductor field effect transistor detector as radiation dosimeter," *Medical Physics*, vol. 21, no. 4, pp. 567–572, Apr. 1994.

[130] "The CubeSats Fly Your Satellite! Program," 2016. [Online]. Available: http://www.esa.int/Education/CubeSats_-_Fly_Your_Satellite

[131] R. Secondo *et al.*, "PSI_testreport_ad8029_ad8030, CERN Document 1729078 (v.1)," 2016. [Online]. Available: https://edms.cern.ch/ui/#!master/navigator/document?D:1888376163:1888376163:subDocs

[132] P. Oser *et al.*, "CEA Radiation Test Report LM317d2t, LM337imp, LM334, OPA2227, LM45, INA146, CERN Document 1386559 (v.1)," 2013. [Online]. Available: https://edms.cern.ch/ui/#!master/navigator/document?D:1576333925:1576333925:subDocs

[133] F. J. Franco and R. Velazco, "A Portable Low-Cost SEU Evaluation Board for SRAMs," in *2007 Spanish Conference on Electron Devices*, Jan. 2007, pp. 165–168.